High-Energy Neutrino Scan of the Galactic Plane

Sirin Odrowski

Dissertation
submitted to the
Combined Faculties of the Natural Sciences and Mathematics
of the Ruperto-Carola-University of Heidelberg, Germany
for the degree of
Doctor of Natural Sciences

Put forward by
Sirin Odrowski
born in Hannover, Germany
oral examination: 23.01.2012

High-Energy Neutrino Scan of the Galactic Plane

Referees: Prof. Dr. Werner Hofmann
Prof. Dr. Marek Kowalski

Abstract

Various searches for galactic high-energy neutrino sources with the neutrino telescopes IceCube and AMANDA are presented. The analysis uses data collected during 2008-2009 when IceCube was half-completed. With AMANDA as an integrated part of the detector, the performance of IceCube below 10 TeV is improved significantly, opening new possibilities to improve the search for soft-spectra neutrino sources. The presented work provided important input to the design of DeepCore, the low-energy extension of IceCube, since it has established that the sensitivity to galactic neutrino sources can be enhanced by the collection of a higher number of neutrino candidates in the 100 GeV to 10 TeV range despite the higher background in this region.
IceCube's currently best soft-spectra upper limits for the Galactic Plane, for six galactic sources and for the star-forming "Cygnus" region have been obtained in this work. The sensitivity improved by at least a factor two with respect to the predecessor analysis.
During the realization of this data analysis, IceCube nearly doubled its instrumented volume from 40 to 79 strings, including the advanced low-energy array DeepCore. The entire preparatory work for an All-Sky point source analysis with the nearly full detector has been performed. This thesis concludes with an outlook on the potential of the analysis of the IceCube 79-strings data.

Zusammenfassung

In der vorliegenden Arbeit werden die Ergebnisse mehrerer Suchen nach galaktischen Quellen hochenergetischer Neutrinos mit den Neutrinoteleskopen IceCube und AMANDA vorgestellt. Die Analyse basiert auf Daten, die im Zeitraum 2008-2009 mit dem zur Hälfte fertiggestellten IceCube-Detektor genommen wurden. Durch die Einbeziehung von AMANDA als integriertem Teil des Detektors konnte die Effizienz von IceCube unterhalb von 10 TeV signifikant erhöht werden. Dadurch bot sich insbesondere die Möglichkeit einer sensitiveren Suche nach Neutrinoquellen mit weichen Energiespektren.
Die Sensitivität der Analyse konnte im Vergleich zur Vorgängeranalyse mindestens verdoppelt werden. Im Rahmen dieser Arbeit wurden IceCubes zurzeit beste Obergrenzen an Neutrinoemissionen mit weichen Energiespektren in der Galaktischen Ebene, für sechs galaktische Quellen und die sternbildende Cygnus-Region erhalten.
Die hier präsentierte Arbeit zeigt unter anderem mit Hilfe von AMANDA, dass die Sensitivität für weiche Neutrinospektren durch die Einbeziehung zusätzlicher Neutrinoereignisse im Energiebereich von 100 GeV bis 10 TeV verbessert werden kann, obwohl der Hintergrund dort deutlich höher ist. Dadurch hat diese Arbeit zur Entwicklung von IceCube DeepCore, der Niederenergieerweiterung von IceCube, beigetragen.
Während der Entwicklung der vorliegenden Analyse hat sich das instrumentierte Volumen von IceCube von 40 Strings auf 79 Strings (DeepCore eingeschlossen) fast verdoppelt. Eine weiterführende Analyse, die mit dem nahezu vollständigen Detektor den gesamten Himmel nach Neutrinoquellen untersuchen wird, wurde in dieser Arbeit komplett vorbereitet. Diese Arbeit endet mit einem Aublick auf das Potential der begonnenen Analyse.

Zwei Dinge erfüllen das Gemüt
mit immer neuer und zunehmender Bewunderung und Ehrfurcht,
je öfter und anhaltender sich das Nachdenken damit beschäftigt:
der gestirnte Himmel über mir und das moralische Gesetz in mir.
Immanuel Kant

Contents

About this Thesis

This thesis presents the work on two major projects. The first and completed project is the search for galactic neutrino sources with the combined IceCube 40-strings and AMANDA detector. The results of this search are reported in this thesis. The use of AMANDA offers both an advantage and a challenge: The more densely instrumented sub-array improves the detector at energies below $\sim$10 TeV. To benefit from this potential however, it is required that the background in a second and less established stream of data is studied and reduced to obtain a combined neutrino sample. The neutrino sample that has been extracted in this way is described and the introductory parts of this thesis are targeted towards the searches that have been performed with this data sample. The focus of these chapters is therefore on the physics of potential galactic neutrino sources and the performance of IceCube for soft-spectra neutrino sources.
The second major project that has been started within this work is an All-Sky search for astrophysical sources of high-energy neutrinos with the IceCube 79-strings detector. The physics program of this search is broader than the one of the galactic neutrino point source search and will also include searches for hard- and soft-spectra neutrino point sources in the southern hemisphere. The entire preparatory work for this analysis has already been performed and as an outlook, we will present the on-going work on the neutrino sample.

Author's Contribution

In a large collaboration such as IceCube, it is often the case that more than one person contributes to a result or study. In exchange, the work of each person often includes many tasks that cannot be completely reflected in a thesis. The main individual contributions of the author since summer 2008 are therefore outlined here:

- I have contributed to the low-level processing of the data from the IceCube 40-strings and AMANDA configuration. An additional processing step to apply additional reconstructions on the combined events has been carried out with support from Cécile Roucelle.
- The development of the combined IceCube 40-strings and AMANDA neutrino sample is a major individual contribution. I have performed two searches for galactic neutrino sources on this data and derived neutrino flux upper limits from these. The third search, a test for neutrino emission inside the Cygnus region, has been carried out in collaboration with Yolanda Sestayo.
- I have contributed at various stages to the off-line processing of the IceCube 79-strings data and the tests of the simulation for this detector configuration. As a major step for analyses of track-like events with this data, I have developed the event selection for a second stage off-line processing to provide additional reconstructions and have together with Olaf Schulz and Andreas Gross worked on the technical implementation. The processing is underway at the time this thesis is written.
- Within this work, I have also developed a first, preliminary analysis level event selection for an All-Sky neutrino point source search with the IceCube 79-strings data which indicates that a significant improvement in efficiency, in particular in the southern hemisphere, can be achieved with respect to previous analyses.

1. High-Energy Neutrino Astronomy

The IceCube neutrino telescope at the South Pole is a unique instrument. It is the first cubic-kilometer scale neutrino telescope to observe the sky at neutrino energies from about 100 GeV up to EeV energies. The detector collects valuable data for many branches of particle and astroparticle physics such as the search for dark matter or the study of atmospheric air showers. However, IceCube is primarily designed and built to search for high-energy neutrinos from the sites of cosmic-ray acceleration. In this chapter, we will review the connection between high-energy neutrino astronomy and the astrophysics of the high-energy cosmic radiation.

1.1. High-Energy Cosmic-Rays

The Earth is subject to a highly energetic radiation of charged particles from the cosmos, consisting of fully ionized nuclei, electrons and positrons. In the context of this work, we are primarily interested in the hadronic component of the cosmic radiation and will thus use the term "cosmic-rays" for this component, neglecting the presence of others.
The cosmic radiation has been discovered in a series of balloon experiments in 1912 [Hes12]. Since then, it has been studied in great detail through the contribution of a constantly growing community. Moreover, since the very early studies, cosmic-rays have proven to be a unique laboratory for particle physics; many discoveries have been made through their investigation. When cosmic-rays reach the atmosphere, they can eventually interact with the air molecules and large cascades of secondary particles develop in the atmosphere. As the cosmic-ray spectrum extends to very high energies, these cascades or air showers contain particles that could not be produced by man-built particle accelerators before their discovery. Among those particles that were discovered through the investigation of cosmic-ray air showers are the positron [And33] and the muon [SS37]. The latter is contained in cosmic-ray air showers in large abundance. Today, these atmospheric muons are used as a tool to study the energy spectrum and composition of the cosmic radiation. On the other hand, they are a major background for IceCube and many other particle detectors, forcing them to be built deep underground. The characteristics of the atmospheric muon background in IceCube is treated in more detail in Chapter 3. Here, the characteristics of the primary cosmic-rays, their sources and their connection to high-energy neutrino astronomy are discussed first. The main characteristics of the cosmic radiation observed at Earth are the energy spectrum, the composition and the distribution of arrival directions.

The Cosmic-Ray Energy Spectrum

The energy spectrum of the cosmic radiation detected at Earth extends up to around 100 EeV. The all-particle energy spectrum is shown in Figure 1.1. It is to be noted that the flux has been multiplied by the energy. Above 1 PeV, the flux of cosmic-rays at Earth drops below a few tens of particles per m^2 and year and large detectors have been (or are being) built to explore this energy regime. Because of the large effective areas required for these measurements, the detectors cannot be mounted on balloons or satellites anymore but are built on the surface of the Earth. Only measurements of the interaction products of the cosmic-ray primaries are therefore available at the very high energies, also known as indirect measurements. Reviews about the experimental techniques used to measure cosmic-rays and about the connection of the properties of the air shower to those of the cosmic-ray primaries can be

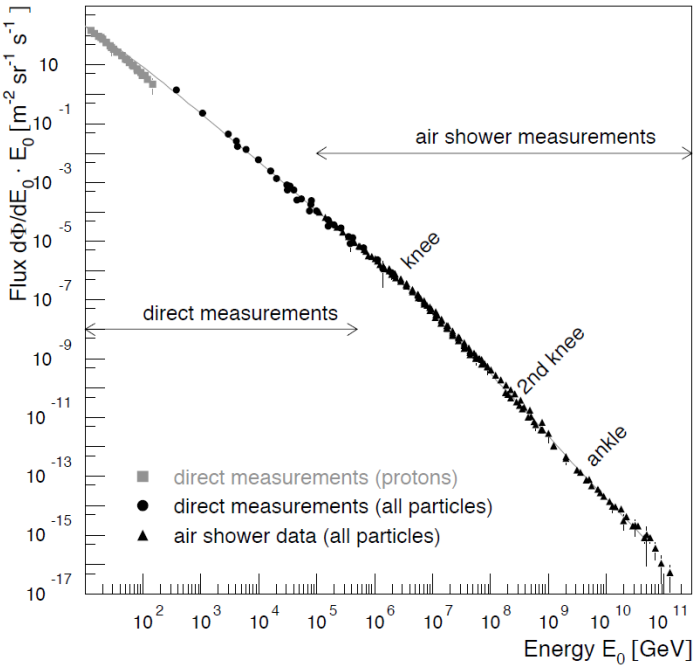

Figure 1.1.: Energy spectrum of the cosmic radiation measured at Earth. From [BEH09].

found for example in [LSS11] and [BEH09].
The cosmic-ray spectrum is almost featureless and follows a power-law $\frac{dN}{dE} \sim E^{-\gamma}$ with spectral index γ between $\sim$ 2.7 and $\sim$ 3.1. A spectral break at the cosmic-ray "knee" and two other features of the cosmic-ray spectrum that are being discussed in the literature, the "second knee" and the "ankle" are highlighted in Figure 1.1. The spectrum follows a spectral index $\alpha \sim 2.7$ up to around 1 PeV. The slope of the spectrum changes at the so-called knee at 3 to 4 PeV. The "second knee" is located at around 400 PeV and the "ankle" around 3 EeV. A cut-off is observed at the highest energies. All spectral features of the cosmic radiation, in particular the knee, are connected to the origin of the cosmic-rays within and without the Galaxy or to their propagation through the Universe and play thus important roles in the study of the cosmic radiation.

Galactic Cosmic-Rays

Cosmic-rays at least up to the ankle are believed to be produced in the jets and shock fronts of violent astrophysical phenomena. Potential astrophysical sources are both of galactic and extragalactic nature but galactic sources are believed to dominate the cosmic-ray spectrum up to energies of about 10^9GeV. The analysis of the IceCube 40-strings and AMANDA data presented in this thesis focuses on the search for neutrinos in association with the galactic cosmic radiation. A recommended review about galactic cosmic-rays is for example [CD11].
Galactic cosmic-rays are produced through the stochastic acceleration of regular galactic matter produced in stellar nucleosynthesis. Supernova remnants (SNR) are considered to be the most promising source candidates. We will discuss the experimental evidence for the acceleration of galactic cosmic-rays in SNR in Chapter 2.
The basis of the acceleration process of cosmic-rays at astrophysical shock fronts has been described by Fermi [Fer49]. The shock front can be regarded as a transition layer propagating through a plasma. The state of the plasma is changed through the transfer of some of the kinetic energy of the incoming

(upstream) plasma to the internal degrees of freedom of the downstream plasma. For a particle whose kinetic energy is high enough so that it does not resonate with the shock wave, the shock front represents a discontinuity in the velocity profile of the plasma. Through scattering on magnetic field inhomogeneities, charged particles can traverse the boundary between the upstream and the downstream region. Each time they do so, they gain a small amount of energy $\Delta E \propto E_0$ due to the velocity of the moving environment. A particle is accelerated until it diffuses outside the acceleration region. The resulting energy spectrum is a power-law with spectral index α between 2.0 and 2.5. Taking into account the diffusion of cosmic-rays in the Galaxy, the spectrum is modified and an observer at Earth will see a spectrum $\frac{dN}{dE} \propto E^{-\gamma}$ with $\gamma = \alpha + \delta$. The size of δ depends on the strength and structure of the galactic magnetic field. In the Fermi acceleration model, the maximum energy that can be obtained is given by the magnetic field B and the size L of the acceleration region [Hil84]:

$$E_{max}[\mathrm{PeV}] \approx Ze \cdot (B/\mu\mathrm{G})(L/\mathrm{pc}) \cdot \beta_{shock} \tag{1.1}$$

where β_{shock} is the shock velocity and Ze the charge of the particle. A more refined description of cosmic-ray acceleration is given in the framework of (non-linear) diffusive shock acceleration. The non-linear version takes the interaction of accelerated cosmic-rays with the shock into account and higher energies can then be obtained through magnetic field amplification. Relevant articles and reviews are for example [Dru83, BE87] and [BV00].

The most prominent feature in the galactic cosmic-ray spectrum is the knee. Different models for the origin of the knee are:

- The knee can be produced by the limited acceleration power of galactic accelerators as the maximum attainable energy is limited by the size and magnetic field of the accelerator.
- The knee can also be described in the context of leakage of higher energy particles from the Galaxy.
- Alternatively, the knee is produced by a single source, or a single prominent source among many weaker sources.
- Finally, models have been proposed that explain the knee through the interaction of accelerated cosmic-rays with until now undiscovered background particles such as heavy neutrinos.

A review of these different models and comparisons of the models to the measured cosmic-ray data can be found in [CD11] and the references therein.

The composition of the galactic cosmic radiation has been studied primarily at lower energies where direct measurements are possible. The composition is very similar to the abundance of the elements in the solar system except for an apparent excess of lithium, beryllium and boron. These are produced in spallation processes of heavier, more abundant elements [BEH09]. At ~1 GeV, measurements of the relative abundance of different neon and iron isotopes with the CRIS spectrometer [BWA+05] as well as measurements of the relative abundance of a number of other isotopes with TIGER [RLL+09] indicate that galactic cosmic-rays contain about 20% material from Wolf-Rayet stars, supporting the theory that galactic cosmic-rays are produced in OB associations, see also [HL06] and [CD11].

Extragalactic Cosmic-Rays

Through their limited size and magnetic fields, the maximal energy that can be reached in a galactic cosmic-ray accelerator is limited. Different values for the maximal cosmic-ray energy from supernova remnants have been derived. Berezhko in [Ber96] calculates a maximum energy of $\sim Z \cdot 10^6$GeV for an ion with charge Ze in the case of a high cosmic-ray acceleration efficiency and assuming that non-linear effects play an important role. In this case, SNR are capable to accelerate cosmic-rays up to the knee but not beyond. A higher value is obtained for young SNR in [PZ03] by Ptuskin and Zirakashvili; they find that young SNR might accelerate particles up to energies $\sim Z \cdot 10^8$GeV while significantly lower energies ($\sim Z \cdot 10$GeV) are reached at later stages. Cosmic-ray acceleration models at the highest energies assume that an extragalactic component of cosmic-rays is produced by astrophysical phenomena of larger size

and/or larger magnetic fields than present in the Galaxy. Potential sources are Active Galactic Nuclei (AGN), radio galaxies and gamma-ray bursts (GRB), see [BEH09] and references therein. The change in the spectrum at the ankle is then explained by a transition to a purely extragalactic cosmic-ray component. The model of cosmic-ray acceleration in GRBs is already now being challenged by IceCube's limits on the high-energy neutrino flux from GRBs [Whi11]. Alternative theories involve the decays of very heavy, exotic particles as sources of the highest energy cosmic-rays, see [BG00] for a review.
An attenuation of the energy spectrum above 3.0×10^{10} GeV has been predicted by Greisen [Gre66] and by Zatsepin and Kuzmin [ZK66] (GZK cutoff) already in 1966, arising from the limited reach of highly energetic protons (and heaver nuclei) when they travel through the cosmic microwave background. As they do so, they interact with the low energetic photon background. Protons lose their energy primarily in the production of pions. The most important energy loss for heavier nuclei is through photodisintegration [BEH09]. The presence of an attenuation at this energy scale has been conclusively proven in 2008 by the HiRes [AAA$^+$08a] and Auger [AAA$^+$08c] collaborations. The observation of a GZK cutoff agrees well with the model that the highest energy cosmic-rays are produced in extragalactic accelerators. The observed attenuation can however also be explained by a limited acceleration power of local sources.

Cosmic-Ray Arrival Directions

The wish to reveal the sources of the cosmic radiation arises not only from the puzzling question about the extreme energies involved. Cosmic-rays can potentially provide unique information about their acceleration sites, i.e. the interior of extreme astrophysical phenomena. In addition, the energy density of the cosmic radiation is very large; it is comparable with the pressure of the galactic magnetic field and with that of the interstellar medium. Cosmic-rays may thus have an important role in the dynamics of the Galaxy and may influence the interstellar chemistry, as described for example in [Gab09] and references therein.
The most conclusive identification of a cosmic-ray source would be the observation of a cosmic-ray flux associated to a particular object. This however is very difficult as charged particles are deflected by magnetic fields. In general, cosmic-rays do therefore not point back to their sources and their arrival directions are isotropic after traversing the Galaxy. The deflection of a charged particle in a magnetic field scales inversely with its energy. At the very highest energies of the cosmic-ray spectrum, the magnetic deflection therefore becomes smaller and cosmic-ray astronomy may be possible at the end of the spectrum albeit with very small statistics. It is to be noted however that the current knowledge about the magnetic fields between the Earth and the cosmic-ray sources, in particular the galactic magnetic field, is incomplete and that the magnetic deflections even at the highest energies may be of the order of few degrees [AAA$^+$08b]. The Auger collaboration has reported hints for a cosmic-ray anisotropy at particle energies above 55 EeV [AAA$^+$08b, AAA$^+$10c]. Most notable is a clustering of events around Centaurus A, the closest active galactic nuclei (AGN). The most significant excess around Centaurus A was identified for an 18° window, in which 13 events were observed with an expectation of 3.2 events. Accounting for the intrinsic trials of the observation induced by the fact that different regions around Centaurus A were considered, the p-value of this observation is 4%. The measurement does therefore not present a statistically significant discovery. In IceCube for example, only a five sigma deviation from the background is regarded as a discovery.
At energies between a few TeV and several 100 TeV, experiments like IceCube collect high statistics data samples of down-wards muons produced in the atmosphere by incoming cosmic-rays and are able to test isotropy down to the 10^{-4} level. As an example, the analysis of the 2009-2010 IceCube data collected 32 billion muon events in the southern hemisphere for this aim. The arrival directions of the cosmic-rays observed by IceCube and other experiments (see [AAA$^+$11f] and references therein) are indeed isotropic to a very high accuracy. However, small but statistically significant anisotropies at the permille level have been observed in this energy range. IceCube is the only instrument able to perform this analysis in

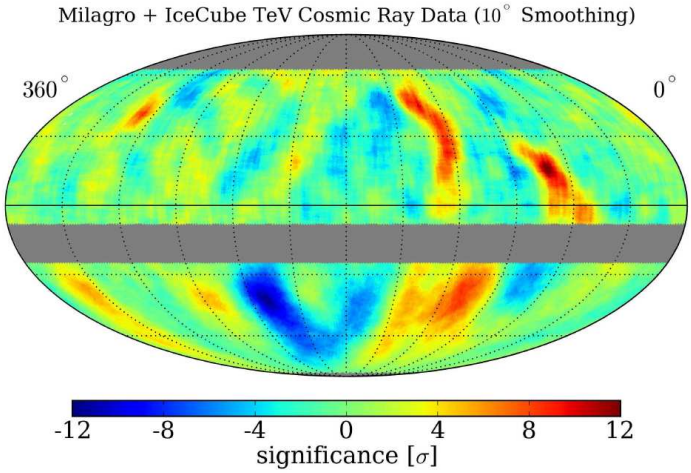

Figure 1.2.: Combined IceCube and MILAGRO cosmic-ray data. 5.6×10^{10} down-going muon events from IceCube with a median energy of 20 TeV are analyzed in the southern hemisphere. From simulation, it is expected that their arrival direction is typically within 0.2° of the direction of the cosmic-ray primary. (The angular resolution of the detector has to be added to this number. For the IceCube events selected here, it is around 3° and depends on the zenith angle.) Both analyses were performed with a 10° smoothing and the combined map shows significant excess regions in both hemispheres. The dipole and quadrupole moments that dominate the cosmic-ray anisotropy have been subtracted. From [AAA+11f]

the southern hemisphere. The data is dominated by a dipole and quadrupole moment but structures down to 15° can be observed once this large scale structure has been subtracted from the data. The observed anisotropy at smaller angular scales is about five times weaker than the dipole and quadrupole moments. The most prominent small-scale anisotropies in the IceCube data from 2009-2010 have relative intensities of 10^{-4} and are observed at right ascension (r.a.) 122.4° and declination −47.4° with a clustering on a 22° scale and a pre-trial significance of 7.0σ (5.3σ post-trial). Remarkably, the second most significant excess (r.a. 128.8°, declination −45.2°, best clustering scale 13°, pre-trial significance of 6.7σ (4.9σ post-trial)) is located close to Vela, one of the closest supernova remnants. Local sources as explanation of the cosmic-ray anisotropy are however excluded in standard propagation models as the cosmic-ray deflection by magnetic fields is too strong. Ideas how this scenario could be challenged in specific cases are put forward by Drury and Aharonian in [DA08]. Both the observed large- and small-scale cosmic-ray anisotropies are not yet fully explained.

In summary, the analyses of the directional data from cosmic-ray air showers have not yet unveiled the sources of the high-energy cosmic radiation. The observed energy spectrum is characterized by a power law and changes in the spectral index might indicate changes from one population of accelerators to the other. Anisotropies at energies up to several 100 TeV have been observed but are not yet explained unambiguously. At the highest energies, the number of recorded events is still very low and an initial observation of anisotropy has become weaker with the inclusion of additional data [AAA+10c].

1.2. High-Energy Neutrinos from Cosmic-Ray Accelerators

In addition to the cosmic-ray primaries themselves, there are alternative messengers to search for the origin of the cosmic radiation. The efficient acceleration of cosmic-rays is coupled to the production of high-energy photons and neutrinos. As neutral particles, they are both capable to identify the sites of

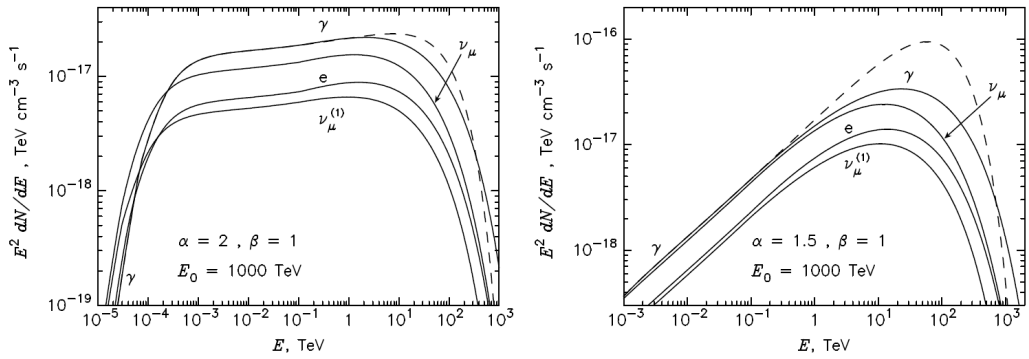

Figure 1.3.: Comparison of neutrino and γ-ray spectra for a cosmic-ray proton source with spectrum $\frac{dN}{dE} \propto E^{-\alpha} \cdot \exp\left(-\left(\frac{E}{E_0}\right)^{\beta}\right)$ interacting via ambient matter. From [KAB06].

their production. In the case of γ-rays however, there are also alternative production scenarios such as Inverse-Compton radiation produced by highly energetic electrons. Even though the mechanisms predict different energy spectra, it is difficult to disentangle the different components and the influence of the local environment of the sources. Therefore, only neutrinos can unambiguously identify the sites of cosmic-ray acceleration since they are only produced in hadronic processes.

When high-energy cosmic-rays interact with matter or radiation fields in the environment of their accelerators, a flux of high-energy neutrinos is produced. Targets for interactions with matter can be for example molecular clouds that are located near the accelerator. High-energy protons can interact with surrounding matter via

$$p + p \longrightarrow \begin{cases} \pi^0 + 2p \\ \pi^+ + n + p \end{cases} \tag{1.2}$$

In addition, π^- are produced in the collisions with neutrons. The dominant channel for pion production in the interaction of cosmic-rays with a surrounding radiation field is

$$p + \gamma \longrightarrow \Delta^+ \longrightarrow \begin{cases} \pi^+ + n \\ \pi^0 + p \end{cases} \tag{1.3}$$

In astrophysical environments, pions will decay before they interact. The π^0 will dominantly decay into two high-energy photons with a branching ratio of 98.8% and the charged pions will lead to the production of neutrinos.

$$\begin{aligned} \pi^0 &\longrightarrow 2\gamma \\ \pi^+ &\longrightarrow \mu^+ + \nu_\mu \quad \longrightarrow e^+ + \nu_e + \overline{\nu}_\mu + \nu_\mu \\ \pi^- &\longrightarrow \mu^- + \overline{\nu}_\mu \quad \longrightarrow e^- + \overline{\nu}_e + \nu_\mu + \overline{\nu}_\mu \end{aligned} \tag{1.4}$$

Following these equations, neutrinos of different flavors (counting ν and $\overline{\nu}$ together) are produced in the ratios

$$\nu_e \,:\, \nu_\mu \,:\, \nu_\tau = 1 \,:\, 2 \,:\, 0 \tag{1.5}$$

Due to neutrino oscillations however, the expected flavor ratio at Earth is changed with respect to the one at the source. In the simplest scenario, equal numbers of neutrinos of each flavor are expected at Earth.

The energy spectrum of the neutrinos observed at Earth depends primarily on the spectrum of the cosmic-ray primaries. In both pp- and pγ-interactions, the production of neutrinos is coupled to the production of high-energy γ-rays. The spectra of these particles are therefore coupled under the assumption that γ-rays are only produced in hadronic interactions. Analytical formulae for the conversion of a measured γ-ray

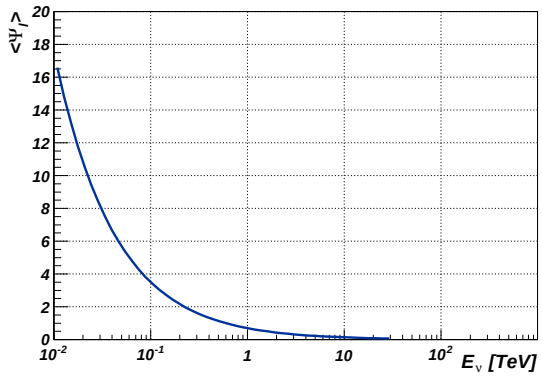

Figure 1.4.: Average angle between the incident neutrino and the lepton in a CC interaction. The vast majority of the events analyzed in this work correspond to neutrino energies above 100 GeV.

flux to an expected neutrino flux under this assumption and in the absence of γ-ray absorption, are given in [KAB06] and [KA08]. Through this connection, detected γ-ray sources present interesting objects for neutrino telescopes and many searches target these objects. The neutrino and γ-ray spectra for a cosmic-ray proton source with spectrum $\frac{dN}{dE} \propto E^{-\alpha} \cdot \exp\left(-\left(\frac{E}{E_0}\right)^{\beta}\right)$ interacting with ambient matter are illustrated in Figure 1.3 (from [KAB06]) for two different sets of parameters (E_0, α, β). The resulting neutrino flux is a factor two lower than the corresponding γ-ray flux and has a lower energy cutoff. The observation of many galactic γ-ray sources that follow a spectrum like the one considered here ([AAB$^+$06c, AAB$^+$07, AAB$^+$06b, AAA$^+$09f]) or unbroken power-law spectra with spectral indexes larger than 2.0 ([AAA$^+$07b, AAA$^+$07a, KCR11, AAA$^+$09g]) is then precisely the motivation to present a search for galactic neutrino sources that is optimized for softer spectra than $\frac{dN}{dE} \propto E^{-2.0}$.

1.3. Neutrino Telescopes

Neutrinos are detected through the detection of the secondary products of their interaction with nuclei in a target material. They interact only by the weak force and at the energies of relevance for neutrino telescopes, neutrinos interact via standard model deep inelastic scattering:

$$\nu_\ell + \mathrm{N} \longrightarrow \mathrm{X} + \ell \tag{1.6}$$

$$\nu_\ell + \mathrm{N} \longrightarrow \mathrm{X} + \nu_\ell \tag{1.7}$$

where N stands for nucleus and $\ell \in (e, \mu, \tau)$ represents a charged lepton or the lepton flavor of a neutrino if used as a subscript. In a neutral current (NC, 1.7) interaction, a neutrino of the same lepton flavor ℓ is found in the final state whereas a charged lepton emerges from charged current (CC 1.6) interactions. Both interactions are accompanied by a hadronic cascade X.
The dependency of the neutrino cross section $\sigma_{\mathrm{NC/CC}}$ from the neutrino energy E_ν can be approximated with

$$\sigma_{\mathrm{NC/CC}} \propto \left(\frac{1}{\left(\mathrm{Q}^2 + \mathrm{M}^2_{\mathrm{W/Z}}\right)}\right)^2 \cdot \mathrm{E}_\nu \tag{1.8}$$

where Q^2 is the invariant squared momentum transfer from the incident ν to the outgoing lepton and $\mathrm{M}_{\mathrm{W/Z}}$ is the respective mass of the $\mathrm{W}^\pm$- or Z-boson. The cross sections for neutrinos and anti-neutrinos are of the same order with a higher cross section for neutrinos especially towards lower energies. Also

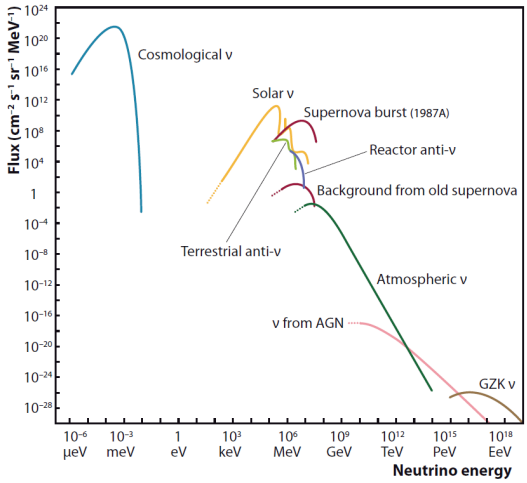

Figure 1.5.: The expected neutrino flux from an AGN as an example of a cosmic-ray accelerating source is compared to other measured and expected neutrino fluxes. From [Spi07].

the cross sections for neutral and charged current interactions are of the same order with a two to three times higher cross section for charged current interactions [GQRS98].
Several methods to detect the products of these interactions are currently in use or are being explored. Radiochemical as well as optical methods are applied in underground detectors for the study of neutrinos of energy below some tens of MeV. For more energetic neutrinos, natural material like water or ice are used in order to reach a larger target mass. In these cases, optical detection methods as well as radio detection methods based on the Askaryan effect [GBB+07] are applied. The use of acoustic detection techniques is still under investigation [AAA+11c]. The optical detection method is used for neutrino energies up to the EeV regime and the focus here will be on this method. Hadronic cascades and energetic leptons deposit light into the surrounding medium. Optical methods can thus detect neutral current interactions if they take place within the instrumented volume and neutrinos with charged-current interactions if the emerging charged lepton passes through or near the instrumented volume. High-energy charged leptons from neutrino-nucleus interactions as well as their secondaries radiate Cherenkov light at an angle [Gro08]:

$$\cos(\theta_c) = \frac{1}{\beta \cdot n(\lambda)} \tag{1.9}$$

if they travel faster than the speed of light in a dielectric medium such as water or ice. The Cherenkov angle θ_c depends on the refraction index $n(\lambda)$ of the medium. For relativistic leptons ($\beta = 1$) in ice and at a wavelength of λ =400 nm, the Cherenkov angle is 41°. Thus, the imaging of Cherenkov rings or the sampling of Cherenkov light along a particle trajectory (particularly in the case of a muon) allow to reconstruct the direction of the lepton. The longer trajectories of the muon with respect to the other leptons make muon neutrinos more suitable for the extraction of directional information. Neutral-current events are less suitable for analyses that require directional information but can be used for a variety of other neutrino analyses. A more complete discussion of the energy loss of high-energy muons in ice is given in Chapter 7. The angle between the incident neutrino and the emerging lepton in a CC interaction decreases with energy [LM00]:

$$\langle \Psi_\ell \rangle = 0.7^\circ \cdot \left(\frac{E_\nu}{1\text{TeV}} \right)^{-0.7} \tag{1.10}$$

(see also Figure 1.4). At energies above a few 100 GeV, the lepton is very well aligned with the incoming neutrino and real neutrino astronomy is possible.

With these prerequisites, the design of an optical neutrino telescope is based on the instrumentation of a large volume of a transparent medium with optical sensors. The required instrumented volume is dictated by the expected flux of neutrinos. Figure 1.5 compares the expected neutrino flux from an AGN as an example of a cosmic-ray accelerating source to other measured and expected neutrino fluxes. The expected flux is significantly lower than for example the fluxes of solar and reactor neutrinos and substantially larger detectors of cubic kilometer scales are required. As a consequence, high-energy neutrino telescopes have to be built in natural reservoirs of transparent media, i.e. in water or in ice. To suppress the background from atmospheric muons and neutrinos (see also Chapter 3), these reservoirs have to be deep underground but nevertheless accessible for the installation of the detector.
Several neutrino telescopes have been built in water [LPRS81, Lub03, AAA$^+$11j] or are planned to be built in water [BCH$^+$11]. The two neutrino telescopes IceCube and AMANDA that have been used in this work, use instead of water the deep antarctic ice shield at the South Pole. IceCube is the currently largest high-energy neutrino telescope and its design and construction are discussed in detail in Chapter 5.

2. The High-Energy Milky Way

The work presented in this thesis is primarily focused on the search for galactic neutrino sources. In the pursue of this goal, three different search strategies have been adopted. One is the selection of interesting (γ-ray) sources to search for neutrino emission from particularly promising objects. Another is the scan of a large region of the Galaxy for neutrino point sources without any further assumption about the location of a potential neutrino source. Finally, a model-independent test for neutrino emission inside the Cygnus region will be presented. We will here discuss shortly the high-energy emission in the Milky Way and the selection of interesting sources and regions for the presented neutrino searches.

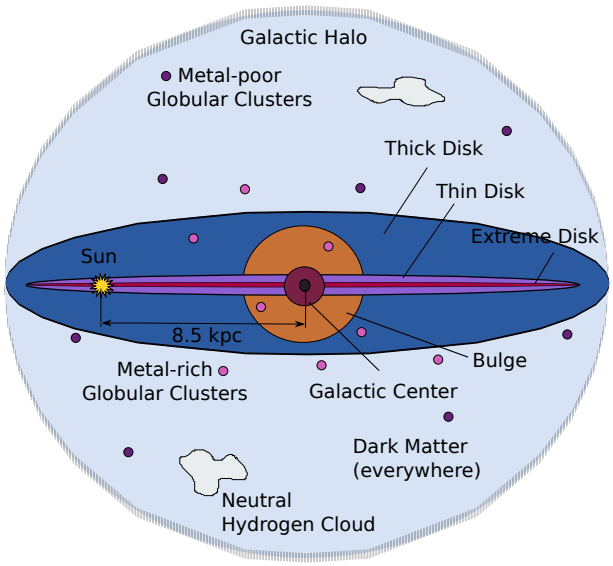

Figure 2.1.: Schematic view of the structure of the Milky Way. Shown is a cross section perpendicular to the plane of rotation. Adapted from [Bus00] and [SG10].

A schematic view of a cross section of the Milky Way perpendicular to the plane of rotation is shown in Figure 2.1. The Galactic Center, a dense nucleus of stars with a central black hole of about $4 \times 10^6 \mathcal{M}_\odot$, is surrounded by a bulge of concentrated luminous matter. The sun is located about 8.5 pc from the Galactic Center. The extreme disk forms a flat distribution of gas and dust. It is embedded within two coplanar regions of a high density of stars, the thin and the thick disk. Most of the gas in the Milky Way is contained within a region of $\pm 5^\circ$ in galactic latitude. This region, as far as accessible to IceCube at the energy range of the analysis, is covered within the scan of the Galactic Plane presented in this work. The outermost part is formed by the Galactic Halo which extends out to $\sim$ 100 kpc. It contains a lower density of stars than the galactic disk and about 170 globular clusters [Bus00, SG10].
The spiral structure of the Galaxy is shown in Figure 2.2. The picture is based on infrared images from the Spitzer Space Telescope [WRL$^+$04]. The Galaxy has a central bar with its two major arms attached to it, the Scutum-Centaurus and Perseus arms. The two minor Norma and Sagittarius arms are located between the major arms. The field of view of the analysis of the IceCube 40-strings and AMANDA data extends from $36^\circ \lesssim \ell \lesssim 210^\circ$ in galactic longitude and is highlighted in the Figure 2.2. This field of view contains the closest approach to the Perseus arm as well as a view along the local arm.
At GeV energies, the γ-ray sky is or has been explored by the satellite experiments EGRET, AGILE and

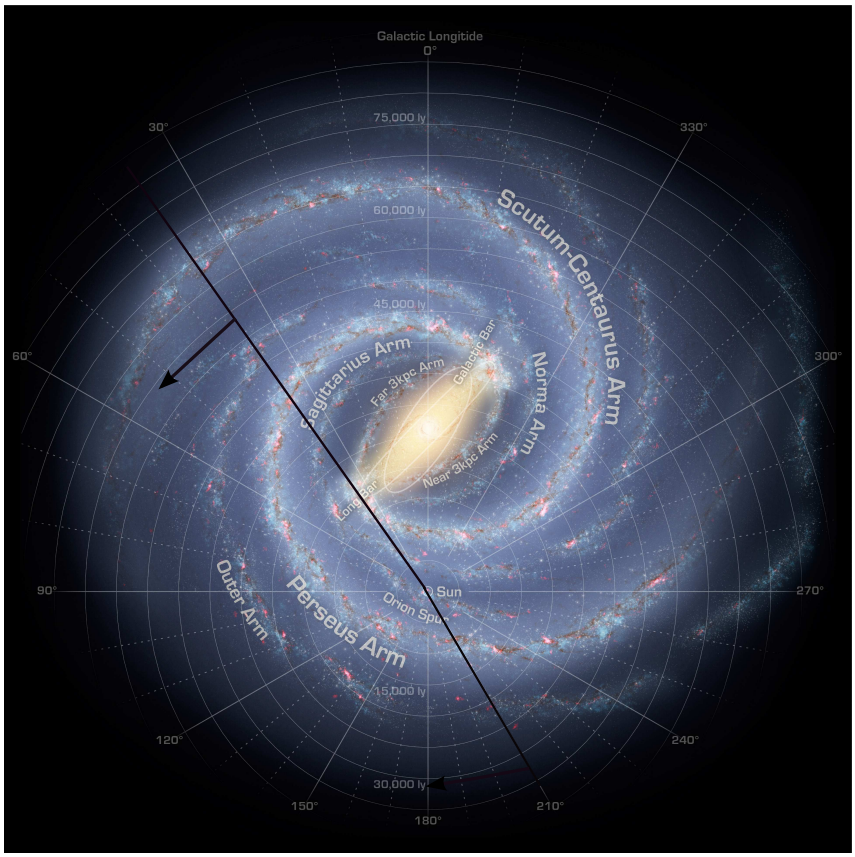

Figure 2.2.: Artist's view of the spiral structure of the Milky Way. From [NJCS08]. The field of view of the search for galactic neutrino sources with IceCube 40-strings and AMANDA is indicated by the black lines and arrows.

Fermi. The galactic diffuse emission detected by Fermi follows the distribution of gas in the galactic disk and is shown in Figure 2.3. Moreover, several galactic sources of GeV γ-rays have been detected. At energies above 100 GeV, the γ-ray sky is studied with two different types of detectors: Imaging Air Cherenkov Telescopes (IACT) like H.E.S.S., MAGIC and VERITAS have a field of view of the order of few degrees, an excellent angular resolution and high sensitivity. Extended Air Shower (EAS) detectors such as Milagro and TIBET on the other hand can observe a larger section of the sky simultaneously but have a reduced sensitivity. The two types of detectors are thus complementary. Figure 2.3 shows the distribution of detected TeV γ-ray sources. Many sources have been detected within the Milky Way and present an accumulation of sources along the Galactic Plane. In particular the H.E.S.S. surveys of the Galactic Plane [AAB$^+$05b, AAB$^+$06d] have detected many sources in this region and contributed to the high-energy picture of the Milky Way.

2.1. Selected Targets for the IceCube 40-Strings and AMANDA Analysis

In the analysis of the IceCube 40-strings and AMANDA data performed in this work, we search for neutrino point sources in the Galactic Plane. This test is performed as a scan and is able to detect neutrino sources at any point in the considered region if the intensity of the source is high enough.
Furthermore, a search for neutrino emission from a short list of interesting known astrophysical sources is conducted. The selection of these sources will be motivated here.

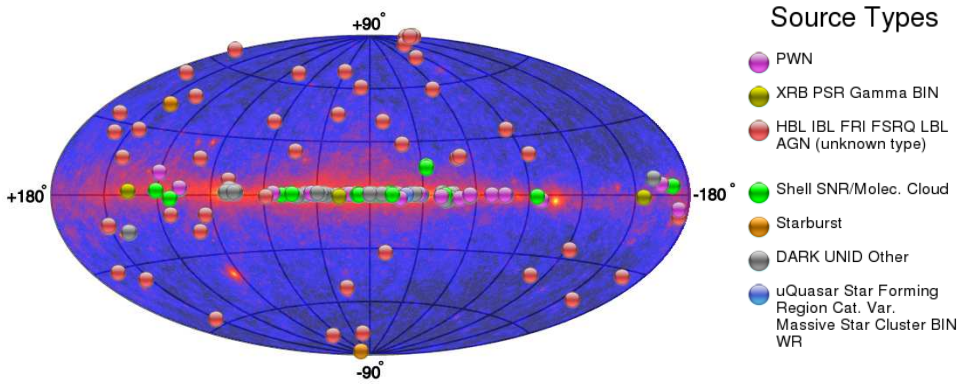

Figure 2.3.: The distribution of detected TeV γ-ray sources is shown with the galactic diffuse emission observed by Fermi presented in the background. From [WH11].

Supernova Remnants

Supernova Remnants (SNR) have been prime candidates for cosmic-ray acceleration since the early days of cosmic-ray physics. Still, until now no conclusive proof of their role in maintaining the galactic cosmic-ray flux up to the cosmic-ray knee exists. There are however accumulating indications that SNR contribute significantly to the galactic cosmic-ray flux up to these energies:

- Their energy budget is sufficient to maintain the cosmic-ray flux even if only a fraction of the energy released in each supernova is converted to cosmic-ray kinetic energy. This is the argument that originally let Baade and Zwicky [BZ34] to propose SNR as cosmic-ray sources. As the cosmic-ray spectrum below the knee is featureless, a single source population is preferred. The argument of the energy budget is nevertheless not conclusive since also other known galactic objects such as stars with powerful winds or pulsars are capable to fulfill this condition.
- The existence of shock fronts in SNR provides an environment where cosmic-ray acceleration is possible. Several calculations of the maximum energy that can be reached in a SNR indicate that they might indeed be able to accelerate particles up to the cosmic-ray knee [Ber96, PZ03].
- Studies of observed thin X-ray synchrotron filaments in the environment of some SNR imply magnetic field strengths of $\sim$ μG which are difficult to reconcile with a leptonic origin of the γ-rays observed in the same SNR, [Gab09] and references therein.
- The γ-ray morphology of some observed SNR supports hadronic scenarios. For example the shell-like morphology of the GeV γ-ray emission from the SNR W44 observed with Fermi is best explained by a hadronic origin of the emission [AAA$^+$10a].
- The observed rapid variability of the synchrotron X-rays from the SNR RXJ1713.7-3946 is difficult to accommodate within leptonic models [Gab09].
- Moreover, the spectral modeling of some SNR yields the best agreement with the experimental results for hadronic models, for example in the case of Cassiopeia A [BPV03].

With the combined IceCube 40-strings and AMANDA neutrino sample described in this work, we are able to search for neutrino emission from SNR with declinations $\delta \gtrsim 5°$. We have selected three SNR in this region for which very high-energy γ-ray emission has been observed, indicating that these objects may potentially be able to accelerate protons up to the energy range of interest for IceCube. The selected SNR are:

Cassiopeia A is the youngest known galactic SNR and is about 300 years old. It is a classical shell-type SNR and located at a distance of about 3.4 kpc. Its progenitor star evolved into a Wolf-Rayet star before the explosion, sweeping up part of the material that once belonged to the star into a dense shell, see [BPV03] and references therein. The source has been observed by HEGRA in the energy

region between 1 TeV and 10 TeV [AAB+01a]. MAGIC [AAA+07b] and VERITAS [AAA+10d] have lowered the energy threshold of the existing observations to 250 GeV and 200 GeV respectively. All three measurements are consistent with an unbroken power-law spectrum $\frac{dN}{dE} \propto E^{-\Gamma}$. The best fits for the spectral index Γ are 2.4 (MAGIC), 2.5 (HEGRA) and 2.6 (VERITAS). All are compatible with each other within the statistical and systematic uncertainties.

IC 443 is an asymmetric shell-type SNR that interacts with a molecular cloud. The MAGIC observations [AAA+07a] are spatially coincident with a molecular line emission region and yield a steep $\frac{dN}{dE} \propto E^{-3.1}$ spectrum. These measurements are compatible with the observation from VERITAS [AAA+09e]. The correlation of the γ-ray emission with the molecular cloud is naturally explained within scenarios of cosmic-ray acceleration and interaction with the molecular cloud. Alternative, leptonic models do exist as well. The spectrum measured with Fermi [AAA+10b] supports an hadronic origin of the γ-rays. A detailed study of the morphology of the γ-radiation detected by AGILE [TGC+10] with nearby molecular gas complexes further supports hadronic scenarios.

W51C is another SNR that is interacting with a molecular cloud. It is located at a distance of 5.5 kpc and is one of the most luminous γ-ray sources in the Galaxy. The Fermi observations [AAA+09d] of this object are well explained by a combination of efficient cosmic-ray acceleration inside the supernova shock and subsequent interactions of these cosmic-rays with the molecular cloud. Very high-energy γ-ray emission from the W51 region has been detected by the H.E.S.S. [FMCT09] and MAGIC [KCR11] telescopes. The emission is compatible with a spectral index of 2.4 and the MAGIC measurements above 700 GeV are spatially coincident with the position of shocked molecular gas, giving further indications of hadronic cosmic-ray acceleration inside the SNR. For these reasons, W51C is an interesting target for IceCube and has been considered in this work.

A search for point-like neutrino emission from these objects has been performed in this work. We note here that the angular resolution of IceCube is worse than the typical angular resolution of IACTs, and thus a source with angular extension in very high-energy γ-rays may still properly treated as point-like in IceCube.

Pulsar Wind Nebulae

In the search presented here, we consider the most studied Pulsar Wind Nebula (PWN), the Crab Nebula.

Crab Nebula appears as the strongest γ-ray source in the sky. Measurements of the γ-ray emission from this source are for example reported in [AABB04] and [AAB+06c]. The emission from the Crab in all wavelengths is well studied and the high-energy emission is consistently explained by leptonic models. Due to its brightness however, the Crab is an interesting source also for neutrino telescopes; IceCube will be able to constrain the fraction of γ-rays from hadronic interactions in this source within few years of operation.

Binary Systems

Searches for steady neutrino emission from two binary systems have been performed within this work. The two selected objects are

LS I+61 303 is a high mass X-ray binary composed of a Be-type star orbiting a compact object whose nature is not known. Both a neutron star model and a microquasar model where the compact object is a stellar mass black hole have been suggested for this source. The orbital period of the system is about 26.5 days. Periodically modulated γ-ray emission from his source has been detected by MAGIC [AAA+09g], VERITAS [ABB+08] and Fermi LAT [AAA+09c]. The maximal flux at TeV energies is observed at apastron, i.e. when the distance between the two objects in the binary system is largest. The measurements of MAGIC are fitted with a soft power law spectrum $\frac{dN}{dE} \propto E^{-2.6}$. The TeV emission on the other hand is peaked close to periastron when the target density is highest and TeV γ-rays may potentially suffer strong absorption. Its brightness and the

considerable amount of both matter and radiation from the companion star to provide a target for hadronic interactions make LS I+61 303 an interesting target for galactic neutrino searches.

SS 433 is a microquasar located near the center of the W50 SNR which is surrounded by a large nebulous structure. The system is composed of a $9\mathcal{M}_\odot$ black hole and a $30\mathcal{M}_\odot$ supergiant star. The microquasar has two relativistic jets which can interact with the ambient matter. Studies of Chandra X-ray data have revealed the presence of hadrons in the jets of SS 433 [MFM02]. For all these reasons, SS 433 represents an interesting target for IceCube. As far as known to us, it has not yet been observed in very high-energy γ-rays. High-energy emission might nevertheless be possible as the system is in an environment where strong absorption of γ-rays might be present. In [DGWL02], a generous steady flux of neutrinos from this source is predicted.

Star-forming Regions

Neutrino telescopes like IceCube observe large regions of the sky simultaneously and without the need of pointing. Apart from single, point-like sources, they can therefore also study whole extended regions with potentially elevated neutrino emission. A statistical test that can be used for this kind of study has been developed in [Ses10] precisely for this purpose and is also described in Chapter 4. A natural target for this kind of study are star-forming regions. These are characterized by a high density of potential cosmic-ray accelerators such as SNR, massive star clusters and pulsar wind nebulae. A very interesting region for the study with IceCube is presented by the Cygnus region.

Cygnus Region This region is the brightest extended region in TeV γ-rays in the northern hemisphere [AABB07]. It is located approximately in the region of $70^\circ \lesssim \ell \lesssim 90^\circ$ in galactic longitude and presents a complex environment where several objects at different distances are observed projected onto a small part of the sky. Observations of γ-ray emission in this region have been made by various instruments and include sources as well as diffuse emission.

Moreover, a predecessor analysis of the Cygnus region with IceCube [Ses10] has detected an upward fluctuation in this region, thus making it even more interesting in the context of this work.

3. Atmospheric Muons and Neutrinos

The major backgrounds in neutrino telescopes like IceCube pertain to the physics of the cosmic-ray air showers that are produced in the atmosphere.

3.1. Production of Muons and Neutrinos in Atmospheric Air Showers

When high-energy cosmic-ray primaries interact with the atmosphere, they produce cascades of secondary particles. These particle cascades or air showers consist of three components: a hadronic, an electromagnetic and a muonic part. These are illustrated in Figure 3.1. Among the hadrons that are produced in the cosmic-ray air showers, the most abundant are pions but also kaons play an important role in the production of atmospheric muons and neutrinos. Depending on the energy of the cosmic-ray primary, charmed mesons and baryons can be produced as well. Decays of the secondary hadrons feed the

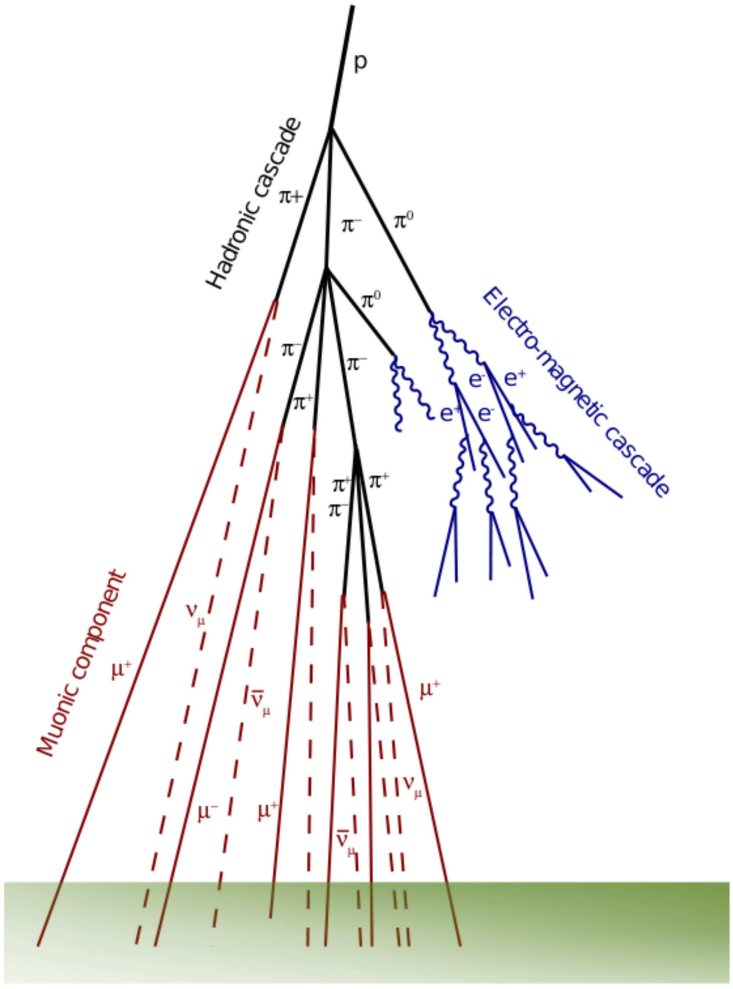

Figure 3.1.: Sketch of a cosmic-ray air shower. Figure kindly provided by O. Schulz [Sch10].

muonic part of the shower and lead to production of atmospheric neutrinos. The production of neutrinos and muons through the decays of pions is the same as described earlier for astrophysical environments

$$\begin{aligned} \pi^+ &\longrightarrow \mu^+ + \nu_\mu \quad \longrightarrow e^+ + \nu_e + \bar{\nu}_\mu + \nu_\mu \\ \pi^- &\longrightarrow \mu^- + \bar{\nu}_\mu \quad \longrightarrow e^- + \bar{\nu}_e + \nu_\mu + \bar{\nu}_\mu \end{aligned} \tag{3.1}$$

The most relevant processes for kaons which lead to production of muons and neutrinos are

$$\begin{aligned} K^+ &\longrightarrow \mu^+ \nu_\mu \\ K^0 &\longrightarrow \pi^+ + \pi^- \\ K^+ &\longrightarrow \pi^+ + \pi^+ \pi^- \\ K^+ &\longrightarrow \pi^0 + e^+ + \nu_e \end{aligned} \tag{3.2}$$

To a first order approximation, the flux atmospheric neutrinos depends on the number of incident cosmic-ray primaries as a function of the energy per nucleon [AGLS96].

3.2. Atmospheric Muons in IceCube

The IceCube detector will be introduced in Chapter 5. Nevertheless, we will already now give an overview of the characteristics of the major background, the atmospheric muons in the detector. The understanding of the detector required for this section is minimal.

The abundance of atmospheric muons is precisely the reason why neutrino telescopes are built deep in the ice or on the ground of the deep sea or deep lakes. Due to the absorption of muons in the Earth, only muons that are produced above the detector constitute a background for neutrino telescopes and the Earth can be used as a shield against the atmospheric muons that are produced on the opposite side of the Earth. For the suppression of the background from above, it is necessary to reconstruct the direction of the incoming particle. Imperfections in the reconstruction give rise to several major categories of muon background in the detector:

Down-going Muon Events The majority of the muon events are correctly reconstructed as down-going events, arriving in the detector from above.

Mis-reconstructed Single Muon Events A non-negligible fraction of the atmospheric muons are mistakingly reconstructed as up-wards moving particles, exceeding the expected number of neutrino events from these directions.

Mis-reconstructed Coincident Events Another background is incurred by events that contain two or more muons from coincident air showers. These event topologies are often mistaken as upwards-going single particles.

Down-going Muon Bundles When bundles of several collimated muons from the same cosmic-ray air shower arrive in the detector, their energy is often overestimated.

Several strategies exist to suppress these backgrounds. In the analysis of the IceCube 40-strings and AMANDA data, a classical strategy for point source analyses is adopted and only upwards-reconstructed events are considered. As the IceCube neutrino telescope is located at the South Pole, the field of view of the analysis is thus restricted to the northern hemisphere. To remove also the mis-reconstructed atmospheric muon background, an event selection is optimized to select well-reconstructed events.

Alternative strategies to open also the region above the detector for point source analyses are the suppression of the single muon and the muon bundle background by the application of an event selection that favors very high-energy events [AAA+09a] or the application of muon vetoes [Sch10]. Both of these strategies will also be explored in the point source analysis that is outlined in the last chapter of this work.

The simulation of atmospheric muons in IceCube is obtained with the CORSIKA [HKC+98]. Alternatively, the data can be used in many applications to study the muon background.

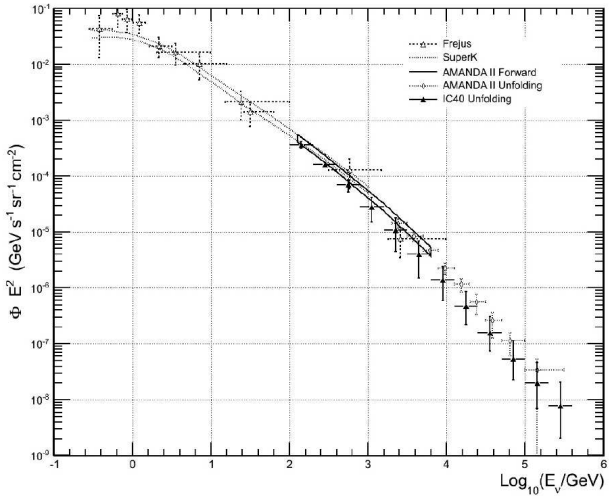

Figure 3.2.: Measurements of the atmospheric neutrino energy spectrum averaged over the zenith region from 97° to 180° in comparison to results from AMANDA and other experiments. The IceCube measurement has been obtained with the 40-strings configuration of IceCube. From [AAA+11d].

3.3. Atmospheric Neutrinos in IceCube

The processes for the production of neutrinos in the atmosphere have been described above. The resulting neutrino flux depends on the production rate of pions and kaons in the atmosphere. At the energies above 100 GeV which are particularly interesting for IceCube, the atmospheric neutrino flux is primarily produced in kaon decays [Gai06]. The flux of atmospheric muons in IceCube is characterized by a steeply falling energy spectrum, as shown in Figure 3.2.

Atmospheric neutrinos present a background that cannot be suppressed on the base of individual event characteristics. Strategies to identify an astrophysical signal above this background include the search for localized sources and the search for an excess of a diffuse neutrino flux over the background at very high energies.

There are two different options to simulate the flux of atmospheric neutrinos. The most complete approach is a full 3-D simulation. In this approach, random cosmic-ray air showers are simulated for example with CORSIKA [HKC+98] and at all position across the globe and all neutrinos that pass through the detector are collected [BGL+04]. In this way, one can simulate the energy and directional dependence of the atmospheric neutrino flux. The downside of this approach is that it obviously requires a large amount of computational power. An alternative approach is therefore to simulate neutrino events with a flat spectrum which are then weighted to a parametrization of the expected atmospheric neutrino flux. Tabulated models for the flux of atmospheric neutrinos are presented for example in [BGL+04] and in [HKKS07]. As these are based on measurements of the atmospheric neutrino flux at lower energies, the parametrization used in IceCube represents an extrapolation to higher energies.

4. Statistical Methods in High-Energy Neutrino Astronomy

The search for high-energy neutrinos from potential cosmic-ray acceleration sites requires to distinguish a weak signal over a dominant background. There are two complimentary approaches to this search: one is to search for a diffuse flux of very high-energy neutrinos beyond the energy range of the atmospheric neutrino background. The other is to search for localized neutrino emission. This second search strategy is the one followed in this work. It presents different advantages with respect to the search for a diffuse very high-energy signal: the background estimation can be based entirely on data and the search is therefore more robust against systematic uncertainties in the simulation. Secondly, while the diffuse search can integrate the signal from many sources, this search strategy can use the directional information and in case also a possible time dependency of the signal to significantly suppress the background. Through this, it is capable to access lower neutrino energies than the diffuse search. From the physics point of view, it allows to search for soft-spectra sources in the Galaxy which are the in particular interest in this work. Finally, a possible detection may then allow to associate cosmic-ray acceleration with a known astrophysical object or at least a position in the sky. A source of neutrinos will thus unambiguously reveal the source of cosmic-rays.
Statistical methods are important instruments for an efficient search for spatially localized high-energy neutrino emission. We summarize here two categories of methods: event classification methods that are used in order to extract neutrino candidates from the atmospheric muon background and the methods that are used to test the data for a localized excess of events over the atmospheric neutrino background.

4.1. Background Rejection

Soft-spectra neutrino source searches with the partial IceCube detector explore the northern sky. The main background are mis-reconstructed atmospheric muons that are produced in the atmosphere above the detector, see also Chapter 3. Event classification methods ranging from the most simple and transparent to more complex methods like Boosted Decision Trees (BDTs) can be used to reject this background. A short introduction to three methods that have been applied in the analysis of IceCube data is given here. All of these methods belong to the class of supervised learning algorithms, i.e. they are developed on a test sample of events for which the nature of each event (background or signal) is known[1].
As the expected signal presents only a very small fraction of the events at every analysis level, a very robust data-driven background estimation can be used throughout this work. Background samples are obtained from the data at each level by randomizing the right ascension of the event positions; the background is expected to be uniform in right ascension [2]. The signal is modeled using Monte Carlo simulation (see Chapter 8).
In general, the performance of an event classification is benchmarked by its signal retention and background rejection power and its robustness against statistical fluctuations and systematic uncertainties.

[1] A very useful summary including analytical derivations of supervised learning algorithms is given in [HTF09].
[2] More careful randomizations have to be performed for analyses that search for phenomena of short duration. These are however not studied in the work presented here.

Rectangular Cuts

Assume that along with the measurements of the incoming direction, energy and time of each event, a list of other properties, the so-called classifiers, $\{c_1, c_2, .., c_n\}$ is available. These could be for example a quality parameter of the event reconstruction or the amount of unscattered light that has been detected. A list of classifiers that has been used in this work is given in Chapter 9. If classifiers are selected which show a different mean behavior for signal and for background, the signal can separated from the dominant background by the identification of an acceptance region for each classifier c_i. These regions define a rectangle in the multi-dimensional space spanned by the classifiers c_i, and all events that lie outside of this rectangle are rejected as background. The acceptance region for each classifier can be defined by hand or optimized with different strategies like the one implemented in the data analysis framework TMVA [HSS+07].
If the decision boundaries are selected by hand, the analyzer has a large control over the outcome and systematics of the event selection that is obtained. An example of an IceCube analysis that is based on rectangular cuts only is presented in [AAA+11i]. The disadvantage of rectangular cuts is that they are considerably less powerful if the background and signal distributions have large overlap regions. In the work presented here, rectangular cuts are used in combination with multivariate classifiers, for low-level data rejection and in cases where the simulation does not allow the use of more advanced event classification methods.

Neyman-Pearson Decision Criterion

In a two class problem like the classification into the two groups "background" and "signal", the optimal test is the one that minimizes the probability to miss an event of the signal class for a given probability α of misclassifying a background event as signal. In other words, the optimal test maximizes the detection probability for a given limit on the false alarm probability α.
In the case of uncorrelated classifiers with continuous values, the Neyman-Pearson lemma states that this requirement is met by a likelihood ratio test, i.e. in this case, the likelihood ratio test is the most powerful test of size α [NP33].
For a list of available classifiers c_i, the likelihood ratio test is constructed from the individual probability density functions for each classifier c_i under the signal and background hypothesis. For each event, the classification rule is based on the parameter

$$\mathcal{L} = \prod_{i=1}^{n} \frac{\mathrm{P}_{\mathrm{signal}}(\hat{c}_i)}{\mathrm{P}_{\mathrm{background}}(\hat{c}_i)} \tag{4.1}$$

where n is the number of classifiers used in the test, $\hat{c}_i$ the measured value of the classifier c_i and $\mathrm{P}_{\mathrm{signal}}(\hat{c}_i)$ ($\mathrm{P}_{\mathrm{background}}(\hat{c}_i)$) the probability to observe the value $\hat{c}_i$ if the event is of the signal (background) class.
The classification obtained in this way combines the separation power of several variables but the classification of each single event can still be traced. A cut based on a likelihood ratio like this is used in Chapter 9; a good signal efficiency is obtained even if the classifiers for an experimental data sample are not strictly uncorrelated.

Boosted Decision Trees

The basic principle of a decision tree is the iterative classification of the data into two groups. Each new level of the tree is called a node. At the root node, all data is in one group. At each following node, the data is divided based on a rectangular cut on the currently most powerful classifier, i.e. at each node, a classifier and corresponding cut value are chosen to maximize the increase of separation between signal and background. In this procedure, the separation of signal and background can be quantified in several

different ways, for example through the misclassification error or the cross entropy. In the application of Boosted Decision Trees in Chapter 11, we use the software package TMVA [HSS+07] which by default uses the Gini Index defined as $p \cdot (1 - p)$, where p is the purity, as measure of the separation. At each node in a decision tree, the difference between the weighted sum over the separation indexes of the child nodes and the separation index of the parent node is maximized. Decision trees divide the space spanned by the classifiers in hypercubes [HTF09]. In usual applications, the number of nodes in a decision tree is either limited or a minimum number of events in each node is required.
Though the number of nodes in a decision tree can be large, the path to the classification of each event is always traceable. On the downside, decision trees are very vulnerable to overtraining. In particular when only small training samples are available, there is a significant danger that the decision tree is impacted by statistical fluctuations in the training sample and a classification on a test sample will not lead to the same efficiencies and purities. Ways to overcome this weakness are pruning, which is the removal of less relevant branches, or boosting. In this context, the focus will be on boosting. Besides reducing the risk of overtraining, this method can also increase the classification power significantly; reference [HTF09] contains relevant comparisons between boosted and non-boosted decision trees.

Boosting

Boosting is the transition from a single decision tree to a forest of many decision trees. The idea is to combine an ensemble of weak classifiers into a single, more powerful classifier. In the training of the first tree, equal weights are used for all events. For each new tree, the weight of each event in the training sample is adapted; higher weights are given to those events that have been misclassified by the previous tree. The final cut parameter, the BDT score, is then calculated as a weighted sum over the scores of the individual trees. Different options for the weighting are available; the two most interesting algorithms for this work are AdaBoost [FS96] and GradientBoost [Fri00]. In the presentation of AdaBoost, we will follow the notation of [HTF09].
Let $G_m(X)$ be the classifier obtained with the mth tree using a vector of input variables X. $G_m(X)$ takes values $\{-1, 1\}$ representing the two possible outcomes "background" and "signal"[3]. With M trees in the forest, the final classifier for an event with measured input variables x is then obtained by the weighted sum over all classifiers:

$$G(x) := \text{sign}\left[\sum_{m=1}^{M} \alpha_m G_m(x)\right] \tag{4.2}$$

where the weighting coefficients α_m are computed by the boosting algorithm and larger values of $G(x)$ indicate signal-like events. The weighting coefficients α_m give higher weights to those trees in the forest that present a smaller signal loss. After the training pf the mth tree, AdaBoost uses the misclassification rate to adapt the event weights for the training of the next tree. For each tree m, the misclassification rate is given by

$$\text{err}_\text{m} := \frac{\sum_{i=1}^{N} w_i \cdot \text{int}\,(y_i \neq G_m(x_i))}{\sum_{i=1}^{N} w_i} \tag{4.3}$$

where y_i denotes the true character of the ith event and is either -1 for background or 1 for signal. $\text{int}(y_i \neq G_m(x_i))$ is 1 if $y_i \neq G_m(x_i)$ and 0 if the event is classified correctly. x_i represents the measurements of the input parameters for an individual event i and N is the number of events in the training sample. In the next step of the boosting, the event weights are changed according to

$$w_i \longrightarrow w_i \cdot \exp\left(\alpha_m \cdot \text{int}(y_i \neq G_m(x_i))\right) \tag{4.4}$$

[3]This implementation is known as "Discrete AdaBoost". Variations where $G_m(X)$ takes any real value between -1 and 1 are called "Real AdaBoost". The difference is however not important for the presentation of the underlying algorithm.

with

$$\alpha_m := \log((1 - \mathrm{err_m})/\mathrm{err_m}) \tag{4.5}$$

α_m is also used to calculate the weighted sum over the trees to obtain the final classifier, see Equation 4.2.
Alternatives to AdaBoost are provided by the GradientBoost algorithm. The description of this algorithm is out of scope of this work and interested readers are referred to [Fri00] and [HTF09]. Mathematically, boosting can be described by the fitting of an additive model with a specified loss function. AdaBoost uses an exponential loss function that is not the most robust against outliers. The key difference between the algorithms is that GradientBoost provides the possibility to use any differentiable loss function even if the corresponding weights α_m cannot be calculated analytically by applying a steepest-descent approach. In the TMVA[HSS+07] implementation of GradienBoost, binomial log-likelihood loss is used. In comparison to AdaBoost, the resulting boosting algorithm can be less sensitive to outliers and mislabeled data points in the event sample. In particular the last point could prove important for the applications within this work as the background training samples are taken from experimental data which contains a fraction of signal-like events.
Boosted Decision Trees can be very powerful out-of-the-box tools especially if many weak classifiers are available. They cannot resolve correlations in the input parameters and their biggest disadvantage is probably that the classification rules are not traceable. Applications of BDTs to IceCube data can be found for example in [Ha11, AAA+11a] and in Chapter 11 of this thesis.

4.2. Statistical Tests on the Final Neutrino Samples

The choice of the best search method depends on the signal hypothesis and the properties of the background. All tests that are used to search for high-energy neutrino sources exploit one or more of the following characteristics of the signal:

- The expected spatial distribution of the signal events.
- The energy spectrum of the neutrino emission.
- A possible time-dependence of the signal.

The neutrino signal from a cosmic-ray accelerator is expected to be clustered around the position of the source and thus presents a localized excess in the event distribution. Neutrino sources are often but not necessarily assumed to be point-like, i.e. it is assumed that the extension of the source is smaller than the angular resolution of the data sample and no structure can be resolved.
If neutrino sources with hard energy spectra are considered, the energy estimates of the detected events can be used to discriminate signal and background. For the most part of this thesis, we consider galactic neutrino sources with soft spectra and this aspect is not relevant. On the other hand, the on-going analysis outlined in Chapter 11 will be more general and will search for a broader category of sources including extragalactic neutrino sources and hard neutrino spectra. For this reason, the use of energy estimates in the statistical test will be of more importance in this analysis.
In this thesis, we present searches for steady neutrino emission. If a time-dependency is however assumed, for example based on the phenomenology of a known astrophysical source, the event times can be used to further suppress the background and increase the power to discriminate a signal. A time-dependent analysis has been applied in [Vog10] to search for neutrino emission from Cygnus X-3 using the data sample prepared in Chapter 9 of this work.
We present here three different methods that can be used to search for steady (soft-spectra) neutrino sources. Two of these tests have been applied in this work, the first is presented for comparison.

Measurement of the Local Event Density

A very robust and simple method to search for a localized excess of events around a fixed position in the sky is to compare the detected number of events in a region around that position with the background expectation. The size of the region is chosen to optimize the sensitivity or the discovery potential of the search and depends on the angular resolution and the event rate of the data sample. The resulting method is fast, the underlying statistics are well understood and thus the significance of the observations can be calculated analytically. Finally, the results are easy to represent and to understand.
On the other hand, the presented method does not fully exploit the available information about each event as the spatial distribution of the events inside the bin is not taken into account. Several analyses of IceCube data have used this method, see for example [Baz10].

Maximum Likelihood Ratio Test

An alternative method is to locally fit a composite model of signal and background to the data and to use a hypothesis test to quantify if this model describes the data better than a pure background model. This hypothesis test can be realized as a maximum likelihood ratio test. The likelihood $\mathcal{L}_{S+B}$ of a model that represents a mixture of signal and background is maximized with respect to the signal strength and compared to the likelihood $\mathcal{L}_B$ of a pure background model. The ratio of the two indicates which model fits the data better. Often, the parameter

$$\lambda = -2.0 \cdot \ln\left(\frac{\mathcal{L}_{S+B}}{\mathcal{L}_B}\right) \tag{4.6}$$

is used as a test statistic. In some particular cases, λ will follow a χ^2-distribution if defined in this way, allowing for a direct conversion into significances. In general however, the distribution of λ is not known analytically and the significance has to be determined with the help of a large number of pseudo-experiments.
The model for a measurement of N events comprised of a mixture of n_s signal and $(N - n_s)$ background events is described by the likelihood function

$$\mathcal{L}_{S+B}(n_s) = \prod_{i=1}^{N}\left[\left(1 - \frac{n_s}{N}\right)\cdot \mathcal{B}\left(\hat{c}_{k,i}\right) + \frac{n_s}{N}\cdot \mathcal{S}\left(\hat{c}_{k,i}\right)\right] \tag{4.7}$$

where $\mathcal{B}$ and $\mathcal{S}$ are the probability density functions (pdf) for the classifiers $c_{k,i}$ under the background and signal hypothesis. The $\hat{c}_{k,i}$ represent the observed values of k classifiers in the event i. The likelihood for the null hypothesis is obtained from Equation 4.7 by setting $n_s = 0$.
The form of the signal and background probability density functions depends on the particular data and the physics scenario to be tested. A likelihood function to fit a neutrino point source as signal to a uniform background of atmospheric neutrinos is proposed in [BDD+08]:
In this case, the classifiers for each event i are the reconstructed direction $\vec{x}_i$ and the uncertainty of the angular reconstruction σ_i. More information about the reconstruction and the estimation of the uncertainty of the reconstruction is given in Chapter 7. If a position $\vec{x}_s$ in the sky is to be tested for neutrino emission, the signal probability density function of an individual event is given by

$$\mathcal{S}\left(\vec{x}_s, \vec{x}_i, \sigma_i\right) = \frac{1}{\sqrt{2\pi}\cdot\sigma_i}\cdot e^{-\frac{\left(\vec{x}_i - \vec{x}_s\right)^2}{2\sigma_i^2}} \tag{4.8}$$

This expression assumes that the true neutrino signal is point-like with a Gaussian uncertainty of width σ_i on the reconstructed direction. The background is uniform in right ascension and can be modeled by

a constant. Considering events in a declination band around the assumed source position in the test, the background probability density function is

$$\mathcal{B} = \frac{1}{\Omega_{Band}} \tag{4.9}$$

with Ω_{Band} the size of the declination band. The method has been used in this form in two of the searches presented in this thesis.
In [BDD+08], it has been shown that for a hypothetical neutrino telescope with a median angular resolution of 0.86°, the maximum likelihood ratio test as defined above leads to an improvement of around 13% in discovery potential with respect to a test based on the mere counting of events. This increase comes however at the cost of a reduced generality, increased computation time and a potentially higher impact of systematic uncertainties through the inclusion of individual estimates of the angular uncertainty. Modifications of the method to include additional information such as the energy of the events or to test for different neutrino source morphologies are straightforward.

Multi Point Source Analysis

The two above-mentioned methods are targeted to detect neutrino emission that is confined to regions in the sky with a size of around the angular resolution of the detector. Their goal is to identify a single, strong source above the background. In the case of the maximum likelihood test described above, the spatial morphology of the neutrino source is modeled as a point-like emission. Even in modifications that account for extended sources, a model for the shape and size of the source is used in the search.
The Multi Point Source (MPS) method presented in [Ses10] represents an alternative approach to search for neutrino emission at astrophysical sites. It is targeted to search for neutrino emission inside regions with a size that is significantly larger than the angular resolution of the detector. The physics case for this method is presented for example by star-forming regions which may comprise several cosmic-ray accelerators. While each individual accelerator may be too weak to produce a statistically significant neutrino signal by itself, a method that can integrate the neutrino emission within a whole region of increased high-energy activity may still be able to identify the signal.
The basis of the method lies in the search for a clustering of events on an angular scale Θ. To achieve this, a clustering function is defined:

$$\Phi(\Theta) = \frac{\int_0^{\Theta} \mathcal{P}_{data}(\Theta')\, d\Theta'}{\int_0^{\Theta} \langle \mathcal{P}_{random}(\Theta') \rangle d\Theta'} \tag{4.10}$$

where $\mathcal{P}_{data}(\Theta')$ is the number of event pairs with angular distance Θ' between them in the data and $\langle \mathcal{P}_{random}(\Theta') \rangle$ the average number of event pairs at distance Θ' from each other in an ensemble of randomized pseudo experiments. In both cases, the distances are calculated for all events within the region of interest with respect to all events in the sample. $\Phi(\Theta) = 1$ means that the degree of clustering at the angular scale Θ is exactly as expected from the background. Larger values of $\Phi(\Theta)$ indicate that a higher degree of clustering than expected is observed.
The test defined through 4.10 is model-independent; it is sensitive to any kind of neutrino emission within the defined region. A diffuse flux of neutrinos across the region increases the number of events and thus also the number of close pairs within the region. Any number of point sources or extended sources would cause a local excess of close pairs as well. Neither the number nor the positions of any potential sources within the region need to be known to the analyzer before the test is performed. The presented test has been applied to IceCube data in [Ses10] and in this work to search for neutrino emission inside the Cygnus region.

5. The IceCube Detector

First plans to build a neutrino telescope at the South Pole emerged in the 1980s [HK08]. The first optical sensors of IceCube's predecessor, the Antarctic Muon And Neutrino Detector Array (AMANDA) [AAB+01c], have been deployed at the end of 1993. More than 600 optical sensors have been installed

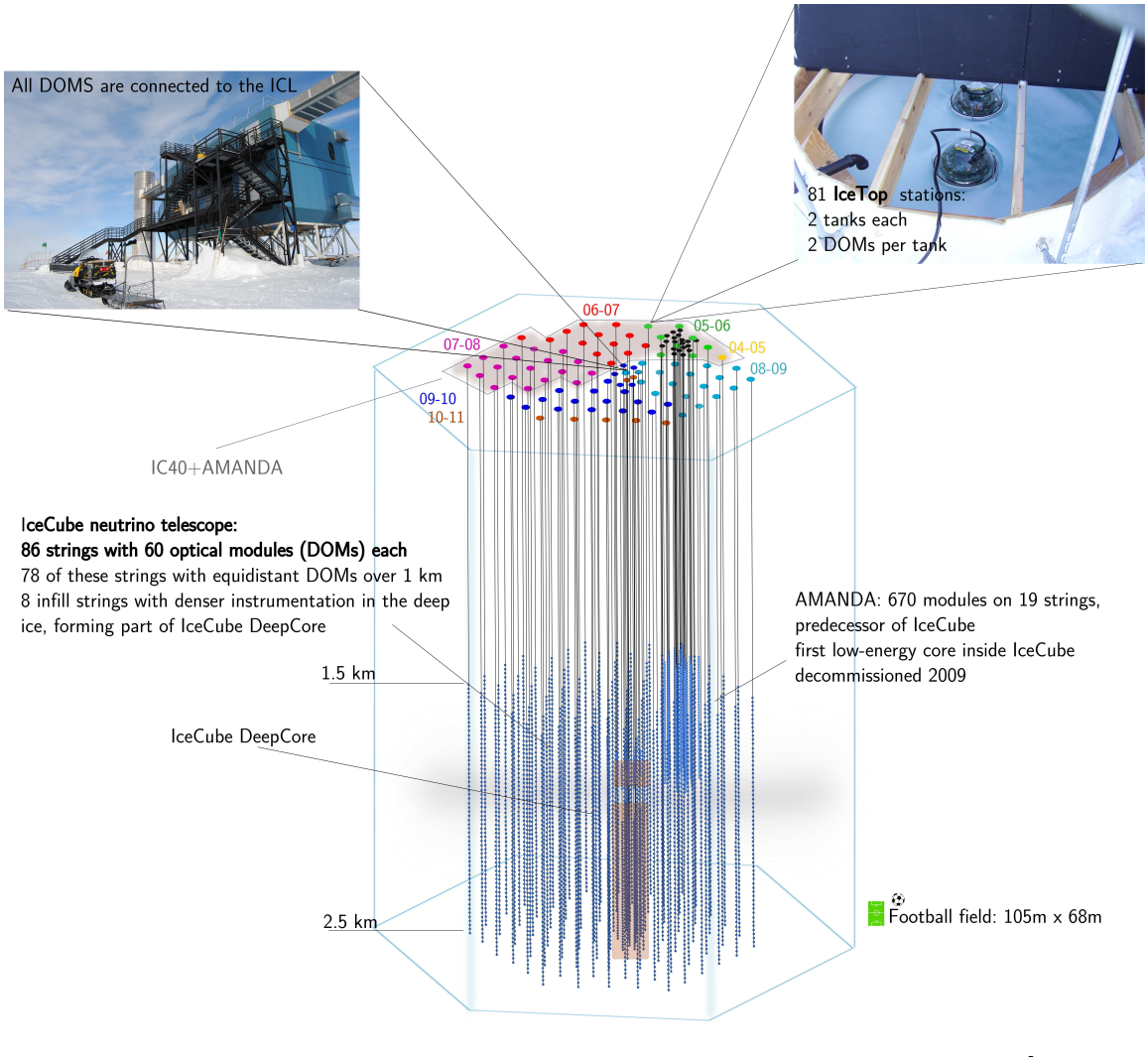

Figure 5.1.: Schematic view of the IceCube detector. The detector consists of the neutrino telescope in the deep ice and the surface air shower detector IceTop. The neutrino telescope instruments about a cubic kilometer of ice with 5160 light sensors aligned on 86 cables called strings. The more densely instrumented region in the deep center of the detector is the low energy extension IceCube-DeepCore. AMANDA, the predecessor of IceCube, is located at smaller depths and is fully surrounded by IceCube strings. It has been decommissioned in 2009 after it took data as an integrated part of IceCube from 2007 to 2009.

Figure 5.2.: A 2.5 km deep hole drilled to accommodate a new IceCube string. Pressurized hot water is used to melt the ice. Photo: R. Maruyama

until 1999, most of them at depths of 1.5 to 2.0 km. Different technologies have been tested and the experience obtained with this detector has been used in the design of the IceCube experiment at the same site. With respect to AMANDA, IceCube is a substantially bigger detector and is deployed at larger depth. IceCube provides a better timing resolution by the use of an improved data acquisition system based on a decentralized signal digitization [AAA+06b]. The installation of the IceCube experiment began in 2004 and has been successfully completed in December 2010. Today, IceCube instruments a volume of approximately one cubic kilometer of the antarctic ice.

5.1. Design and Construction

Figure 5.1 presents a schematic view of the IceCube experiment. The detector consists of two main components: The neutrino telescope in the deep ice and IceTop, an air shower detector at the surface. The neutrino telescope comprises a central, more densely instrumented region named IceCube-DeepCore which enhances the performance at low energies. AMANDA, the predecessor of IceCube, is also embedded in the IceCube array and acted as integrated part of IceCube from 2007 until it was decommissioned in 2009. More details about AMANDA and its integration in IceCube are given in the next chapter.
The very clear, deep ice at the South Pole and the bedrock below the ice serve as interaction medium for high-energy neutrinos. The ice is instrumented with 5160 light sensors to detect Cherenkov light produced by muons and electromagnetic and hadronic showers produced in the interactions of high-energy neutrinos (see Chapter 1). The light sensors, called Digital Optical Modules (DOMs) (see section 5.2), are aligned on 86 strings and deployed at depths from 1.4 km to 2.4 km. For the deployment of these strings vertical, 2500 m deep holes are drilled into the ice sheet using pressurized hot water. The optical modules are then attached to the string and are gradually lowered into the water-filled hole. Figure 5.2 shows a photograph of one of these holes before a new string is deployed.
78 of the 86 IceCube strings are equipped with 60 equally spaced optical modules. The distance between the optical modules is about 17 m on these strings and they are arranged on a hexagonal grid with 125 m inter-string distance. Eight strings are installed with a smaller inter-string spacing in the center of the grid. With these, IceCube-DeepCore provides a more densely instrumented volume in the center of the detector. As described in section 5.3, the ice sheet at the South Pole is structured and its optical properties change with depth. The two most prominent features are a dust layer at medium depths in the detector and a very high transparency in the deepest ice. The infill strings in IceCube-DeepCore primarily instrument the deepest and clearest ice with 50 optical modules per string. Another ten optical modules are placed above the dust layer to enhance the veto capabilities [Sch10]. The denser instrumentation in

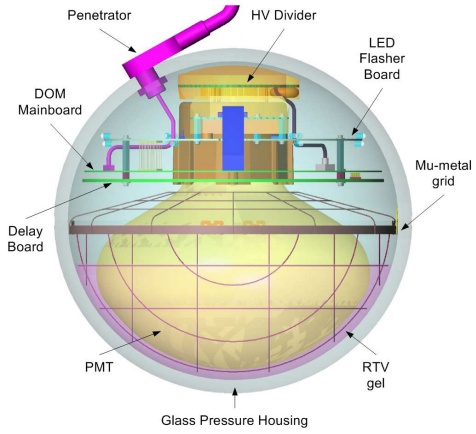

Figure 5.3.: Schematic view of the IceCube Digital Optical Module (DOM). The task of the DOM is to capture light and to record and digitize waveforms. Main components are a photo multiplier tube surrounded by a glass sphere and the DOM mainboard that holds all the necessary on-board electronics. Power and communication to the outside are provided through cables entering through the cable penetrator assembly. From [AAA+09b].

the IceCube-DeepCore allows to lower the energy threshold of IceCube.
The remote site of the detector at the South Pole prohibits installation and shipping of hardware from around February to October. The IceCube detector has thus been built in several stages by adding new strings each antarctic summer. In the meanwhile, data has been taken in each configuration and physics results have been obtained with the partially built detector. The deployment order of the IceCube strings is indicated in Figure 5.1.
In addition to the neutrino telescope in the deep ice, 81 IceTop stations are installed on the surface. Each station is composed of two tanks filled with ice and equipped with two optical modules each. IceTop is a cosmic ray air shower detector and designed to measure cosmic rays from the knee to the ankle [KKKW09]. The combination of the air shower detector with the neutrino telescope offers advantages for both fields of physics. Coincident events between the two components of the detector allow a measurement of the cosmic ray composition with IceTop [And11]. In exchange, IceTop can be used to veto highly energetic cosmic ray air showers that constitute a background in the neutrino telescope [Auf11, ACM11].

5.2. The Digital Optical Module

Besides the antarctic ice, the Digital Optical Module (DOM) is the most substantial constituent of the IceCube detector, including DeepCore and the surface array IceTop. The DOM's task is to detect the light generated by leptons as they pass through the ice and to provide an on-board digitization of the signal.
To this aim, each DOM contains a 25 cm diameter photomultiplier tube (PMT) housed in a 33 cm diameter glass sphere to be protected against the high pressure in the ice [AAA+09b]. Standard IceCube DOMs are equipped with commercial HAMAMATSU R7081-02 PMTs with a quantum efficiency of about 20%. The majority of the DOMs on the DeepCore infill strings contain a newer PMT model, the R7081MOD that presents an improvement of about 40% in quantum efficiency [AAA+11h]. Other main components of the DOMs are a high voltage unit, an LED board and an on-board digital data acquisition system.
The environment of the IceCube detector place stringent requirements on the quality and stability of all

Figure 5.4.: Illustration of the steps each IceCube DOM has to pass before it forms an active part of the detector. Each DOM is tested at several stages before and after it has been deployed in the ice.

components of the DOMs. As the majority of the DOMs is positioned deep in the antarctic ice, they cannot be recovered once they have been deployed. In addition, the DOMs have to work reliably in an environment of high pressure and at temperatures ranging from -6° C at the deepest positions in the ice to -50° C in the IceTop air shower detector. [AAB+01b] discusses the requirements on the DOMs as they are dictated by the science goals of the experiment. Very high-energy muon showers generate as many as 1000 photo electrons within 150 ns if they are close enough to a DOM. A high dynamic range was thus required to ensure that not all DOMs saturate in view of such an event. The IceCube DOMs are designed to have a dynamic range of 200 photoelectrons per 15 ns.

The full recording of waveforms can help to distinguish between close, dim light sources and far-away high-energy tracks and can therefore improve the angular reconstruction and the rejection of background. To this aim, waveforms have to be recorded over a sufficiently long time. The most stringent requirements in this aspect came from the intention to be able to detect double bang events from tau neutrino interactions. A waveform capture of around 4 µs is needed to catch a significant fraction of these events. A high stability is required as DOM failure could result in a reduction of the trigger and filter efficiency in particular for short tracks. Accordingly, a high stability is especially important for all analyses such as measurements of the atmospheric neutrino spectrum that study the lower energy end of the particle energy distribution in IceCube. The design goal of IceCube was a DOM failure rate of less than 5% and has been more than fulfilled.

Another important parameter in the design of the optical modules is the noise rate. As ice is a low noise environment, radioactivity in the building blocks of the DOMs is the dominant source of noise. The noise rate of the DOMs directly impacts the sensitivity for supernovae as their signature is a short, synchronous rise in the single photon electron rates throughout the detector. A noise rate below 500 Hz was the design goal for IceCube. The timing resolution was required to be smaller than 5 ns. A better resolution is difficult to achieve due to the scattering of light in the ice and the availability of PMTs with a better resolution.

Figure 5.3 shows a schematic view of a DOM. The PMT and the electronics are fully embedded in a glass sphere interrupted only by a cable penetrator assembly providing power and a path for communication

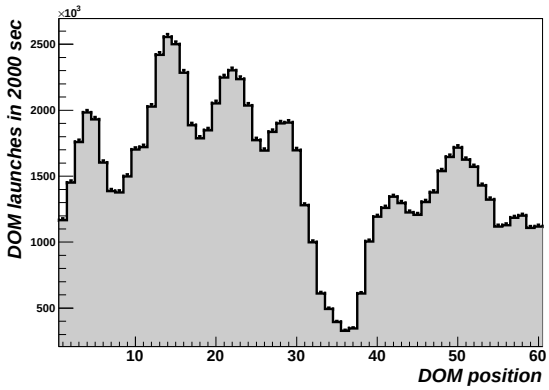

Figure 5.5.: The structure of the ice is clearly visible in the data. Shown is the number of DOM launches versus the DOM position summed over all DOM on strings 1 through 78. The plot was made using minimum bias data from the 79-string array requiring at least eight hit DOMs in each event. The big dust layer (see text) is located around the 36th DOM layer.

to the outside. According to the design requirements, the glass was chosen for its high stability, high transparency in the UV and low radioactivity. A silicone gel increases the optical coupling between the glass sphere and the PMT while it serves at the same time to hold the PMT and the electronics in place. The PMT is shielded against magnetic fields by a metal cage. The DOM mainboard contains all necessary devices to read out the waveforms from the PMT, to digitize and to store them. In addition to these components, each DOM includes an integrated LED board with 12 LEDs of 405 nm wavelength. These LEDs are used to calibrate the detector [AAA$^+$09b] and to study the properties of the ice [AAB$^+$05a].
To record and digitize the signal, each DOM disposes of two Analog Transient Waveform Digitizers (ATWD) and a Flash Analog to Digital Converter (FADC). The ATWDs are switched-capacitor arrays with four channels each. The four channels can simultaneously digitize waveforms and each of them records 128 samples with a 3.3 ns resolution. The first three channels are used to record the waveform, the fourth is reserved for calibration purposes. The three channels used to capture the waveform are operated at a different gains: 16x, 2x and 0.25x respectively. In most cases, only the highest gain channel is used for data analysis but in case of saturation, one of the lower gain channels can be used. By using the two ATWDs in a DOM in a ping-pong fashion, dead-time is reduced. Each DOM contains a local clock used to assign a time stamp to the beginning of each recorded waveform. The FADC allows to capture longer waveforms of up to 6.4 µs with a coarser binning [AAA$^+$09b].
Communication to the DOMs is provided via cables that meet in the IceCube Control Lab (ICL) at the surface. DOMs communicate with the surface but also with each other to exchange local coincidence information. The relevant parts of the data acquisition of IceCube are described in section 5.4.
All IceCube DOMs undergo rigorous testing before they are shipped to the South Pole and again before they are installed in the ice. New strings can be integrated into the data taking once the water in the hole is fully frozen and once the DOMs passed a series of stability test to ensure they will not cause detector downtime and that they will not be damaged during operation[1]. The whole chain of steps that each DOM has to go through before it becomes an active part of the detector, is illustrated in Figure 5.4.

5.3. The Antarctic Ice

The realization of the IceCube experiment was possible because of the high transparency of the ice at the South Pole; for wavelengths in the range from ∼200 to ∼400 nm, glacial ice is the most transparent

[1]The author of this work contributed to the commissioning of the strings deployed in the 2009/2010 season

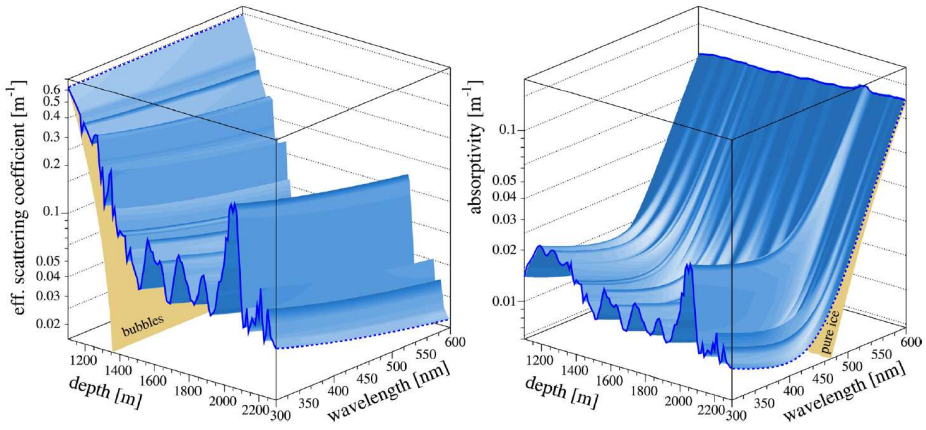

Figure 5.6.: Measurements of scattering and absorption in the Antarctic ice and their dependence on wavelength and depth. The contribution of trapped air bubbles to the scattering of light in the shallow ice is highlighted in the left plot. The layered structure of the ice is clearly visible in both scattering and absorption. From [AAB$^+$05a].

solid known, see [AAB$^+$05a] and references listed therein. In the absence of bioluminescence it provides a low noise environment. As a natural medium, the properties of the ice cannot be controlled by the experimenter. Instead, a deep understanding of its structure and optical properties is crucial.

At the site of the IceCube detector, the antarctic ice sheet is about 2800 m thick and temperatures range from -50°C at the surface to -6°C at the bottom of IceCube. The ice is between 30 000 and 100 000 years old. Most relevant for IceCube are the optical properties of the ice, in particular the scattering and absorption of light. The scattering of light in the ice is caused by dust and air bubbles that are trapped between the ice crystals. The main contribution to the absorption comes from dust in the ice. Both the concentration of air bubbles and dust in the ice depend on the depth. The concentration of dust traces changes the climate conditions at the time the ice was formed [AAB$^+$05a].

Air bubbles are concentrated at depths above 1400 m and in the new ice that forms in the holes drilled to deploy the IceCube strings. As the pressure rises at larger depths, air bubbles get compressed and undergo a phase transition to the solid state. The air hydrates that are produced in this way do not contribute significantly to the scattering as they have almost the same refractive index as the ice itself [AAB$^+$05a]. Ice that formed during times with a high concentration of dust in the atmosphere contains more dust than ice that accumulated in other times. This leads to a layered structure of the ice. The most prominent features of this layering are a big horizontal dust layer in the middle of the detector and a very clear region in the deepest ice. The structure of the ice is clearly visible in the IceCube data. Figure 5.5 shows the number of DOM launches against the position of the DOM in minimum bias data (see section 6.3) taken with the IceCube 79-strings array.This data is dominated by down-going atmospheric muons. Regions with a high DOM occupancy correspond to clear ice layers. The occupancy at the highest and lowest DOM positions is reduced by the local coincidence condition (see next section).

The optical properties of the ice are measured through the detector response to short light pulses emitted by the on-board flasher LEDs of the optical modules. In addition, ice core data from different sites is available and can be used to interpolate the ice properties. Figure 5.6 shows the optical properties of the ice as derived from AMANDA flasher LED data and ice core measurements in [AAB$^+$05a]. The layered structure is clearly visible and the scattering coefficient varies by almost an order of magnitude. An update of this work using newer data from IceCube gives a similar result. An alternative approach is reported in [AAA$^+$11g] leading to a similar structure but larger variations of the optical properties. In addition to the on-board flasher LEDs, there are several other special devices that are used to infer the

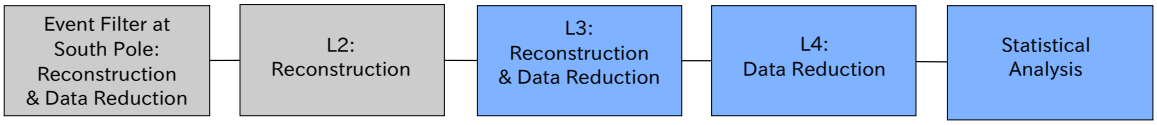

Figure 5.7.: Schematic view of the data processing from Pole filter to the final statistical analysis on the example of the IceCube 40-strings and AMANDA analysis. Individual contributions of the author are highlighted in blue. The number of processing steps between the application of reconstructions at level 2 and the statistical test depends on the analysis. In addition, contributions have also been made in the first two steps of the processing chain.

properties of the ice. Among them is a device to measure the concentration of dust in the ice and the so-called Swedish Camera deployed in the season 2010/2011 at the bottom of one of the strings. The camera delivered pictures from the refreezing ice in the hole.

5.4. Data Acquisition and Filtering

IceCube data is recorded at the South Pole but large parts of the data analysis take place in the North. As the South Pole is not accessible during the largest part of the year, a timely analysis of the IceCube data requires to transfer the data to the North via a satellite link. The available bandwidth on this satellite link is limited and it is thus necessary to reduce the rate of events that are recorded and selected for transfer to the North.

The first step to reduce the data rate in IceCube is the suppression of pure noise events via local coincidence conditions and software triggers. Only DOM launches that fulfill a local coincidence condition can contribute to trigger the readout of an event. The local coincidence condition requires that a DOM launch is accompanied by another launch on one of the four nearest DOMs within a time window of 1 μs to suppress uncorrelated noise. DOM launches that fulfill this local coincidence condition are called “HLC” (hard local coincidence) launches. DOMs with launches that do not fulfill the local coincidence condition (“SLC” (soft local coincidence) launches) can be read out as well[2] but transfer only compressed hit information instead of full waveforms.

All HLC launches serve as input for the evaluation of software trigger algorithms that eventually lead to the creation of an event. The trigger is part of the surface data acquisition system, a set of high performance computers located in the IceCube Laboratory (ICL). The trigger algorithms are based on the number of launches and their distribution along the strings. In the context of the analysis presented in this thesis, the Simple Multiplicity trigger is of main interest. This trigger requires at least eight DOM launches within a time window of 5 μs. Once a trigger has been issued, all DOMs with HLC launches within ±10μ sec around the trigger time send the collected waveforms to the surface where they are time-ordered and merged into events. The trigger window is expanded as long as the trigger condition stays active. In the next step fast, on-line reconstructions are applied to the events and physics filters select interesting events based on the results of these reconstructions. Of particular interest to this work are filters that select track-like, up-going events that are likely to be muons produced in muon neutrino interactions. The implementation of the selected filters are summarized in section 6.3 for the IceCube 40-strings and AMANDA configuration and in section 11.1 for the IceCube 79-strings configuration. All events that pass one or more of the physics filters are transferred north and are available for off-line data analyses. The most important processing steps of the data from the filtering at the South Pole to the final analysis are illustrated in Figure 5.7 on the example of the analysis presented in this work.

[2]This has been done in the 59-, 79- and 86-strings configurations of IceCube while earlier configurations used only HLC launches.

Figure 5.8.: An IceCube surface cable as used to provide the connection from the surface junction box to the IceCube laboratory (ICL) at the South Pole. Cables like this provide communication to one of the IceCube strings respectively and the two associated IceTop stations. Each string is controlled by a DOMHub computer in the ICL.

6. IceCube and AMANDA as a Combined Detector

The AMANDA neutrino telescope [AAB+01c], the predecessor of IceCube, is used in this work as a more densely instrumented sub-array of IceCube itself. This chapter provides an overview of the AMANDA detector and its integration into IceCube. The characteristics of the data taken with this combined detector from April 2008 to May 2009 are introduced and the low-level data selection for the analysis is presented.

6.1. Design and Construction of AMANDA

The AMANDA neutrino telescope, as IceCube, is composed of a number of optical modules (OM) that are frozen into the ice on vertical strings. The design of the optical modules - a downward facing photo multiplier tube enclosed in a glass sphere - is similar to that of IceCube. The signal transmission and on-board electronics are however very different; except for one string, all optical modules in AMANDA transmit analog signals to the surface instead of the digitized format that is used in IceCube. As the first detector of its kind in the antarctic ice, AMANDA comprises a larger range of different technologies of which many proved successful and have therefore also been employed in the larger IceCube detector.

Construction

The construction of AMANDA started with the installation of four strings (AMANDA-A) in 1993/94, exploring the feasibility to build a neutrino telescope at the South Pole. These strings were however deployed at shallow depths between 800 m and 1000 m where the concentration of air bubbles in the ice (see section 5.3) is very high and leads to a strong scattering of light. The experience obtained with AMANDA-A proved nevertheless that the developed electronics were reliable and able to withstand the large pressure in the ice; none of the deployed modules failed during the first two years [AAB+00].
The first strings at larger depths were installed in 1995/96 as an array of 80 OMs on four strings at depths between 1545 m and 1978 m (AMANDA-B4). The optical modules were distributed equally between these four strings with a vertical spacing of 20 m. The optical properties of the ice at the depth of these strings were shown to be better than in the shallow ice, first tools for track reconstruction were developed and first neutrino candidate events were selected. The detector served also to establish the large absorption length of the deep antarctic ice of more than 200 m at a wavelength of 410 nm [AAB+00]. Another six strings with 216 OMs in total were installed in 1996/1997. Together with the previously deployed AMANDA-B4 strings they formed the AMANDA-B10 array.
The final nine strings of the AMANDA array were deployed in the seasons 1997/98 and 1998/99. The three strings deployed in 1997/98 span a larger range of depths from 1150 to 2350 m to explore both the shallower and the deeper ice for the future IceCube detector. The last set of strings includes string 18, the prototype string for IceCube [AAB+06a]. The final stage of the AMANDA detector was operational in 2000 and contained 670 OMs on 19 strings. An overview of the detector geometry is given in Figure 6.1.

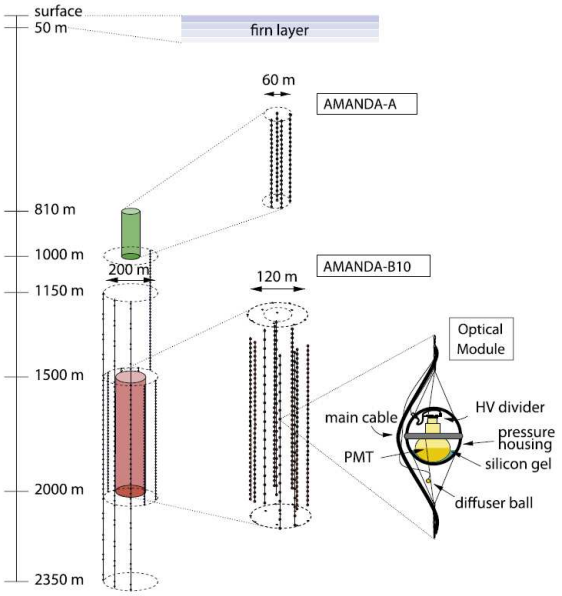

Figure 6.1.: The AMANDA neutrino telescope. The detector was build in several stages and explored the optical properties at different depths of the ice for neutrino astronomy. The strings of the AMANDA-B10 array and the nine strings surrounding them were used as an integrated part of IceCube from 2007 to 2009. As illustrated in Figure 5.1 on page 29, AMANDA was in this configuration fully surrounded by IceCube strings. From [AAB+05a].

Technological Progress

As the first neutrino telescope in the antarctic ice and testbed for the technologies used in IceCube, AMANDA is a less uniformly designed detector than IceCube. After the season 1995/96, the choice of glass for the optical modules was revised and changed for a glass with a higher transmittance in the UV [AAB+05a]. AMANDA has experienced an evolution of signal transmission cable types from coaxial cables (AMANDA-B4) to twisted copper pair cables (AMANDA-B10 strings 5-10) to optical fiber [AAB+06a]. With the larger depth of IceCube and the need to provide mechanical support to the DOMs through the cable, robust copper cables were used in IceCube.
AMANDA string 18 served as a prototype for the on-board signal digitization applied in IceCube [AAB+06a]. Except on this one string, all AMANDA OMs pass only analog waveforms to the surface. An alternative candidate for the IceCube optical modules, the digitally controlled Analog Optical Module, was also tested.
AMANDA took data as a stand-alone neutrino telescope until 2006. From 2007 on, it formed an integrated part of the IceCube detector until it was decommissioned in 2009. Its science capabilities as a low-energy sub-array of the detector are now covered by IceCube-DeepCore.

6.2. Integration of AMANDA into IceCube

Being about eight times more densely instrumented than IceCube, AMANDA provides the possibility to lower the energy threshold of IceCube. The combination of IceCube and AMANDA data for low-energy events provides a better angular reconstruction than could be achieved with AMANDA alone [Res09]. Finally, being embedded in IceCube, it provided for the first time the possibility to use vetoes for the rejection of background events (see for example [AAA+11e]).

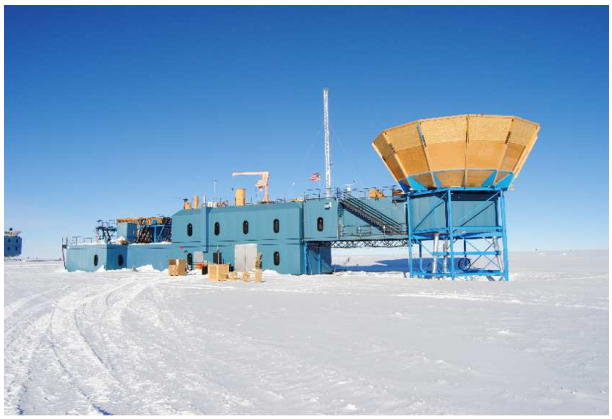

Figure 6.2.: The Martin A. Pomerantz Observatory, home to the AMANDA DAQ.

The integration of AMANDA into IceCube was however not trivial. As the newer IceCube detector builds on the experience obtained with AMANDA, it is in many aspects technologically more advanced than its predecessor. Several differences in the data acquisition systems and the format of the data from the two detectors had to be bridged before the data from the two neutrino telescopes could be combined. The optical modules in AMANDA transferred analog waveforms to the surface[1] while IceCube data is fully digitized on-board the DOMs. A time synchronization between the two detectors had to be ensured. Moreover, the data acquisition systems of the two detectors were housed in different buildings about 300 m apart from each other and physical connections between them had to be created. The full details of the integration of AMANDA into IceCube are reported in [Tep09]. Table 6.1 summarizes the main issues in the integration of AMANDA and their solution.

issue	solution	time of implementation
AMANDA dead time	TWRDAQ[Tep09]	2002-2005
Non-uniformity of the data	TWRDAQ[Tep09]	2002-2005
Communication between the DAQs	Connection via optical fibers	2006-2007
Time synchronization	GPS module	2006-2007

Table 6.1.: Overview of the most important milestones in the integration of AMANDA into IceCube: Even though the original purpose of the implementation of the TWRDAQ was not the integration of AMANDA into IceCube, it presents a major step towards this achievement.

Despite its denser instrumentation, AMANDA would not have had the capability to enhance IceCube's performance at lower energies without an upgrade of the DAQ that was implemented from 2002 to 2005. This new DAQ, the TWRDAQ [Tep09] (Transient Waveform Recorded, see below), reduced the dead time of AMANDA substantially. It was operated in parallel to the original AMANDA DAQ until 2006 and finally replaced it. The combined IceCube and AMANDA detector used only the TWRDAQ.
The original AMANDA DAQ was based on a hardware trigger requiring at least 24 hits within a time window of 2.5 µs. The high multiplicity threshold resulted from the slow analog readout which could not be parallelized. Even with this high trigger threshold, the dead time fraction was at 15%. With the TWRDAQ, the trigger threshold could be lowered to 18 hit modules with a simple multiplicity trigger and down to 8 hit modules with additional requirements on the spatial distribution of the hits. With the faster TWRDAQ, the multiplicity threshold was no longer constrained by the dead time of the DAQ but

[1] The optical modules on AMANDA string 18 had the capability to digitize the signal directly [AAB+06a].

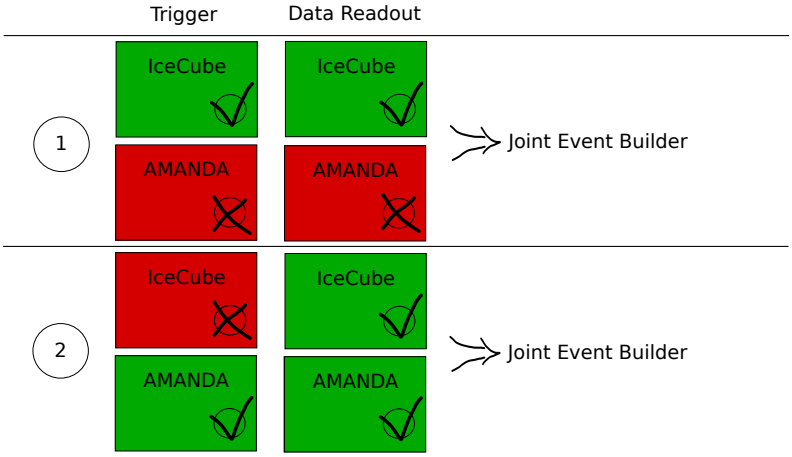

Figure 6.3.: Two kinds of events are present in the combined detector mode: Events with and without AMANDA trigger. Events without AMANDA trigger contain only the information collected with IceCube while AMANDA triggers initiate a readout of IceCube too.

by the high noise rates of up to 1.1 kHz of the optical modules on the AMANDA-B4 strings [Tep09]. The trigger conditions relevant to the IC40+AMANDA analysis are reported later in this chapter.
The digitization of the analog AMANDA waveforms was performed by a set of Flash ADC modules called Transient Waveform Recorders (TWR). With these, the TWRDAQ provided also for higher resemblance of the AMANDA data to the IceCube data. In addition, the TWRDAQ allowed to store valuable additional information such as the number and the arrival times of individual pulses.
AMANDA was the first low-energy core ever used within a neutrino telescope. The data collected in this way proved to be valuable for several analyses like the one presented in this work or for example the one in [AAA$^+$11e]. The successful analysis of AMANDA data gave the initiative to design and build an advanced low-energy core, IceCube-DeepCore [AAA$^+$11h]. This new sub-array is placed within the deep center of the detector and thus provides improved veto capabilities to reject the muon background. Besides, a full uniformity of the data is achieved with IceCube-DeepCore and the energy threshold could be lowered further. With the prospect of this new low-energy sub-array ahead, AMANDA was decommissioned in 2009 as the building that housed its data acquisition system was in danger through the accumulation of snow [Res09].

6.3. 2008-2009 Data: IceCube 40-strings and AMANDA

After the deployment season 2007/2008, 40 IceCube strings have already been installed. The AMANDA array served as an additional, integrated part of the detector. Data was taken in this configuration from April 5, 2008 on. AMANDA was turned off on May 11, 2009 while IceCube 40-strings continued to take data until May 20, 2009. Correcting for detector down-time, 375.8 days of data were taken with the IceCube 40-strings array. Of these, 306 days include AMANDA data. The main causes for detector downtime were scheduled operations in the course of the integration of new strings during the deployment season and for detector calibration.

Trigger Conditions in IceCube 40-strings and AMANDA

Even as a combined detector, AMANDA and IceCube were still triggered separately. A readout of IceCube was initiated every time AMANDA was triggered. The reverse logic was neither possible nor necessary; no significant improvement in the reconstruction is achieved when AMANDA infor-

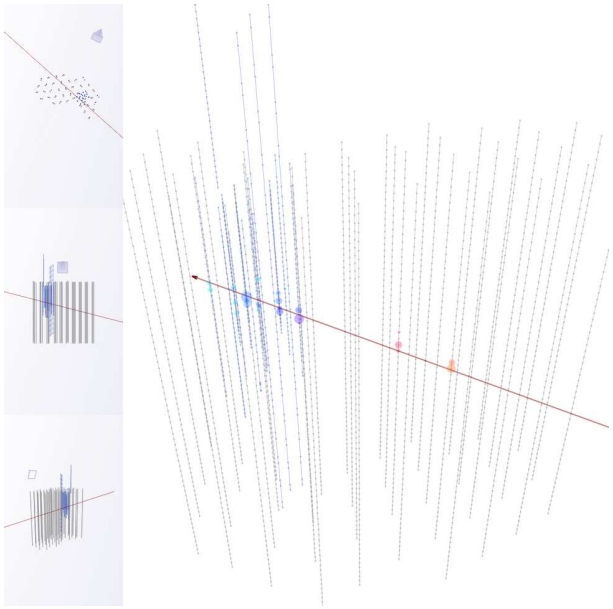

Figure 6.4.: Event display from a combined event taken from the final IC40+AMANDA data sample. The regular IceCube strings from the 40-string configuration are shown in gray and AMANDA strings in blue. The reconstructed track is shown in red. The colored circles along this track are the hits recorded in the detector, with colors from yellow to green indicating the time of the hits and the size of the circles corresponding to the recorded charge. The event shown here did not leave enough hits on IceCube strings to pass the standard muon filter but is recovered by the use of the light recorded in AMANDA.

mation is included into IceCube-triggered events as these typically have a higher energy and are already well-reconstructed [GRTT07]. The trigger logic is illustrated in Figure 6.3. Events from IceCube and AMANDA are merged on a time coincidence base by the Joint Event Builder. The illustrated trigger logic leads to the presence of two different kinds of events in the data taken in this configuration:

- Events with AMANDA trigger. A readout of IceCube is initiated and the events contain the hits recorded in both parts of the detector. These events will be referred to as **"combined events"** in this work. An example event is shown in Figure 6.4.
- Events without AMANDA trigger. These events contain only hits that were recorded in IceCube and will be referred to as **"IceCube events"** in this work.

IceCube operated several software triggers during the time the data for this analysis was taken. The IceCube Simple Multiplicity Trigger (SMT 8) required 8 hit DOMs within a time window of 5 µs. Only modules with a local coincidence (see 5.4) participate in the trigger. On the AMANDA side, a multiplicity trigger was configured to select events with at least 18 hit modules within a time window of 2.5 µs. No local coincidence condition was applied to these hits. Taking into account the smaller spacing of the optical modules in AMANDA, this trigger had a lower energy threshold than the IceCube Simple Multiplicity Trigger. In addition, a string trigger was active and selected events with an even lower energy threshold by taking the hit topology into account to suppress the background. A list of all active triggers during the data taking period of the combined IceCube 40-strings and AMANDA detector is given in Table 6.2.

Subdetector	trigger name	trigger condition	trigger rate
IceCube	Simple Multiplicity (SMT 8)	8 hit modules with local coincidence within 5 μs	1 kHz
IceCube	String	5 hit modules in a series of 7 consecutive modules on a string within 1.5 μs, no hits in the top three DOM layers	1 kHz
IceCube	Minimum Bias	select events with at least one hit module in regular time intervals	30 Hz
AMANDA	Simple Multiplicity	18 hit modules in AMANDA within 2.5 μs, no local coincidence condition	0.1 kHz
AMANDA	String	3 hit modules in a series of 5 consecutive modules on a string within 1.5 μs on strings 1-4 or 3 hit modules in a series of 3 consecutive modules on a string within 1.5 μs on strings 5-19, at least 8 hit modules in total	0.2 kHz
AMANDA	Minimum Bias	select random events in AMANDA with a fixed rate	1 Hz

Table 6.2.: Active triggers during the IceCube 40-strings and AMANDA data taking. Additional IceTop trigger algorithms are not listed here. Listed trigger rates are as of run 111471.

Filter Conditions in IceCube 40-strings and AMANDA

As described in 5.4, not all triggered events can be transferred north via satellite and on-line filters are applied to select the more interesting events. A list of all active filters in the IceCube 40-strings and AMANDA configuration is given in Table 6.4, along with a summary of the events that are targeted with each filter and a typical filter rate. The two most important filters for the analysis presented here are the IceCube Muon Filter and the JAMS (Combined) Muon Filter.

The IceCube Muon Filter

The IceCube Muon Filter [LH07] is designed to select track-like events in IceCube with a high efficiency while the background has to be reduced significantly to comply with the bandwidth constraints of the satellite transfer. As discussed in Chapter 3, multiple muons reaching the detector from coincident cosmic-ray air showers constitute one of the primary backgrounds in the northern hemisphere. In the southern sky, well-reconstructed single muons and muon bundles dominate the data. The cut logic of the muon filter in IceCube 40-strings is thus adapted to different regions of the sky. All cuts in the muon filter are based on the number of channels, the average number of pulses per channel and the reconstructed direction obtained with two different likelihood reconstructions. To apply these cuts, a standard, single-seeded likelihood reconstruction based on the first-guess reconstruction LineFit (see section 7.2) and a dual-seeded likelihood reconstruction based on the LineFit and its inverse as seed are applied.
The first branch of the muon filter requires that the events have at least 10 hit channels (NCh) and that both likelihood reconstructions result in a zenith angle larger than or equal to 70°. This branch of the muon filter is used in the analysis presented in this work. It reaches an efficiency of above 70% for

Filter Branch	Cut
Branch 1	NCh $\geq$ 10 AND BOTH single-seeded and dual-seeded likelihood reconstruction zenith angles$\geq$ 70°.
Branch 2a	NCh $\geq$ 10 AND average number of pulses per channel $\geq$ 5 AND at least one of the likelihood reconstructions has a zenith angle$\geq$ 70°.
Branch 2b	NCh $\geq$ 20 AND average number of pulses per channel $\geq$ 5 AND at least one of the likelihood reconstructions has a zenith angle$\geq$ 50°.

Table 6.3.: Event Selection of the IceCube 40-strings On-line Muon Filter [LH07].

neutrino events with energies above 1 TeV and more than 80% above 10 TeV.
In the second branch, designed to make the southern sky accessible to IceCube, the zenith cuts are weakened with respect to the first branch. To pass the cut, only one of the two likelihood reconstructions needs to result in a zenith angle larger than the required value. In addition, the average number of pulses per channels has to be larger than 5 and the required number of channels is adapted to keep a sufficient background suppression. The event selection criteria of the IceCube 40-strings muon filter are summarized in Table 6.3

The JAMS (Combined) Muon Filter

The JAMS (Combined) Muon Filter [Gro07a] has been designed to complement the IceCube Muon Filter by adding additional events at lower energy that pass through AMANDA. As such, it operates only on events that have a trigger in AMANDA and that have less than 20 hit DOMs in IceCube. The name of the filter derives from the AMANDA first guess reconstruction JAMS which is introduced in section 7.2. A cut on the reconstructed zenith angle of the JAMS algorithm is applied at 75°. This setting ensures a reasonable reduction of the background while it leaves enough room to improve the reconstruction at later stages of the data processing. A harder cut on the zenith angle would have improved the background rejection by a factor of three but would also have resulted in a loss of signal efficiency around the horizon. In addition, a cut is placed on the quality parameter of the JAMS first guess fit (see also section 7.2). With the parameter varying between 0 (poor reconstruction) and 1 (good reconstruction), the cut has been applied at a value of 0.6. The resulting filter has an estimated signal efficiency of more than 80% for neutrino-induced events passing through AMANDA at energies between 10 GeV and 10 TeV.

6.4. Run Selection for the IceCube 40-strings and AMANDA Analysis

IceCube(+AMANDA) data is divided into runs of up to 8 hours length[2]. The data used in this analysis is selected on a run-by-run basis[3]. The decision if a run is good to use can depend on the sub-detector; it is possible that a run contains good IceCube data while the combined events do not meet all quality criteria. However, very similar requirements are placed on the quality of the data collected by the two parts of the combined detector for this analysis:

[2] It is planned to switch to 24 h runs in the future.

[3] The selection of smaller data units is possible as well and can be important for analyses that search for phenomena of short duration. As the data taking is usually very stable during a run, a run-based data selection is sufficient for this work and does not lead to a significant loss of lifetime.

- Runs with non-standard DAQ or detector configurations are excluded.
- Runs with a length shorter than 20 minutes are excluded.
- Runs that do not pass the IceCube monitoring are excluded.

IceCube includes several in-situ light sources to calibrate the detector (see chapter 5). Data with light contamination poses a strong risk to pick up non-particle induced events. All data that has been taken while these light sources were in operation, is thus excluded from the analysis.
A monitoring of the rates of several triggers and physics filters as well as DOM-based information such as DOM launch rates, provide the base for a run-based data quality monitoring as a joint effort of the IceCube collaboration. Only runs without indications of problems in this monitoring are selected.
In addition, each run is required to have a length of at least 20 minutes. The monitoring of shorter runs is difficult due to the larger statistical fluctuation of the filter rates. Also, the shortness of the run is most often caused by a failure in the detector (for example DOMs or strings not starting up) that caused the run coordinator to restart the run.
For the short period of 7 days after New Year 2009, the time synchronization between AMANDA and IceCube was off by one second due to a bug in the data acquisition[4]. For the data taken during this period we only consider IceCube and discard all combined events - the relative timing between the two detectors is crucial for the reconstruction of these events.
In addition to the application of these selection criteria, the stability of the rate of up-going events is tested on the level where the data is still dominated by mis-reconstructed atmospheric muons as well as on the final level. Furthermore, it has been checked that the event ids and event times in the final level event selection increase monotonically. Adding all these considerations together, 92% of the total detector up-time with IceCube 40-strings and AMANDA are considered in the analysis.

6.5. Cleaning of Combined Events for the IceCube 40-strings and AMANDA Analysis

AMANDA strings 5-10 use twisted copper pair cables. These cables are vulnerable to pick-up of electronic noise, in particular during periods of strong wind at the South Pole. The result of this vulnerability is a class of non-particle induced events, the so-called ”flary” events, that has to be identified and removed from the data. These events have characteristic waveforms that differ from the ones of particle-induced events. A software to identify these events based on their waveforms is available [Gro07b]. The algorithm has been used already in the analysis of the IceCube 22-strings and AMANDA data [Ses10] and the validity of the cuts has been reassessed for the analysis presented here. The algorithm makes use of two characteristic features of the waveforms recorded with AMANDA:

- The division of waveforms into waveforms segments.
- The median rate of local maxima in the waveforms.

The AMANDA DAQ produces a waveform segment whenever the measured charge in an OM exceeds a certain, predefined value. The measured charge is recorded as long as it stays above the baseline and a few sample points around the pulse are added to the waveform segment. If one of two succeeding waveform segments has only a single sample point over threshold, the two waveform segments are merged into one. Each waveform segment is thus a part of a full waveform that ends and starts with the baseline charge and comprises at least one pulse. Noisy, non-particle induced events tend to lead to the collection of more waveform segments than other events.
In addition, they also often show waveforms with several local maxima or peaks. At moderate energies, most particle induced events have exactly one peak per waveform. ”Flary“ events are identified by the

[4] On December 31, 2008 a leap second was to be added to the UTC time. This operation was performed correctly in the AMANDA DAQ while two leap seconds were added in the IceCube DAQ. This lead to a mismatch between the two detectors.

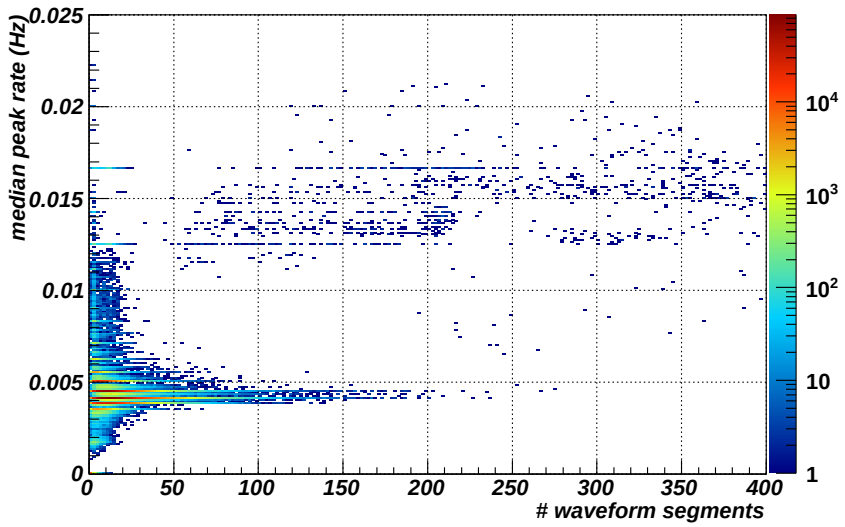

Figure 6.5.: Distribution of the two waveform characteristics that are used to identify non-particle induced events in the combined detector. The median peak rate is plotted against the number of waveform segments. The z-axis represents the number of events in each bin. Events with both a high median peak rate and a large number of waveform segments are more likely to be induced by electronic noise. The analysis uses only events with a median peak rate smaller than 0.005 Hz or less than 20 waveform segments. The tail of events with a moderate median peak rate and a high number of waveform segments corresponds to real events with higher energies which typically leave many hits in IceCube as well. The plot uses data from runs 112000 to 112099 at L3, taking into account only events with a successful likelihood reconstruction of the combined pulse series and an upgoing zenith angle.

combination of a high median rate of local maxima in the waveforms and a high number of waveform segments on AMANDA strings 5-10. Figure 6.5 shows the distribution of the two waveform characteristics for a number of runs (112000 to 112099) from the IC40+AMANDA data. The majority of events are located at low values of the median peak rate and the number of waveform segments. There is however a second population of events with higher values in both parameters. These are the ”flary” events. For the analysis, only events with a median peak rate equal to or below 0.005 Hz or with 20 or less waveform segments are considered. All other combined events are rejected. Through this cut, less than half a percent of the combined data is removed from the analysis. The effect on the signal, though not simulated, can be estimated to be of the same size.

Figure 6.6 illustrates the non-particle induced nature of the events that are removed from the data sample in this way. To illustrate the effect better, a selection of events with median peak rate above 0.006 Hz and more than 30 waveform segments (in red) is compared to the events that are considered as good to be used in the analysis (in blue). It can be clearly seen that the ”flary“ events have a higher occupancy on the affected strings and leave very little light in the surrounding IceCube detector.

Active on	filter name	goal	filter rate
IceCube	Muon	select up- and down-going track-like events, suppress coincident muons from multiple cosmic-ray primaries and single downgoing muons.	19.8 Hz
IceCube	Atmospheric Muon	select a complimentary sample of down-going atmospheric muons	0.3 Hz
IceCube	EHE	select up- and down-going events at the highest energies	1.1 Hz
IceCube	Cascade	select cascade-like events based on the LineFit velocity (see 7.2) and the event topology	16.2 Hz
IceCube	Downgoing Starting	select down-going low-energy starting tracks for Galactic center analyses using the top layer of the detector as veto	1.7 Hz
IceCube	Moon	select events from the direction of the moon when visible for moon shadow analyses	–
IceCube	ULEE	select ultra low-energy events at energies of a few tens of GeV for GRB searches and atmospheric neutrino studies using a veto	1.7 Hz
IceCube	Physics Mininum Bias	select a random sample of events with Physics Min Bias trigger	0.5 Hz
Combined	Mininum Bias	select a random sample of triggered events in IceCube and/or AMANDA	0.5 Hz
Combined	JAMS Muon	select low-energy up-going muon tracks with a trigger in AMANDA	3.1 Hz
Combined	Low Energy Upgoing	select low-energy up-going muon tracks in IceCube or AMANDA for WIMP searches	11.1 Hz
Combined	Low Energy Contained	select low-energy contained events	4.6 Hz
Combined	Low Energy Cascade	select cascade-like events in AMANDA and surrounding IceCube strings using part of the detector as veto	7.2 Hz
Combined	Downgoing Contained	select down-going contained events in AMANDA	11.9 Hz

Table 6.4.: Active filters during the IceCube 40-strings and AMANDA data taking. Additional IceTop filters are not listed here. Rates are as of run 111471. The Moon filter did not collect data during this run. The relevant filter algorithms for this work are the IceCube Muon Filter and the AMANDA JAMS filter. Descriptions of all deployed filters are available on [Bla08].

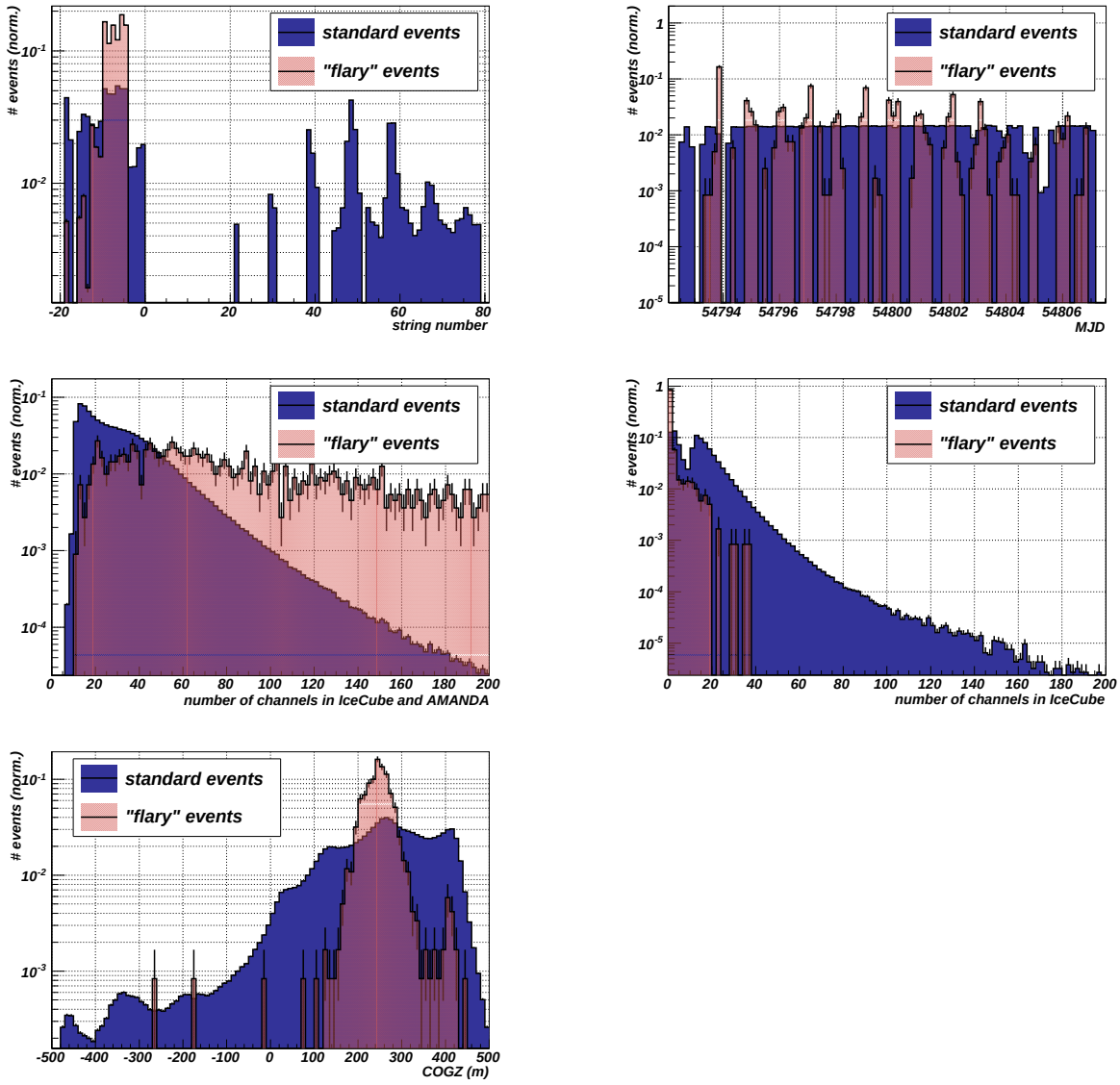

Figure 6.6.: Illustration of the characteristics of the so-called ”flary” events in AMANDA. The same data as in Figure 6.5 is divided into two separate samples: “standard“ events (blue) are those that are used in the analysis and have either a low median peak rate ($\leq$0.005 Hz) or a low number of waveform segments ($\leq$ 20). ”Flary” events (red) are selected to be events with a median peak rate $\geq$0.006 Hz and more than 30 waveform segments. The top left plot shows the string occupancy for “flary“ and standard events, AMANDA strings have negative string numbers. As expected, AMANDA strings 5-10 contribute most to the ”flary” events. The top right plot shows the comparison of the time of the events for both populations. The middle row shows the total number of channels (left) and the number of channels in standard IceCube strings. “Flary“ events reach up to high numbers of channels if AMANDA is taken into account but have very few hits in IceCube alone, stressing their non-particle induced character. Finally, the z-position of the charge-weighted center of gravity is shown at the bottom left. The origin of the IceCube coordinate system is in the center of the detector and the z-axis points away from the center of the Earth. With few hits on standard IceCube strings, ”flary” events are more abundant at the position of AMANDA at the top of the combined detector.

7. Reconstruction in the Muon Neutrino Channel

When neutrinos interact in charged-current interactions, a lepton of the same flavor is produced. The average angle between the neutrino and the emerging lepton falls below 4° for neutrino energies above 100 GeV. The directional reconstruction of the incoming neutrino can therefore be based on the reconstruction of the direction of the lepton. A more detailed look at neutrino interactions is provided in Chapter 1.
This chapter will primarily treat the track reconstruction in the muon neutrino channel and is structured as follows: First, the energy loss and light deposit of high-energy muons in ice are reviewed. The topology of the light that is detected by the DOMs provides the base for both directional and energy reconstruction in IceCube. The most important reconstruction algorithms are introduced and their application within the presented analysis of IceCube 40-strings and AMANDA data is discussed.

7.1. Muon Energy Loss in the Ice

Cherenkov Light

Ice is a dielectric medium and at the energy range GeV to EeV energies as of interest for IceCube, all leptons are above the threshold for Cherenkov light emission $\beta > \frac{1}{n}$, i.e. their velocities are higher than the speed of light in the ice. Cherenkov light is emitted at a characteristic angle which depends on the refractive index $n(\lambda)$ of the medium:

$$\cos(\theta_c) = \frac{1}{\beta \cdot n(\lambda)} \tag{7.1}$$

The Cherenkov angle in ice with a refractive index of $\approx$ 1.32 at 400 nm is 41° and the emission is peaked in the ultraviolet. The observed light pattern depends on the lepton type of the neutrino and on its interaction. The differences are illustrated in Figure 7.1: A highly energetic muon produced in a charged-current interaction of a muon neutrino is able to travel over a long distance through the detector and emits Cherenkov light along the track. Neutral-charge interactions as well as charged-current interactions of electron and tau neutrinos lead to the observation of spherical Cherenkov fronts

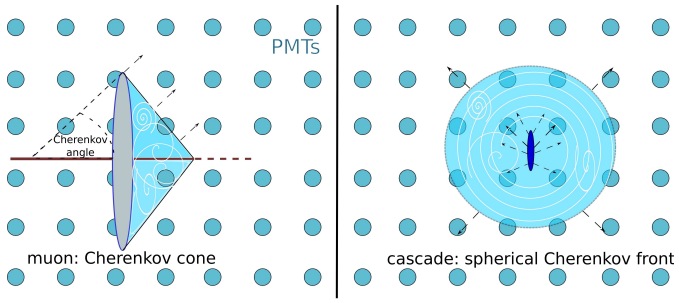

Figure 7.1.: Left: schematic view of a muon track with generated Cherenkov light in a neutrino telescope. Right: Electron and tau neutrinos generate forward-peaked cascades in the detector. After [ABB+04].

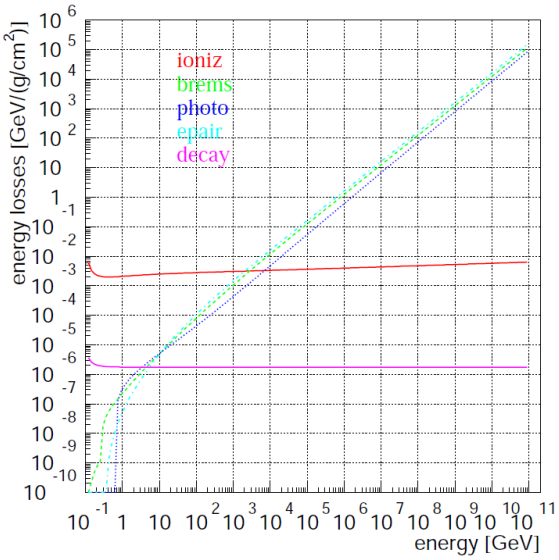

Figure 7.2.: Muon energy loss in ice: the contributions of ionization, bremsstrahlung, photo-nuclear interactions, $e^{\pm}$ pair production and muon decay are shown. Ionization dominates up to energies of a few 100 GeV. At higher energies, bremsstrahlung, photo-nuclear interactions and electron pair production contribute more and the energy loss scales with the energy of the muon. From [RC01].

(cascade) within a confined volume of the interaction point[1].
The differences in the event topologies are precisely what makes muon neutrinos more suitable for analyses that rely on a good angular reconstruction, such as those presented in this work. Therefore, only the reconstruction of muons from charged-current interactions of high-energy neutrinos will be treated in this chapter. It is to be noted however that also the cascade channel has advantages; as the energy deposit is more often contained within the detector than for charged-current muon neutrino events, a better energy reconstruction is possible. Moreover, the cascade channel is sensitive to all three neutrino flavors.
The total amount of energy that goes directly into Cherenkov light from the muon is negligible in comparison to other energy losses (see next section). However, the summed Cherenkov light emission from the muon and its secondaries plays the key role in the detection and angular reconstruction.

Stochastic Energy Loss

A muon that travels through matter can lose energy through different processes: ionization, bremsstrahlung, photo-nuclear interactions, i.e. the exchange of a photon between the muon and the nucleus, and $e^{\pm}$ pair production. Ultimately, the muon will decay and lose all its remaining energy. The relative importance of each process depends on the cross section of the process and through this on the energy of the muon. The contributions of the different processes in ice are illustrated in Figure 7.2.
Ionization of the atoms in the ice is dominant at energies below several 100 GeV. The mean energy loss per unit length through ionization is given by the Bethe-Bloch equation [Gro08]:

$$-\left\langle \frac{dE}{dx} \right\rangle = K \frac{Z}{A} \frac{1}{\beta^2} \left[\frac{1}{2} \ln \left(\frac{2 m_e c^2 \beta^2 \gamma^2 T_{max}}{I^2} \right) - \beta^2 - \frac{\delta(\beta\gamma)}{2} \right] \tag{7.2}$$

[1] If the energy is high enough, also a tau will be able travel beyond the interaction point.

where K is a constant factor, Z the atomic number of the stopping medium and A its atomic mass number. I is the mean excitation energy in electronvolt and T_{max} the maximum kinetic energy that can be transferred to a free electron. The function $\delta(\beta\gamma)$ is a correction term for polarization effects that reduce the energy loss through ionization. The Bethe-Bloch equation is valid for $0.1 \lesssim \beta\gamma \lesssim 1000$ in media with intermediate Z. It is to be noted that ionization is a stochastic process. Most single energy losses are much smaller than the mean energy loss since the distribution of energy losses has long tails.
At higher energies, where radiative processes dominate the energy loss, the average energy loss per unit length can be written as a function of the form [Gro08]:

$$-\left\langle \frac{dE}{dx} \right\rangle = a + b \cdot E \tag{7.3}$$

where a is given through Equation 7.2 and b describes the sum of bremsstrahlung, photo-nuclear interactions and $e^{\pm}$ pair production. Hard, i.e. more energetic single energy losses are more likely to occur through bremsstrahlung than through photo-nuclear interactions or $e^{\pm}$ pair production [Gro08]. This relation of the energy loss to the particle energy provides the base for many energy reconstructions in IceCube.

7.2. Muon Angular Reconstruction

A muon event from the 40-string configuration of IceCube is shown in Figure 7.3 for illustration. A muon (atmospheric or induced by a neutrino) crossing the instrumented volume of IceCube will be characterized and reconstructed via the photon arrival times t_i, the number of photo electrons detected with the DOMs and the positions of the active DOMs $\vec{r}_i = (x_i, y_i, z_i)$[2]. The result of the reconstruction consists of the muon direction and its estimated energy E_0. The two angles θ (zenith) and ϕ (azimuth) define the direction of the movement. Even though it is possible to fit direction and energy at the same time, the addition of a sixth free parameter[3] in the minimization makes the reconstruction significantly slower [ABB+04]. Usually, the reconstruction is thus divided in two steps; the particle's direction is reconstructed first and the energy reconstruction is then seeded with the previously obtained best track. As a compromise between CPU-consumption and the quality of the reconstruction, the best track is obtained by the successive application of different reconstructions, starting with the fastest and simplest that will then be used as a seed for more elaborate reconstructions on a smaller selection of events.

First Guess Reconstruction for IceCube Events: LineFit

The LineFit reconstruction [AAA+11b] ignores both the geometry of the Cherenkov cone and the properties of the ice [ABB+04]. The assumption of light traveling through the ice at a constant speed $\vec{v}$ along an infinite, straight line is fit to the data. The location of a DOM $\vec{r}_i$ that detected a photon at time t_i can always be written as

$$\vec{r}_i = \vec{r_0} + \vec{v} \cdot t_i \tag{7.4}$$

The corresponding χ^2 function is

$$\chi^2 = \sum_{i=1}^{N_{hit}} (\vec{r}_i - \vec{r_0} - \vec{v} \cdot t_i)^2 \tag{7.5}$$

where N_{hit} is the number of hits in the detector. The analytical solution for the minimum of the χ^2 function as function of $\vec{r_0}$ and $\vec{v}$ is:

$$\vec{r_0} = \langle \vec{r}_i \rangle - \vec{v} \cdot \langle t_i \rangle \tag{7.6}$$

[2] It is also possible to use the full waveforms rather than the extracted pulses in the reconstruction. Both analyses presented in this work are however based only on reconstructions of the extracted pulses.
[3] The track is fully defined through the two angles θ and ϕ and the coordinates $\vec{r_0}$ of the particle at a time t_0

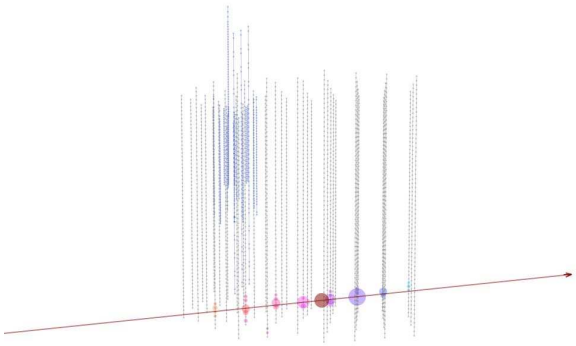

Figure 7.3.: A muon event in the IceCube 40-strings detector. The colors indicate the arrival times of the light in the DOMs; early hits are orange, the latest hist are cyan. The red arrow represents the directional reconstruction obtained with the MPE likelihood reconstruction.

and

$$\vec{v} = \frac{\langle \vec{r}_i \cdot t_i \rangle - \langle \vec{r}_i \rangle \cdot \langle t_i \rangle}{\langle t_i^2 \rangle - \langle t_i \rangle^2} \tag{7.7}$$

where $\langle ... \rangle$ denotes the mean of the parameter with respect to all hits. The magnitude of the constant speed $\vec{v}$ can be used as a cut parameter to distinguish between minimally ionizing muon tracks and cascade events or events with dominant stochastic energy losses [ABB+04]. The performance of the LineFit as a track reconstruction is shown in Figure 7.5 for simulated neutrino events from the IceCube 40-strings configuration which pass the online filter and a moderate cut on the direction and quality of a likelihood reconstruction that has been applied in addition to the LineFit. For this event selection, a median angular resolution between 7° and 28° is observed with the LineFit. The LineFit is not only used as a first guess reconstruction in the IceCube 40-strings configuration but also for data that has been taken with later configurations. Within this work, the LineFit velocity is used as a cut variable for the selection of neutrino candidates from the IceCube 79-strings data.

First Guess Reconstruction for Combined IceCube 40-strings and AMANDA Events: JAMS

For AMANDA, both as a stand-alone neutrino telescope and as a part of the combined IceCube detector, a different first guess algorithm has been used: the JAMS (Just Another Muon Search) algorithm. Descriptions of this algorithm can be found in [Bur08] as well as in [Fra07] where an optimization of the algorithm has been performed.
The algorithm is based on a cluster search: For the true particle direction, it is expected that many hits cluster with each other if their positions are projected onto a plane perpendicular to the track. A cluster is then characterized by a high number of close hits in this plane. This property can be used to obtain a first guess for the particle direction. The JAMS algorithm starts by quantifying the amount of clustering for a number of random track hypotheses. For each of these random directions, the clustering is quantified by the number of hit pairs that fulfill

$$D_{ij}^2 = \left(\hat{x}_i - \hat{x}_j\right)^2 + \left(\hat{y}_i - \hat{y}_j\right)^2 + c^2 \cdot \left(\hat{t}_i - \hat{t}_j\right)^2 < D_{max} \tag{7.8}$$

where $\hat{x}$, $\hat{y}$ and $c\hat{t}$ are the positions of the hits in a coordinate system whose z-axis points in the direction of the hypothesized track. A typically used value of D_{max} is 100 m. The direction with the largest number of

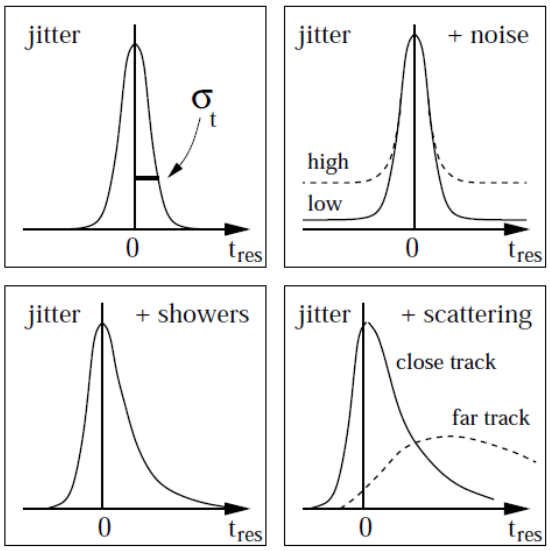

Figure 7.4.: Illustration of the effects of several detector properties on the distribution of time residuals at the DOMs. In an ideal detector, t_{res} would be a δ-function at zero. In reality however, the distribution is distorted by the effect of PMT jitter, i.e. the limited timing resolution of the PMT. Random noise adds a constant component to the distribution. Secondary showers along the track increase the probability to observe late photon hits. At DOM positions far away from the track, the photon arrival time is strongly distorted by scattering. The scattering also leads to a different time residual distribution for DOMs that are oriented away from the track with respect to the one of a DOM which is oriented towards the track. From [ABB+04].

hits which fulfill Equation 7.8 is used as a seed to a simplified likelihood reconstruction. In comparison to the LineFit, JAMS is more robust against coincident muons from multiple cosmic-ray primaries.
In addition to the track reconstruction, JAMS also calculates a quality parameter Q. This quality parameter is based on the output of a Neural Network that has been trained with simulated data and uses information about the reconstructed track such as the track length and the number of hits close to the track. If JAMS was ever to be used on IceCube events, a new training of this Neural Network would be necessary as well as a new optimization of the distance D_{max}. It has also to be taken into account that the algorithm can be slow for events with a high number of hits such as events with very high energies or events that pass through the more densely instrumented DeepCore region.

Maximum Likelihood Reconstructions

A better angular resolution than with the first guess algorithms is achieved with maximum likelihood reconstructions (see also Figure 7.5). A set of parameters $\vec{a}$ is deduced from the measurement $\vec{x}$ by maximizing the likelihood function $\mathcal{L}(\vec{x}|\vec{a})$. For particles above $\sim$ 100GeV, an infinite muon track moving with the speed of light is used as the track hypothesis.
To define the likelihood functions used in IceCube, it is convenient to introduce the concept of *time residuals*. In a non-scattering medium, the expected arrival time t_{geo} of a photon from the Cherenkov cone at a DOM at position $\vec{r_i}$ can be calculated from the distance of the DOM to the track and the geometry of the Cherenkov cone. The time residual t_{res} is defined as the difference between the observed hit time and expected hit time t_{geo}. In an ideal detector, the distribution of t_{res} would peak sharply at zero for the best track hypothesis. In reality however, several detector effects distort the distribution and make it wider. The impact of several of these effects is illustrated in Figure 7.4. It is to be noted that the

distribution of the time residuals at a given DOM depends on the local properties of the ice, in particular the scattering.
The differences in the maximum likelihood reconstructions that are available in IceCube are primarily defined trough the time residual pdf that is used in the reconstruction. The two most important ones are the “Single Photo Electron” pdf and the “Multi Photo Electron” pdf.

Single Photo Electron (SPE) Reconstruction

The “Single Photo Electron” (SPE) reconstruction searches the most likely track hypothesis, i.e. the best fit particle direction, by maximizing the likelihood function

$$\mathcal{L}_{SPE}(\vec{t_{res}}|\vec{a}) = \prod_{i=1}^{N_{hit}} p_1(t_{res,i}|\vec{a}) \tag{7.9}$$

that is equivalent to the probability to simultaneously observe the time residuals $t_{res,i}$ if the true particle track is described by the parameters $\vec{a}$. The product runs over all the DOMs and takes into account the first hit. Later hits are more likely to originate from strongly scattered light and are more challenging to describe. $p_1(t_{res,i}|\vec{a})$ is the probability density function (pdf) for the time residual $t_{res,i}$ under the variation of $\vec{a}$ in the first hit in the DOM assuming that no additional photons have been detected with this DOM. While it is possible to use tabulated probability density functions to include a detailed description of the detector, it is more economical to use an analytical approximation of the time residual pdfs. The analytical approximation in use is the so-called “Pandel” function, a gamma distribution of the following form:

$$p_1(t_{res}) \equiv \frac{1}{N(d_{eff})} \frac{\tau^{-(d_{eff}/\lambda)} \cdot t_{res}^{(d_{eff}/\lambda - 1)}}{\Gamma(d_{eff}/\lambda)} \cdot e^{-\left(t_{res}\cdot(\frac{1}{\tau}+\frac{c_{ice}}{\lambda_a})+\frac{d_{eff}}{\lambda_a}\right)} \tag{7.10}$$

where

$$N(d_{eff}) = e^{-\frac{d_{eff}}{\lambda_a}} \cdot \left(1 + \frac{\tau \cdot c_{ice}}{\lambda_a}\right)^{d_{eff}/\lambda} \tag{7.11}$$

d_{eff} is an effective distance from the DOM to the track taking into account the orientation η of the PMT with respect to the track. c_{ice} is the speed of light in ice, λ_a the absorption length and $\Gamma(d/\lambda)$ is the gamma function. λ and τ are functions of the distance d_{eff}. λ, τ and λ_a as well as the connection between d_{eff} and the real distance d are determined from simulation of Cherenkov light in the detector. The following values [ABB+04] are obtained from an ice model based on the work of [AAB+05a]:

$$\tau = 557\text{ns}, \lambda = 33.3\text{m}, \lambda_a = 98\text{m}, d_{eff} = 0.84\text{m} + \left(3.1\text{m} - 3.9\text{m} \cdot \cos(\eta) + 4.6\text{m} \cdot \cos^2(\eta)\right) \tag{7.12}$$

and are used in current reconstruction algorithms. The Pandel function includes the effect of scattering. It does however not take into account the effect of PMT jitter illustrated in Figure 7.4. This is included in the pdf by a convolution with a Gaussian of configurable width.

Multi Photo Electron (MPE) Reconstruction

The presence of additional pulses is taken into account in the so-called “Multi Photo Electron” (MPE) likelihood. The pdf of the time residuals is then defined as

$$p_N^1(t_{res}) = N \cdot p_1(t_{res}) \cdot \left(\int_{t_{res}}^{\infty} p_1(t)dt\right)^{N-1} \tag{7.13}$$

This is the probability density function for the observation of the time residual t_{res} for first of N pulses. By using this pdf in the likelihood function $\mathcal{L}_{MPE}$, the MPE reconstruction yields a better angular resolution

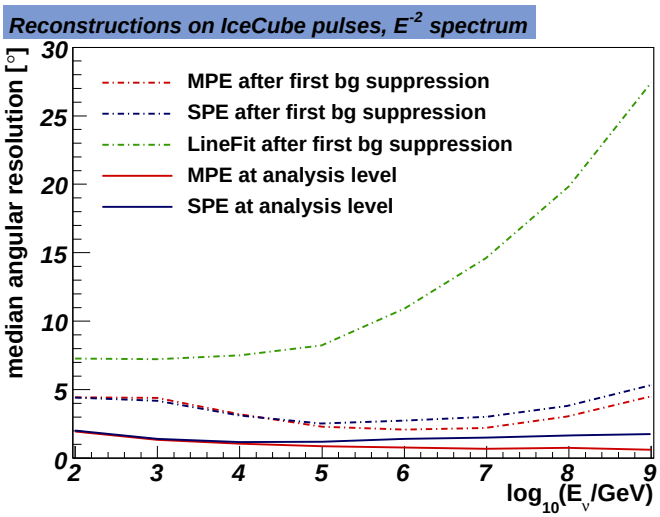

Figure 7.5.: The median angular resolution of the two maximum likelihood reconstructions is compared to the first guess algorithm LineFit for the IceCube 40-strings configuration. All reconstructions shown in this plot have been applied to the IceCube-only pulses. For the first background suppression mentioned here, events with up-going MPE fit and MPE rlogl (see Chapter 9) smaller than 12 have been selected. The event selection at analysis level is described in Chapter 9 and targeted to select events with a good MPE reconstruction.

than the SPE reconstruction for high-energy particles where multiple pulses are dominantly observed. At the same time, it is more sensitive to the timing resolution of the pulse extraction. Figure 7.5 shows a comparison between the MPE and the SPE reconstruction run on the IceCube pulses from the IceCube 40-strings configuration for two different event selections. The event selection labeled with "first background suppression" is obtained by applying two additional cuts with respect to the on-line IceCube Muon Filter (see section 5.4): The MPE reconstruction is requested to be up-going and a soft cut on the quality parameter of the MPE fit (i.e. the reduced likelihood, see also Chapter 9) has been made at a value of 12.0, corresponding to a soft cut on the quality of the reconstruction. At energies below 10 TeV, the SPE and MPE reconstructions show a similar performance with a difference of less than 0.1° in median angular resolution between them. At higher energies, the MPE reconstruction is clearly better than the SPE reconstruction, with a difference of up to 0.7° in median angular resolution. Therefore, the MPE reconstruction is used in this work whenever possible. Both likelihood reconstruction are clearly superior to the LineFit first guess reconstruction which shows an undesirable degradation in angular resolution as the energy of the events increases.

The two reconstructions are also compared at analysis level after the event selection described in Chapter 9 has been applied to the simulated events. The applied event selection is targeted to select well-reconstructed events and a clear improvement with respect to the previous cut level is seen. The MPE reconstruction has a slightly better angular resolution than the SPE reconstruction. It is however to be noted that the event selection at analysis level is biased towards events that are well-reconstructed with the MPE reconstruction since the quality parameters of this reconstruction are used in the selection of events.

Maximum Likelihood Reconstructions for Combined IceCube 40-strings and AMANDA Events

During the development of the combined data sample from the IceCube 40-strings and AMANDA data, new challenges emerged in the use of the MPE reconstruction: contrary to the expectation, the MPE

reconstruction performed clearly worse than the SPE reconstruction when both were applied to the combined IceCube and AMANDA pulses. AMANDA is the first low-energy core that has been used in a neutrino telescope and none of the reconstruction algorithms has been designed to be applied to data with two regions of different PMT density nor to data that has been merged from two different data acquisition systems that may among other differences have different timing resolutions. The MPE reconstruction is indeed more sensitive to the timing resolution than the SPE reconstruction as the MPE pdfs are narrower than the SPE ones.
Within this work, several variations of the settings of the MPE reconstruction have been tested to account for the differences in detector and data acquisition between IceCube and AMANDA. These include changes of the noise probability, the timing error and the size of the PMT jitter effect in the likelihood reconstruction. None of them lead to an improved or equal angular resolution with respect to the SPE reconstruction if both were applied to the combined pulses.
A possible consequence of the superiority of the SPE reconstruction on the combined pulses would have been to use the SPE reconstruction for all combined events while the MPE reconstruction is used for IceCube events. Instead, a hybrid approach has been chosen in this work for the combined events to obtain the best possible angular resolution. Within the data processing of the combined data, two different reconstructions have been applied to all combined events:

- The above-mentioned SPE reconstruction, performed on the data of all PMTs with a signal in the event, i.e. using both IceCube and AMANDA.
- An MPE reconstruction that omits the pulses recorded with AMANDA and uses only the information collected in IceCube.

Both of these reconstructions do not use the full information that is available about the event. The SPE reconstruction does not take into account the presence of multiple pulses per PMT while the MPE reconstruction in this particular case uses only a subset of the available pulse series. It is not a priori clear which of the two reconstructions is better for an individual event as the performance of both depends on the energy of the event in a different way. For low energetic events, it will be important to include the additional information collected in AMANDA. High-energy events however that go for example through the short axis of the asymmetric IceCube 40-strings detector and pass AMANDA may have only intermediate numbers of channels in IceCube but multiple pulses in each channel. In this case, the MPE reconstruction on the IceCube-only pulses may be superior to the SPE reconstruction on all pulses.
Figure 7.6 compares the angular resolution of the combined SPE reconstruction (red) to the angular resolution that would be achieved if the optimal reconstruction between the combined SPE and the IceCube-only MPE reconstruction was selected based on the MC information about the true track direction. While this selection cannot be applied to experimental data, it can serve to benchmark the performance of the reconstruction. The angular resolution is compared for three different spectra: a very hard neutrino signal spectrum with spectral index 1 on the left, an intermediate neutrino signal spectrum with spectral index 2 in the middle and the soft E^{-3} spectrum that has been used as a benchmark signal spectrum in the IceCube 40-strings and AMANDA analysis in the right plot. The event selection described in Chapter 9 has been applied to the simulated events.
A spectrum like the one in the first plot includes many events at the highest energies. The angular resolution of the SPE reconstruction on the combined pulses has a median of around 1.3° and is significantly below the one that could be achieved if the best of the two reconstructions was selected. This optimal selection has a median angular resolution below 0.4°. For intermediate (spectral index 2, middle) and soft spectra (spectral index 3, left), the difference between the SPE reconstruction and the optimal selection between the two reconstructions is much smaller, indicating that the SPE reconstruction is indeed the better of the two for the majority of the events.
The blue lines in Figure 7.6 represent the angular resolution for combined events that is achieved with the choice of reconstruction that is used in the IceCube 40-strings and AMANDA point source analysis. A hybrid approach has been chosen that selects the reconstruction to be used in the final test based on

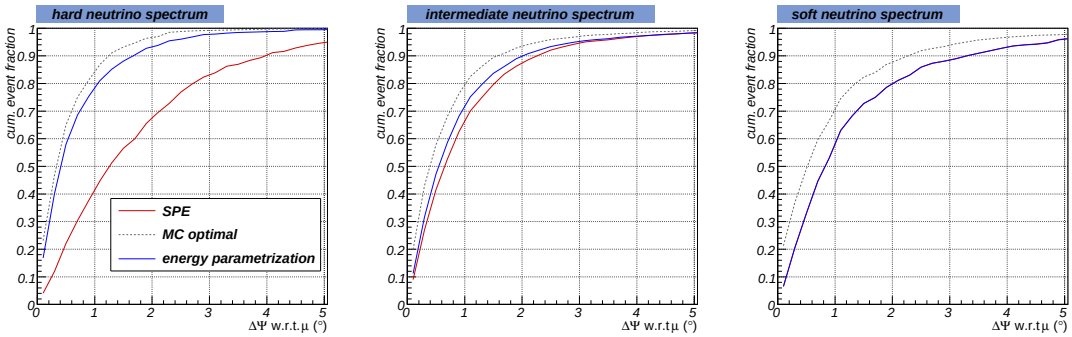

Figure 7.6.: Comparison of the angular resolution for combined IceCube 40-strings and AMANDA events with the event selection described in Chapter 9. Shown are three different neutrino spectra: a very hard spectrum with spectral index 1 at the left, an intermediate spectrum with spectral index 2 in the middle and a very soft spectrum with spectral index 3 at the right. The comparison shows the angular resolution of the SPE maximum likelihood reconstruction of the combined pulses (red) with the angular resolution that would be achieved if the best reconstruction between the SPE on combined pulses and the MPE on IceCube-only pulses was selected (gray, only possible on MC) and the combination (blue) of SPE and MPE depending on the estimated energy of the event.

∢ SPE-MPE	energy estimate (EE)	selected reconstruction
$< 0.5°$	–	SPE
$\geq 0.5°$	$\log_{10}(\mathrm{EE}) \leq 4.5$ or energy reco failed	SPE
$\geq 0.5°$	$\log_{10}(\mathrm{EE}) > 4.5$	MPE

Table 7.1.: For events with AMANDA data, the combined SPE reconstruction or a pure IceCube MPE reconstruction is used depending on the energy estimate (EE) for the event and the angle between the two reconstructions. The energy estimate is obtained with MuE (see Chapter 7) applied to the IceCube-only pulses.

the characteristics of the event. The estimated energy of the event (based on the IceCube-only pulses) and the angular distance between the two reconstructions are used to decide which reconstruction should be used. The full decision criteria are summarized in Table 7.1. An improvement with respect to the use of only the SPE reconstruction for combined events is clearly visible in Figure 7.6 for harder neutrino signal spectra than E^{-3}. The angular resolution for this soft spectrum is unaffected.
The overall angular resolution of the neutrino sample derived in Chapter 9, is characterized in Figure 7.7. For a soft E^{-3} signal neutrino spectrum, a median angular resolution of 1.2° is obtained. This includes both IceCube and combined events. As can be seen in the comparison of this number to the right plot in Figure 7.6, combined events do indeed obtain a better angular reconstruction at low energies than IceCube events; the median angular resolution of the combined events in a E^{-3} signal neutrino spectrum is below 1°.

Estimation of the Uncertainty of the Angular Reconstruction

IceCube's pointing capabilities are studied through the detailed analysis and monitoring of the moon shadow [BGK09]. Moreover, a limited sample of tracks that trigger both IceTop and IceCube is also used for the verification of the angular reconstruction.

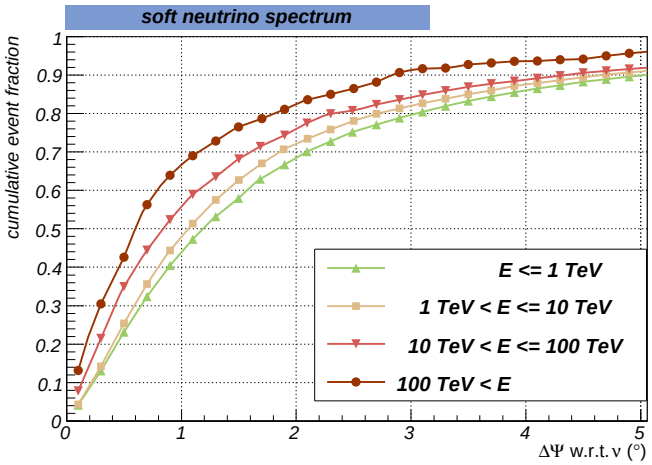

Figure 7.7.: The angular resolution of the IceCube 40-strings and AMANDA neutrino sample is shown for four different neutrino energy regions based on simulated data. The kinematic angle between the neutrino and the detected muon is included and impacts the pointing capability at the lowest energies. In addition, high-energy events are better reconstructed than low-energy tracks because of their longer track length and higher number of hit channels in the detector. For an E^{-3} neutrino spectrum as considered in this plot, the median angular resolution ranges from 1.2° for neutrino events below 1 TeV to less than 0.6° above 100 TeV. All events, including combined events, that pass the event selection described in Chapter 9 are included in this plot and the reconstruction is chosen according to the type of event.

The uncertainty in the angular reconstruction of a distribution of events is determined using simulated neutrino events. The true simulated track direction is compared with the reconstructed one providing a measurement of the performance of the reconstruction algorithm. Figures 7.6 and 7.7 characterize the performance of the reconstructions on the events selected for the IceCube 40-strings and AMANDA point source analysis in this way.

In both simulation and data, it can be shown that the error in the reconstruction depends on the characteristics of the events that are considered. Events with a high number of hits in the detector, i.e. high-energy events and events that pass through the core of the detector, are typically better reconstructed than low-energy events or events that do not pass through the instrumented volume. This implies an energy dependence of the performance of the reconstruction that is evident in Figures 7.7 and 7.5. It is therefore desirable to obtain an estimate of the angular uncertainty in the reconstruction of individual events. These estimates can be used to select well-reconstructed events for point source analyses. Besides that, they can be used in the statistical analysis itself to weight events with their probability to originate from the direction of interest. A test of this kind is described in Chapter 4 and applied to the event selection developed in this work.

The method that is used to obtain the angular uncertainty estimates for this work[4] is described in [Neu06] and is available as part of IceCube's reconstruction software. The method samples the likelihood space around the best fit track and by fitting a paraboloid finds those variations in azimuth and zenith angle that correspond to a predefined decrease in the value of the likelihood function[5]. The result of the method is an error ellipse that is however well-approximated with a circular uncertainty region defined through the variable σ.

[4] Alternative methods have been developed in the meanwhile but were not available for this analysis.

[5] In fact, the algorithm uses an internal coordinate transformation. The results can however be transformed back into equatorial coordinates.

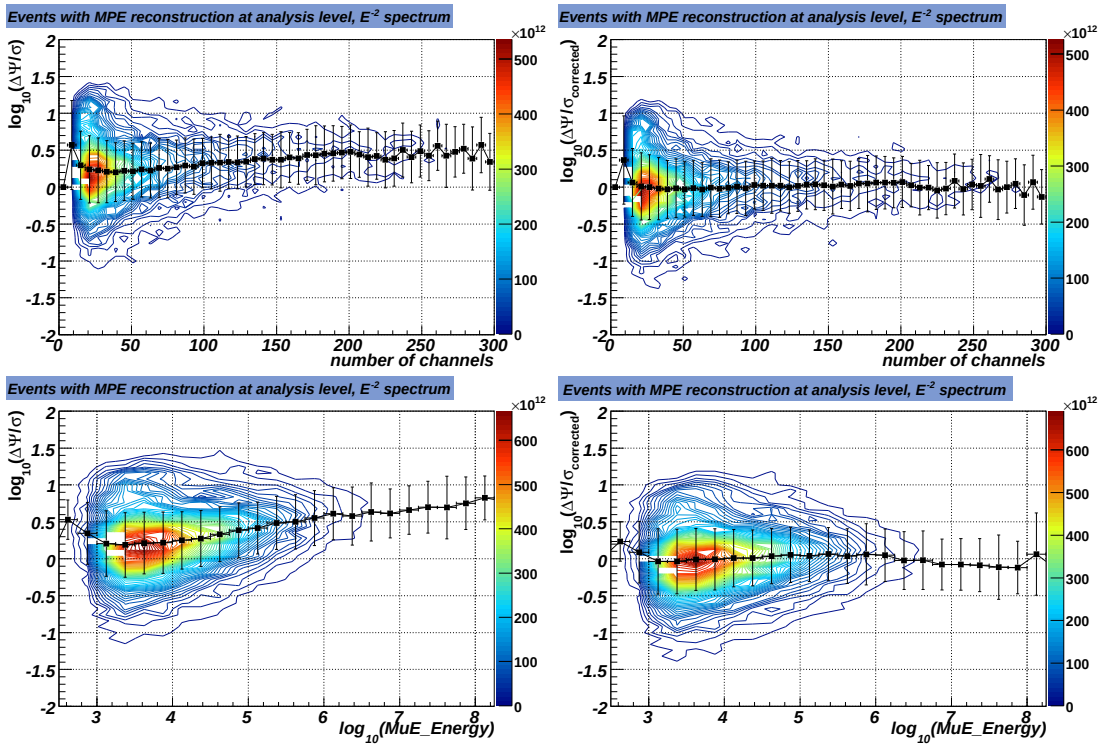

Figure 7.8.: The logarithm of the ratio of the true error in the reconstruction and the paraboloid σ is shown versus the number of active channels (top) and the estimated event energy (bottom). Shown are simulated events reconstructed with the MPE reconstruction and selected by the cuts described in 9. The plots on the left show the uncorrected paraboloid σ, the plots on the right the paraboloid σ after an energy-dependent rescaling. The black boxes represent the mean of the ratio in each bin and the standard deviation of the ratio in each bin is shown with the error bars. For a perfect angular uncertainty estimator, the mean would be constant at zero. Before rescaling, a clear energy dependence is visible with an underestimation of the error of the reconstruction in particular at high energies.

The performance of the paraboloid uncertainty estimate is evaluated on simulated neutrino events for the IceCube 40-strings and AMANDA analysis. The pull ratio of the estimated uncertainty and the error in the reconstruction with respect to the true MC direction should be centered at 1 and be constant as a function of energy. Figure 7.8 shows the logarithm of the pull ratio of the paraboloid angular uncertainty estimator σ and its dependence on two energy estimators: the number of hit channels on the top and the MuE energy reconstruction (see next section) on the bottom. The left column shows that the ratio is not constant at 1 (0 in logarithm) and that the angular resolution is overestimated in particular at high energies. The cause of this is that the pdf in the likelihood describes the data less accurately at high energies than at low energies. It is therefore necessary to rescale the paraboloid σ. The same rescaling as in [AAA$^+$11i] is used here:

$$\sigma_{corrected} = 1.19 \cdot \left(4.97 - 1.97 \cdot \log_{10}(\text{MuE Energy/GeV}) + 0.27 \cdot \log_{10}(\text{MuE Energy/GeV})^2\right) \cdot \sigma \quad (7.14)$$

The plots in the right column show the pull ratio after the rescaling; an improved agreement between the paraboloid σ and the MC angular reconstruction error is achieved.
Figure 7.9 shows the pull ratio of the combined SPE paraboloid σ. The plot on the left shows the dependence on the number of channels as energy proxy. No strong correlation is visible and no rescaling is necessary.

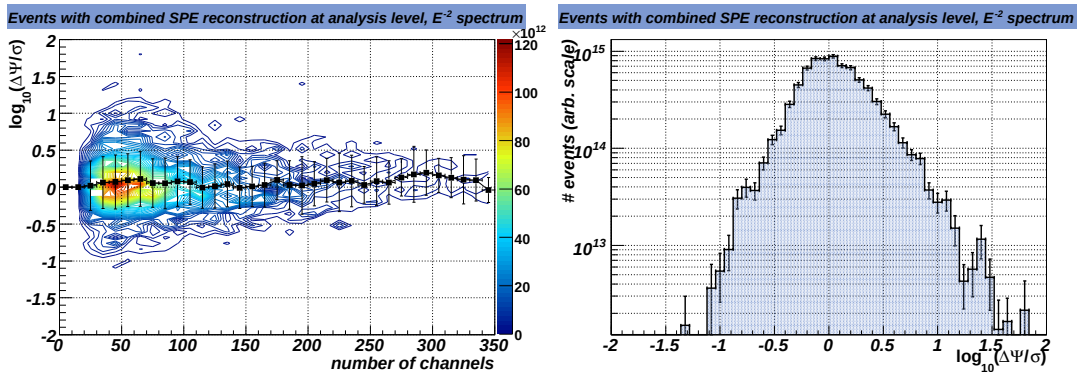

Figure 7.9.: The logarithm of the ratio of the true error in the reconstruction and the paraboloid σ is shown for the combined SPE reconstruction. The left plots shows the dependence on the number of channels while the right plot shows the distribution of the parameter. The black boxes represent the mean of the ratio in each bin and the standard deviation of the ratio in each bin is shown with the error bars. For a perfect angular uncertainty estimator, these would be constant at zero. No rescaling of the SPE paraboloid σ is necessary.

7.3. Energy Estimation

The estimation of the energy of a muon in IceCube can be based on one or more of the following characteristics of the event:

- The length of the muon track if contained events are considered.
- The energy of the cascade at the interaction point if it is located inside the instrumented volume of IceCube.
- The energy loss along the muon track for muon energies above a few 100 GeV.

Different algorithms are developed and used in IceCube to exploit these characteristics for the energy measurement. The analysis presented here uses to a large fraction through-going events whose energy cannot be estimated on the base of the track length or the energy of the cascade at the interaction point. The energy estimate that is used in this analysis is therefore based on the energy loss along the muon track. As illustrated in Figure 7.2, the energy loss scales roughly linear with the muon energy above a few 100 GeV.

The algorithm applied in this work, MuE [ZC08, Chi08], estimates the muon energy by reconstructing the photon density at the point of closest approach to the center of gravity of the hits in the detector with a maximum likelihood approach, taking into account the absorption and scattering in the ice in a bulk ice model [6]. The number of photons per unit length from the muon N_c is then related to the muon energy by [ZC08]

$$N_c = 3 \cdot 10^4 \mathrm{m}^{-1} (1.22 + 1.36 \cdot 10^{-3} \frac{E}{\mathrm{GeV}}) \tag{7.15}$$

The performance of the MuE energy reconstruction is shown in Figure 7.10 and compared to the number of active channels as energy estimator. An approximately linear scaling[7] of the MuE energy estimate with the muon energy is observed at energies above 10 TeV. The linearity range of MuE as energy estimator extends farther than if the number of channels is used as energy proxy. The energy resolution that is obtained on the presented event selection (see Chapter 9) is better than at lower level event selections as most of the events are passing through the instrumented volume of the detector. Both MuE and the

[6] Alternative energy estimators are available or are becoming available at this time. On-going studies indicate that another energy estimator will preferred for the analysis of IceCube 79-string data.

[7] A gradient of 1 in a log-log plot corresponds to a linear scaling, all other slopes translate into a power-law.

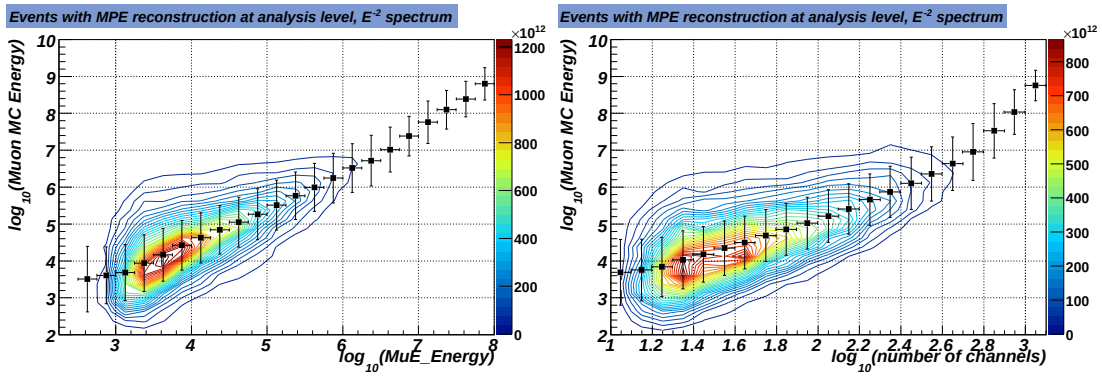

Figure 7.10.: The MC muon energy in GeV at the interaction point is plotted against the MuE energy estimate (left) and the number of channels (right) for all events with a successful MuE energy reconstruction in the event selection described in Chapter 9. The black squares represent the mean of the MC muon energy distribution in each energy estimate bin and the error bars show the standard deviation of the distribution. The color scale represents the number of events for an arbitrary flux scale. The color scale represents the number of events for an arbitrary flux scale.

number of channels do not perform very well for events that do not pass through the detector. MuE results in an overestimate of the energy for these events while the number of channels underestimates the energy. These events are selected with a lower efficiency.

7.4. Background Rejection with Additional Reconstructions

In addition to the directional and energy reconstructions described above, it can be useful to apply a set of reconstructions that are targeted to identify and reject certain classes of background. In the analyses presented here, three such additional reconstructions have been applied:

- A SPE maximum likelihood reconstruction with down-going Bayesian prior.
- A set of SPE maximum likelihood reconstructions based on two pulse series obtained by splitting the original pulse series using geometrical criteria.
- A set of SPE maximum likelihood reconstructions based on two pulse series obtained by splitting the original pulse series using the time of the pulses.

One of the major backgrounds for neutrino searches in the northern sky are down-going atmospheric muons that are wrongly reconstructed as up-going events. To better reject these events, a reconstruction with down-going prior is applied to the data. The likelihood ratio between this reconstruction and the original, up-going reconstruction can then be used as a cut variable. It is used in the event selection described in Chapter 9.

The other dominant background are coincident, down-going muons from more than one cosmic-ray air shower arriving at the detector within the same read-out window. An attempt to reduce this background can be undertaken by splitting the pulse series into two parts to check if both parts are reconstructed as up-going. For a neutrino event, both split reconstructions are expected to point in the same direction. For a coincident muon event however, it is possible that one of the two split pulse series result in a down-going reconstruction. Two different ways to split the pulse series are used: one is a geometrical split that divides the pulse series at a plane that is perpendicular to the original track reconstruction and intersects with the mean position of the hits along this track. The second splitting divides the pulse series at the mean of the times of the pulses. The efficiency of the use of these reconstructions in the event selection is characterized in Chapter 9.

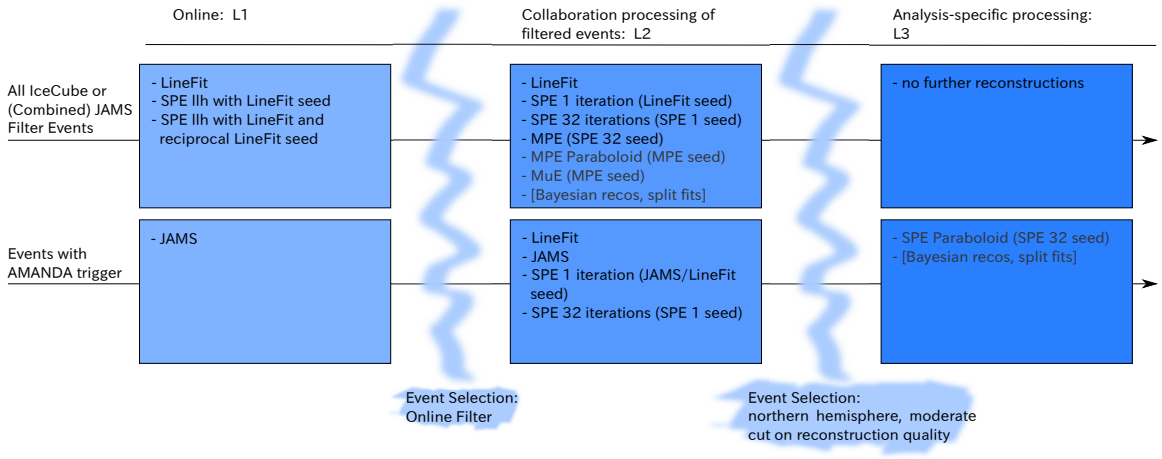

Figure 7.11.: Reconstructions as applied to the IceCube 40-strings and AMANDA data in the first three processing and event selection steps. No further reconstructions are applied at later stages.

7.5. Application of Reconstructions within the Off-line Data Processing for IceCube 40-strings and AMANDA

An overview of all relevant reconstructions applied to the IceCube 40-strings and AMANDA data and the processing steps at which they have been applied is shown in Figure 7.11. Events with AMANDA data receive a special treatment at each processing step.

The first reconstructions are applied on-line at the pole and are used in the physics filters (see 5.4) to select the more interesting events. All events are reconstructed with the LineFit first. The result is then used as a seed for two likelihood reconstructions. Both use the SPE pdf and a single iteration is performed for each of them. One is seeded only with the LineFit result while the other receives the reciprocal of the LineFit as an additional seed to improve the rejection of down-going events.

Combined events, i.e. events with AMANDA trigger are also reconstructed with the JAMS algorithm at this level and the results of this reconstruction are used in the on-line filter. In the next step, the so-called Level 2 (L2), all filtered events are processed to apply higher quality reconstructions. A LineFit, SPE and MPE reconstructions are applied to both event classes based on the IceCube-only pulses. For a subsample of events, a paraboloid fit to estimate the angular uncertainty of the MPE fit and a MuE energy reconstruction are applied. A range of other fits that are useful for background rejection is also performed for these events such as a fit with down-going prior and reconstructions on split parts of the pulse series. For events with combined data, a 32-iterations SPE fit is applied to the combined pulses. This processing has been conducted centrally for the IceCube collaboration.

For combined events, an additional processing step (L3) has been carried out by the author of this work to provide additional reconstructions based on the combined pulse series. A paraboloid fit and several other reconstructions for background rejection are applied. The angular uncertainties are determined for the 32-iterations SPE fit. Apart from the different likelihood function, the settings for the two paraboloid uncertainty estimates are the same for combined and IceCube events. The previous point source analysis with combined IceCube and AMANDA data [Ses10] used a coarser grid for the evaluation of the likelihood function with the paraboloid method; a study of this parameter however revealed a slightly better performance when a finer grid (2° instead of 5°) was used. The application of additional reconstructions at L3 provides the base for an event selection of both combined and IceCube events as the one presented in Chapter 9.

8. Simulation and Systematic Error Analysis

In the development of analyses such as the one presented in this work, it is crucial to simulate a neutrino signal flux in order to be able to optimize the event selection and to calculate upper limits on the observed flux of neutrinos. Atmospheric muon background simulation is used to estimate the muon contamination of the neutrino sample and to validate the quality of the detector simulation on background dominated data. A short overview of the simulation chain as used in IceCube data analyses is given before the impact of systematic uncertainties on the IceCube 40-strings and AMANDA analysis is discussed[1].

8.1. The Simulation Chain

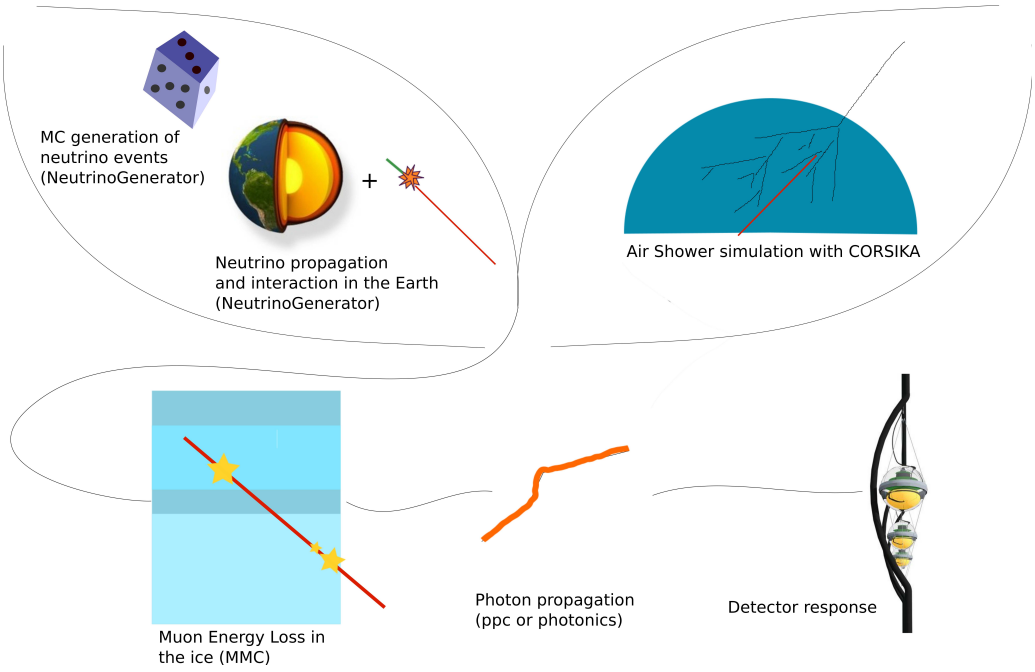

Figure 8.1.: Illustration of the simulation chain. Neutrinos, their propagation through the Earth and interaction are simulated with NeutrinoGenerator. In the example illustrated here, a muon is produced in the interaction. Muons are also produced with CORSIKA, a program to simulate atmospheric air showers that has been adapted for IceCube. Muons from either neutrino interaction or air shower simulation are then treated in the same way in the remaining steps of the simulation chain: the muon propagation through the ice and its energy loss are simulated with MMC and two different programs are available to simulate the propagation of photons through the ice (photonics and ppc). Finally the detector response and data acquisition are simulated.

[1] In addition to the work presented here, i.e. the use of simulation in the context of a physics analysis, the author of this work has also contributed to validate the simulation release for the mass production of simulation for the IceCube 79-strings detector.

The analysis presented in this work uses the muon neutrino channel. In the description of the simulation, the focus will therefore be on this channel. The simulation of both signal and background events follows a chain of distinct steps:

- **Generation of Monte Carlo events**, either of signal or of background nature.
- **Muon propagation** through the ice and the simulation of the energy loss of the muon along its path. The program used for this step is called MMC (Muon Monte Carlo) [RC01].
- **Propagation of the Cherenkov light** from the track to the optical modules.
- **Detector response** (hardware)
- **Data acquisition** (software) according to the treatment of experimental data.

The atmospheric muon background is simulated using a modified version of CORSIKA (COsmic Ray SImulation for KAscade) [HKC+98] accounting for the fact that IceCube is not a flat surface detector as was the original target of the program. CORSIKA is capable to fully simulate extensive air showers induced by cosmic-ray primaries and their development in the atmosphere. To save computing time, the electromagnetic component is neglected in IceCube as it does not reach the deep detector[2]. For IceCube, cosmic-ray primaries from 600 GeV to 10^{11}GeV are typically simulated following the primary composition and spectrum of the *poly-gonato* model [Hoe03]. Cosmic-ray primaries up to $Z = 26$ are taken into account.

Neutrinos are generated using NeutrinoGenerator, an implementation of ANIS (All Neutrino Interaction generator) [GK05] which is capable to simulate all three neutrino flavors and to propagate them to the detector. All possible interactions within the Earth are taken into account. The neutrinos are simulated with a configurable power-law spectrum and can then be weighted to the neutrino spectrum of interest to the analysis. The simulated spectrum is chosen according to the analysis and is usually flatter than the energy spectrum of interest to the analysis to provide sufficient statistics at the highest energies. Even though the atmospheric neutrino background is produced in cosmic-ray induced air showers in the atmosphere, it is usually simulated with NeutrinoGenerator rather than with CORSIKA to save CPU time. The generated neutrinos are then weighted following models of the atmospheric neutrino flux interpolated to high energies for example from the work of [BGL+04] and [HKKS07].

The propagation of the Cherenkov light is simulated using either photonics [LMW+07] or ppc (photon propagation code) [AAA+11g]. Photonics provides the expected number of photons at the position of an optical module and probability density functions for the arrival times of independent photons in a tabulated format. The nature of the light (cascade or track) is taken into account. ppc does not use tables but performs a full photon propagation through the ice. While potentially offering a better description of the detector by avoiding the necessary interpolation when tables are used, ppc is slower and has therefore in the past been less suitable for mass production [3]. Both ppc and photonics take the inhomogeneous nature of the ice into account by the use of an "ice model" following either the measurements of [AAB+05a] (AHA ice model) or the work of [AAA+11g] (SPICE ice models). For a discussion of the optical properties of the ice, see also Chapter 5.

8.2. Systematic Uncertainties in the IceCube 40-strings and AMANDA Analysis

In analyses that derive the background expectation from the data (see chapter 4) such as the one presented in this work, the main cause for systematic uncertainties is the simulation of the signal used in the calculation of the neutrino flux upper limits. Major sources of uncertainty in the signal simulation

[2] The electromagnetic component of the shower is of high relevance for analyses using the surface array IceTop and is included in dedicated simulations.

[3] The increasing availability of GPUs has changed this and ppc-based mass production is available for the IceCube 79-strings detector configuration.

set	detector	spectral index	ice model	x-sections	DOM eff.	absorption	scatt.
2972a	IC40	1	SPICE2+	CTEQ5	–	-10%	-10%
2972b	IC40	1	SPICE2+	CTEQ5	–	+10%	+10%
5040	IC40+AMA	1	SPICE1	CTEQ5	–	–	–
5107	IC40+AMA	1	AHA	CSS	–	–	–
5114	IC40+AMA	1	AHA	CSS-	–	–	–
5122	IC40+AMA	1	AHA	CSS+	–	–	–
3248	IC40+AMA	2	AHA	CTEQ5	-10%	–	–
3247	IC40+AMA	2	AHA	CTEQ5	+10%	–	–

Table 8.1.: Simulation data sets used to study the systematic uncertainties for the IC40+AMANDA analysis. Sets 2972a and 2972b have been generated using ppc while all others use photonics tables for the photon propagation. Listed are the data set number, the simulated detector configuration, the spectrum that has been simulated, the ice model, the neutrino cross sections that have been used and the variations of the DOM efficiency, absorption and scattering. "–" means that the default values have been used.

are: the modeling of the ice, the neutrino deep inelastic scattering cross section and the photon collection efficiency of the DOMs. Uncertainties on the modeling of the background do not affect the signal simulation.
The impact of the most important systematic uncertainties is studied by the use of dedicated simulated data sets in which the corresponding parameters have been varied within their uncertainties. The size of the effects is evaluated at the final analysis event selection level. The cuts that have been applied to reach this level are presented in Chapter 9. Table 8.1 summarizes the settings of the simulation data sets that have been used in this evaluation. The settings of the parameters and their impact on the event selection will be discussed in the following. For each of the simulation sets, the number of events at the final event selection level for a E^{-3} signal neutrino flux as well as the energy and zenith distributions of these events are compared to the default simulation. If neither the energy nor the zenith distribution changes with the variations, it can be assumed that every uncertainty on the number of events translates directly into an uncertainty on the flux upper limit.

Description of the Ice

The description of the ice is a crucial part of the detector simulation. An overview of the properties of the Antarctic ice at the site of the IceCube detector is given in section 5.3. The default simulation that has been used in IceCube 40-strings uses an ice model based on the work of [AAB+05a] (AHA model). To study the systematic uncertainties that enter through the modeling of the optical properties of the ice, one can either benchmark the difference between separate ice models, i.e. study the impact of a different layering of the ice, or vary the optical parameters within a set ice model. The second way has been adopted by the IceCube collaboration to determine the size of the systematic uncertainties that enter through the modeling of the ice.
The availability of data sets with varied ice properties is limited and include only data sets that have been produced for IceCube alone, not including combined events. The data sets that have been used for this test have been generated using the SPICE2+ model derived with a global fit to bright flasher data as described in [AAA+11g]. Figure 8.2 compares the distributions of energy and zenith angle obtained in four different simulations: the default simulation (data sets 2114 and 2326), using the AHA ice model and photonics as photon propagator is shown in gray and is the baseline for all comparisons. Compared to that are a simulation based on the SPICE2+ ice model produced with ppc as photon propagator and

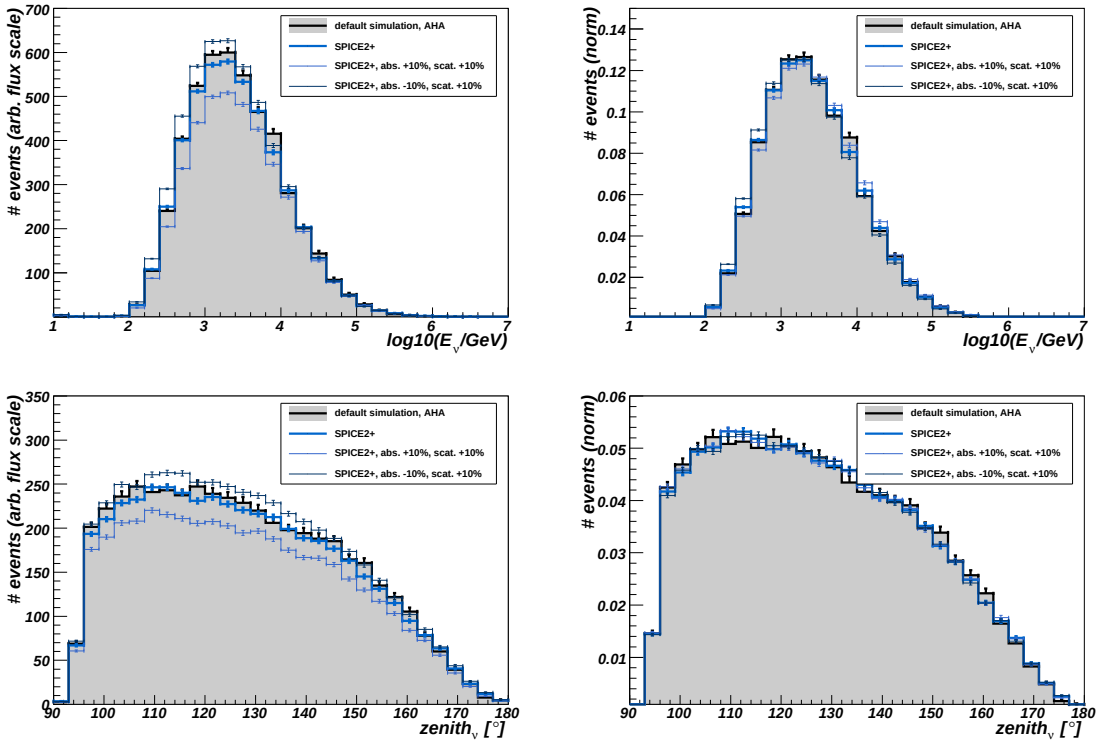

Figure 8.2.: Energy and zenith distribution of E^{-3} signal neutrinos at analysis level are compared to each other. IceCube events with a reconstructed zenith larger than 95° are shown and the plots on the right are each normalized to one. The variations between the SPICE2+ model and the SPICE2+ model with increased/decreased absorption and scattering give the systematic uncertainty of the ice model.

two variations of this ice model. The variations have been obtained by varying the absorption length and scattering by 10% each and present two extreme deviations from the baseline ice model. The plots on the left represent the number of events that are observed in each bin for an arbitrarily scaled E^{-3} signal neutrino flux. The plots on the right are normalized to one to provide a better comparison of the shapes of the distributions.
The difference in the total number of events between the default AHA simulation and the SPICE2+ simulation with its standard parameters is 2.0% with less event observed in the SPICE2+ model. A $+8\%/-12\%$ change is observed with respect to the baseline number of events in SPICE2+ if absorption and scattering are simultaneously varied. These changes are larger than the difference between the two ice models and give the systematic uncertainty induced by the ice model. The shapes of the energy and zenith distribution do not change significantly and it can be assumed that the uncertainty on the combined events is the same.

Neutrino Cross Sections

High-Energy neutrino cross sections are based on parton distribution functions measured at collider experiments. The implementation of ANIS [GK05] used in the default neutrino simulation for IceCube 40-strings is based on the parton distribution functions from CTEQ5 [LHK+00]. The high-energy neutrino cross sections from CSS [CSS08] include newer ZEUS data with respect to the ones based on CTEQ5. Besides, they also provide an uncertainty band of the neutrino cross sections. The differences between CTEQ5 and CSS are largest at the highest energies.

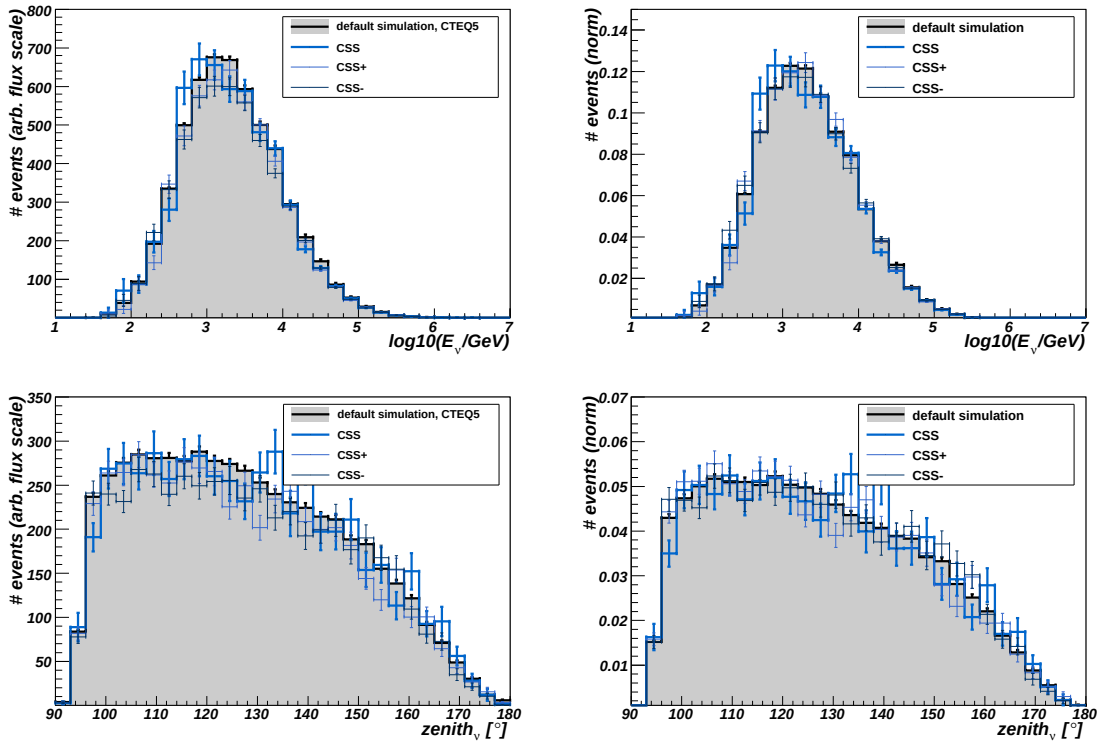

Figure 8.3.: Energy and zenith distribution of E^{-3} signal neutrinos at analysis level are compared to each other for four different high-energy neutrino cross sections. Events with a reconstructed zenith larger than 95° are shown and the plots on the right are each normalized to one. Within the statistical uncertainties, all data sets are compatible with each other.

To assess the impact of the uncertainty on the neutrino cross section on the analysis, three data sets are compared to the default simulation. The first one uses the CSS cross sections, the other two represent the error band of the CSS cross sections. The resulting changes in energy and zenith distribution are shown in Figure 8.3. Within the statistical uncertainties, all of the four data sets are compatible with each other. The CSS data sets are high-energy data sets with suboptimal statistics in the energy range that is most relevant to the analysis presented here. Therefore, the systematic uncertainty of 3% derived in [AAA+06a] for the effects of neutrino cross sections and rock density are used as uncertainty for this analysis as well.

DOM Sensitivity

Another source of uncertainty is the detector response to the Cherenkov light. Variations of ±10% in the DOM efficiency are considered to benchmark the effect on the signal neutrino flux. The data sets 3247 and 3248 have been generated with the exact same settings as the baseline simulation and are compared to this in Figure 8.4. The changes in the distributions are small as can be seen in the plots on the right. The number of events however changes by $+12\%/-13\%$ and is thus one of the major contributions to the simulation of the signal flux.

Summary of the Systematic Uncertainties

A summary of all the considered systematic uncertainties is provided in Table 8.2. Assuming that all effects are independent, a net uncertainty of $+15\%/-17\%$ is calculated for an E^{-3} signal neutrino flux.

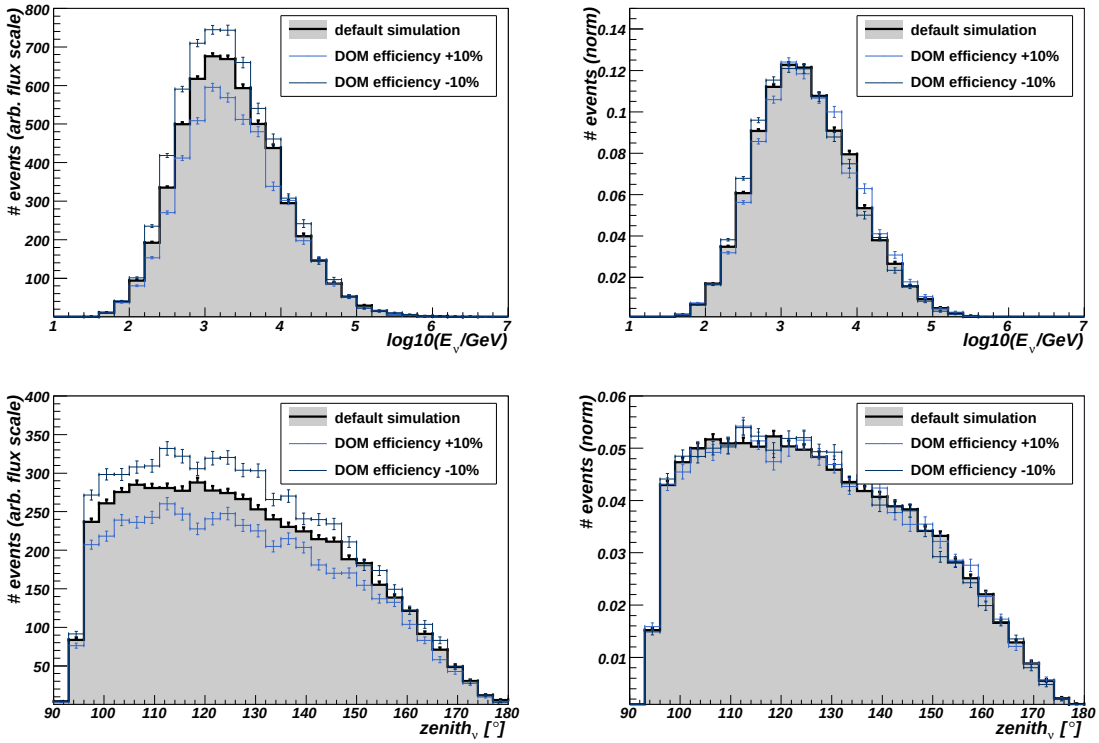

Figure 8.4.: Energy and zenith distribution of E^{-3} signal neutrinos at analysis level are compared to each other. Events with a reconstructed zenith larger than 95° are shown and the plots on the right are each normalized to one. The sensitivity of the DOMs is varied by ±10% in two data sets that ore otherwise identical to the baseline simulation.

In the limit calculation, Gaussian errors of 17% will be assumed.

source of uncertainty	variation in signal events (E^{-3})
DOM sensitivity	+12% / -13%
photon propagation	+8% / -13%
ν-x-sections and rock density	+3% / -3%
total	**+15% / -17%**

Table 8.2.: Summary of systematic uncertainties. The uncertainties arising from neutrino cross sections and rock density are based on the studies in [AAA$^+$06a].

9. IceCube 40-Strings and AMANDA Neutrino Sample

A sample of 19797 neutrino candidates has been selected from the combined IceCube 40-strings and AMANDA data to search for soft-spectra neutrino sources. The event selection is optimized for soft spectra to provide an optimal sensitivity to potential Galactic neutrino sources and presents the best sensitivity for these among all point source analyses that were performed on data from the same period. The optimization for soft-spectra sources is partially achieved through the use of combined IceCube-AMANDA events next to the standard IceCube events (see section 6.3). Combined events are those events which have an AMANDA trigger that initiated the recording of data with IceCube and AMANDA. The use of these events is unique to the analysis presented here among all IceCube 40-strings point source analyses.

Due to the different spacing of the optical modules in the two parts of the detector as well as to the different filtering that is applied on-line at the South Pole, the two event populations have different energy distributions. Furthermore, combined events are treated with a different hit cleaning and a different first-guess reconstruction is used for them (see Chapter 7). The two event classes differ thus also in the background composition and separate event selections are therefore developed for them to extract a sample of neutrino candidates.

Both event selections are developed and tested on three different neutrino spectra:

- An E^{-3} spectrum is used as the benchmark neutrino signal spectrum.
- The atmospheric neutrino spectrum represents an even softer spectrum. The event selection is developed to extract a clean atmospheric neutrino sample from the data.
- An E^{-2} spectrum is used to benchmark the performance for hard spectra. Even though the analysis is optimized for soft spectra, it is still desirable to retain a competitive efficiency for very high-energy events.

The consideration of two very soft spectra in the development of the event selection is a key point to improve the sensitivity for galactic neutrino sources. For illustration purposes, a few possible neutrino energy spectra are shown in Figure 9.1, the detector response is not taken into account.

The background estimation at any point of this work is obtained directly from the experimental data and presents therefore a robust estimation that is independent of the correct modeling of the background in the simulation. If integrated over the whole year, the detector response is uniform in right ascension and pseudo-background samples are obtained from the data by the assignment of a random right ascension to each event. Even if present in the data, the expected signal from any neutrino point source represents a small number of events in comparison to the integrated atmospheric neutrino background in each declination band. Any potential discovery in this analysis will be apparent as an unambiguous excess in the number of events over this robust background estimation. In accordance with the IceCube analysis standards and to reduce the risk to introduce biases, the presented analysis is performed as a blind analysis with respect to the position of the events. The right ascencion and the times of all events are thus blinded until the final statistical test is performed on the data.

A short overview of the cut variables that have been used in this analysis is given before the event selection for both event streams is discussed. The resulting neutrino sample and the performance of the event selection are characterized. Finally, the properties of the surviving muon background are studied in data.

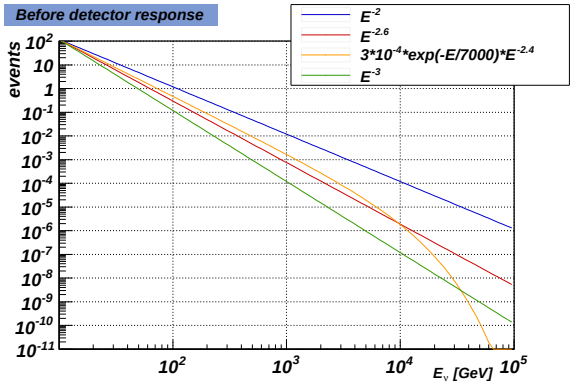

Figure 9.1.: Illustration of different neutrino energy spectra: All four curves are normalized to the same number of events at 10 GeV. The shape of the energy spectrum shown in orange corresponds to a the neutrino flux from the Crab if all γ-rays were produced in pp-interactions, see also Equation 10.1 and the accompanying text. The observed energy distribution in IceCube is a convolution of these spectra with the detector acceptance.

9.1. Cut Variables

As discussed in Chapter 3, the IceCube data at filter level is dominated by atmospheric muons. Even if a cut is made to select only up-going events, mis-reconstructed atmospheric muons still outnumber atmospheric neutrinos by four orders of magnitude. Given the low expected flux of neutrinos from astrophysical sources, it is not possible to identify a signal above the background of atmospheric muons unless this background is reduced substantially at minimal signal loss. The remaining background of atmospheric neutrinos is indistinguishable from the signal on an event-by-event basis. The analysis presented here uses a set of well-established, powerful cut variables to select neutrino candidates among the background of mis-reconstructed atmospheric muons:

NCh The number of hit DOMs (channels) in an event correlates with the particle's energy as well as with the angular uncertainty of the reconstruction.

rlogl or "reduced loglikelihood" is an indicator of the quality of the likelihood fit. In analogy to the quality parameter of a χ^2-fit $\frac{\chi^2}{n_{dof}}$, it is defined as rlogl = $\frac{-\text{logl}}{(\text{NCh}-n_{par})}$[1] where logl is the value of the likelihood function at the best fit and $n_{par} = 5$. While this variable has a good separation power between mis-reconstructed atmospheric muons and signal neutrinos, it also has a strong energy dependence. In contrast to the quality parameter of a χ^2-fit, the distribution of rlogl does not peak around one for well-reconstructed events. Instead, the optimal range of values has to be determined from signal simulation.

plogl is a variation of rlogl that has been developed to reduce the energy dependence. In this work, it is defined as plogl = $\frac{-\text{logl}}{(\text{NCh}-x)}$ with $x = 2.0$ [2].

paraboloid σ measures the angular uncertainty of the likelihood reconstruction. It has been studied in detail in section 7.2. In particular, a rescaling is applied for IceCube events to reduce an underestimation of the angular uncertainty at high energies.

Bayesian likelihood ratio is defined as the ratio of the likelihood of the SPE fit with uniform prior and the likelihood obtained from a reconstruction with a down-going Bayesian prior. The logarithm of

[1] The definition of this cut variable is often stated without the minus sign. This does however belong to the fully correct definition.

[2] Other definitions are possible and have been used in other IceCube analyses. The particular definition used in this work has been selected based on its discrimination power between background (atmospheric muon-dominated data) and a soft neutrino signal with an E^{-3} spectrum. For harder neutrino spectra, larger values of x are preferred.

this ratio is used to suppress mis-reconstructed down-going muons. Since two likelihood functions with two different pdfs are used in the ratio, the optimal range of values of this parameter is determined with simulated signal neutrino events.

MuE Energy The reconstructed energy, obtained with the MuE reconstruction ([Chi08], see also section 7.3), is a powerful variable to identify high-energy events.

NDirPulses A direct pulse is defined as a pulse for which the difference between the detected arrival time t and the expected arrival time t_{geo} fulfills $-15\text{ns} \leqslant t - t_{geo} \leqslant 75\text{ns}$[3], i.e. the scattering of the light has been small. NDirPulses is the number of direct pulses [4]

LDirPulses The maximum distance between the projections of the direct pulses on the reconstructed muon trajectory.

SDirPulses is the smoothness of the direct pulses, i.e. describes the distribution of direct pulses along the track. Possible values are in the range $[-1, 1]$. SDirPulses $= 0$ corresponds to a uniform distribution of direct pulses along the length of the track while the values -1/1 indicate a clustering of direct pulses at the beginning/the end of the track.

In addition the variables listed above, it is often useful to apply dedicated reconstructions to identify and reject down-going coincident muon events (see section 7.4). For this purpose, each event has been split into two halves with two different algorithms and each of the four resulting split pulse series has been reconstructed with a SPE likelihood reconstruction (see Chapter 7). In one of the splitting algorithms, the events are split at the mean of the time of all hits ("time split"). In the other algorithm, they are split at a plane perpendicular to the original reconstruction and positioned at the mean of the hit positions along the track ("geo split"). A cut on the zenith angles obtained with these additional reconstructions can be used to reject coincident muons. Coincident events, both of two atmospheric muons or of a muon and a neutrino, are more abundant in the later, larger configurations of IceCube. Considerable additional effort has therefore been spent on this topic for the IceCube 79-strings analysis outlined in Chapter 11 to identify background and signal events with complicated event topologies.

9.2. Selection of IceCube Events

The IceCube events that are selected for this analysis undergo four different processing steps. The first step is the initial event reconstruction and event selection at the South Pole. The details are described in sections 5.4 and 6.3. The IceCube Muon Filter selects a first sample of interesting events. The data rate at filter level is about 19.8 Hz for up- and down-going events together.

Level 2 Off-line Processing and Event Selection

After the data has been transferred north, additional reconstructions are applied in the first off-line processing, called Level 2[5]. The following processing steps and reconstructions are applied to IceCube events:

- Removal of data from few unreliable DOMs, Waveform Calibration and Extraction.
- Hit Cleaning: only pulses within a sliding time window of 6 µs are kept. The position of the time window is chosen to maximize the number of pulses that are kept.
- LineFit

[3] Different time windows can be used for this definition. In IceCube internal notation, this analysis uses C-type definitions of all direct variables.

[4] An even better cut variable is the number of direct channels, i.e. the restriction to only one direct pulse per DOM. This cut variable is used in the work presented in Chapter 11.

[5] The Level 2 off-line processing of the IceCube 40-strings data has been repeated several times because bugs in the processing script have been discovered. All updates of the Level 2 off-line processing are fully reflected in the analysis presented in this work.

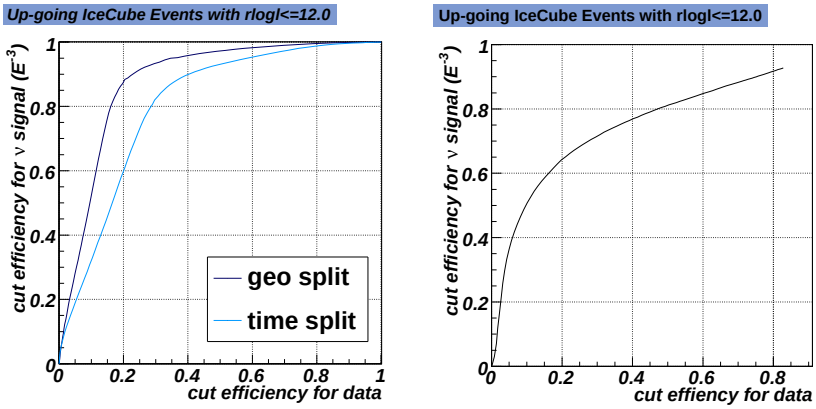

Figure 9.2.: Left: Signal vs data efficiency for cuts on the smallest of the two zenith angles obtained by splitting the pulse series into two parts based on geometrical (dark blue) or temporal (light blue) criteria. The data at this cut level is dominated by atmospheric muons and can thus be used to evaluate the background rejection power of the cut. The cut has been varied between 180° (no cut) and 0° (removing all events). Right: Signal vs data efficiency for cuts on the rescaled MPE paraboloid σ, varying the the threshold between 10° (soft cut) and 0° (removing all events).

- SPE reconstruction, using the LineFit as seed.
- Iterative SPE reconstruction, using the single iteration SPE reconstruction as seed. 32 iterations are performed.

For a selection of events whose 32-iterations SPE reconstruction has a zenith angle larger than 80° and which have rlogl $\leq$ 12.0 (indicating that the quality of the reconstruction is not very poor), additional reconstruction are added:

- SPE Paraboloid fit to provide an estimate of the angular uncertainty of the reconstruction.
- 32 iterations SPE fit with down-going prior (Bayesian SPE fit).
- MPE reconstruction.
- MPE Paraboloid fit.
- MuE Energy reconstruction.
- Splitting on geometrical criteria and a 16 iterations SPE reconstruction on each of the partial pulse series.
- Splitting on temporal criteria and a 16 iterations SPE reconstruction on each of the partial pulse series.

Besides the reconstructions listed here, several other reconstructions are applied within the Level 2 processing to serve other detection channels. All reconstructions that are used in this work are also introduced in Chapter 7.

Level 3 Off-line Processing and Event Selection

A second off-line processing, called Level 3, is carried out to provide more reconstructions for the combined events. For the IceCube events, all reconstructions that are needed in the analysis are already available at this stage. The Level 3 off-line processing for IceCube events therefore consists only of a reduction of the data volume. Only events with an MPE reconstructed zenith angle $\theta^{MPE} \geq 90°$ and MPE rlogl $\leq$ 12.0 are kept for the analysis. The data rate after this cut is 4.6 Hz, three orders of magnitude above the atmospheric neutrino rate of 2.2 mHz.
In addition, two quality cuts are applied before the final cut optimization is performed. The application

of these cuts before the final, multivariate cut has been observed to improve the signal efficiency of the event selection. A requirement on the zenith angle obtained with the reconstructions of the split pulse series is made, asking all of them to be larger than 80° in order to remove coincident muon events. The left plot in Figure 9.2 shows how cuts on the zenith angles of the geometrical and temporal split pulses series affect data and signal. The cut value has been varied between 180° (no cut) and 0° (removing all events). A cut at 80° on the reconstructions performed on the geometrically split pulse series removes 80.9% of the background (data) while it keeps 86.3% of a soft spectrum neutrino signal with spectral index 3. The same cut on the zenith of the temporally split pulse series rejects 79.3% of the background and keeps 83.1% of the same signal.
Only events with a (rescaled) paraboloid $\sigma \leq 4°$ are kept. This cut preserves 75.3% of all E^{-3} neutrino events with up-going MPE reconstruction and MPE rlogl$\leq$ 12.0. 36.8% of the data pass this cut. The signal efficiency increases if only events with a good angular reconstruction are considered. Moreover, the cut is very safe since events with large σ contribute very little in the statistical analysis (see Chapter 4) and their rejection does therefore not harm the sensitivity of the search. The combination of these cuts keeps 0.02 Hz of the experimental data, representing a reduction of 99.6% of the data with respect to the 4.6 Hz after the previous cut. 0.8 mHz of atmospheric neutrinos pass this cut that prefers well-reconstructed events.

Event Selection with the Neyman-Pearson Decision Criterion

The final selection of IceCube events is divided into two different branches: a main branch using a multivariate yet very simple cut and an additional high energy-optimized branch based on rectangular cuts. Multivariate cuts offer an advantage in particular for soft neutrino spectra since they allow to combine the discrimination power of several variables in a single cut. 81.3% of all events in the final neutrino sample are selected by this multivariate cut.
A likelihood ratio based on several variables is used to select IceCube events for the point source analysis. In the case of strictly uncorrelated variables, the Neyman-Pearson lemma (see also Chapter 4) states that the cut obtained in this way is the most efficient cut that can be derived from the given set of cut variables at each required level of purity. Even though the variables that are used in this work are not strictly uncorrelated, a good discrimination power is achieved. Moreover, the same method has already been used successfully in the combined IceCube 22-strings and AMANDA analysis [Ses10]. The cut variable used in this work is defined as:

$$\mathcal{NP}(\mathrm{i}) = \log\left\{\frac{\mathcal{P}_{sig}(\mathrm{plogl}|\mathrm{i})}{\mathcal{P}_{bg}(\mathrm{plogl}|\mathrm{i})}\cdot\frac{\mathcal{P}_{sig}(\sigma|\mathrm{i})}{\mathcal{P}_{bg}(\sigma|\mathrm{i})}\cdot\frac{\mathcal{P}_{sig}(\mathrm{bay}|\mathrm{i})}{\mathcal{P}_{bg}(\mathrm{bay}|\mathrm{i})}\cdot\frac{\mathcal{P}_{sig}(\mathrm{NDir}|\mathrm{i})}{\mathcal{P}_{bg}(\mathrm{NDir}|\mathrm{i})}\cdot\frac{\mathcal{P}_{sig}(\mathrm{LDir}|\mathrm{i})}{\mathcal{P}_{bg}(\mathrm{LDir}|\mathrm{i})}\cdot\frac{\mathcal{P}_{sig}(\mathrm{SDir}|\mathrm{i})}{\mathcal{P}_{bg}(\mathrm{SDir}|\mathrm{i})}\right\} \quad (9.1)$$

where $\mathcal{P}_{sig}(\mathrm{x}|\mathrm{i})$ ($\mathcal{P}_{bg}(\mathrm{x}|\mathrm{i})$) is the probability to observe the measured value of the parameter x in event i under the assumption that i is a signal event (background event). The cut variables used in Equation 9.1 are, in order of appearance: plogl, the paraboloid σ, the Bayesian likelihood ratio, the number and length of the direct pulses and the smoothness of the direct pulses. They have been selected for their good separation power between atmospheric neutrinos and mis-reconstructed down-going muons. Data-MC comparisons of for these cut variables are shown in Figures 9.3 and 9.4. The Level 3 event selection for IceCube events has been applied to both data and simulation. Discrepancies are mostly observed at the high energy ends of the distributions, in particular for the number and length of the direct pulses, where the statistics of the simulation are limited and the modeling of the atmospheric muon spectrum is most difficult. A reasonably good agreement is achieved in the low-energy regions with sufficient statistics in the simulation.
To avoid that uncertainties in the modeling and simulation of cosmic-ray air showers propagate into the data selection, the data itself is used to for the background probability distributions. 10.4 days of data have been used to generate the background probability distributions. The performance of the cut was

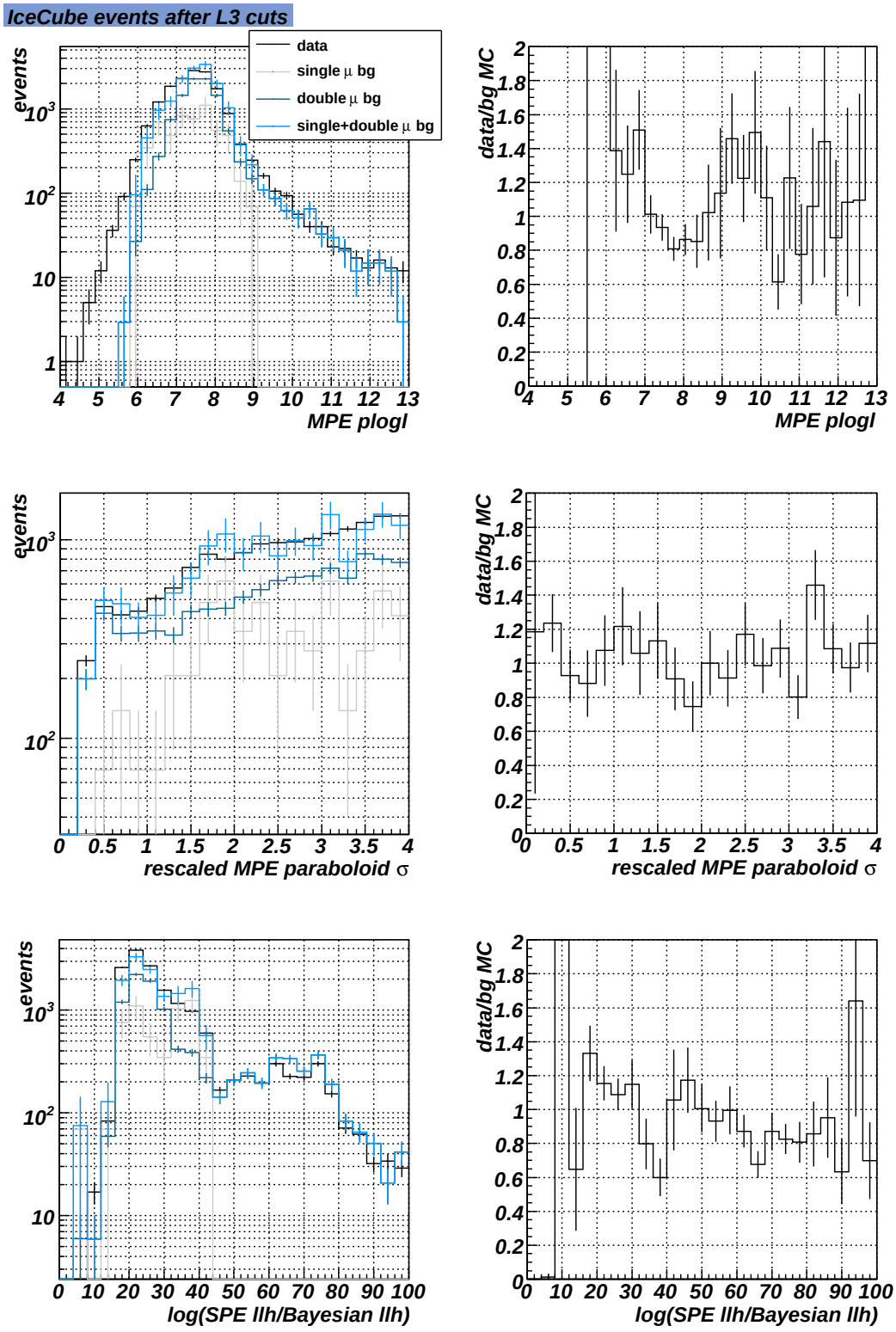

Figure 9.3.: Data-MC comparisons for three of the six variables that are used in the Neyman-Pearson likelihood ratio cut. Data in black is compared to atmospheric muon simulation. The components of single and double muons are shown separately and combined. The plots on the right show the ratio of data and the sum of the two simulated background components.

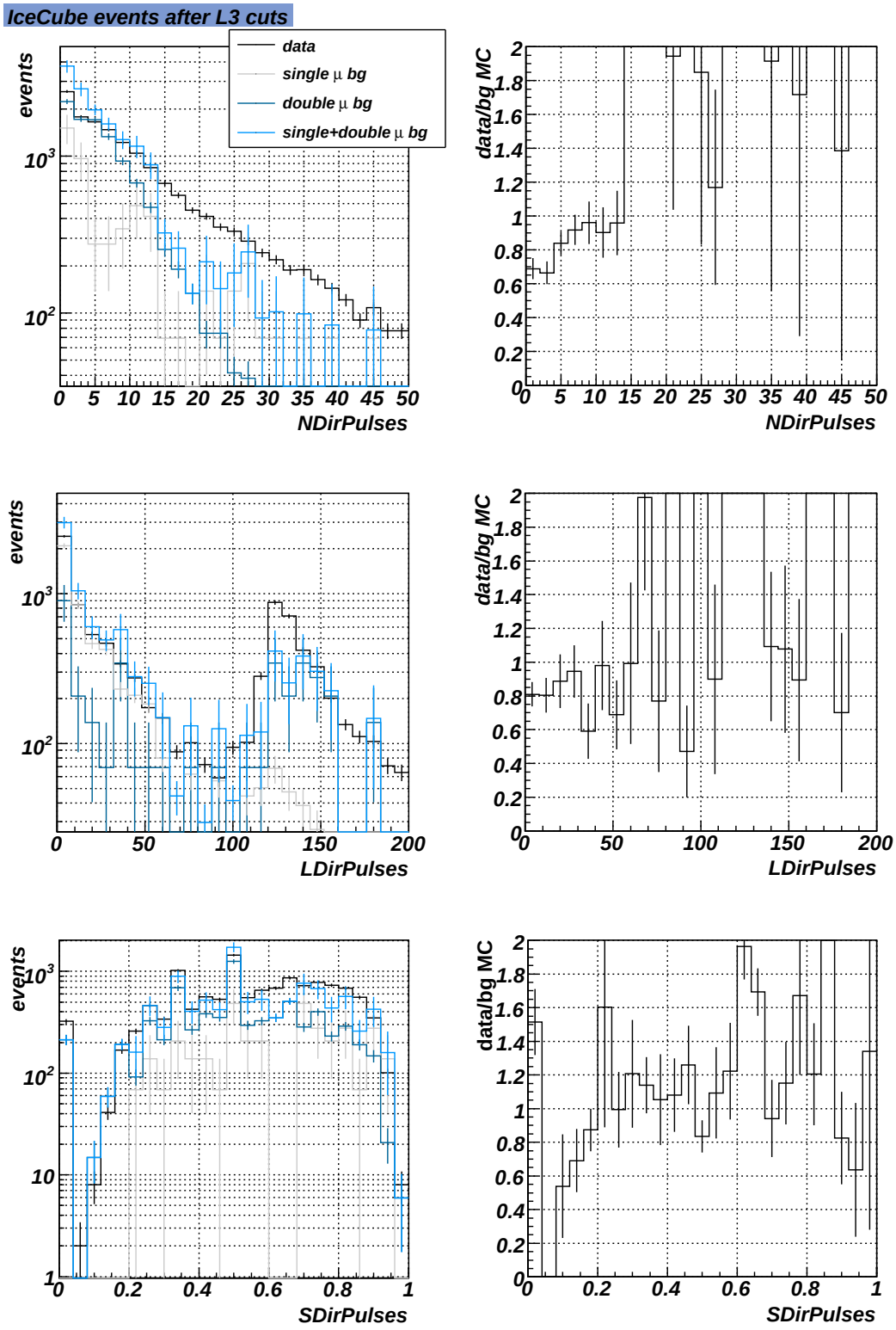

Figure 9.4.: Data-MC comparisons for three of the six variables that are used in the Neyman-Pearson likelihood ratio cut. Data in black is compared to atmospheric muon simulation. The components of single and double muons are shown separately and and combined. The plots on the right show the ratio of data and the sum of the two simulated background components.

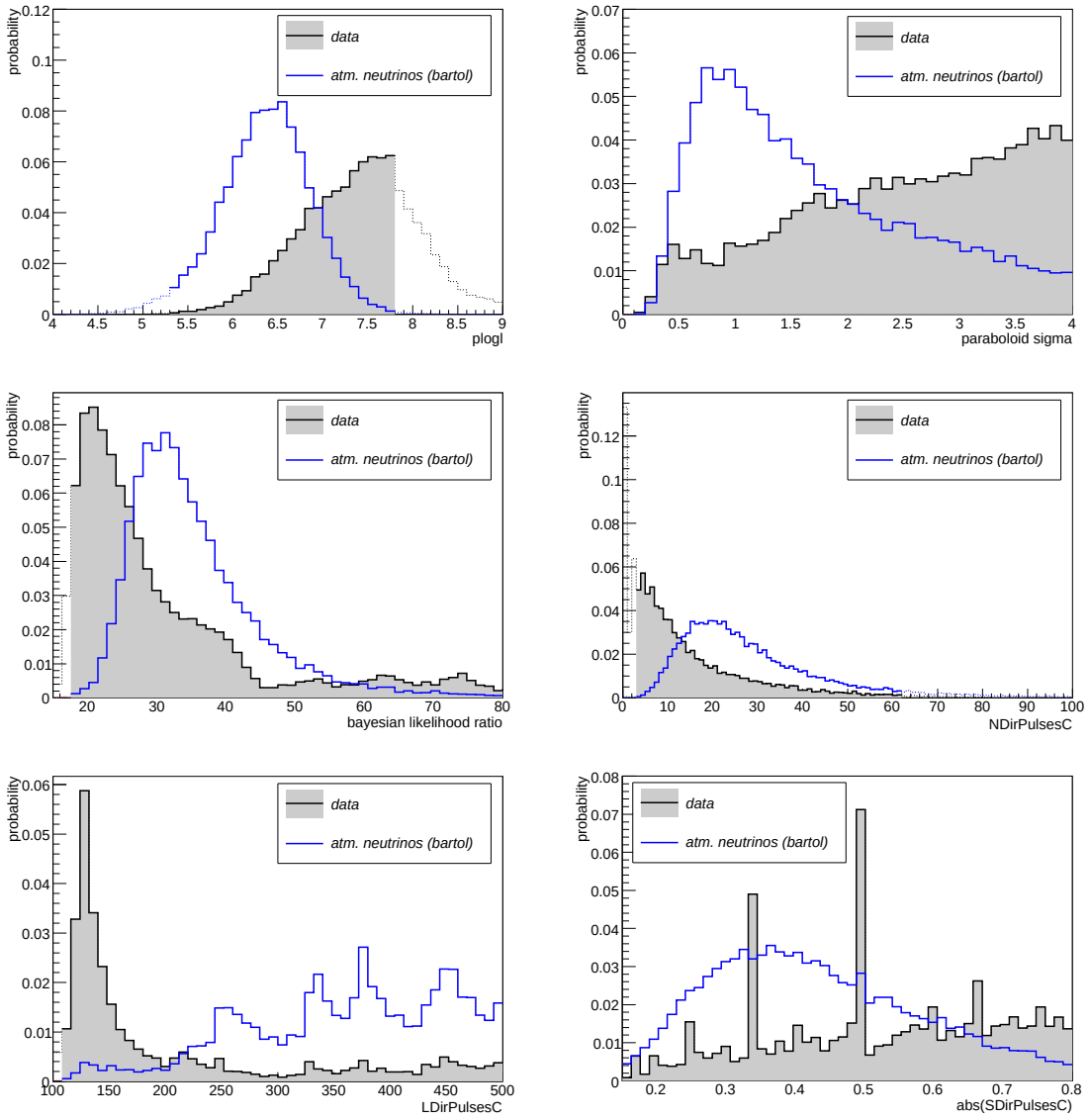

Figure 9.5.: Probability distributions for background (data) and signal (atmospheric neutrinos) as they have been used to construct the likelihood ratio that is used as the main cut variable for IceCube events. Six different cut variables are combined into a single cut. The regions where either one of the distributions falls below 0.001 are considered in under- and overflow bins and illustrated here with dotted lines. The structure in the distribution of the direct length are caused by two effects: The direct length is always a multiple of an existing inter-DOM distance. In addition, the IceCube 40-string detector has an asymmetric shape with a long and a short detector axis, limiting the direct length for some azimuth angles more than for others.

tested with a separate set of data. The probability distributions that have been used in the cut are shown in Figure 9.5.

The probability distributions for the signal hypothesis are generated from atmospheric neutrino simulation using the Bartol model [BGL$^+$04] for conventional atmospheric neutrinos (see also Chapter 3). Atmospheric neutrinos are used in the construction of the signal probability distributions to ensure a good performance at low energies.

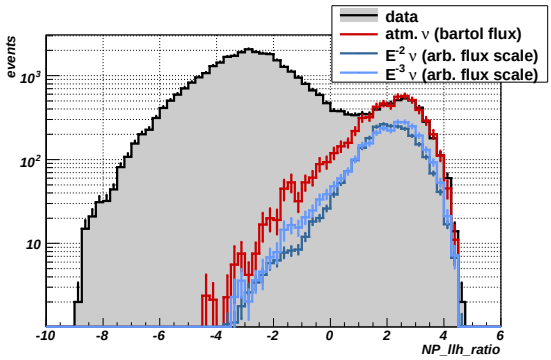

Figure 9.6.: Distribution of the main cut variable for IceCube events in data (black), simulated atmospheric neutrinos (red), and a simulated neutrino signal with two different spectra of arbitrary flux scale. A cut at a value of 1 is applied to the data to select a neutrino sample. The agreement of data and simulated atmospheric neutrinos is very good in the signal region.

With respect to the cut used in the combined IceCube 22-strings and AMANDA point source analysis [Ses10], several improvements have been made:

- plogl is used instead of rlogl and provides a better efficiency for soft neutrino spectra. This change also reduces the correlations with the other cut variables that are used in the likelihood ratio.
- The MPE reconstruction is used. This results not only in a better angular resolution but also resolves a problem with the SPE reconstruction that diminishes the separation power of direct variables that are calculated with respect to the SPE fit.
- The application of a few additional quality cuts before the Neyman-Pearson multivariate cut is applied has been observed to increase the separation power of the cut.

Figure 9.6 shows the distribution of the cut variable for data (black), atmospheric neutrinos (red) and two different signal spectra. A good separation power between data and atmospheric neutrinos as well as both signal spectra is achieved. In the signal region, a good agreement between data and simulated atmospheric neutrinos is observed. The cut is applied at a likelihood ratio value of 1.0 to obtain the best sensitivity to soft-spectra sources and to select a high purity atmospheric neutrino sample. Variations of the cut around the chosen cut value have been tested and resulted in a worse sensitivity for soft-spectra neutrino point sources. Other tested variations of the cut include the removal of variables from the likelihood ratio. These variations did however result in a worse separation power. Also the addition of a hard cut on the Bayesian likelihood ratio has been tested. A cut at $\log\left(\frac{\text{SPE likelihood}}{\text{Bayesian likelihood}}\right) \geq 25.0$ improved the sensitivity of the search for soft-spectra neutrino sources at all zenith angles. An even harder cut at 30 was disfavored as it decreased the sensitivity for soft spectra sources except for the region around the horizon. If harder spectra such as E^{-2} were regarded, the cut improved the sensitivity at all declinations. As the search is however optimized for soft spectra sources, a cut value of 25.0 was chosen. This is one of the observations that lead to the decision to divide the event selection for IceCube 79-strings analysis outlined in Chapter 11 in two different zenith region in order to obtain the best sensitivity across the whole northern sky. Finally, a cut on LDirPulses $\geq$ 150m for all IceCube events has been observed to improve the sensitivity of the search and to increase the purity of the neutrino sample.

Selection of Additional High-Energy Events

In the energy range above a few $\sim$ 10 TeV, the background of atmospheric muons and neutrinos can be suppressed with energy estimators or strongly energy-dependent variables without a significant signal loss. The event selection presented so far however is optimized for soft spectra for which the bulk of

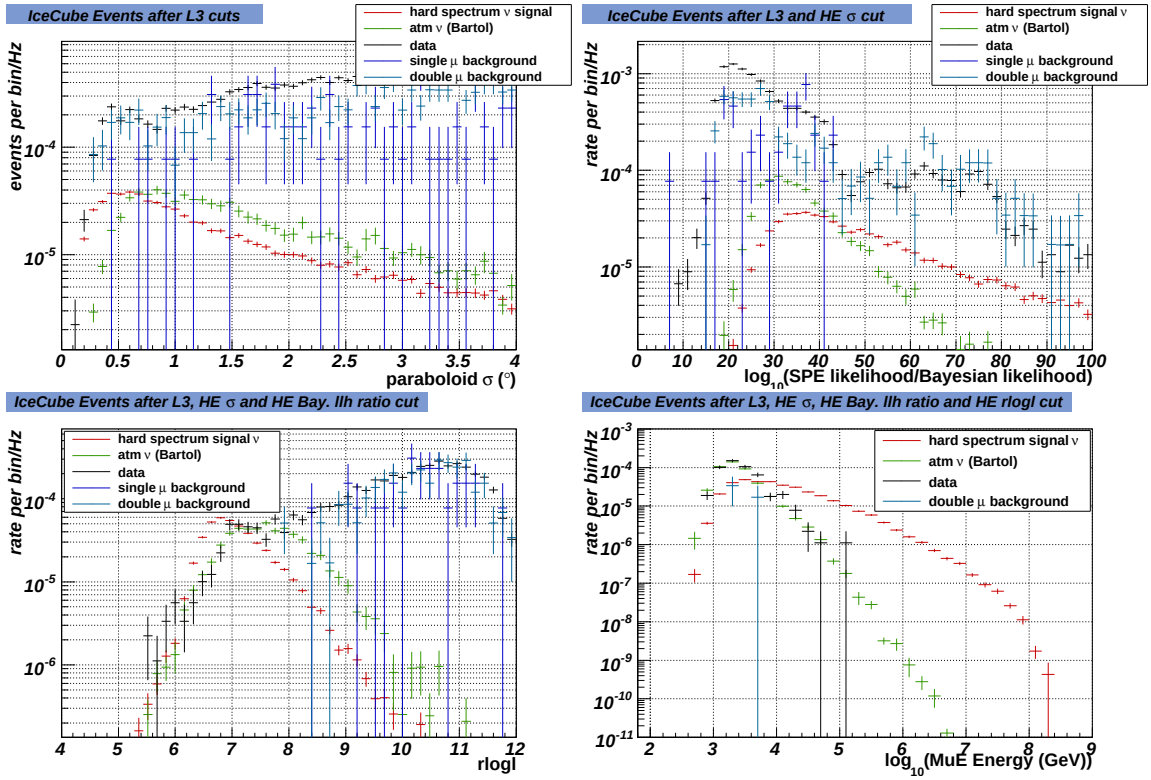

Figure 9.7.: Cut progression for high-energy IceCube events. Five simple cuts are to select high-energy neutrino events. The distributions of data, muon background simulation and atmospheric neutrino simulation are shown alongside with an arbitrarily scaled hard E^{-2} signal neutrino flux. A cut on the rescaled MPE Paraboloid $\sigma \leq 3.0°$ is applied, followed by a cut at $\log\left(\frac{\text{SPE likelihood}}{\text{Bayesian likelihood}}\right) \geq 30.0$. For high-energy events, rlogl is a good cut parameter and events with rlogl ≤ 8.3 are selected. A cut on the reconstructed energy $\log(\text{MuE Energy}) \geq 3.0$ reduces the data a little bit further. Finally (not shown here), a cut on LDirPulses ≥ 150m for all IceCube events has been found to improve the sensitivity of the search and to increase the purity of the neutrino sample.

the signal events would be lost with this kind of high-energy optimized event selection. On the other hand, we observe that the ability of the Neyman-Pearson likelihood ratio cut to select signal events at the highest energies is not optimal. This is illustrated in Figure 9.10. It is related to that fact that the cut has been optimized for atmospheric neutrinos which due to their lower energy often present different values in the considered cut variables than very high-energy events. Atmospheric neutrino events have on average larger angular uncertainties and less direct pulses. A second branch for the selection of very high-energy events has therefore been introduced to combine the power of the multivariate cut with the possibility to select very high-energy events based on their reconstructed energy or energy-correlated cut variables.

The high-energy optimized event selection for IceCube events is illustrated in Figure 9.7. To pass this cut, each event is required to have a small rescaled MPE paraboloid σ of less than 3.0°. The reconstructed energy is required to fulfill $\log(\text{MuE Energy}) \geq 3.0$ and a cut on the Bayesian likelihood ratio at $\log\left(\frac{\text{SPE likelihood}}{\text{Bayesian likelihood}}\right) \geq 30.0$ is made to suppress the down-going muon background. A hard cut on the MPE rlogl is made, requiring MPE rlogl ≤ 8.3.

The combination of the Neyman-Pearson likelihood ratio cut with this cut improves the signal efficiency above 10 TeV, see Figure 9.10. The efficiencies shown in this plot are calculated with respect to all

IceCube and combined events with up-going reconstructions and rlogl ≤ 12.0 for an E^{-2} neutrino signal spectrum.

9.3. Selection of Combined Events

Combined events are selected on-line by the JAMS (Combined) Muon Filter (see section 6.3). This filter selects about 3.1 Hz of data and is based on the JAMS first guess reconstruction.

Level 2 Off-line Processing and Event Selection

The standard Level 2 processing does not apply any cuts on the combined events. The following processing steps and reconstructions are applied on the combined pulse series for all events that were selected by the JAMS (Combined) Filter:

- Removal of data from few unreliable (D)OMs, Cross-Talk Cleaning for AMANDA, Waveform Calibration and Extraction.
- Hit Cleaning: only pulses within a sliding time window of 4 µs are kept. The position of the time window is chosen to maximize the number of pulses that are kept. The time window cleaning is followed by an isolated hits cleaning, requiring each hit to have at least one other hit within a radius of 150 m and within a time window of 500 ns.
- SPE reconstruction, using the JAMS reconstruction run at Pole and the LineFit on the IceCube pulses as seed.
- Iterative SPE reconstruction, using the single iteration SPE reconstruction and the 32 iterations SPE fit on the IceCube pulses as seed. 32 iterations are performed.

Level 3 Off-line Processing and Event Selection

Only events with an up-going combined SPE reconstruction (zenith$\geq 90°$) and SPE rlogl≤ 12.0 are selected for further processing at Level 3. The Level 3 serves to add a further set of reconstructions and verification tools:

- Waveform-based identification of non-particle induced events in AMANDA (see section 6.5).
- SPE Paraboloid fit to provide an estimate of the angular uncertainty of the combined SPE reconstruction.
- 32 iterations SPE fit with down-going prior (Bayesian SPE fit).
- Splitting on geometrical criteria and a 16 iterations SPE reconstruction on each of the partial pulse series.
- Splitting on temporal criteria and a 16 iterations SPE reconstruction on each of the partial pulse series.

As described in section 6.5, the following cut is applied to clean the combined data from non-particle induced events caused by electronic noise in the AMANDA cables: The median peak rate in the waveforms of AMANDA strings 5-10 has to smaller than or equal to 0.005 Hz or the number of waveform segments in these strings has to be smaller than or equal to 20. The data rate after these cut is 0.5 Hz while atmospheric neutrinos are at a level of 0.9 mHz.

Final Event Selection for Combined Events

AMANDA is the first low-energy core that has ever been used in a neutrino telescope. The different PMT spacing and the two different data acquisition systems present a challenge not only to the integration and operation of the detector but also to the simulation. The agreement between data and simulation for the combined events is worse than for IceCube events at atmospheric muon dominated data selection

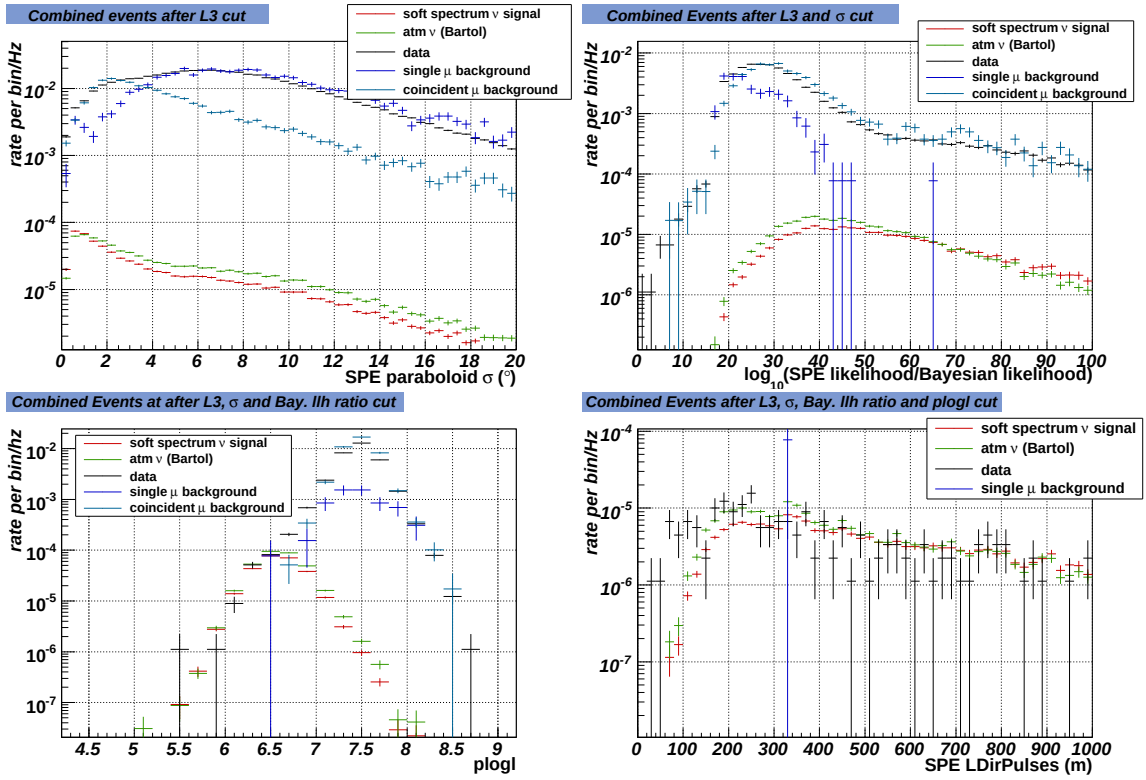

Figure 9.8.: Cut progression for combined events. Six simple cuts are applied to arrive at neutrino level with a good sensitivity for soft spectra neutrino sources. The distributions of data, muon background simulation and atmospheric neutrino simulation are shown along with an arbitrarily scaled E^{-3} signal neutrino flux. A cut at $\sigma \leq 3.0°$ is applied, followed by a cut at $\log\left(\frac{\text{SPE likelihood}}{\text{Bayesian likelihood}}\right) \geq 30.0$ and the selection of events with plogl ≤ 6.7. Finally, cuts at LDirPulses $\geq$ 150m and NCh ≥ 20 have been observed to improve the sensitivity of the search and to increase the purity of the neutrino sample.

levels. For this reason a manual event selection through the progressive application of straight cuts is preferred over a multivariate cut for the combined events in this analysis. Moreover, comparisons with a multivariate cut on a likelihood ratio such as the one used for the IceCube events have revealed a similar separation power between background (data) and signal.

Figure 9.8 presents the progression of cuts that is applied to the combined events. The first cut variable is the paraboloid σ obtained for the combined 32 iteration SPE reconstruction shown in the upper left plot. Experimental data (black) is compared to the simulated muon background. Single and double muon events are shown separately. Adding the two components leads to a 30% excess of simulation over data. Besides the uncertainties in the simulation of the detector discussed in Chapter 8, also the modeling of the cosmic-ray flux and the air shower development in the atmosphere add to the differences between data and simulation. For large values of the paraboloid σ, the data is dominated by the single muon component and the shape of the distribution is reasonably well-described by the simulation. The applied cut at paraboloid $\sigma \leq 3.0°$ selects primarily double muon events. Again, events with large paraboloid σ values cannot contribute very much in the statistical analysis described in Chapter 4 as events with a large σ receive low weights.

The top right plot in Figure 9.8 shows the Bayesian likelihood ratio after the cut on paraboloid σ has been applied. A cut at $\log\left(\frac{\text{Bayesian likelihood}}{\text{SPE likelihood}}\right) \geq 30.0$ removes a large fraction of the remaining single muon background while most of the signal is kept.

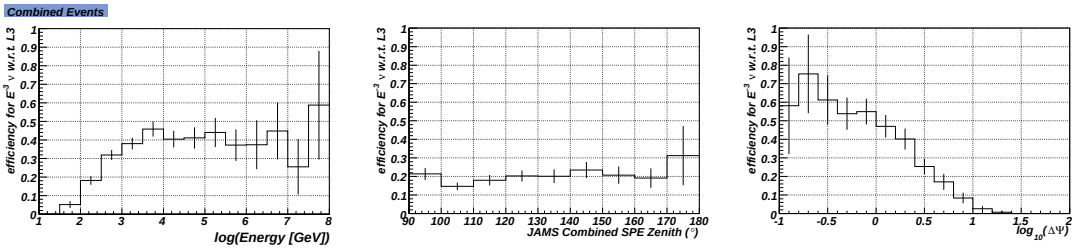

Figure 9.9.: The cut efficiency for combined events is shown in dependence of the neutrino energy, the reconstructed zenith angle and the deviation of the angular reconstruction from the true direction of the track. Well-reconstructed events are preferred by the event selection.

The left plot in the bottom row of Figure 9.8 shows the distribution of plogl. All previously discussed cuts on paraboloid σ and the Bayesian likelihood ratio have been applied to data and simulation. The parameter presents an indicator of the quality of the likelihood reconstruction. A cut at plogl $\leq$ 6.7 selects a sample of data that is dominated by atmospheric neutrinos.
Finally, cuts on the direct length of the track and the number of channels have been observed to increase the sensitivity of the search and the purity of the sample. The bottom right plot of Figure 9.8 shows that the data at small values of the direct length exceeds the rate of events that are expected from atmospheric neutrino simulation even if the statistics of the background simulation are not sufficient to demonstrate the background contamination of the data. Events with LDirPulses $\leq$ 150m or NCh $\leq$ 20 are rejected.
In addition, it is allowed that combined events that pass all the cuts except for the cut on plogl are allowed to enter in the data sample if the part of the event that is in IceCube would by itself pass the high-energy branch cuts for IceCube events except for the direct length cut. The purpose of this cut is to potentially save very rare high-energy events that pass through AMANDA and have a good reconstruction with the combined pulses. A hard cut on plogl as is applied in the standard branch of the combined events can be harmful at high energies. Only 15 events are added to the final sample through this cut.
The cut efficiency for combined events in a soft E^{-3} neutrino spectrum is shown in Figure 9.9. The acceptance is relatively flat in the zenith and selects primarily well-reconstructed events.

9.4. Characterization of the Combined IceCube 40-strings and AMANDA Neutrino Sample

The data sample presented here is the largest neutrino sample extracted from the 2008-2009 data taking period that has been used in a point source search. 19797 neutrino candidates have been selected. The data rate at final level is 0.6 mHz if averaged over the whole data taking period. 16.3% of the selected events are combined events that would not have been in the sample if AMANDA had not been part of the data taking. The majority of the events (16097, 81.3%) are selected by the multivariate Neyman-Pearson likelihood ratio cut. The IceCube high-energy cut is fulfilled for 10558 (53.3%) of the events in the final sample. The overlap with the Neyman-Pearson likelihood ratio cut is however large and only 438 (2.4%) additional events are added in the sample through this cut if data is regarded. As can be seen in Figure 9.10, the high-energy cut branch adds significantly to the efficiency at energies above 100 GeV.
Figure 9.11 shows the energy distribution of simulated atmospheric neutrino events at the final event selection level. If the atmospheric neutrino model of [BGL$^+$04] is used, 90% of the events are contained in the central energy interval 0.2 TeV - 7.9 TeV. Table 9.1 summarizes the central energy intervals for three different neutrino spectra.
The angular resolution of the event selection presented here has already been discussed in Chapter 7. From simulation, the median angular resolution is estimated to be 1.2° for a soft E^{-3} neutrino spectrum.

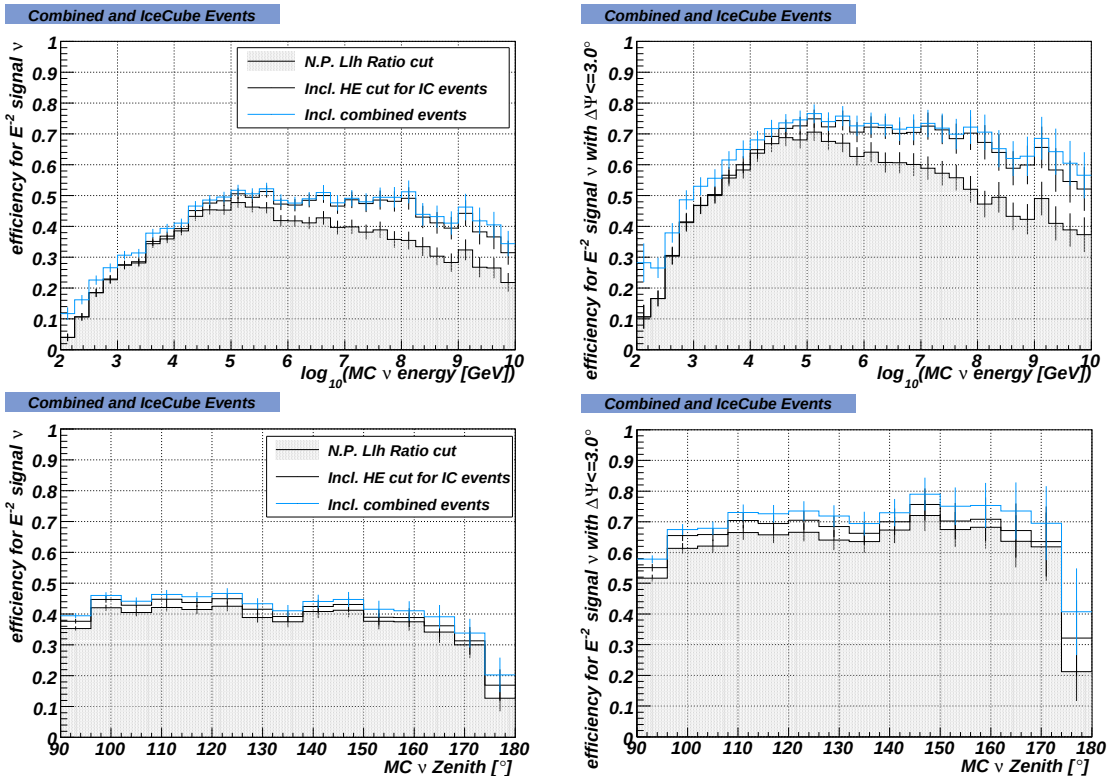

Figure 9.10.: E^{-2} signal neutrino efficiency of the final neutrino selection. The efficiency is calculated with respect to all IceCube and combined events with up-going reconstruction and rlogl $\leq$ 12.0. The plots on the left take all events into account while the plots on the right consider only events that were reconstructed within 3° of their MC truth direction. The high-energy branch for IceCube events improves the efficiency above $\sim$ 10TeV, combined events add efficiency primarily at energies below $\sim$ 50TeV. The acceptance in zenith angle is comparably uniform except for border effects at the horizon and a reduced efficiency for very large zenith angles. The efficiency for well-reconstructed events is significantly better than if all events are considered and ranges between 60% and 80% for almost all zenith angles.

Neutrino Spectrum	90% Energy Interval
Atmospheric Neutrinos [BGL$^+$04]	0.2 TeV - 7.9 TeV
E^{-3} Neutrino	0.2 TeV - 20.5 TeV
E^{-2} Neutrino	2.4 TeV - 750.0 TeV

Table 9.1.: List of the central energy intervals which contain 90% of the neutrinos for three different spectra.

The bulk of the events in such a soft spectrum are at low energies. For higher energies, the angular resolution is better, reaching a median of 0.6° above 100 TeV.

The effective area of the event selection is shown in Figure 9.12. Three different declination bands are considered. The decrease in effective area at the higher energies that is observed for the vertical up-going events is related to the fact that the Earth starts to become opaque to neutrinos at these energies. The contribution from AMANDA is strongest at energies below 10 TeV. For illustration, we present a zoom

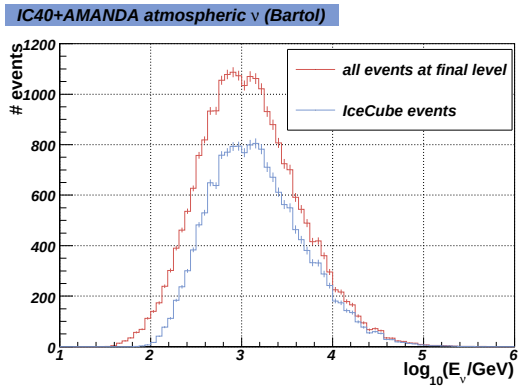

Figure 9.11.: Energy Distribution of Atmospheric Neutrinos in the IC40+AMANDA Data Sample. The model of [BGL+04] has been used to weight neutrino simulation to an atmospheric neutrino spectrum.

into the region around 1 TeV. The increase in effective area through the use of AMANDA is between 10% and about 20%, depending on the declination band. The representation in the left plot of the Figure is chosen to provide an easy comparison to the work presented in [AAA+11i], a point source analysis with the same data sample that has been optimized for hard spectra and does not use the combined events collected through AMANDA. At high energies above ~ 10 TeV, the effective areas of the two analyses are very similar. At lower energies than this however, an increase in the effective area obtained in this work is observed with respect to the analysis presented in [AAA+11i]. At 1 TeV for example, an increase of a factor 1.4 to 2.0 is achieved, depending on which declination band is considered. The improvement is achieved partially by the inclusion of AMANDA in the analysis and partially through the optimization for soft-spectra neutrino sources.

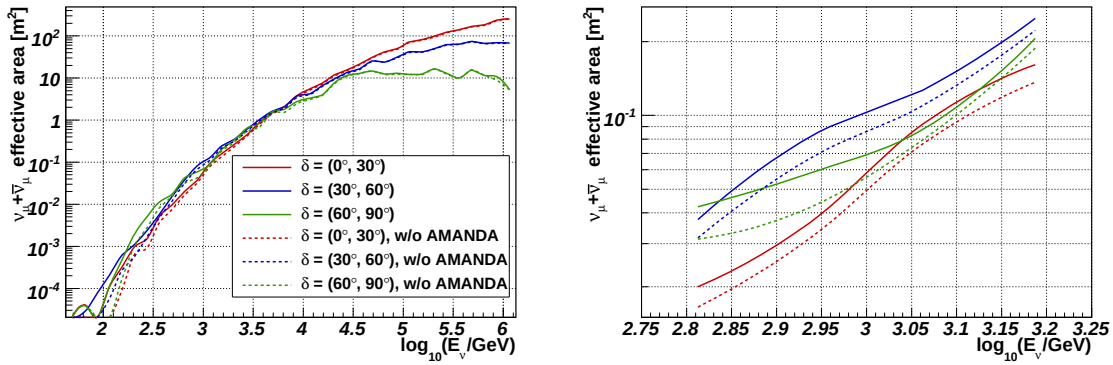

Figure 9.12.: Effective area of the neutrino sample. The plot on the right offers a zoom into the region around 1 TeV to better illustrate the contribution from AMANDA.

Figure 9.13 shows the distribution of data and simulation at the final level. From atmospheric muon simulation, the background contamination of the data is estimated to be 2.5%. The total expectation for the number of events from the simulation are 21057 events, 6% more than observed in data. A zenith dependence of the disagreement is seen in the top left plot of Figure 9.13. It is to be noted however that the disagreement does not harm the potential of the search to identify a possible astrophysical neutrino signal. Cuts to further improve the data-MC agreement at the horizon have been avoided as they hurt the sensitivity at other declinations. The region from 90° to 95° in zenith has been excluded from the analysis but studied more in detail in section 9.5. Moreover, the observed discrepancy is well-contained

within the systematic uncertainties of the simulation:

- A major component of uncertainty is the atmospheric neutrino flux. Changing from a model based on the work of [BGL+04] as used in the plot to a model based on the work of [HKKS07], the expected number of events decreases to 19644. Both models are extrapolated from energies below 1 TeV.
- The systematic uncertainty on the DOM sensitivity and photon propagation through the ice (absorption and scattering of the ice) sum up to 18% if both effects are varied independently, see also Chapter 8.
- Recent improvements in the neutrino simulation suggest a zenith dependent uncertainty of the simulation that was used in this work [6]. These improvements imply that more atmospheric neutrinos are expected at the horizon while the zenith region around 40° to 60° sees less events.
- Uncertainties in the modeling of the higher-energy cosmic-ray air showers could lead to an underestimation of the muon contamination at the horizon.
- Finally, the simulation of noise in the detector is constantly being improved and might have a small influence on analyses such as this one where noise cleaning for the IceCube events is pursued only with a time window cleaning.

It is potentially possible that also new, not simulated physics distort the zenith distribution such as oscillations of sterile neutrinos into muon neutrinos [Cho07]. No tests in this direction have been pursued in this work.

9.5. Surviving Muon Background

A study of horizontal events has been performed on the data sample presented in this thesis. From the top left plot in Figure 9.13, it is evident that the data at the horizon contains a significant muon background component. In addition, the number of events in data exceeds the expectation from simulation if atmospheric neutrinos and muons are summed up. Possible reasons for this have been discussed in the previous section. While the discrepancy is not outside the systematic and statistical uncertainties of the simulation, it is still of interest to investigate the nature of the events at the horizon. Any understanding obtained in this region can help to improve future analyses and to enhance the understanding of the detector and possible weaknesses of the reconstruction.

The study presented here is complimentary to MC based studies. Based on the event selection presented in this work, a fifth of the IceCube events in the zenith region from 90° to 93° has been visually inspected. In comparison to 309 experimental data events selected in this way, 238 neutrino events were expected from simulation as well as 29 double muon events. Within the limited statistics of the single muon simulation, no event survived the event selection. The visual inspection of events is able to provide small samples of double muon and mis-reconstructed single muon events. Both of these can then be used to study why these events survived the cuts and how they could have been rejected. It might be also possible to check if the contributions of single and double muon background are incompatible with the simulation in the case that significantly more events in these categories are observed than expected from simulation. Within the study, 7 interesting candidate coincident muon events could be identified. Note that not all coincident events can be identified in a visual inspection; in particular particles that overlap in space and in time are difficult to identify. While no statement on the validity of the simulation can be derived from the observed number of coincident muon events, the observed sample of events is nevertheless interesting. Event displays are shown in Figures 9.14 and 9.15. The colors indicate the photon arrival times at the DOMs, orange hits are first, cyan last. The size of the hits illustrates the charge that was measured in each DOM. The red arrows/lines represent the MPE reconstruction. All events that are shown here have up-going, near horizontal MPE reconstructions. The same event is always shown twice:

[6] Improved simulation is not available for the detector configuration used in this work.

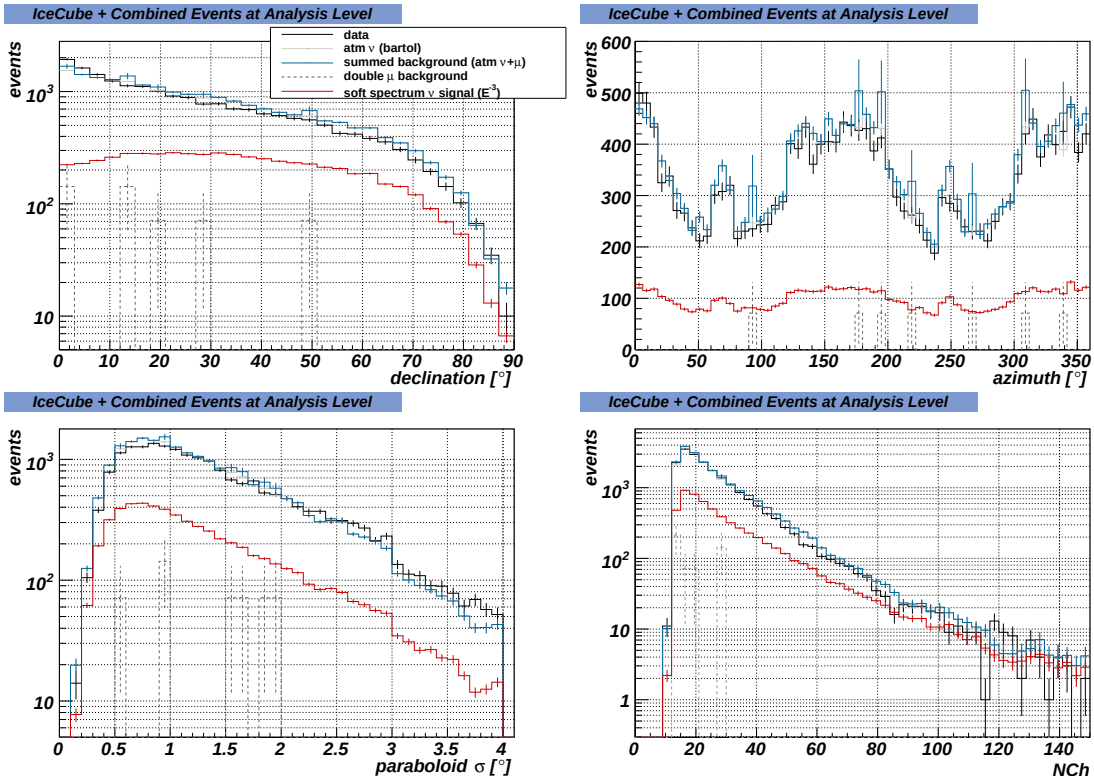

Figure 9.13.: Declination, azimuth, paraboloid sigma and number of channels at analysis level. The data in black is compared to the expected distributions from the sum of the different background components: atmospheric neutrinos, atmospheric single muons and atmospheric double muons. The distributions for atmospheric neutrinos and double muons are shown separately as well. The statistics of the coincident muon simulation is limited. Error bars are purely statistical. The azimuth distribution results from the combination of a uniform flux in azimuth with the detector geometry. For a more thorough discussion of the data simulation agreement, see text.

a side view on the left and a top or bottom view on the right. It is evident that all of these events can be clearly separated into two parts. Indeed, it is almost surprising that these events were able to pass as single muon events. Three of the candidate coincident events shown here (from runs 111322, 113608 and 113659) are also contained in the data sample presented in [AAA+11i] that was optimized for harder spectra and could those apply more stringent quality cuts.

The properties of the candidate double muon events are summarized in Table 9.2. The first event that is shown is unusual due to its position deep in the detector. With all the early hits on a single string, it is possible that the event is a combination of correlated noise and a downgoing muon.

Three of the events could have been rejected with a harder cut on the Bayesian likelihood ratio at around $\log\left(\frac{\text{SPE likelihood}}{\text{Bayesian likelihood}}\right) \geq 30.0$. This cut has been studied during the development of the event selection but has not been applied as it significantly reduces the signal efficiency in other zenith regions. A solution for future analyses could be the development of zenith dependent cuts or the division of the up-going sky into two zenith regions with different cuts. This last strategy is being followed for a follow-up analysis on the IceCube 79-string data also reported in this thesis (see the outlook in Chapter 11).

It is very notable that all the selected candidate coincident events have large direct lengths. The distribution of the hits along the track is however unusual with large parts of the track having no hits within close perpendicular distance of the track. While SDirPulses does characterize the distribution of direct

Run	N-P. Llh ratio	NCh	NDir	LDir [m]	SDir	COGZ [m]	Bay. Llh ratio
110948	1.61	20	15	780.6	-0.49	43.0	28.3
111295	1.18	14	44	665.0	0.79	439.3	25.2
111322	1.94	15	25	625.0	-0.70	434.1	35.4
111958	1.22	15	13	752.0	0.28	191.3	29.5
113608	0.06	22	11	760.5	-0.77	435.2	36.7
113641	1.96	15	17	576.0	0.56	192.0	35.2
113659	2.09	16	18	638.3	-0.42	261.3	31.1

Table 9.2.: Characteristics of candidate double muon events at the horizon. Events are listed in the same order as they are shown in Figures 9.14 and 9.15. The main cut variable for IceCube events, the Neyman-Pearson likelihood ratio, the number of channels and direct pulses, the direct length and the smoothness of the direct length are given. The z-coordinate of the charge-weighted center of gravity of the hits (COGZ) is measured in meters from the origin of the IceCube coordinate system in the center of the detector. The z-axis is pointing away from the center of the Earth. The last entry is the Bayesian likelihood ratio. All events in this selection have passed the cuts for IceCube events and have therefore a good paraboloid σ below 4.0°. The event from run 113608 passes the high-energy cut branch for IceCube events.

hits along the track, it is not possible to be used as cut parameter against these events: As can be seen in Figure 9.5, it is not a very powerful cut parameter and could not have been used to reject these event without significant signal loss. An alternative is to order the projections of the hits on the track by their position on the track and to calculate the largest distance between them as a cut variable. As long as large enough cut values are chosen[7], the signal loss of such a cut is expected to be very small. The sample of events selected here is not large enough to perform a statistical study of the potential of such a cut. Moreover, the geometry of the IceCube 40-strings detector is not ideal for that either. The cut has however been studied for IceCube 79-strings and is used in one of the processing steps (see Chapter 11).
In addition to the 7 candidate coincident events, also 7 candidate down-going muon events have been identified by visual inspection. Their event displays are shown in Figures 9.16 and 9.17 and their properties are listed in Table 9.3. The first and last event are also in the event selection presented in [AAA+11i]. The first, sixth and seventh event are characterized by early pairs of noise hits that distort the reconstruction. The second event has a late pair of noise hits deep in the detector. The remaining events are probably cases where the reconstruction reaches a local minimum. For the fourth event, two other reconstructions are shown next to the MPE reconstruction. The LineFit of the event was down-going, the 32 iterations SPE reconstruction is horizontal and the final MPE reconstruction horizontal up-going.
Again, four of these events could have been rejected if the cut on the Bayesian likelihood ratio had been raised to $\log\left(\frac{\text{SPE likelihood}}{\text{Bayesian likelihood}}\right) \geq 30.0$ on the cost of loosing sensitivity for soft spectra sources in other zenith regions. This strengthens the argument that zenith-dependent cut optimizations can help to improve analyses.
Since the inclusion of triggers with a lower multiplicity threshold in the IceCube IC79-strings configuration, a more rigorous noise cleaning is applied to the data. This cleaning is very likely to reduce the component of single down-going muons in combination with noise pairs that survive at analysis levels.
It is also notable that all of the 7 candidate down-going muon events are in the upper third of the detector, all except one even in the top 100 m. In general it is observed at all event selection levels that the muon background is more abundant at the top of the detector. It is therefore an interesting idea to include the z-coordinate of the center of gravity of the hits or similar variables in the cut variables. This approach

[7] Possible cut values are naturally limited by the spacing of the strings.

Run	N-P. Llh ratio	NCh	NDir	LDir [m]	SDir	COGZ [m]	Bay. Llh ratio
110913	1.55	21	25	1011.6	-0.72	460.5	37.7
110997	1.71	46	24	444.1	-0.32	434.7	28.9
111080	1.80	27	29	323.8	-0.25	303.5	25.0
111365	2.65	20	38	246.4	0.44	428.5	25.5
110877	1.05	21	7	451.9	-0.32	456.8	27.1
112284	1.10	14	12	778.2	-0.76	433.7	45.7
113799	1.19	21	15	457.1	-0.92	454.9	32.5

Table 9.3.: Characteristics of candidate down-going muon events at the horizon. Events are listed in the same order as they are shown in Figures 9.16 and 9.17. The main cut variable for IceCube events, the Neyman-Pearson likelihood ratio, the number of channels and direct pulses, the direct length and the smoothness of the direct length are given. The z-coordinate of the charge-weighted center of gravity of the hits (COGZ) is measured in meters from the origin of the IceCube coordinate system in the center of the detector. The z-axis is pointing away from the center of the Earth. The last entry is the Bayesian likelihood ratio. All events in this selection have passed the cuts for IceCube events and have therefore a good paraboloid σ below 4.0°.

could not be followed in this analysis as the simulation that was existing at the time was not able to reproduce the distribution of this parameter, neither at background-dominated event selection levels nor at neutrino level. The simulation has improved since then and future analyses will be able to apply cuts like this. The work presented in 11 will explore this possibility.

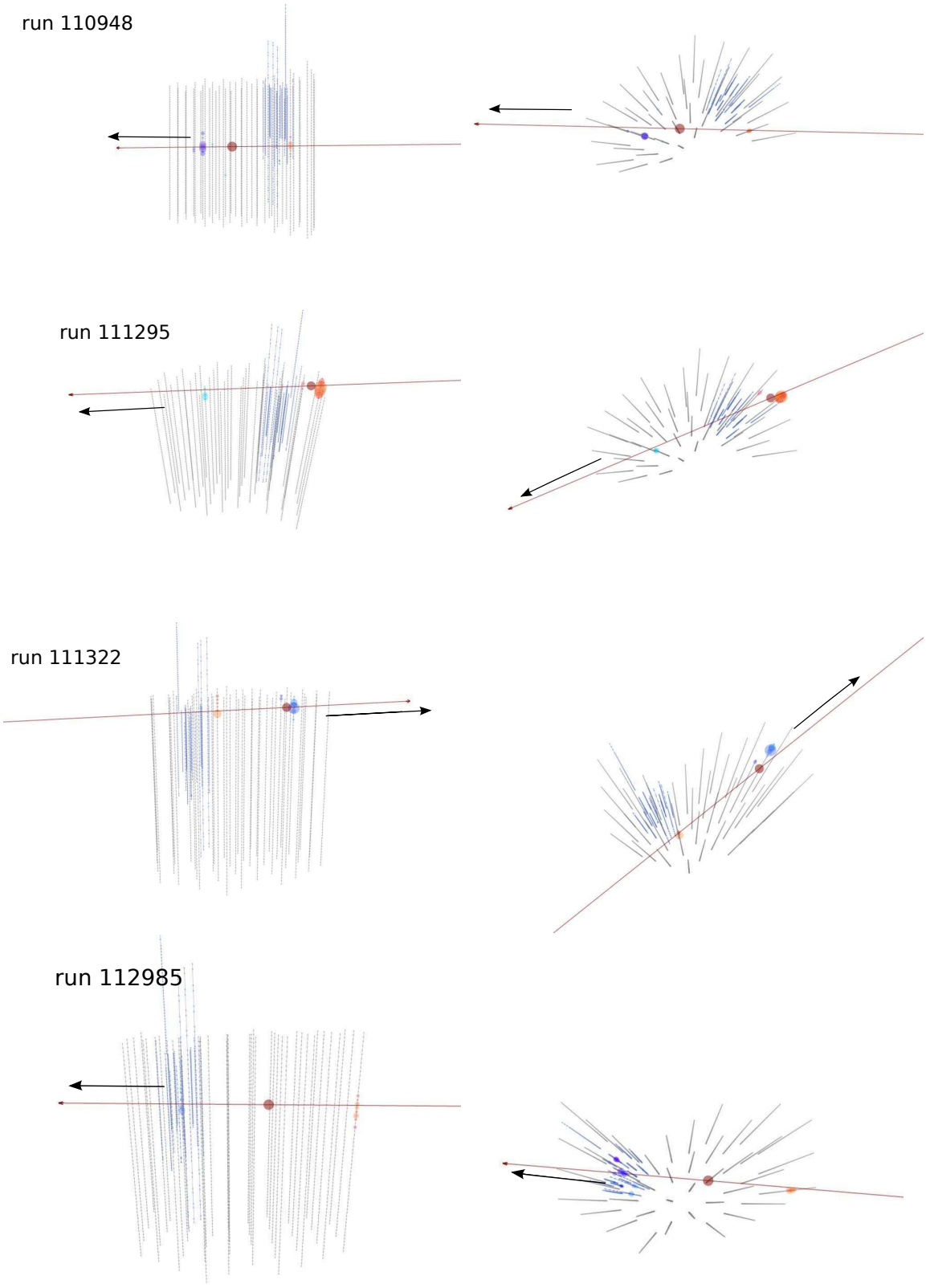

Figure 9.14.: A selection of candidate coincident muon events from the final neutrino sample. The events were selected by eye among IceCube events that are within 3° of the horizon. The colors indicate the photon arrival times at the DOMs, orange hits are first, cyan last. The size of the hits illustrates the charge that was measured in each DOM.

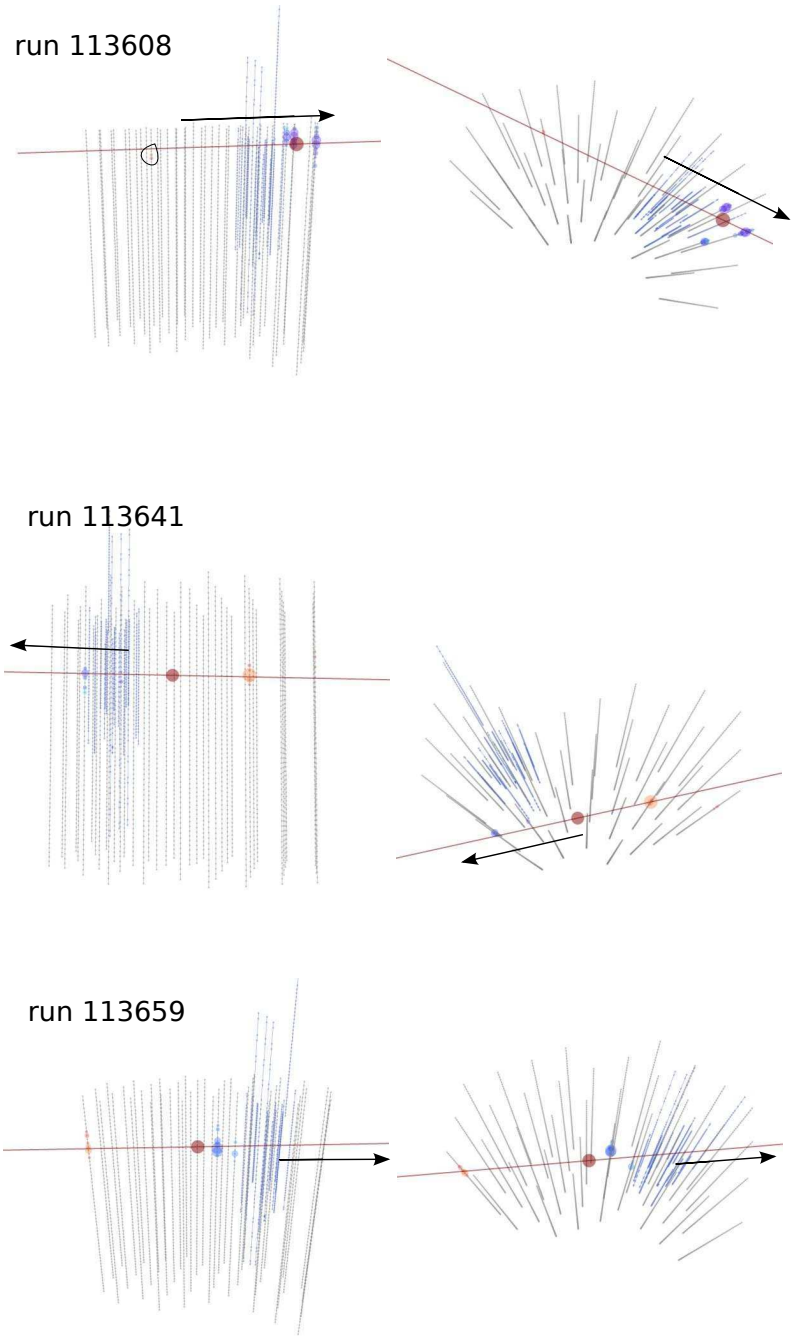

Figure 9.15.: A selection of candidate coincident muon events from the final neutrino sample. The events were selected by eye among IceCube events that are within 3° of the horizon. The colors indicate the photon arrival times at the DOMs, orange hits are first, cyan last. The size of the hits illustrates the charge that was measured in each DOM.

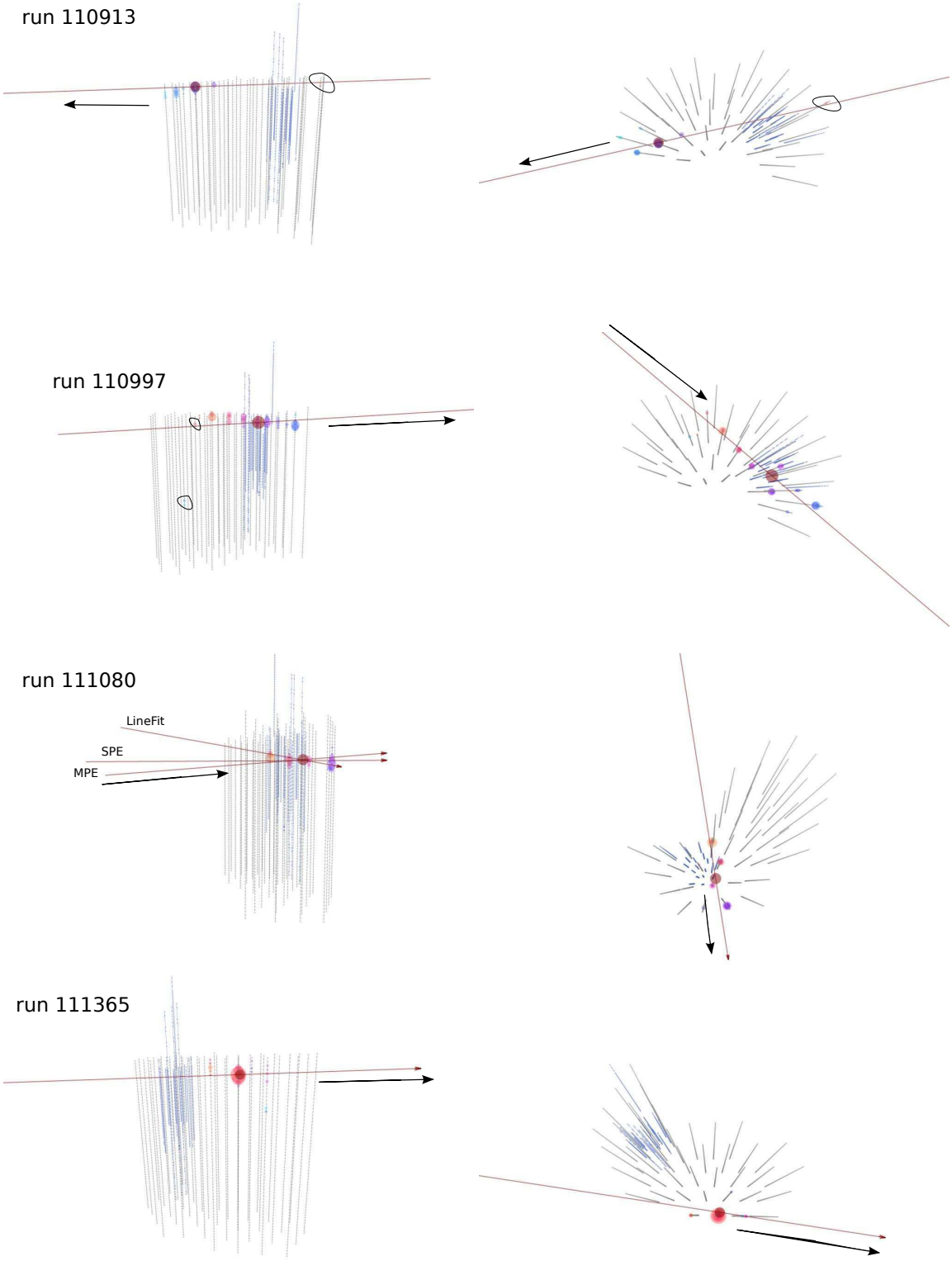

Figure 9.16.: A selection of candidate down-going muon events from the final neutrino sample. The events were selected by eye among IceCube events that are within 3° of the horizon. The colors indicate the photon arrival times at the DOMs, orange hits are first, cyan last. The size of the hits illustrates the charge that was measured in each DOM.

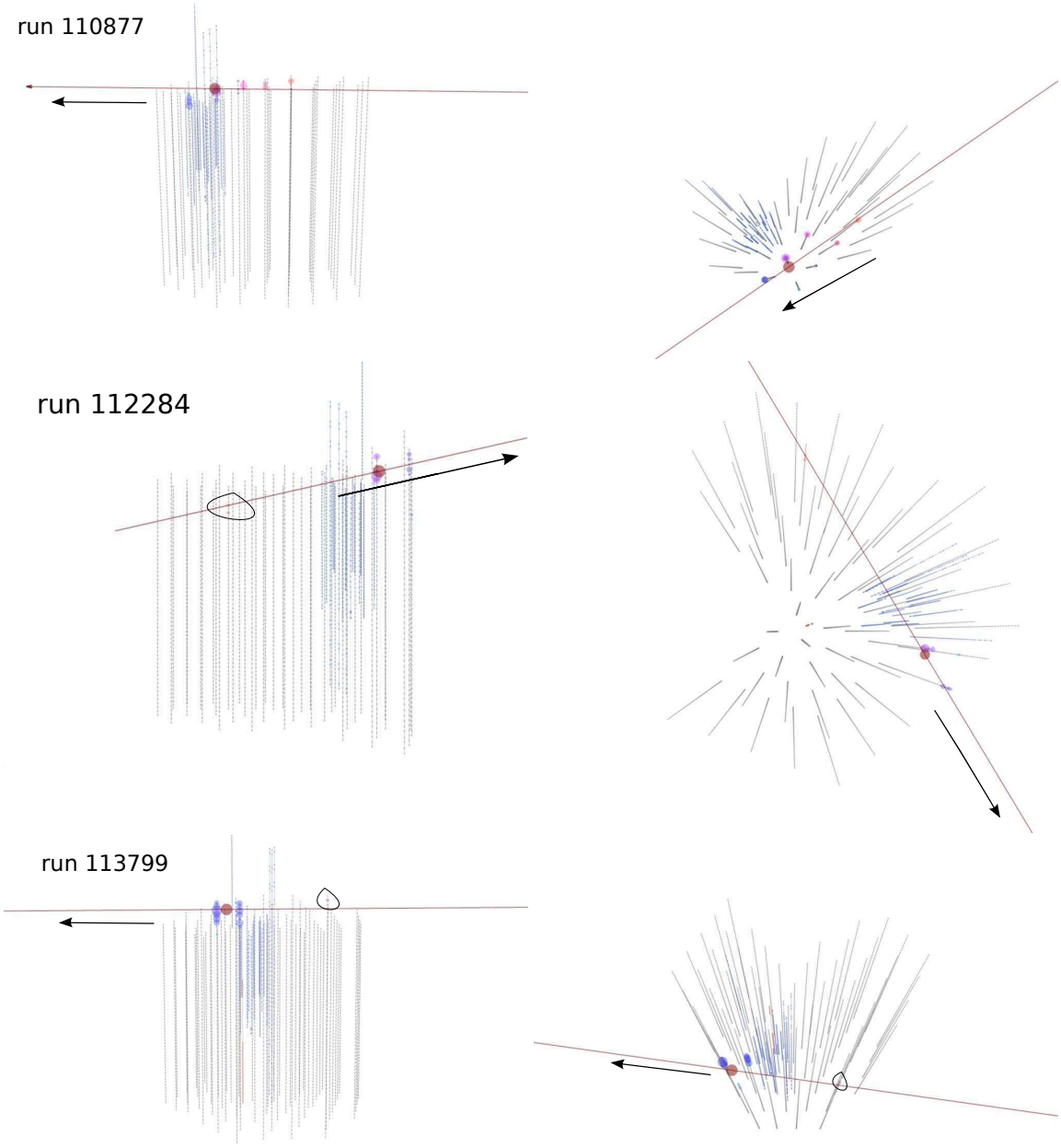

Figure 9.17.: A selection of candidate down-going muon events from the final neutrino sample. The events were selected by eye among IceCube events that are within 3° of the horizon. The colors indicate the photon arrival times at the DOMs, orange hits are first, cyan last. The size of the hits illustrates the charge that was measured in each DOM.

10. Results of the Searches for Galactic Neutrino Sources

The combined IceCube 40-strings and AMANDA neutrino sample that has been developed and studied in the previous chapters is finally used for various searches aiming to detect the first astrophysical sources of high-energy neutrinos. The searches have been concentrated on the Galactic Plane due to the fact that galactic cosmic-ray accelerators are more likely to be located in this region. Three different hypotheses have been defined a priori before the directions of the neutrino candidates have been unblinded. The results of these searches are reported here and IceCube's currently best upper limits for soft-spectra galactic neutrino sources are presented.

10.1. Galactic Plane

The event selection presented in this work is optimized to provide the best sensitivity to soft spectra sources. These scenarios are, as discussed in Chapter 2, highly relevant if galactic neutrino sources are targeted. To be sensitive to any galactic neutrino point source in the northern sky, a scan of the accessible part of the Galactic Plane is performed. The region of $35.875^\circ < \ell < 209.875^\circ$ in galactic longitude and $-5^\circ \leq b \leq 5^\circ$ in galactic latitude is considered. The region has been extended with respect to the region scanned in a previous work of [Ses10] to fully comprise the Cygnus region. The considered part of the Galaxy includes the Local Arm and the closest parts of the Perseus Arm and comprises several γ-ray sources such as the ones considered in the next section.
Under the assumption that a signal is characterized by a point-like emission pattern, the maximum likelihood ratio test as in [BDD+08] and described in Chapter 4 can be applied to locally fit the best composite signal and background hypothesis to the data and compare this to the pure background hypothesis. The likelihood ratio of the two hypotheses is used as test statistic.

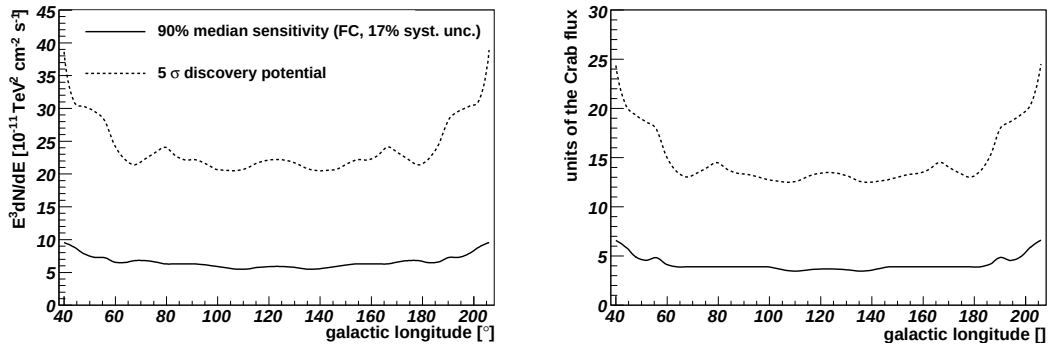

Figure 10.1.: Sensitivity and discovery potential of the point source search with IceCube 40-strings and AMANDA: a source with a generic soft E^{-3} neutrino spectrum at galactic latitude 0° is considered in the left plot. In the plot on the right, the "Crab-like" neutrino flux of Equation 10.1 is used to benchmark the performance for even softer spectra with cutoff at low energies.

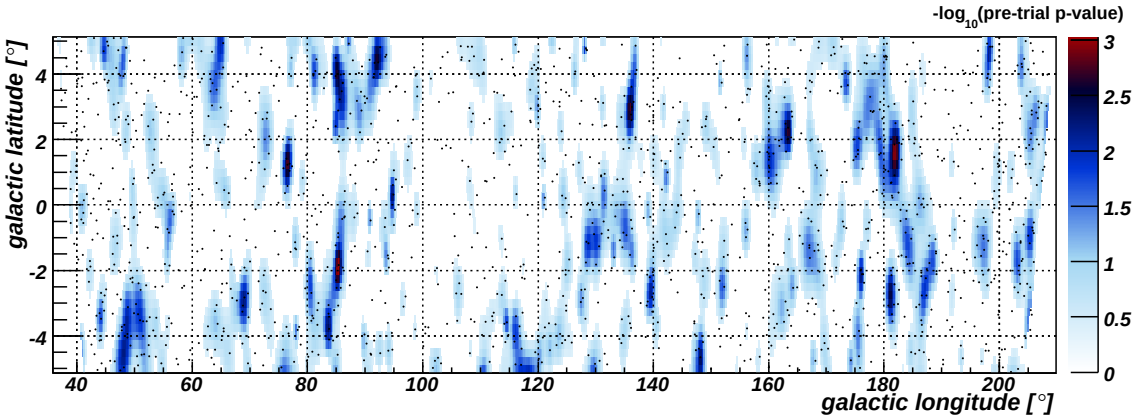

Figure 10.2.: Distribution of events and significance in the Galactic Plane: Each black dot represents the position of a neutrino candidate. The color scale represents the significance of the observation at each point of the grid quantified by the negative logarithm of the *p*-value (pre-trial). The most significant spot is at $(85.5°, -2.0°)$ and has a pre-trial p-value of 0.000934 ($-\log(p\text{-value}) = 3.03$). The trial-corrected *p*-value for the whole scan of the Galactic Plane is 88%.

The median sensitivity and 5σ discovery potential of this search at each accessible galactic longitude are presented in Figure 10.1 for a hypothetical source at a galactic latitude of 0°. The systematic uncertainties of the signal flux simulation as discussed in Chapter 8 are included in the sensitivity curve. The sensitivity is however dominated by statistical uncertainties; the sensitivity flux corresponds to low numbers of signal events around 3-4 and is therefore affected by large relative statistical uncertainties. In equatorial coordinates, both sensitivity and discovery potential depend only on the declination of the source and not on its right ascension. The sensitivity to sources at different galactic longitudes in Figure 10.1 can therefore be identical if the corresponding source declination in equatorial coordinates is the same. The representation in galactic coordinates is chosen to facilitate the comparison to the result of the analysis shown in Figures 10.2 and 10.3.

Two different spectra are considered in Figure 10.1: a soft E^{-3} unbroken power-law spectrum and a "Crab-like" spectrum. The "Crab-like" spectrum is the expected neutrino flux if all the γ-ray flux from the Crab measured by H.E.S.S.[AAB+06c] was produced in pp-interactions. In this case, a neutrino flux of

$$\frac{dN}{dE} = 3.0 \cdot 10^{-7} \cdot \left(\frac{E}{1\text{TeV}}\right)^{-2.4} \cdot \exp\left(-\frac{E}{7\text{TeV}}\right) \text{GeV}^{-1}\text{cm}^{-2}\text{s}^{-1} \tag{10.1}$$

would be expected using the conversion of [KAB06]. With an exponential energy cutoff at 7 TeV this presents a very soft spectrum (see also Figure 9.1). It is thus excellently suited to benchmark the low-energy performance of the search even if it is unlikely that the neutrino flux from other sources than the Crab follow the exact same spectrum or present a cut-off at the same energy. With respect to the predecessor analysis presented in [Ses10], an improvement of about a factor of two has been achieved in the discovery potential for this neutrino spectrum. This improvement is to the largest part due to the increase in the number of strings in IceCube which increased the instrumented volume, as well as to the longer detector up-time in AMANDA and an improved event selection[1]. In comparison to the analysis presented in [AAA+11i], an All-Sky point source search with the IceCube 40-strings data that has been optimized for harder spectra, we obtain an improvement between 15% and 40% in sensitivity for an E^{-3} neutrino spectrum, depending on the declination of the source. The expected improvement for a

[1] Many of the improvements in the event selection that have been achieved in this work however affect the higher energies and are not relevant for this very soft spectrum.

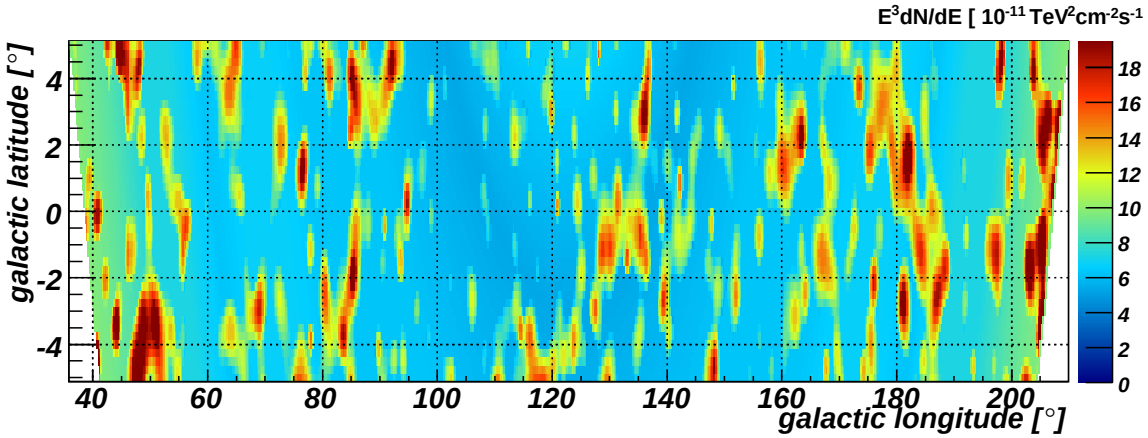

Figure 10.3.: E^{-3} neutrino ($\nu_\mu + \bar{\nu}_\mu$) upper limits for the Galactic Plane. The observed limit depends both on the declination (see Figure 10.1) and the observed local event density (see Figure 10.2).

"Crab-like" spectrum with cut-off is larger but has not been quantified.
When performing a scan, a trial factor is incurred by the application of the test to many positions in the sky. As customary within the IceCube collaboration, this trial factor is not taken into account in the presented discovery potential. The effect of the trial factor on the presented discovery potential would be to increase the flux needed for a discovery by the multiplication with a constant factor. The effective number of trials scales with the number of uncorrelated tests that are performed and is thus proportional to the area that is scanned[2]. The number of trials in this analysis is therefore reduced with respect to an All-Sky scan and a potential discovery or any indication of a possible neutrino source would be more significant in this scan than in an All-Sky search. The selected area within the Galactic Plane covers around $\frac{1}{23}$ of the area of the full sphere and the effective number of trials is reduced by about this factor if a uniform angular resolution across the whole sky is assumed. From the 19797 neutrino candidates in the data sample, 1455 are localized in the considered region for the scan of the Galactic Plane. Figure 10.2 shows the result of the analysis along with the distribution of the selected neutrino candidates. The region was scanned on a $0.25^\circ \times 0.25^\circ$ grid. The color scale represents the p-value of the observation at each point of the grid, i.e. the probability to locally observe a higher or equal value of the test statistic if the test is performed on a pure background sample. As described in Chapter 4, the background samples for comparison have been generated from the data by assigning a random right ascencion to each event. Any possible signal is small enough in comparison to the number of events observed in each declination band that it will not influence these pseudo background samples significantly. A small p-value implies that the observation is very improbable to occur through random fluctuations of the background. Within the scan, the most significant deviation from the background hypothesis is observed at (85.5°,-2.0°) and has a pre-trial p-value of 0.0934% ($-\log(p\text{-value}) = 3.03$). The post-trial probability to observe a similar or larger deviation from the background expectation on any of the points within the Galactic Plane is 88%. The performed test has thus not revealed any statistically significant neutrino source and the distribution of events along the Galactic Plane is uniform on small angular scales[3]. In the absence of a statistically significant signal, 90% upper limits on a generic soft spectrum E^{-3} neutrino flux have been calculated

[2] In addition, the number of independent trials scales inversely with the angular resolution for the events in the sample

[3] An extended large scale structure around galactic longitude 180° might be apparent to some readers, in particular as they might find a similar but not identical structure in the scan of the Galactic Plane performed in [Ses10]. The direction of this "structure" is towards the closest approach to the Perseus Arm of the Milky Way. The significance of any large scale structure of this kind cannot be determined on unblinded data as it is not possible to get a handle on the involved trial factor. It is also to be noted that the color scale of the Figure is optimized to make it easy to pick the "warmest" spot in the Galactic Plane. Small differences in the pre-trial p-value might thus be overrated in the human perception. Only future analyses have the potential to test for an excess of events in this region.

Object	R.A.	Dec	n_s	pre-trial p-value	$\Phi^{90\%}_{\nu_\mu+\bar{\nu}_\mu}$
Crab Nebula	83.63°	22.02°	0	1	7.3
LSI +61 303	40.13°	61.23°	1.6	0.247	8.3
W51	290.82°	14.15°	0.6	1	8.3
CasA	350.85°	58.82°	0	1	5.9
SS433	287.96°	4.98°	0	1	9.8
IC443	94.18°	22.53°	0	1	7.3

Table 10.1.: Upper limit on the flux of muon neutrinos from the six considered galactic sources, assuming an E^{-3} neutrino spectrum. The flux limits $\Phi^{90\%}_{\nu_\mu+\bar{\nu}_\mu} = E^3 \cdot \frac{dN}{dE}$ are given in units of $10^{-11}\mathrm{TeV}^2\mathrm{cm}^{-2}\mathrm{s}^{-1}$. The limit setting ability of the analysis depends on the declination of the source. The best flux limit is obtained for CasA. Listed are also the positions of the sources, the pre-trial p-value for each source and the best fit number of signal events. A p-value of 1 indicates that no positive fluctuation has been observed, i.e. all background samples show an equal or larger value of the test statistic.

with the method of Feldman & Cousins [FC98] and the additions of [CBHP03, Hil03] to include a 17% systematic error on the neutrino flux. This method is the standard method for the calculation of upper limits in neutrino point source searches with IceCube. A component of ν_τ oscillating into ν_μ is not included in the limits as considered of secondary importance here. The limits obtained in this way are conservative and will be superseded by measurements with the more sensitive larger configurations of IceCube. The limits are reported in Figure 10.3. The observed limit depends both on the declination and on the observed local event density.

10.2. (γ-Ray) Source List

On the base of the phenomenology of galactic accelerators, six interesting sources, five of which have been detected in γ-rays, are selected in Chapter 2. Unbinned maximum likelihood ratio tests with point-like signal hypotheses centered at their positions have been performed to search for neutrino emission from these objects. With respect to the scan of the Galactic Plane, it is guaranteed in this way that the test is performed directly at the position of the γ-ray source with no offset imposed by the binning of the search grid. Moreover, an additional reduction of the statistical penalty coming from the scan of large regions is here obtained by considering only a short list of interesting objects. While the scan of the Galactic Plane has already shown that no strong clustering of events is detected around any of these sources, we present here the detailed results of this a priori defined test.
The distribution of the selected neutrino candidates in the environment of the six γ-ray sources are shown in Figure 10.4. The color scale represents the event-based angular uncertainty of the reconstruction (paraboloid σ, see Chapter 7). No indication of a clustering of events around any of the objects can be discerned. Indeed, no significant deviation from the background expectation is observed in the statistical tests. The results of these tests are reported in Table 10.1. The smallest pre-trial p-value is observed for LSI +61 303; but a similar or higher deviation from the background expectation at this position is detected in 25% of all randomized data sets. Correcting for the trials in the source list, the final p-value of this observation is 42%.
In the absence of a detection, 90% upper limits are placed on the flux of neutrinos from the six listed objects. An E^{-3} neutrino spectrum is assumed in Table 10.1 and a 17% systematic uncertainty (see Chapter 8) is taken into account. With an upper limit of $E^3 \cdot \frac{dN}{dE} = 5.9 \cdot 10^{-11}\mathrm{TeV}^2\mathrm{cm}^{-2}\mathrm{s}^{-1}$, the lowest

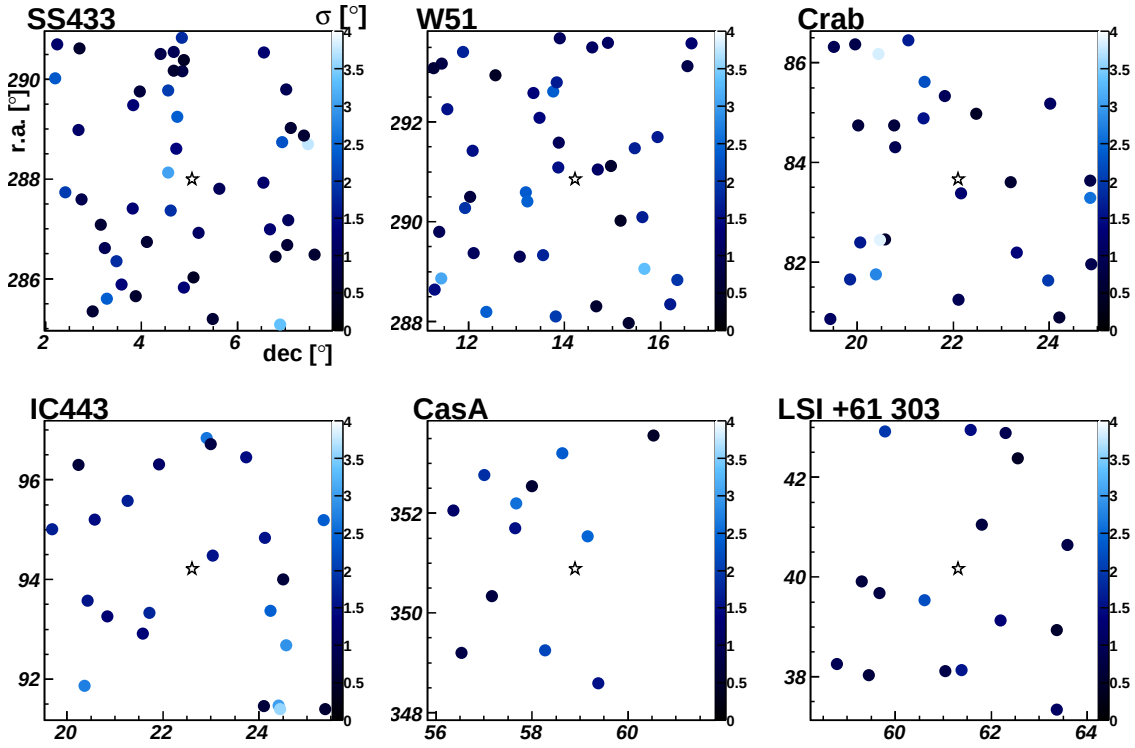

Figure 10.4.: Distribution of events around the six selected γ-ray sources. The uncertainty of their angular reconstruction is indicated by the color of the marker. The position of the source is represented by a star. The local event density depends on the declination of the source with most events observed at small declinations. The sources are shown in increasing order in declination. No significant clustering of events above the background expectation has been observed for any of the six objects.

flux limit is found for the flux of neutrinos from the direction of Cassiopeia A. For the Crab, a limit on the flux in Equation 10.1 has been derived as well and is 4.5 times above the expected flux if all the γ-rays detected with H.E.S.S. [AAB+06c] were produced in pp-interactions.

10.3. The Cygnus Region

The Multi Point Source (MPS) analysis [Ses10] has been applied to a $7° \times 11°$ region of the Galaxy that includes the most active parts of the Cygnus region. The statistical test, also described in more detail in Chapter 4, tests the event distribution inside an extended region for clustering on a range of different angular scales. The interest in the Cygnus region as potential site of cosmic-ray acceleration has been motivated in Chapter 2. Moreover, the region showed a positive fluctuation in the previous year: 40 events were observed in the considered region in the combined IceCube 22-strings and AMANDA data over a background expectation of 27 events. The application of the statistical test to that data lead to the observation of an increased clustering of events with a 2.3 σ significance at an angular scale of 2° [Ses10]. In the analysis performed there, the angular scale was fixed a priori to reduce the statistical penalty involved with testing different angular scales.
The positive fluctuation of the Cygnus region observed in the IceCube 22-strings and AMANDA search, while far from being a discovery, increased the interest in the application of the same test on a larger and more sensitive data sample even further and has been one of the main motivations to extract a neutrino

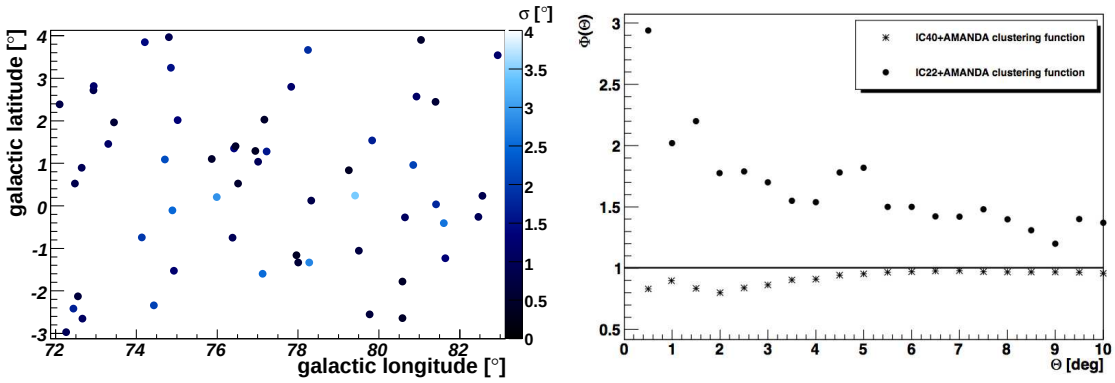

Figure 10.5.: The distribution of events inside the search box for the Cygnus region is shown on the left. The uncertainty of their angular reconstruction is indicated by the color of the marker. 55 events are observed inside the region while 60 are expected from pure background and no significant clustering of events above the background is observed. The degree of clustering is quantified with the clustering function $\Phi(\Theta)$ and compared to the results from the previous year's analysis. With less events detected than expected from the background, the data is less clustered than the average background distribution at $\Phi(\Theta) = 1$ (Credit for this plot: Y. Sestayo.)

sample from the IceCube 40-strings and AMANDA data. The same analysis but performed on the data set presented in this work and with the addition of scanning different angular scales improves the discovery potential by a factor of two if only diffuse emission, i.e. randomly distributed emission within the region, is considered. A larger improvement is achieved when the presence of neutrino point sources within the region is assumed.

The same region from 72° to 83° in galactic longitude and −3° to 4° in galactic latitude as in the previous analysis has been considered and the clustering of the events characterized on angular scales from 0.5° to 10° in 0.5° steps. In the data sample presented in this work, 55 events were observed inside the considered region while 60 background events were expected. The background expectation is again derived directly from the experimental data by randomizing the right ascension of the neutrino candidates. This estimate is therefore robust and unaffected by any imperfections of the detector simulation or the modeling of the background. The result therefore presents a slight negative fluctuation with respect to the background expectation, in contrast to the positive fluctuation observed in the previous year's data sample. This result weakened then the possible presence of a signal component unless a time dependency is assumed or strong fluctuations of the background are invoked. The distribution of the observed events is shown in the left plot of Figure 10.5. With less events observed than expected, the event distribution is more sparse than in an average background sample and no significant clustering has been observed on any angular scale. The value of the clustering function $\Phi(\Theta)$ (see Chapter 4) at each considered angular scale is shown for each considered angular scale Θ and compared to the results from the IceCube 22-strings and AMANDA data.

From the results obtained in this work, strong limits on the flux of neutrinos from the Cygnus region can be set even when only a diffuse emission is assumed. The γ-ray emission from the Cygnus region has been studied by the MILAGRO collaboration [AABB07] and quantified for a $E^{-2.6}$ flux, corresponding to the spectrum of the Crab measured by HEGRA [AABB04]. The same spectrum is used to calculate IceCube's limits for the Cygnus region. Under the assumption that no energy cut-off below 1 PeV is present in the neutrino flux, a neutrino flux upper limit at $\Phi^{90\%}_{Cygnus} = 3 \cdot 10^{-11} \mathrm{TeV}^{-1}\mathrm{cm}^{-2}\mathrm{s}^{-1}$ is set. This flux upper limit is a factor three above the expected flux of neutrinos if the γ-ray flux measured in

[AABB07] was produced in pp-interactions and the conversion of [KAB06] is used. The approach to study large regions proved to be very powerful and appropriate for the study of star-forming region in the Galaxy. It is therefore planned to extend this search also to other star-forming regions in future data analyses.

10.4. Discussion

A neutrino sample to search for galactic neutrino point sources has been developed based on the combined IceCube 40-strings and AMANDA data. With respect to the predecessor analysis, an improvement of at least a factor of two in discovery potential has been achieved even for very soft neutrino spectra. Three blind tests have been performed to identify a possible signal over the background of atmospheric neutrinos. None of the three tests has revealed the presence of galactic neutrino sources in the data. IceCube's currently strongest neutrino flux upper limits for Galactic sources are derived.
The distribution of events observed in the considered part of the Galactic Plane is characterized in Figure 10.2 and is uniform on small angular scales. The upper limits on the flux of neutrinos at each position in the Galactic Plane are presented in Figure 10.3 for a generic power law spectrum with spectral index 3.
No accumulation of events near the six considered objects SS433, W51, the Crab, IC443, Cassiopeia A and LS I +61 303 has been observed. For an E^{-3} flux, the resulting limits range between $E^3 \cdot \frac{dN}{dE} = 5.9 \cdot 10^{-11}\mathrm{TeV}^2\mathrm{cm}^{-2}\mathrm{s}^{-1}$ and $E^3 \cdot \frac{dN}{dE} = 9.8 \cdot 10^{-11}\mathrm{TeV}^2\mathrm{cm}^{-2}\mathrm{s}^{-1}$. For the Crab, a limit on the spectrum 10.1 has been set at 4.5 times the flux that would be expected if all γ-rays were produced in pp-interactions.
A previously observed positive fluctuation of the number of events in the Cygnus region could not be strengthened on the larger and more sensitive data sample presented here; less events than expected from randomized sky maps have been observed. Depending on the assumed energy cutoff, the obtained neutrino flux upper limits range between $\frac{dN}{dE} = 6 \cdot 10^{-11}\mathrm{TeV}^{-1}\mathrm{cm}^{-2}\mathrm{s}^{-1}$ (cutoff at 10 TeV) and $\frac{dN}{dE} = 3 \cdot 10^{-11}\mathrm{TeV}^{-1}\mathrm{cm}^{-2}\mathrm{s}^{-1}$ (no cutoff below 1000 TeV) for an $E^{-2.6}$ neutrino flux.
The non-detection of a neutrino source in the presented tests does not imply that IceCube will not see any (galactic) neutrino source in the future. Neutrinos from cosmic-ray accelerators may have eluded a detection until now in several different ways. First and most importantly, the analyzed data has been collected with a partial configuration of the detector. It forms part of the steps that lead up to the scientific program that will be realized on the full detector. The non-detection of neutrino sources at this stage is not surprising given the known flux of γ-rays and cosmic-rays in the Galaxy. Even with this in mind, analyses of partial IceCube data such as the one presented here provide important experience with the detector and contribute to the development of mature analyses. For these reasons, it is most important to apply the obtained knowledge to the newest data and the author of this work is already active on the analysis of data from the almost-complete detector (IceCube 79-strings).
The complete and almost-complete detector configurations of IceCube 86-strings and IceCube 79-strings present a significantly larger neutrino effective area and will have a much improved sensitivity. Based on the results reported in this thesis, we are confident that the full detector will after few years of operation provide significant contributions to the understanding of the high-energy universe even if no neutrino sources were to be discovered. Under the conservative assumption[4] that the full detector's sensitivity to the Crab will be a factor two better than in the presented data sample, IceCube will be able to constrain the fraction of γ-rays from pp-interactions from the Crab within 4-5 years of operation. Given the fact however that it is very likely that most of the emission from the Crab is of leptonic origin, it might take longer until IceCube enters the interesting regime for this source. As hadronic scenarios are more relevant in star-forming regions like the Cygnus region, it is more inspiring to observe that the limits for

[4] This assumption is conservative as it only takes into account the larger size of the detector. It is however expected that future data samples will not only profit from this but also from improved reconstruction and event selection tools as well as from the presence of IceCube-DeepCore that will help to select low-energy events more efficiently than it was possible with AMANDA.

this region presented here are already now only a factor of two to four above the expected neutrino flux if all γ-rays from the region were from pp-interactions. With the larger detector, IceCube might thus after few years of operation be able to constrain the fraction of γ-rays that are produced in pp-interactions in the Cygnus region.

Another important aspect to consider is the power of the statistical test that is applied. Even if present in the data, a signal may go undiscovered if an inappropriate or suboptimal test is used. In this work, a large part of the Galactic Plane has been scanned for steady neutrino sources with no extension beyond the angular resolution of the detector. With a median angular resolution of 1.2°, this still presents a fairly general search for steady neutrino sources. Sources with angular extensions above this range may however have escaped detection. Dedicated searches for extended sources can be performed with a simple extension of the applied maximum likelihood ratio test. The inclusion of the event times in the statistical test can significantly reduce the background and thus improve the discovery potential if a time dependence of the neutrino signal is present. A test of this kind has been performed on the event selection developed in this work in [Vog10]. The development of adequate non-parametric tests that do not include a fully defined signal hypothesis is more challenging. One such test is the analysis of the Cygnus region applied here and developed in [Ses10]. This method is sensitive to a wide range of signal hypotheses through the characterization of the second order properties of the spatial distribution of the events, i.e. the distances between the events. The application of similar tests to other regions of the sky such as the Galactic Center will provide interesting results in the future. Another interesting area to exploit is the development of non-parametric tests on smaller angular scales[5].

In the analysis performed in this work, a neutrino source could also have hidden in the southern sky. Even in analyses such as the ones presented in [AAA+11i] which consider the whole sky, it is still possible that a neutrino point source is present in the southern hemisphere but not yet detected; the sensitivity of the search is an order of magnitude worse in the southern sky and neutrino sources at energies below ~50 TeV are not yet accessible in large parts of the sky. In an analysis of the IceCube 79-string data (see Chapter 11), the author of this work is currently mining the possibility to improve this situation in two different ways:

The low-energy extension DeepCore has now replaced AMANDA and offers the possibility to suppress the down-going muon background by the use of atmospheric muon veto strategies[Sch10]. This totally new potential will be exploited in the analysis. The work presented on the IceCube 79-string data will thus continue the use of a low-energy core for point source analyses that has been advanced in this work and follow along the line of low-energy point source analyses performed during the work reported in this thesis. In addition, it is attempted to suppress the major background at high energies - bundles of low-energy muons that are reconstructed as single high-energy muons - as much as possible by the use of cut variables that are sensitive to the distribution of the energy loss along the track. In this way, it may be possible to lower the energy threshold of the analysis.

[5] A parametric search is characterized by a background hypothesis as well as a signal hypothesis that is described through a set of parameters such as the energy spectrum or source extension. These parameters can either be fixed or varied to maximize the significance. A maximum likelihood ratio test of this kind provides an excellent sensitivity to the considered source hypothesis but is affected by trials if the parameters are fitted to the data and suboptimal if the true signal deviates from the considered signal hypotheses. A non-parametric test such as MPS [Ses10], quantifies the deviation of the data from the background hypothesis without the use of a fully defined signal hypothesis. An example of a non-parametric test at small angular scales is an analysis that simply counts the number of events in a search bin around the position of interest and compares this number to the background expectation. As this method includes only a small fraction of the available information about the events in the search bin, improvements may be possible.

11. All-Sky Neutrino Source Search with IceCube 79-strings - First Steps

The construction of IceCube continued while the work presented in the previous chapters has been performed. The nearly complete 79-strings configuration of IceCube has been operated from 2010 to 2011 when the final strings of the IceCube array were deployed. All experiences gained with this detector will set the ground for years of analyses with the full IceCube detector. Moreover, analyses of this data sample will benefit from several advantages with respect to the previous configurations:

- The larger instrumented volume allows to collect more and better reconstructed events. With respect to the analysis presented earlier in this work, the instrumented volume has been increased by almost a factor of two.
- The detector geometry is more symmetric and thus the event selection is more efficient. In contrast to this, IceCube 40-strings had a long and a short detector axis while the intermediate detector configuration IceCube 59-strings contained a non-instrumented region in the shape of a wedge.
- This configuration includes the first six DeepCore infill-strings. The value of this more densely instrumented sub-array has already become evident in a study of atmospheric cascade events [Ha11]. For point source analyses, the work presented in this thesis and in [Ses10] provide the proof-of-principle that the sensitivity to soft-spectra sources can be improved with an increased effective area in the 100 GeV to 10 TeV range despite the larger background at these energies. The work started here will explore the use of the veto tools described in [Sch10] to improve IceCube's sensitivity to southern sky sources by the collection of additional events between 100 GeV and a few TeV.
- More elaborate software such as new reconstruction algorithms is available for many aspects of the analysis. One important point is for example the availability of better energy estimators. A comparison [Wol11] indicates that a new algorithm called TruncatedMean [Mia11] has a larger range of linearity than the MuE energy reconstruction that has formerly been used in point source analyses.
- The IceTop array on top of the neutrino telescope allows to veto down-going muons from cosmic-ray air showers at the highest energies. Studies of this capability have been performed in [Auf11, ACM11] and a software to apply this veto is now available.

In view of all this progress, I took the initiative to realize an IceCube 79-strings All-Sky point source search in collaboration with the other members of our group. The primary search will be a scan of the full sky to search for neutrino point sources. To perform this scan, we plan to apply the maximum likelihood ratio test described in [BDD$^+$08]. Once the full data sample is available, we will however also study the performance of other, faster statistical tests on the data. In addition, a range of more specific physics scenarios will be studied. Among the most interesting results obtained in the previous chapters are the limits for the Cygnus region. IceCube-79 strings will provide a much larger data sample on which the same test for the Cygnus region will be repeated. The same statistical test can also be applied to other star-forming regions. Furthermore, we plan to study the correlation of neutrino events with different classes of objects such as AGNs with evidence of a jet, Globular Clusters with a high content of Millisecond Pulsars and to massive star clusters.

To achieve this goal, we have started the development of the event selection from the lower level off-line data processing on. In particular, a first background rejection has been developed to select a reduced

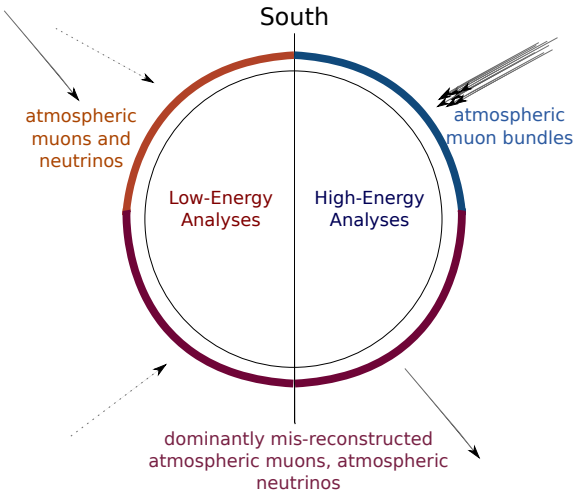

Figure 11.1.: Overview of the different background in the southern and northern sky: In the up-going region, i.e. in the northern sky, both low- and high-energy oriented analyses have to reject the background of mis-reconstructed down-going muons. The secondary background of atmospheric neutrinos cannot be rejected ultimately. In the down-going regime, two different strategies can be followed to suppress the background of down-going muons. Low-energy analyses aim to select a sample of events with interaction vertex inside the detector. High-energy analysis can suppress the background by selecting only events with very high energy estimates. The remaining background is dominated by bundles of atmospheric muons that are mistaken as high-energy single muons.

sample of events on which more CPU-intensive reconstructions can be applied and provided to the collaboration. This effort has recently been completed and the processing of the data is taking place at this time. In parallel to the off-line processing, I have also developed a preliminary analysis level event selection. This event selection is currently still being optimized and additional studies of the background will be undertaken as soon as this document is submitted. A preliminary effective area has been calculated to benchmark the expected performance and clearly indicates that in particular a substantial improvement of the high-energy event selection in the southern hemisphere with respect to previous analyses is already achieved.

11.1. Selection of Track-like Events for the Application of Additional Reconstructions

As part of this work, we have prepared the second step of the off-line processing of track-like events in the IceCube 79-strings data sample, the so-called Level 3 (off-line) processing. The aim of this processing step is to perform higher level reconstructions on a smaller data sample with respect to the data volume obtained from the on-line filter. The resulting data set serves various physics analysis which are based on the muon neutrino channel like diffuse and atmospheric neutrino analyses as well as the point source analysis started here. The final event sample that will be used for the point source analysis will consist of up to three different streams of events:

- A selection of well-reconstructed, up-going neutrino candidates. Targeted neutrino energy range: above a few 100 GeV. At the on-line filter level, the events that are relevant for this stream are selected by the IceCube Muon filter.
- A sample of down-going, very high-energy events. The dominating background at analysis level

Zenith Region	Cut
All	NCh≥ 8 and ((NCh≥ 10) or ($\theta^{\mathrm{LineFit}} > 70°$))
$0° \leq \theta^{\mathrm{SPE}} < 60.0°$	$\log(\text{total charge}) \geq 0.6 \cdot \left(\cos(\theta^{\mathrm{SPE}}) \cdot 0.5 + 2.5\right)$
$60.0° \leq \theta^{\mathrm{SPE}} < 78.5°$	$\log(\text{total charge}) \geq 3.9 \cdot \left(\cos(\theta^{\mathrm{SPE}}) \cdot 0.5 + 2.5\right)$
$78.5° \leq \theta^{\mathrm{SPE}} < 180.0°$	$\frac{-\mathrm{SPE\ logl}}{\mathrm{NCh}-2.0} \leq 8.1$

Table 11.1.: Event selection in the IceCube 79-strings on-line muon filter [Bak09]. The applied cut depends on the reconstructed zenith angle θ.

are high-energy muons and muon bundles. Targeted neutrino energy range: above a few 10 TeV. The IceCube Muon filter also provides the on-line selection for these events.

- A selection of up- and down-going neutrino candidates with interaction vertex inside a fiducial volume around DeepCore. Targeted neutrino energy range: 100 GeV to a few TeV. At the South Pole, a sample of potentially interesting events for this stream is selected by the DeepCore filter.

As illustrated in Figure 11.1, the background in each of these streams is different from the others. To be able to perform the point source analysis, all of these streams had to be considered in the Level 3 off-line processing and a dedicated event selection had to be developed for each of them.

On-line Filter and First Off-line Processing

The data that provides the base for the work presented here already passed two processing steps. First, fast reconstructions have been applied at the South Pole and interesting events have been selected by the on-line filters. After satellite transfer to the North, a first off-line processing called Level 2 has been applied. The relevant aspects of the on-line filter and the Level 2 off-line processing are described briefly. The off-line processing [GS11] has been performed on all on-line filtered data without any additional event selection. In the context of this work, we are primarily interested in the Muon and DeepCore filter streams as mentioned above.

The requirements of the Muon filter are summarized in Table 11.1. The cuts are based on a LineFit and a SPE likelihood reconstruction (see Chapter 7), both of which are performed on-line at the South Pole. An up-going stream where a decent quality of the track reconstruction is required is combined with a down-going stream where a zenith dependent cut on the detected charge is applied. The charge is a measure of the detected number of photo electrons and thus the total amount of light in the event.

The Level 2 off-line data already contains a range of interesting reconstructions for the Muon filter events. For the first time, both DOM launches with and without local coincidence condition (see section 5.4) are used in the reconstruction within a standard processing. To reduce the impact of noise, an iterative isolated launch cleaning (SeededRTCleaning) [Sch10] as well as a time window cleaning of (−4 ns, +10 ns) around the trigger time are applied. The following reconstructions are the performed:

- The LineFit first guess reconstruction.
- The SPE reconstruction, 4 iterations.
- The MPE reconstruction.
- A fast angular uncertainty estimator called CramerRao [Lue08], applied for the MPE and the SPE reconstruction.
- The MuE Energy Reconstruction [Chi08].
- Another Energy Reconstruction called Photorec [GBH08].
- A vertex reconstruction called Finite Reco [Eul08].

The DeepCore filter requires a trigger of at least 3 hit optical modules (SMT3) inside the DeepCore

volume. In addition, down-going muons are vetoed by an advanced veto algorithm; only hits that are causally connected with the hits inside a fiducial volume around DeepCore are considered in the veto. For more details see [Gra09]. Again, DOM launches with and without local coincidence condition are used in the reconstruction. An iterative isolated pulse cleaning and a static time window cleaning of (−5 ns, +4 ns) around the first trigger in DeepCore are applied. The following reconstructions are then added:

- The Linefit first guess reconstruction.
- The SPE reconstruction, 4 iterations.
- A fast angular uncertainty estimator called CramerRao [Lue08], applied for the SPE reconstruction.
- A vertex reconstruction called Finite Reco [Eul08].

The rate of events that pass the Muon filter is about 33 Hz. With the off-line MPE reconstruction based on the pulse cleaning described above, the rate of up-going events is about 6 Hz, the remaining 27 Hz are reconstructed as down-going. Note that not all of these events have been reconstructed as down-going with the reconstructions that were applied on-line at the South Pole - the on-line reconstruction had 19 Hz of up-going events in this filter. The DeepCore filter has a data rate of about 17 Hz.

First Off-line Background Rejection

To provide higher level reconstructions and quality parameters needed for the final physics analyses of IceCube data, it is mandatory to reduce the data volume in order to save CPU time and to reduce the storage requirements. The cuts that are applied to achieve this reduction have been designed and studied by the author of this work. Since the processing effort is meant to serve a large part of the IceCube Collaboration, the final cut selection has been presented to all the interested analyzers and represent a compromise between various needs. The three different event streams introduced above are studied and optimized: up- and down-going events that have been selected by the Muon filter and the events that have been collected by the DeepCore filter.

Up-Going Muon Filter Events

The up-going muon stream is of primary importance for point source analyses as the best sensitivity can be achieved in this region. The cuts for this region have been designed to reduce the data rate to $\sim$ 1Hz with the goal to preserve 98% of all neutrinos in a soft E^{-3} signal neutrino spectrum that can be reconstructed within 3° of their MC truth direction. A soft spectrum is chosen for the cut optimization as it is generally more difficult to obtain a good efficiency for these spectra. In addition, the performance for a harder spectrum, an E^{-2} neutrino spectrum is evaluated as well. The dominant backgrounds at this level are mis-reconstructed single and coincident muons from atmospheric air showers above the detector.
The applied event selection is primarily based on a variable introduced in the Level 3 off-line processing of the previous year [BSW10], named “Direct Ellipse”. This variable is defined as

$$\text{Direct Ellipse} = \left(\frac{\text{LDirChannel}}{60.0}\right)^2 + \left(\frac{\text{NDirChannel}}{15.0}\right)^2 \tag{11.1}$$

where NDirChannel is the number of channels with direct pulses (see Chapter 9) and LDirChannel the direct channel length. Besides this variable, a variation of plogl = $\frac{-\text{MPE logl}}{\text{NCh}-3.5}$ (see also Chapter 9) is used. To further suppress the coincident muon background, we use two additional cut variables. The first is called “Separation” and is defined very similar to a variable of the same name that has previously been used in WIMP analyses. The second has been developed based on the work presented in section 9.5 and is named “LEmpty”. The definitions of these two variables as used in this work are described here.

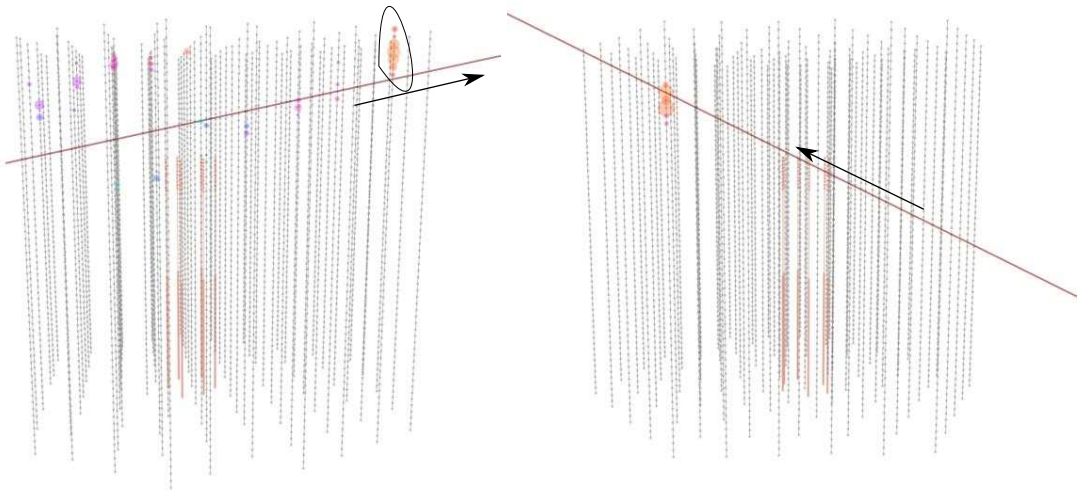

Figure 11.2.: Two events from the IceCube 79-string data with up-going MPE reconstruction and a poor (small) value in the Separation variable (see text). The first is a coincident muon event with an up-going reconstruction. The first quartile of hits is dominated by the highlighted orange hits. The Separation value is therefore negative and the event is rejected. The second event is a correlated noise event or a very low energy muon with all hits on a single string. The Separation of this event is 0 and it is rejected. Note that a full angular reconstruction of this event class is not possible - the azimuth angle cannot be determined.

Both Separation and LEmpty aim to quantify the distribution of the hits in the detector with respect to the reconstructed particle trajectory. To do this, a coordinate transformation is performed. The z-axis of the new coordinate system is aligned with the particle track and the z-coordinates z_{track} of the recorded hits in this coordinate system are used to calculate the values of Separation and LEmpty.
For the Separation, all hits are ordered in time and the center of gravity (COG) of the first and the last quartile of hits is calculated. Their positions are transformed into the new coordinate system and the Separation is defined as $z^{\text{last quartile}}_{\text{track, COG}} - z^{\text{first quartile}}_{\text{track, COG}}$. In essence, Separation is a measure of the track length. Two typical events from the IceCube 79-string data with a poor value in this variable are shown in Figure 11.2. The first is a coincident muon event with an up-going MPE reconstruction. The value of Separation for this event is negative as the MPE reconstruction seems to go backward with respect to the positions of the two calculated centers of gravity. The second is a single-string event. These events are not very valuable for point source analyses since their azimuth angle is completely degenerate. The only difference in the definition of this variable here and in previous works is the consideration of the orientation of the track with respect to the positions $\vec{r}^{\,\text{last/first quartile}}_{\text{detector coordinates, COG}}$ which improves the rejection of coincident atmospheric muon events. This is useful since the event selection developed for this stream aims at the identification of well-reconstructed up-going events.
LEmpty is a variable that has been developed based on the work presented in section 9.5 of this thesis. The variable is calculated from the coordinates $z^{150\text{m}}_{\text{track, i}}$ of all hits i within a cylindrical volume of 150 m radius around the track. The hits are sorted in increasing order of $z^{150\text{m}}_{\text{track, i}}$ and the maximum of $\left(z^{150\text{m}}_{\text{track, i+1}} - z^{150\text{m}}_{\text{track, i}}\right)$ is the value of LEmpty. In other words, LEmpty is the maximum distance along the

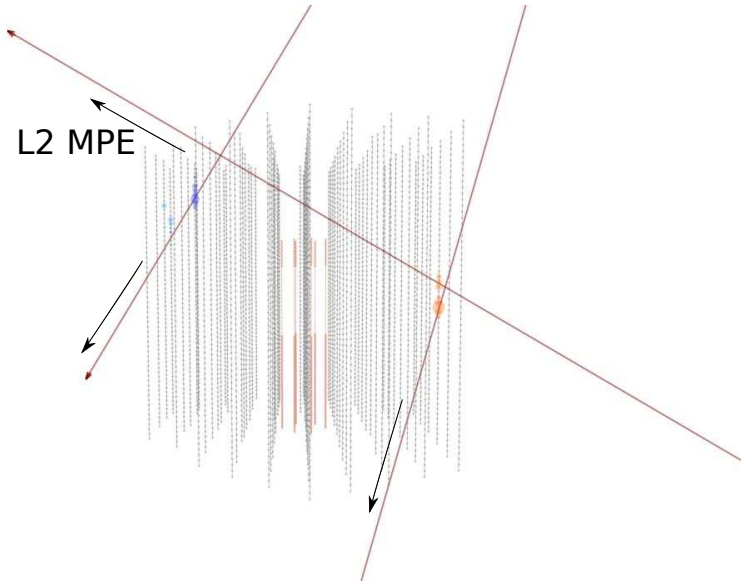

Figure 11.3.: An event from the IceCube 79-string Level 2 off-line data with a poor (large) value in LEmpty. The original Level 2 off-line MPE reconstruction is up-going but the event is in fact composed of two coincident muons. A clustering algorithm has been used to identify the two muon tracks shown in this picture.

Proposed Off-line Event Selection: Up-Going Muon Filter Stream
Direct Ellipse > 2
Separation > 0m
LEmpty ≤ 500m
plogl ≤ 12.0

Table 11.2.: Proposed event selection for the up-going muon filter stream in the IceCube 79-string Level 3 off-line processing.

reconstructed particle trajectory without any hits within 150 m of the track. The variable is primarily designed to suppress coincident events with minimal signal loss. An example of an event from the IceCube 79-strings data with a large value of LEmpty is shown in Figure 11.3. The range of reasonable cut values for LEmpty is naturally limited from below by the spacing of the strings in IceCube.
The event selection for the up-going ($\theta^{\mathrm{MPE}} \geq 90°$) muon stream is summarized in Table 11.2. The cuts have been developed on experimental data which is dominated by atmospheric muons and on signal simulation. The majority of the rejected background is removed by the Direct Ellipse cut. While it would have been possible to achieve the same reduction in the data rate with a similar signal efficiency at high energies with a stronger Direct Ellipse cut alone, the additional cuts on LEmpty, Separation and plogl allow to reject more coincident muon events and keep more low-energetic atmospheric neutrino events instead.
The performance of the cuts has been evaluated on experimental data, signal and background simulation. The results are summarized in Table 11.3. In order to evaluate the performance, simulated data based on the IceCube-86 geometry and re-triggered to the IceCube-79 configuration has been used. Updated studies show no significant changes in the signal efficiency [Gro11, Sch11b]. For comparison, the IceCube 59-strings Level 3 off-line processing which dealt with a smaller detector applied a less stringent

Event Type	Cut Efficiency w.r.t. L2	Event Rate after Cuts
μ background (data)	0.13	0.9 Hz
μ background (sim)	0.14	0.7 Hz
coincident μ background (sim)	0.06	0.2 Hz
atmospheric ν (sim)	0.77	7 mHz
E^{-2} ν (sim)	0.86	–
E^{-2} ν, within 3° of MC truth (sim)	0.99	–
E^{-3} ν (sim)	0.79	–
E^{-3} ν, within 3° of MC truth (sim)	0.98	–

Table 11.3.: Efficiency of the event selection for the up-going muon stream in the IceCube 79-string Level 3 off-line processing. The event selection is capable to keep 77% of the up-going atmospheric neutrinos and favors well-reconstructed events. The rate disagreement between data and background simulation is about the same size as at the on-line filter level.

background suppression and kept a similar rate of data. Despite this, the signal efficiency of the IceCube 59-strings Level 3 off-line event selection was lower. There, an efficiency of 74% (IceCube 79-strings, this work: 77%) was achieved for up-going atmospheric neutrinos selected by the on-line filter. For up-going E^{-2} neutrinos, the efficiency there was 76% (IceCube 79-strings, this work: 86%) [BSW10]. The presented event selection therefore improves the data reduction as well as the neutrino efficiency significantly with respect to the previous year's Level 3 off-line filter. 98% of the events which are reconstructed within 3° of the MC truth are retained in this work for an E^{-3} neutrino signal spectrum. The remaining 2% are primarily lost with the Direct Ellipse cut because they do not have a single direct hit in the detector. It is thus very unlikely that any analysis that aims to select well-reconstructed events would have been able to save these events at later stages of the event selection. The fraction of coincident events in the muon background decreases from 64% at Level 2 to 28% at Level 3.
The efficiency of the first up-going muon stream off-line event selection is characterized also in Figure 11.4. The best efficiency is reached above 10 TeV and well-reconstructed events are favored over events with a poor reconstruction. Finally, we have studied if the applied event selection introduces a bias in the zenith angle distribution and obtained that this is not the case. The signal acceptance is uniform in the zenith angle.

Down-Going Muon Filter Events

The on-line Muon filter [Bak09] for down-going events is optimized for very high energies. The selection of events from the DeepCore filter which targets up- and down-going low-energy events will be discussed later. In the Muon filter, a zenith-dependent cut on the total detected charge is used to select events. Previous southern sky point source analyses such as [AAA+11i] have applied strong, zenith-dependent energy cuts[1] at analysis level to suppress the down-going muon background. While we are currently mining to improve the background rejection in the southern sky, it is unlikely that the resulting event selection will be able to keep events down to 1 TeV at all zenith angles - the down-going muon background is too large. We can therefore safely adopt a zenith-dependent energy cut to achieve a first suppression of the background. The data rate of events that pass the Muon filter and have a down-going MPE reconstruction in the Level 2 off-line processing is about 27 Hz while an acceptable rate for further processing is 2 Hz[2].

[1] For geometrical reasons, the background is in principle largest for vertical down-going events.
[2] A higher rate of down-going events than up-going events is accepted for two reasons: First, we will apply more additional reconstructions for up-going events than for down-going events. Secondly, the event selection for the southern hemisphere

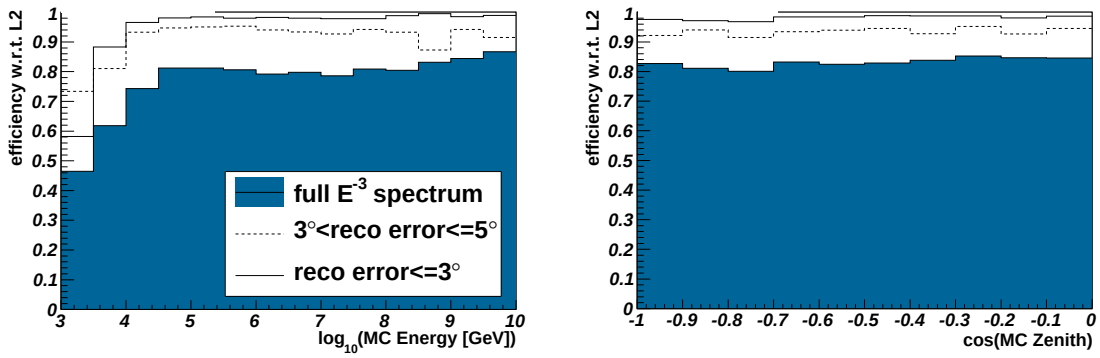

Figure 11.4.: Efficiency of the event selection in the IceCube 79-strings Level 3 off-line processing for up-going muon filter events. The cuts reach their best efficiency above 10 TeV and present a uniform acceptance in zenith. Well-reconstructed events are favored by the cuts. In an E^{-3} spectrum, 98% of all events that are reconstructed within 3° of the MC truth direction are kept.

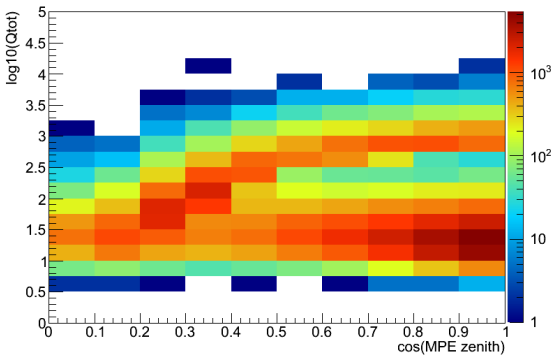

Figure 11.5.: The total charge (Qtot) is plotted against the zenith angle of the Level 2 MPE reconstruction for Muon filter events from the IceCube 79-strings Level 2 data. Despite the fact that a zenith dependent charge cut is applied as part of the on-line filter (see Table 11.1), there is a significant fraction of events with down-going reconstruction and low values of the total charge. These are events that were reconstructed as up-going with the on-line reconstruction and passed the up-going branch of the Muon filter.

Figure 11.5 shows the dependence of the total charge from the zenith angle obtained in the Level 2 off-line processing for Muon filter events with a reconstructed zenith angle above the horizon. The color scale represents the number of events in each bin. Within the Level 2 off-line processing, a different hit cleaning has been applied than on-line at the South Pole. This hit cleaning applies a different time window cleaning as well as a reduction of isolated hits, see also above. The differences in the hit cleaning are largest for coincident muon events or events with a contribution of noise. For a considerable fraction of these events, the more stringent hit cleaning of the Level 2 off-line processing eliminates the noise or the contribution of the second muon. As a result, more than two thirds of the events that have been reconstructed as up-going with the South Pole hit cleaning, are now correctly reconstructed as down-going in the Level 2 off-line processing but are still kept in the data stream. The reconstruction shown in Figure 11.5 is based on this new hit cleaning. Despite the fact that a charge cut was applied in the

is less mature than for the up-going region and we want to leave enough room for improvements.

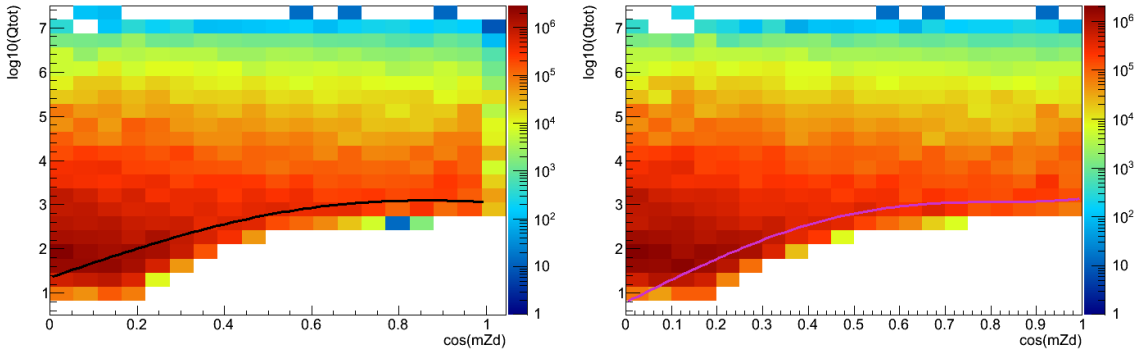

Figure 11.6.: Two alternative cuts on the total charge for the down-going muon stream: Shown is the distribution of the total charge in data in dependency of the reconstructed direction. In both of the plots, the on-line filter charge cut has been re-applied with respect to the L2 off-line MPE reconstruction. In the left plot, a charge cut is fit to to the data to keep approximately 2 Hz of data with a uniform distribution. In the plot on the right, an additional set of quality cuts has been applied to the data before an alternative charge cut was fit to the remaining data in the same way. This cut is used in the Level 3 processing.

down-going sector of the on-line processing, there is now a large fraction of events with low total charge. This is a direct consequence of the often large differences in the reconstructed zenith angle obtained in the off-line and in the on-line processing. A potential component of high-energy signal neutrinos in this low charge sector is very small. The first step in the development of the down-going high-energy event selection has therefore been to reapply the charge cut from the Muon filter (see Table 11.1) with respect to the MPE reconstruction that has been performed in the Level 2 off-line processing. This cut reduces the data rate by almost a factor of three to about 10 Hz and allows to keep 91% of the down-going neutrinos in an E^{-2} spectrum that passed the on-line filter. For neutrinos that are reconstructed within 3° of the MC Truth direction, the passing rate of this cut is 99% [3] An E^{-2} neutrino spectrum is used to benchmark the performance in this event stream has it is designed to search for hard spectra neutrino sources.

At this stage, the data already contains a considerable fraction of background events that are indistinguishable (down-going single muon events) or almost indistinguishable (down-going bundles of muons) from the signal and further energy cuts represent an easy way to suppress them if the event selection is targeted towards very high neutrino energies. In the course of the development of the event selection, we have studied three different parametrizations of a zenith-dependent energy cut.

All three considered cuts are designed to keep a data rate of about 2 Hz and to distribute this rate of events approximately uniformly across the southern sky. The first option that is considered is the application of a zenith-dependent charge cut. This cut is illustrated in Figure 11.6 on the left. The second alternative is to first apply the quality cuts of the up-going Muon Level 3 stream on the down-going data and to subsequently apply a different zenith-dependent charge cut, shown in Figure 11.6 on the right. Finally, we consider to apply a softer version of the zenith-dependent energy cut that has been applied in the previous year's point source analysis [Agu11]. This cut is based on the MuE energy reconstruction [Chi08]. To reach about the desired level of data reduction, the cut value at each zenith angle is scaled down by a factor 0.85.

The performance of these three cuts is compared in Table 11.4 and Figure 11.7. The efficiencies quoted in Table 11.4 are given with respect to the Level 2 data while the numbers in Figure 11.7 have been calculated with respect to an event selection where the charge cut of the on-line filter has already been

[3] For the perspective, in the previous year's point source analysis[Agu11], only 5-10% of the neutrino events that were selected in the second off-line processing step have been kept at the analysis level.

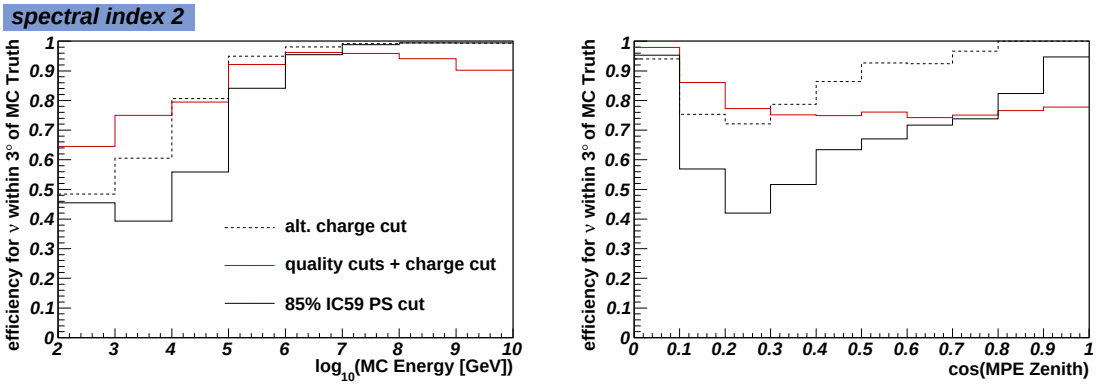

Figure 11.7.: Efficiency of three alternative cuts for the down-going region of the muon stream versus energy (left) and reconstructed zenith angle (right). The efficiencies are given with respect to the event selection that is obtained after the zenith-dependent charge cut of the on-line filter has been reapplied to the data with the Level 2 off-line MPE reconstruction as reference. The combination of a charge cut with the same quality cuts as for the up-going muon stream is chosen as a cut for the Level 3 off-line processing.

reapplied with the Level 2 MPE reconstruction as reference. All three cuts keep a similar amount of data. If integrated over the whole spectrum and the whole zenith region under consideration, the signal efficiency for E^{-2} neutrinos is very similar in the three different event selections. With 64% to 66%, it is considerably lower than for the up-going stream.
The left plot of Figure 11.7 shows the energy dependency of the efficiency of the three considered cuts. The application of quality cuts on the reconstruction reduces the efficiency for events above 10 PeV but allows to keep more events at lower energies. The degradation of the efficiency at the highest energies is not considered as a problem here. It is caused mainly by the requirements of the Direct Ellipse cut, i.e. the event needs to have at least two channels with direct pulses to pass the quality cuts. All previous southern sky point source analyses with IceCube [AAA$^+$09a, AAA$^+$11i, Agu11] have applied quality cuts at analysis level, including cuts on the direct length of the event. Also the work presented in Chapter 11 of this thesis explores the use of the direct length or the number of direct channels as cut parameter at later event selection steps. It is therefore to be assumed that the events that are removed through the application of quality cuts on the event topology and the reconstruction would in any case be removed at later stages by any analysis that aims to select events with a good angular reconstruction.
The zenith dependency of the three considered cuts is shown in Figure 11.7 on the right. The combination of the quality cuts with the charge cut has the highest efficiency around the horizon. As all previous southern sky point source analyses with IceCube [AAA$^+$09a, AAA$^+$11i, Agu11] have been most sensitive

Cut	Data rate	Efficiency for E^{-2} ν	Efficiency for E^{-2} ν, 3° of MC Truth
total charge	2.1 Hz	0.66	0.67
total charge + quality cuts	2.2 Hz	0.67	0.84
MuE Energy	2.1 Hz	0.64	0.67

Table 11.4.: Comparison of three alternative event selections in the high-energy down-going muon stream. The two first options use zenith dependent cuts on the total charge and are both illustrated in Figure 11.6, the third is a softer version of the zenith-dependent energy cut applied in [Agu11].

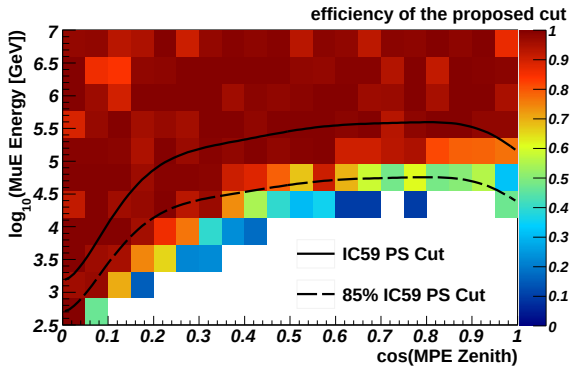

Figure 11.8.: Efficiency of the Down-Going IC79 Level 3 Cuts versus MuE Energy and Zenith

around the horizon and considerably less powerful at smaller zenith angles, we consider the horizontal region as the most important one and the combination of quality cuts with a charge cut is chosen for the Level 3 off-line event selection. The precise parametrization of the cut is

$$\log\left(\text{total charge}\right) \geq 1.05 \cdot \left(0.755 + 4.885 \cdot \cos(\theta) - 4.778 \cdot \cos(\theta)^3 + 2.134 \cdot \cos(\theta)^5\right) \qquad (11.2)$$

where θ is the zenith angle of the event as reconstructed with the Level 2 off-line MPE reconstruction. Finally, the efficiency of the proposed cut is set into perspective with the zenith-dependent energy cut that has been used in the point source analysis of IceCube 59-strings data. Figure 11.8 shows the efficiency of the proposed cut for well-reconstructed neutrino events in dependency of the reconstructed zenith angle and the MuE energy estimate. The energy cut of [Agu11] is shown as well as the softer version of this cut that has been considered for the event selection developed here. Note that in [Agu11], the illustrated cut has been combined with strong cuts on the direct length and the angular uncertainty estimator paraboloid σ. Figure 11.8 shows no indication of any alarming inefficiency in the region that is potentially of interest to analyses such as the one in [Agu11].

Notes on Neutrino Events with a Coincident Muon

In the previous sections, we have discussed the rejection of coincident atmospheric muon events. In principle however, it is not only possible that two atmospheric muons reach the detector at the same time but also that a neutrino is accompanied by a randomly coincident muon. Figure 11.9 shows an event from the IceCube 79-string data with this event topology. The up-going neutrino candidate enters the detector from below. As the size of the detector grows, the number of events with topologies like this increases. This event topology is not taken into account in the standard simulation. Dedicated simulation that allows to study these events is available now but was not ready yet when the event selection for the off-line processing was first developed. Recent studies [Kur11, Gro11] have shown that the fraction of atmospheric neutrinos with a coincident muon is about 8% for neutrinos with energies above ~100 GeV which are selected by the Muon on-line filter. Events like these pose two problems to the event selection and processing:

- The probability that such an event is rejected by the cuts developed above is high. The cuts are particularly designed to efficiently reject events of a similar topology that are composed of two atmospheric muons as these constitute a major background.
- Even if the event was kept by the event selection, the previously applied off-line reconstruction is not useful and the event will be rejected once stronger cuts on the quality of the reconstruction are made.

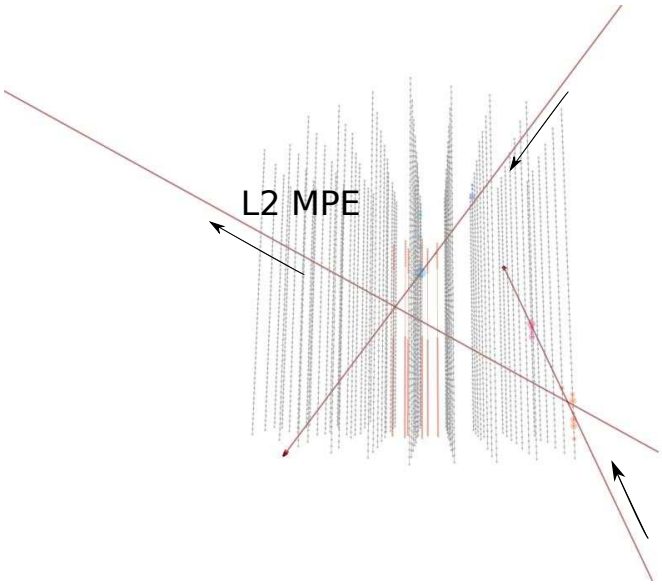

Figure 11.9.: A neutrino candidate event from the IceCube 79-string experimental data that is accompanied by a down-going atmospheric muon. A clustering algorithm has been used to identify the neutrino and muon tracks shown in this picture.

The same problems have existed already in previous analyses with the only differences that the detector is now larger and that the rejection of coincident muon events has been improved in this work with respect to the previous years. The approach to avoid a strong degradation of efficiency for coincident neutrino-muon events is therefore:

1. Select a sample of events that are likely to belong to this class of events.
2. Apply a clustering algorithm to find particle candidates.
3. Perform reconstructions on each of the obtained particle candidates.
4. Apply the Level 3 off-line event selection on the new reconstructed particles.

To this aim, we have studied the clustering algorithm Topological Trigger [Chi11]. The algorithm is simple and can achieve a very good separation of coincident particles. The algorithm considers two hits as topologically connected if all of the following conditions are fulfilled:

- The difference in depth between the two hits is smaller than a configurable distance $ZDOMDist$. The distance is given in units of the nominal DOM spacing on standard IceCube strings.
- The distance between the two hits in the x-y-plane is smaller than $XYDist$. The value of this parameter is given in meters.
- A time residual is defined as $dt - \frac{dr}{c}$ where dt is the difference between the two hit times, dr their spatial distance and c the speed of light. Two hits are connected if this time residual is smaller than a configurable time $TimeCone$.

The output of the algorithm are one or more sets of hits. Based on these, new reconstructions can be applied. Topological Trigger has already been used in the off-line processing of the IceCube 59-strings data [BSW10]. The priority there was to reject the coincident muon background on the base of additional reconstructions. Consequently, aggressive settings have been chosen for the parameters of the clustering algorithm. The chosen values were $XYDist$ = 300m, $ZDOMDist$ = 30 (in units of the vertical DOM spacing) and $TimeCone$ = 450ns.
If the clustering algorithm Topological Trigger is applied to IceCube 79-strings atmospheric muon simulation with these settings, 86% of the events with a second coincident muon are divided into at least two parts but also 26% of the single muon events are split. The splitting of single particle events into

several parts becomes stronger with higher energies. This is caused by the dust layer in the ice, see Chapter 5. At higher energies, the length of the muon trajectory increases and it is more likely that an event traverses the dust layer, leaving hits on both sides of it. These events are often split precisely at the dust layer if aggressive settings are used in the splitting algorithm. This behavior has been studied in detail in the work of [Sch11a]. To avoid the splitting of single atmospheric muon and in particular single neutrino induced muon events, the parameters of the clustering algorithm have been reevaluated. With the settings obtained here, which are $XYDist$ = 300m, $ZDOMDist$ = 15 (in units of the vertical DOM spacing) and $TimeCone$ = 1000ns, the algorithm still separates 77% of the simulated coincident muon events but splits only 2% of the single muon events. The performance of the splitting has also been verified by an extensive study of event displays that have been obtained from IceCube 79-strings experimental data. Examples are shown in Figures 11.3 and 11.9. The same settings for the clustering algorithm have also been used in an off-line processing for WIMP analyses with the IceCube 79-string data [DS11].
Since the application of Topological Trigger and all subsequent reconstructions is too CPU extensive to be applied to all events, we restrict their application to those events that are more likely to show the topology of a coincident event. These events are selected from the Level 2 off-line data before further event selections are applied. Based on the work in this thesis and on the studies presented in [Kur11] and [Gro11], two classes of events are selected to this means:

1. Events with LEmpty≥ 250m. Large values of this parameter indicate that a coincidence might be present and that the spatial separation between the particles might be large enough to separate them[4].
2. Events for which more than eight pulses have been removed in the time window cleaning. The hit cleaning of the Level 2 off-line processing includes a time window cleaning that can at times remove a significant fraction of the neutrino if a coincident muon is present. Similarly, it can also remove a part of the muon but leave enough hits to distort the reconstruction. These events are identified by the difference in the number of pulses in the time window cleaned pulse series and the non-time window cleaned pulse series.

For the events listed above, Topological Trigger is applied to the pulse series without previous time window cleaning and the resulting particle candidates are reconstructed. With these settings, the efficiency for neutrino events with a coincident muon is improved and is on average only less than 10% below the efficiency for single neutrino events.

DeepCore Filter Events

In addition to the events from the Muon filter, also events from the DeepCore filter are presently investigated to be used for the All-Sky point source analysis started here. The aim is to select a sample of neutrino candidates which can be well-reconstructed and which have the interaction vertex within a fiducial volume inside the detector. The depth of the vertex z_{vertex} measured from the center of the detector and the radial distance r_{vertex} of the vertex to the z-axis of the IceCube coordinate system are available in the simulation and are used to define the signal region for the event selection. In this first event selection, a cylindrical fiducial volume of $z_{vertex} \leq -200.0$m and $r_{vertex} \leq 200.0$m has been considered. If necessary for the background rejection, a smaller fiducial volume can be chosen at later stages of the analysis. As well-reconstructed events are preferred for point source analyses, we aim to achieve the best efficiency for these. Events which are reconstructed within 5° of the MC truth are used to benchmark the signal efficiency of the event selection. A SPE fit with four iterations based on the DeepCore pulse cleaning described above is used as reconstruction.
A first problem is that the simulation of low-energy events is still under improvement. In fact, the data rate at Level 2 is ∼17 Hz, exceeding the event rate expected from MC simulations by a factor

[4]Topological Trigger can only distinguish particles that are separated in space or in time.

Event Type	Cut Efficiency w.r.t. L2
μ background (data)	0.06
E^{-3} ν, $z_{vertex} \leq -200.0$m, $r_{vertex} \leq 150.0$m, E $\geq$ 100GeV, within 5° of MC truth	0.98
E^{-3} ν, $z_{vertex} \leq -200.0$m, $r_{vertex} \leq 150.0$m, E $\geq$ 50GeV, within 5° of MC truth	0.97
E^{-3} ν, $z_{vertex} \leq -200.0$m, 150m $\leq r_{vertex} \leq 200.0$m, E $\geq$ 50GeV, within 5° of MC truth	0.95

Table 11.5.: Efficiency of the event selection for the DeepCore filter events in the IceCube 79-string Muon Level 3 processing.

two. This discrepancy is to a large extent owned to the incomplete simulation of noise in the detector [Cab11, Sec11]. Pure noise events are characterized by a low number of channels and as a first cut, a cleaning cut is therefore applied to the data, requiring that at least eight DOMs were hit. A cut at plogl=$\frac{-\text{SPE logl}}{\text{NCh}-3.5} \leq 8.8$ favors well-reconstructed events. Finally, cuts on the reconstructed vertex position are used to suppress the muon background.

To estimate the position of the vertex, a simple vertex reconstruction called FiniteReco [Eul08] is performed within the Level 2 off-line processing. In this vertex reconstruction, the scattering of light in the ice is neglected and it is thus assumed that light emitted at the Cherenkov angle travels directly from the reconstructed particle trajectory to the receiving DOMs. Each receiving DOM can then be identified with a position on the reconstructed track at which the light detected in this DOM has been emitted. These positions are calculated for all hit DOMs within a cylindrical volume of the track and the hits are ordered according to this position. The projection of the first receiving DOM is then used as an estimate of the position of the interaction vertex. The depth of the reconstructed vertex z^{FR}_{vertex} and the radial distance r^{FR}_{vertex} of the vertex to the z-axis of the coordinate system are used as cut parameters. For the Level 3 off-line processing, we require that $r^{FR}_{vertex} \leq 300$m and $z^{FR}_{vertex} \leq -100$m.

The remaining data rate for DeepCore events is about 1 Hz. The efficiency of these cuts for an E^{-3} signal neutrino spectrum is shown in Figure 11.10 and in Table 11.5. Only events with interaction vertex within the fiducial volume are considered in the plots in the top row of Figure 11.10. The efficiency is best at neutrino energies around 100 GeV. Note that the statistics above 10 TeV is low. The acceptance in zenith is uniform. The performance of the cuts with respect to the vertex position is benchmarked in the bottom row of Figure 11.10. In the left plot, the event sample is restricted to events with $r_{vertex} \leq 200.0$m and in the plot on the right to events with $z_{vertex} \leq -200.0$m. The efficiency for well-reconstructed events is best for events with interaction vertex within the fiducial volume that has been defined for this analysis. The plots indicate that the estimation of the radial distance of the vertex to the detector center is very poor if the event is not well-reconstructed.

At the time that this thesis is being written, the off-line processing of the IceCube 79-string data is being performed with the event selection described here and the fully processed data sample will become available within few weeks. The data from $\sim$ 33.5 days, the so-called burn sample, is already available and the zenith distribution of the events with Muon filter in this set of data is shown in Figure 11.11 and compared to simulation. The yellow band represents the statistical uncertainty of the Monte Carlo (MC) prediction. 2.3 days of atmospheric muon simulation are used in the comparison.

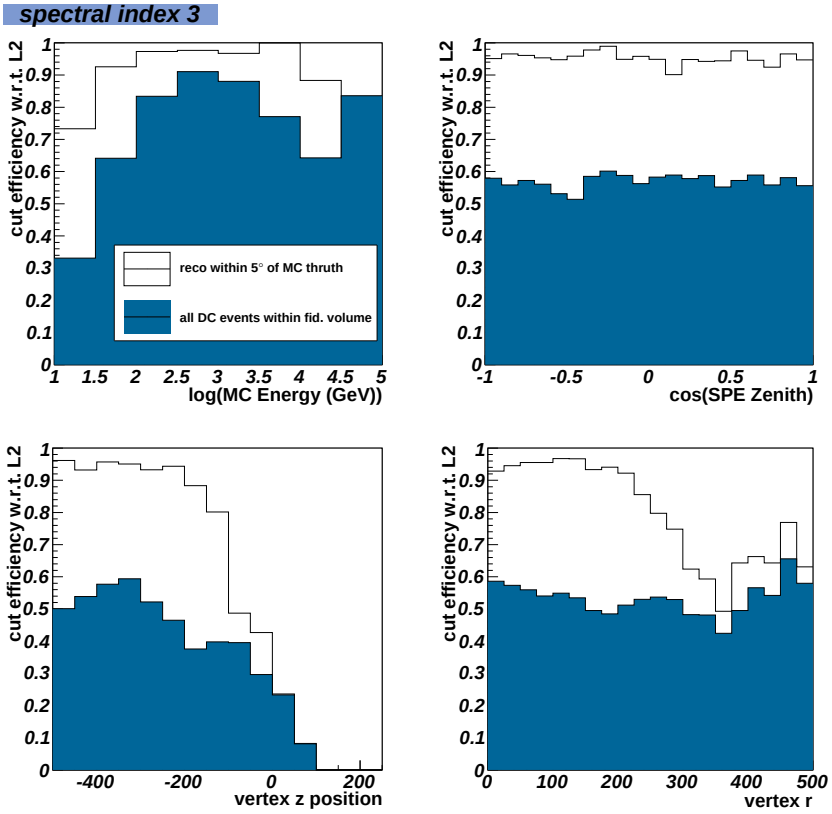

Figure 11.10.: Efficiency of the DeepCore Level 3 off-line processing event selection. In the top row, only events within the fiducial volume defined for this analysis are considered. The acceptance is uniform in zenith and reaches its best efficiency around 100 GeV. The statistics above 10 TeV is low. In the bottom row, the event selection is restricted to events with $r_{vertex} \leq$ 200.0m (left) and to events with $z_{vertex} \leq -200.0$m (right). A very good efficiency is achieved within the fiducial volume that was targeted for this analysis.

11.2. Analysis Level Event Selection - First Steps

To illustrate the potential of the IceCube 79-strings data sample, we present a first, preliminary analysis level event selection. The presented event selection uses the experience obtained in the previous chapters of this work as well as in other analyses that have been performed on the IceCube data by our collaborators. The optimization for the best sensitivity as well as a deeper study of the background are not yet completed and will both help to further improve the event selection.
As discussed above, we aim to use three different streams of events in the analysis. The main event selection in each of the three streams will be obtained with a set of Boosted Decision Trees (BDT). An introduction to BDTs is given in Chapter 4. They are chosen here for several reasons:

- Multivariate event selection techniques can improve the signal efficiency as the discrimination power of several variables is combined.
- Each BDT provides a single cut parameter, allowing for a full optimization of the discovery potential or the sensitivity.
- BDTs are powerful out-of-the-box classification algorithms that are well-suited for experiments where many but sometimes weak cut variables are available [HTF09]. This is exactly the situation in IceCube.

BDTs have been used successfully in previous IceCube data analyses (for example [AAA+11a, Ha11,

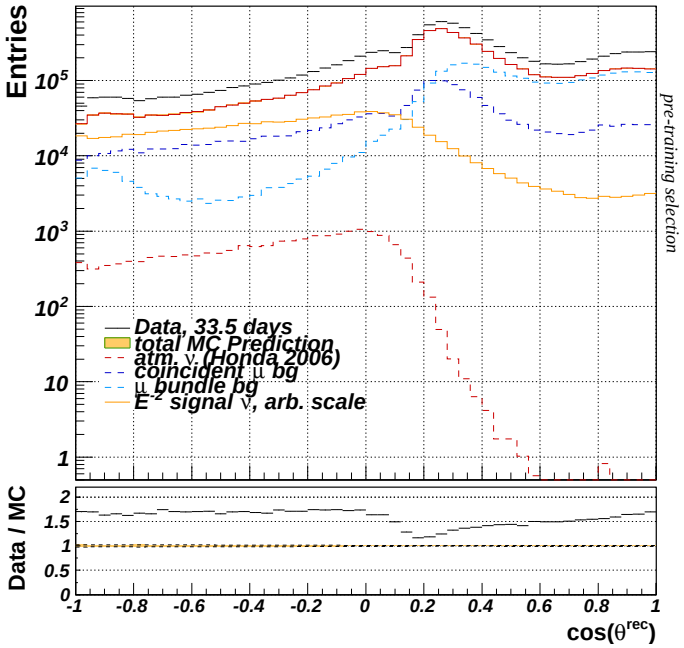

Figure 11.11.: Zenith angle distribution of the IceCube 79-strings Muon filter data after off-line processing and event selection: Data from the 33.5 days burn sample is compared to simulation. The total MC prediction includes atmospheric muons and atmospheric neutrinos. The yellow band represents the statistical uncertainty of the MC. Three different background components are highlighted for illustration purposes: atmospheric neutrinos, coincident atmospheric muon events and atmospheric muon bundle events which have more than 10 muons with energies above 500 GeV in the ice. An overall disagreement between the data and the MC prediction is observed with a ratio of up to about 1.8 between them. A similar level of disagreement is observed at on-line filter level. A possible explanation of this discrepancy is an underestimation of high-energy muons and muon bundles due to an incomplete modeling of the cosmic-ray primary composition. To circumvent this problem and to obtain a robust description of the background, the data itself is used to describe the background at all stages. The structure at $\cos(\theta^{rec}) \sim 0.2$ is more pronounced at on-line filter level and partially survives the background rejection developed in this work.

Agu11]). On the downside, BDTs are vulnerable to overtraining, as discussed also in Chapter 4. Care is taken therefore to avoid this weakness. Several different settings for the BDTs have been or will be tested in this work. The TMVA [HSS+07] analysis framework is used for all studies.

Selection of Neutrino Candidates in the Northern Hemisphere

Based on the experience obtained in the IceCube 40-strings and AMANDA analysis, the northern hemisphere has been divided into the two zenith angle regions $90° \leq \theta^{rec} < 130.0°$ and $130° \leq \theta^{rec} < 180.0°$ and two BDTs have been trained for each of the two regions. Within this work, it has thus been attempted for the first time to take into account that the vertical and the horizontal region differ in the background composition and, in this case more importantly, in the energy distribution of the signal. In the PeV range, the Earth becomes opaque to neutrinos. Very high-energy neutrinos are therefore more abundant in the horizontal region.
The same input variables are used in all four BDTs and a cut on the paraboloid σ angular uncertainty

estimator (see also Chapter 9) is applied at a value of 10° before the training is performed. In each case, experimental data is used to model the background. In this way, we obtain a robust description of the background and avoid part of the inconveniences that arise from the fact that the background simulation shows significant discrepancies from the data at the on-line filter level as well as at all stages of the off-line processing. As the signal, we consider two different neutrino spectra: a hard E^{-2} spectrum and a soft, Crab-like spectrum as in Equation 10.1 with an exponential energy cutoff at 7 TeV. The goal is to obtain a good efficiency for both high and low energies. Only signal events that are reconstructed within 5° of the MC Truth direction are used in the training phase of the BDTs.

We present the distributions of the variables that have been used in the BDTs in Figures 11.14 and 11.15. The zenith region $130° \leq \theta^{rec} < 180.0°$ is chosen for illustration purposes. The presented total MC prediction includes both atmospheric muons and atmospheric neutrinos. The yellow band represents the statistical uncertainty of the MC. The systematic and theoretical uncertainties of the simulation are not taken into account. In the analysis presented in the previous chapters of this work, the systematic uncertainties have been estimated to be around 17%, a similar systematic uncertainty can be expected here. The theoretical uncertainty on the atmospheric neutrino flux is between 7% and 25% depending on the energy. While an off-set in the event rates is observed, the distribution of the variables that have been used is well-simulated. Three different background components are highlighted for illustration purposes: atmospheric neutrinos, coincident atmospheric muon events and atmospheric muon bundle events which have more than 10 muons with energies above 500 GeV in the ice. The classification as muon bundle or coincident muon event is not exclusive; it is possible that the same event belongs to both classes. The variables that have been used for a first study of the performance are, in the same order as presented in Figures 11.14 and 11.15:

Angle between standard and high noise fit Various studies like for example [Dum09] have shown that the noise probability in the MPE likelihood (see Chapter 7) can be tuned to obtain a better reconstruction in particular for atmospheric muon events. A MPE reconstruction with a 10^6 times higher noise probability is performed as part of the Level 3 off-line processing. The angle between this and the standard Level 2 off-line MPE reconstruction can be used as a powerful cut against coincident muon events. This can be seen on the top left of Figure 11.14. This variable has not been used in previous point source analyses.

LineFit Velocity The definition of this parameter is given in Chapter 7. The variable is used here to reject cascade-like or small events. It has also been used in the work of [Agu11].

closest approach to center of gravity The distance of the reconstructed track to the charge-weighted center of gravity of the hits at the point of closest approach is expected to be very small for a neutrino event. In the presence of noise or additional coincident particles however, large distances can be observed. This variable is studied here for the first time for a point source analysis.

smoothness of all hits The smoothness of all launches is a weak cut parameter against coincident muons. A value of 0 corresponds to a uniform distribution of DOM launches along the length of the track while values -1/1 indicate a clustering at the beginning/the end of the track. The absolute value of the variable is used here.

DOMs with direct hits The number of DOMs with direct hits (NDirChannel) is an indicator for high-energy events with a good track reconstruction.

plogl here defined as $\frac{-\text{MPE logl}}{\text{NCh}-3.5}$, is a very powerful variable to select well-reconstructed events. An apparent mismatch in the shape of the distribution is caused by a transition from atmospheric muon to atmospheric neutrino dominated regions which have different uncertainties.

Separation is a measure of the track length and the definition has been given above. In this form, it is a modified version of a variable that has previously been used in WIMP analyses and in the analysis of [AAA+11a].

MPE paraboloid σ is a measure of the angular uncertainty of the reconstruction, see Chapter 7, and is used in many analyses to select well-reconstructed events and to suppress the atmospheric muon

background.

Tacc is defined as the time (in ns) to accumulate 75% of the charge in the event. It is a variable that has previously been used primarily in WIMP searches but presents a discrimination power against coincident muon events that can be used also for high-energy analyses.

log(Truncated Mean Energy / GeV) Truncated Mean [Mia11] is a new energy estimator that has been shown to have a better energy resolution towards low energies than the MuE energy estimator [Wol11] that has previously been used in all point source analyses. Energy estimators can be used to suppress a low-energy muon background.

Ztravel is a variable that has been used in WIMP analyses as well as in [AAA+11a]. It measures the vertical extension of the event by calculating the mean spread of the z-coordinates of all hits in the first quartile of hits in the event.

Finally, also the reconstructed zenith angle has been included in the BDTs. For this selection of input variables and this definition of zenith regions, the AdaBoost algorithm [FS96] has been observed to provide an excellent separation between background and signal. The distribution of the BDT scores obtained in the two different zenith regions are shown in Figures 11.12 and 11.13. The distributions of the BDT scores in the simulation agree well with the data in the peaks of the signal region. In the tails of the distribution, we observe a deficit of data with respect to the simulation that is also observed in the distribution of plogl in the bottom left of Figure 11.14. This disagreement is therefore very likely not connected to the properties of the BDTs.

The BDTs obtained through the training with two different signal spectra are combined in the preliminary event selection. For this study, cuts have been chosen to reduce the muon background contamination in the northern hemisphere to around 4%. This corresponds to about the same level of background contamination as in the analysis of [Agu11] and allows to compare the two event selections. The cuts for this region are summarized in Table 11.6. The cuts have not yet been optimized for the best sensitivity and also the selection of input variables for the BDTs is still on-going.

Zenith Region	Cuts before BDT training	Cuts on the BDT scores
$90° \leq \theta^{rec} < 130.0°$	MPE Paraboloid $\sigma \leq 10°$	BDT^{hard} score ≥ 0.144 or BDT^{soft} score ≥ 0.195
$130° \leq \theta^{rec} < 180.0°$	MPE Paraboloid $\sigma \leq 10°$	BDT^{hard} score ≥ 0.137 or BDT^{soft} score ≥ 0.185

Table 11.6.: Preliminary cuts applied on the BDT scores in the up-going region.

With these preliminary cuts, a rate of 2.2 mHz of events is selected from the experimental data. This represents an increase of a factor of 1.6 with respect to the event selection used in the IceCube 59-strings point source analysis at the same level of muon contamination [Agu11]. It is more than expected from the increase in instrumented volume. The total rate predicted by the simulation is 2.4 mHz, which is about 10% above the observed data rate. This difference is well-contained within the uncertainties of the simulation but will still be studied further. At this cut level, an efficiency of 72% with respect to the Level 3 off-line processing event selection for this filter stream is achieved for up-going signal neutrinos with an E^{-2} spectrum. The efficiency for atmospheric neutrinos is 47%. The acceptance is nearly uniform in the northern sky as can be seen in Figure 11.21. Both of these efficiencies are substantially above the efficiencies achieved in [Agu11] where a 58% efficiency was observed for up-going signal neutrinos with an E^{-2} spectrum and 28% for atmospheric neutrinos. The comparison is however not straight-forward as the signal-to-background ratio in the IceCube 59-strings Level 3 off-line processing was different than in the work presented here. The IceCube 79-strings Level 3 off-line processing event selection contains a higher fraction of atmospheric neutrino events than the one for IceCube 59-strings. The dependency of the cut efficiency from the neutrino energy and the performance of the reconstruction are shown in Figure 11.4.

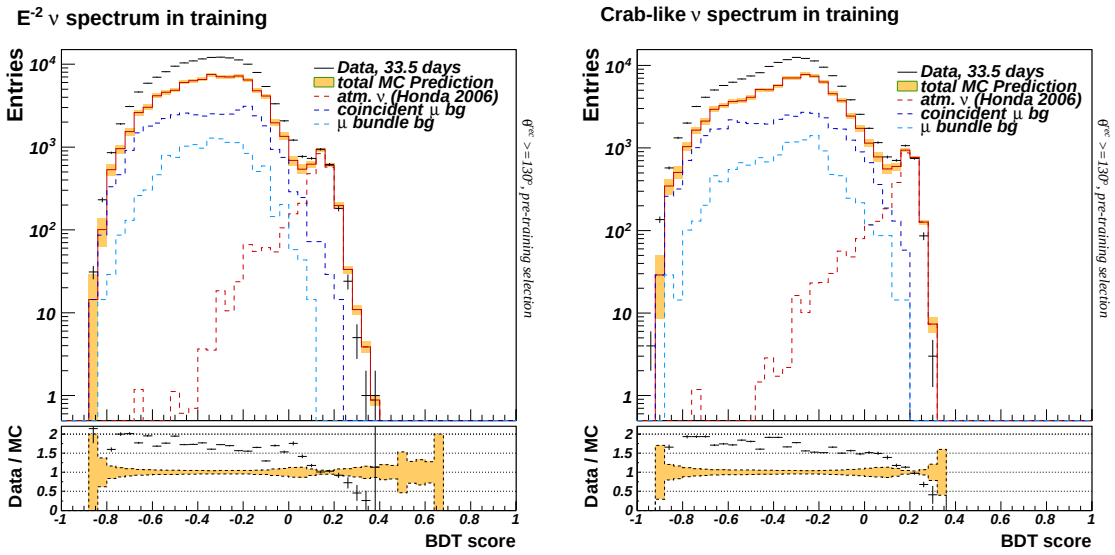

Figure 11.12.: BDT Scores for the zenith region $130° \leq \theta^{rec} < 180.0°$ obtained with training on two different neutrino spectra. An excess of the data over the background expectation in the atmospheric muon-dominated regions is observed in all distributions and at all processing levels. This discrepancy might arise from the incomplete modeling of the cosmic-ray primary spectrum. To circumvent this problem and to obtain a robust description of the background, the data itself is used in the training of the BDTs. A better agreement is observed in the high-statistics bins of atmospheric neutrino-dominated region. The excess of simulated neutrino events over the data is not only observed in this distribution but also in the neutrino dominated regions of the Level 2 off-line data (see the bottom-right plot in Figure 11.14) and is therefore very likely not an artifact of the BDT. Further investigations are on-going.

We will continue to improve the event selection before the analysis will be performed. In particular we will work further on the selection of the BDT input variables. A powerful variable to reject mis-reconstructed down-going single muon events, the Bayesian likelihood ratio (see Chapter 9) was not available at this moment but will be included in the future. Moreover, we will test if the BDTs can be improved by removing or substituting variables with strong correlations to the other variables. First tests in that direction have not yielded a better discrimination power though. Already studied variations of the BDT include the application of a principal component analysis of the input variables before the training as well as variations of the training settings.

Very High-Energy Event Selection in the Southern Hemisphere

We present here the first attempts to improve the very high-energy event selection in the southern hemisphere. The pioneering work for very high-energy southern sky point source searches with IceCube has been performed in [AAA$^+$09a]. The analysis presented there opened the sky above the horizon for IceCube through the careful selection of high-energy events by the use of rectangular cuts on six variables that are correlated with the energy or the quality of the track reconstruction. In later analyses [AAA$^+$11i, Agu11], a slightly different approach has been followed; only few variables were considered and very hard cuts have been applied before a zenith-dependent energy cut has been performed to keep an approximately uniform data rate across the southern sky. In the analysis of [Agu11], a first generation IceTop veto has been used to lower the energy threshold for vertically down-going events. In the analysis started here, we aim to apply an improved selection of well-reconstructed tracks of very high-energy

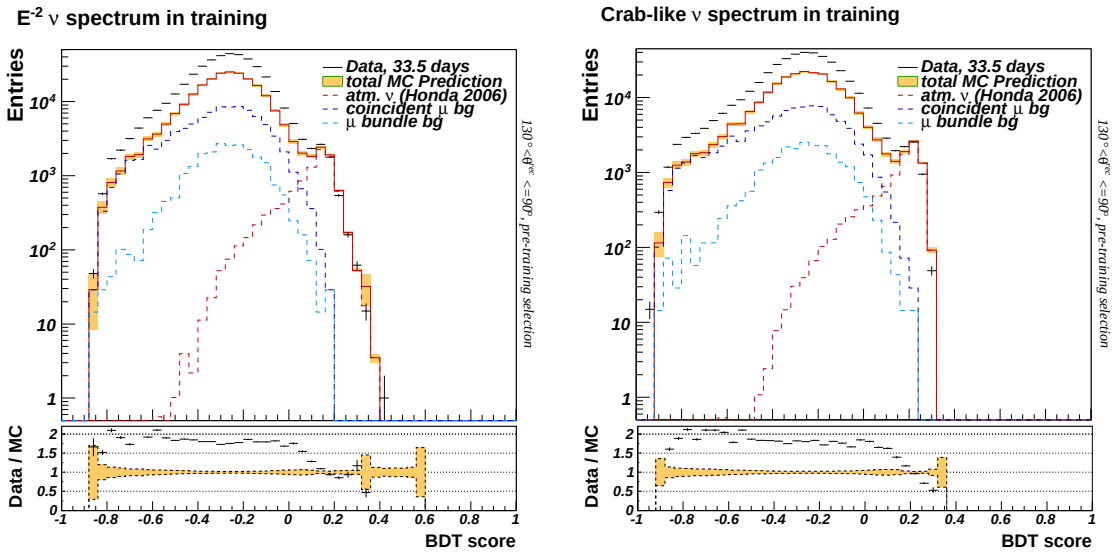

Figure 11.13.: BDT Scores for the zenith region $90° \leq \theta^{rec} < 130.0°$ obtained with training on two different neutrino spectra. An excess of the data over the background expectation in the atmospheric muon-dominated regions is observed in all distributions and at all processing levels. This discrepancy might arise from the incomplete modeling of the cosmic-ray primary spectrum. To circumvent this problem and to obtain a robust description of the background, the data itself is used in the training of the BDTs. A better agreement is observed in the high-statistics bins of atmospheric neutrino-dominated region. The excess of simulated neutrino events over the data is not only observed in this distribution but also in the neutrino dominated regions of the Level 2 off-line data (see the bottom-right plot in Figure 11.14) and is therefore very likely not an artifact of the BDT. Further investigations are on-going.

neutrino events through the use of a multivariate cut obtained with a BDT. In this way, we hope to be able to lower the energy threshold of the analysis. The selection will be completed by the use of the advanced IceTop veto described in [Auf11, ACM11].

As can be seen in Figure 11.11, the background components in the horizontal down-going region are single muons, coincident muons and muon bundles in about equal fractions. In the vertical down-going regime, muon bundles dominate the background. The contribution of coincident muons is an order of magnitude smaller. The input variables for the BDTs are selected for their discrimination power between signal neutrinos and at least one of the described background components.

For the preliminary event selection presented here, two BDTs have been trained. The first is obtained for the zenith region $0° \leq \theta^{rec} < 75°$ and the second for the region $75° \leq \theta^{rec} < 90°$. Experimental data has been used to model the background in both cases and simulated E^{-2} neutrinos that are reconstructed within 5° of their MC truth direction are used as signal.

For the moment, the same twelve variables have been considered in each of the two BDTs. For illustration, their distributions after a cut on the paraboloid σ angular uncertainty estimator (see also Chapter 9) has been applied at a value of 10°, are shown in Figures 11.18 and 11.19 for the zenith region $0° \leq \theta^{rec} < 75°$. A description of the variables is given here, in the same order as in the Figures:

Charge Ratio The charge ratio is here defined as $\log\left(\frac{Q_{max}^{DOM}}{Q_{total}}\right)$, where Q_{max}^{DOM} is the maximum charge, i.e. amount of light detected in a single DOM while Q_{total} is the total charge in the event. The variable presents a discrimination power against single muons and coincident muon events. It has not been used in any point source analysis before but in the work of [Ber11].

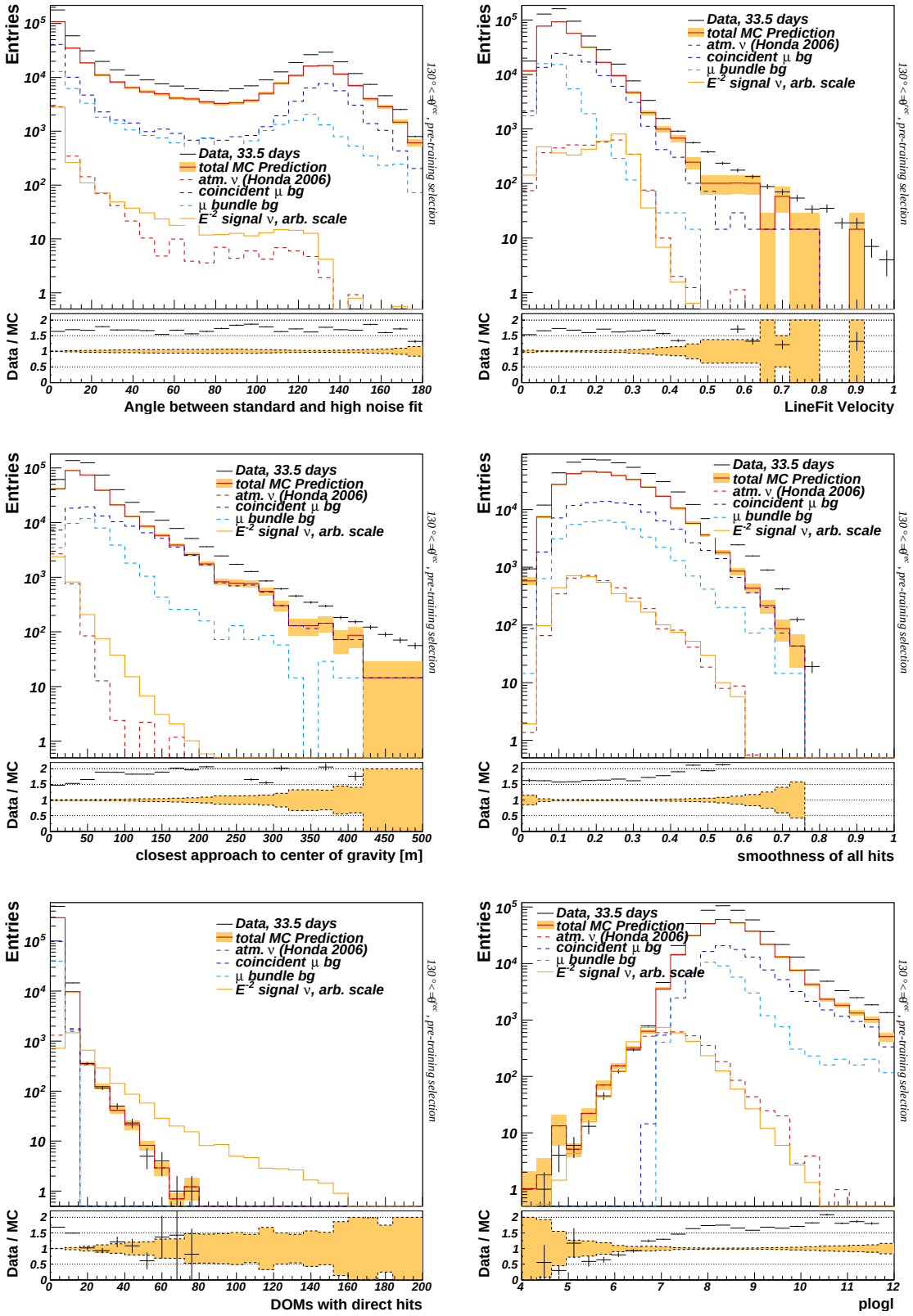

Figure 11.14.: BDT input variables for events in the zenith region $130° \leq \theta^{rec} < 180.0°$.

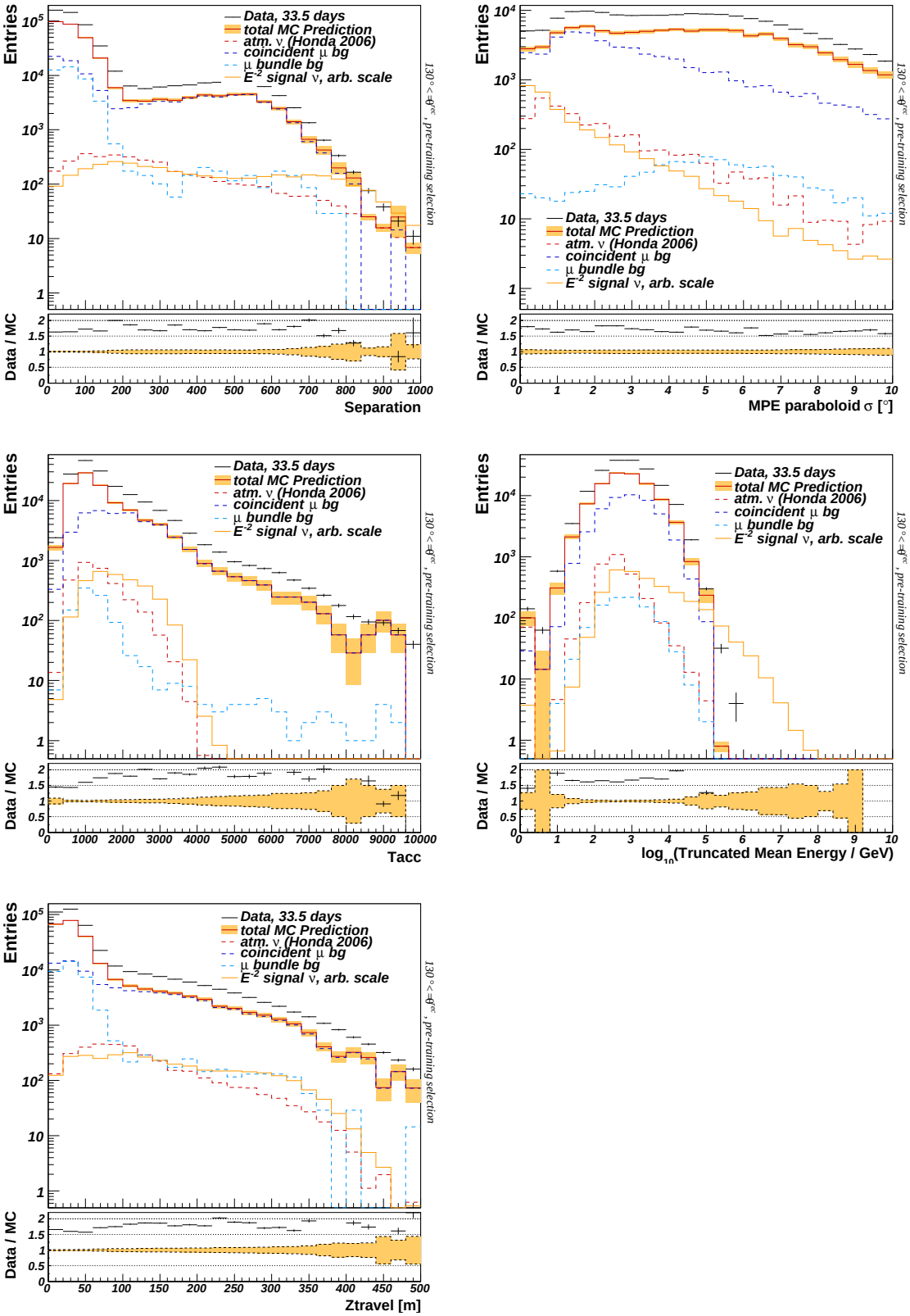

Figure 11.15.: BDT input variables for events in the zenith region $130° \leq \theta^{rec} < 180.0°$.

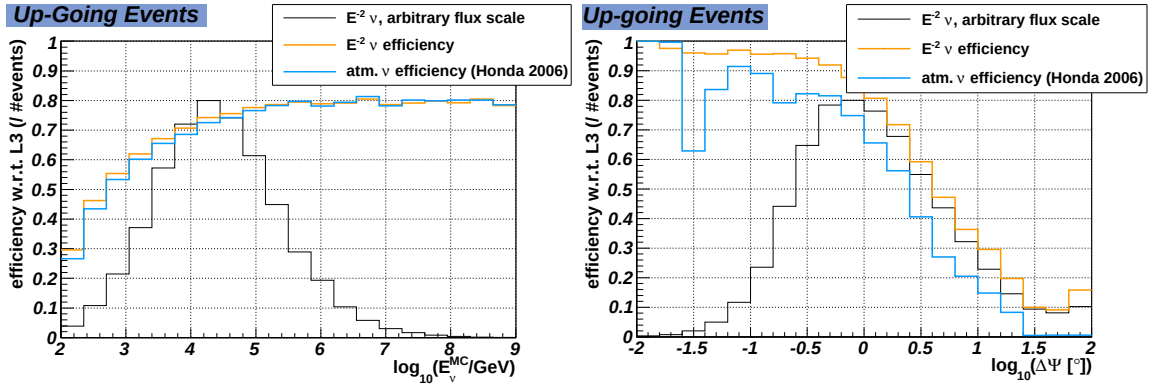

Figure 11.16.: Efficiency of the preliminary IceCube 79-strings analysis level event selection in the up-going region in dependence of energy (left) and the angle between the MC truth and the reconstructed direction.

Center of Gravity, z The depth of the charge-weighted center of gravity of the hits presents a weak discrimination power against the muon background in the zenith region $75° \leq \theta^{rec} < 90.0°$; both data and muon simulation contain a small excess of events at the very top of the detector.

LineFit Velocity The definition of this parameter is given in Chapter 7. The variable is primarily useful to identify cascade-like events. However, it is also observed that coincident muon events in the zenith region $75° \leq \theta^{rec} < 90°$ produce a tail towards higher values in this variable.

MuEX Energy Energy estimators can efficiently reduce the background in the southern hemisphere. Here, an improved version of the MuE energy estimator ([Chi08], see also Chapter 7), called MuEX is used. In contrast to the MuE energy estimator, MuEX takes the structure of the ice into account. The study in [Wol11] has shown an improved performance.

Mean_Square_DistTrack_ChargeWeighted The mean of the charge-weighted, squared distances of the hit DOMs to the track. This as well as the next variable have been chosen based on the work of [ACM11]. For vertical down-going events, a discrimination power against muon bundles is evident.

Mean_TimeResidual_ChargeWeighted The mean of the charge-weighted time residuals (see Chapter 7) of all pulses with respect to the track. Coincident events show a tail towards negative values. Again, for vertical down-going events, a discrimination power against muon bundles and coincident muon events is evident.

MPE rlogl The variable has been defined and discussed in Chapter 9 and selects well-reconstructed high-energy events.

MPE paraboloid σ Selects events with a small angular uncertainty.

Smoothness of all hits The absolute value of the smoothness can be used to reject a fraction of single and coincident muon events in the down-going region.

Tacc has been defined earlier in this chapter. It has a discrimination power against coincident muon events and even muon bundles that can be used for very high-energy analyses.

Zsigma-abs(Ztravel) is the difference between two measures of the depth extension of the event. Ztravel is the mean spread of the depths of all hits in the first quartile of hits in the event while Zsigma is the standard deviation of the depth off all hits. Zsigma is strictly positive while Ztravel can be negative as well. This combination of variables has never been used before as far as we know but presents a good discrimination power against muon bundles.

Distance to detector center / number of strings is the ratio of the distance of the reconstructed track to the center of the detector at the point of closest approach and the number of strings with hit DOMs. The variable is used to preferentially select events where the reconstructed track intersects

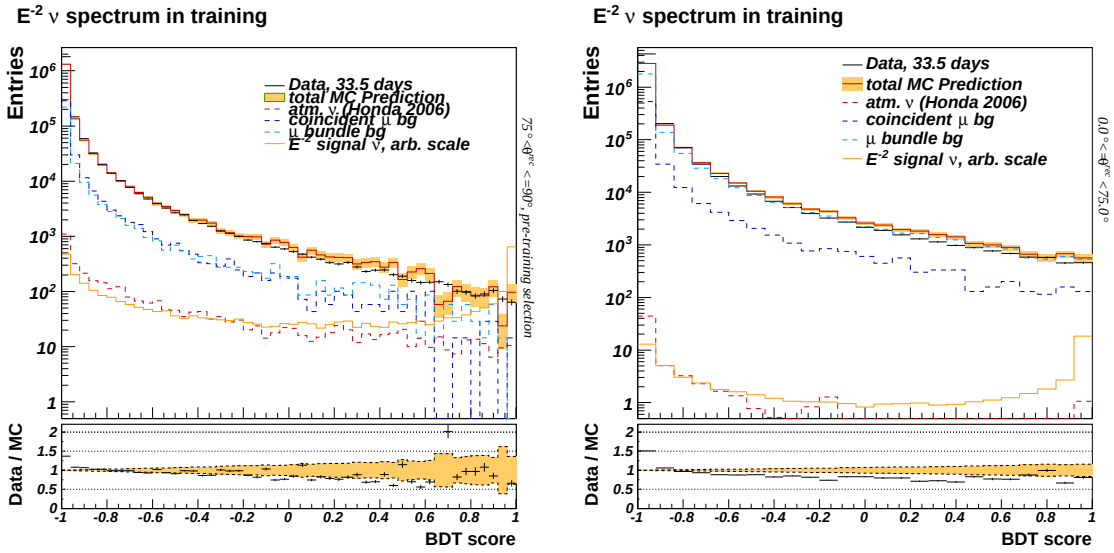

Figure 11.17.: BDT Scores for the zenith region $75° \leq \theta^{rec} < 90°$ (left) and $0° \leq \theta^{rec} < 75°$ (right).

with the detector.

As can be seen in Figures 11.18 and 11.19, the data is consistently above the expected background from simulation. In particular transitions between the different background components are not well-described in the simulation. The most likely reason for these disagreements lies in the modeling of the cosmic-ray spectrum. Further studies with dedicated background simulation that allows to study the impact of different cosmic-ray primaries are planned.

For the selection of input variables and zenith regions used here, the GradientBoost algorithm [Fri00] has a better performance than AdaBoost [FS96]. This is presumably connected to the fact that the data in the down-going region contains a higher fraction of signal-like events than the data in the up-going region. The distribution of the BDT scores in data and simulation obtained for the two zenith regions is shown in Figure 11.17. The ratio between data and simulation is approximately flat in both distributions.

As in previous southern sky point source analyses [AAA+09a, AAA+11i, Agu11], we have taken care to choose the cuts in the down-going region in such a way that a smooth transition between up- and down-going events at the horizon is guaranteed and an approximately uniform event density in the southern sky is achieved. As the density of background events is zenith-dependent, the strength of the cut to suppress the background needs to be zenith-dependent as well. We have therefore parameterized cuts on the obtained BDT scores to keep an approximately uniform event density across the southern sky. The distribution of the BDT scores in dependence of the reconstructed zenith angle in data is shown in Figure 11.20 along with the parametrization of the cut that is applied for the first studies presented here.

With these cuts, approximately 3.2 mHz of experimental data are selected across the southern sky. The ratio in the rates in the up-going and down-going region is about the same as in the IceCube 59-strings point source analysis. While this is not necessary, it facilitates the comparison of performances until the final sensitivity is calculated. The MC prediction of the rate obtained after these cuts is 3.7 mHz and thus about 16.5% above the observed rate in experimental data. The statistical uncertainty on the MC estimate is however very high as only the equivalent of 2.3 days of lifetime was available at this moment for the atmospheric muon simulation. The background estimate will be improved with higher statistics in the future. Averaged over the southern hemisphere, the presented preliminary cuts keep 40% of E^{-2} signal neutrino events with respect to the Level 3 off-line event selection presented earlier in this chapter. The zenith dependency of the cut efficiency for the whole sky is shown in Figure 11.21. An efficiency of at least 30% for E^{-2} signal neutrinos is achieved at any position in the southern sky.

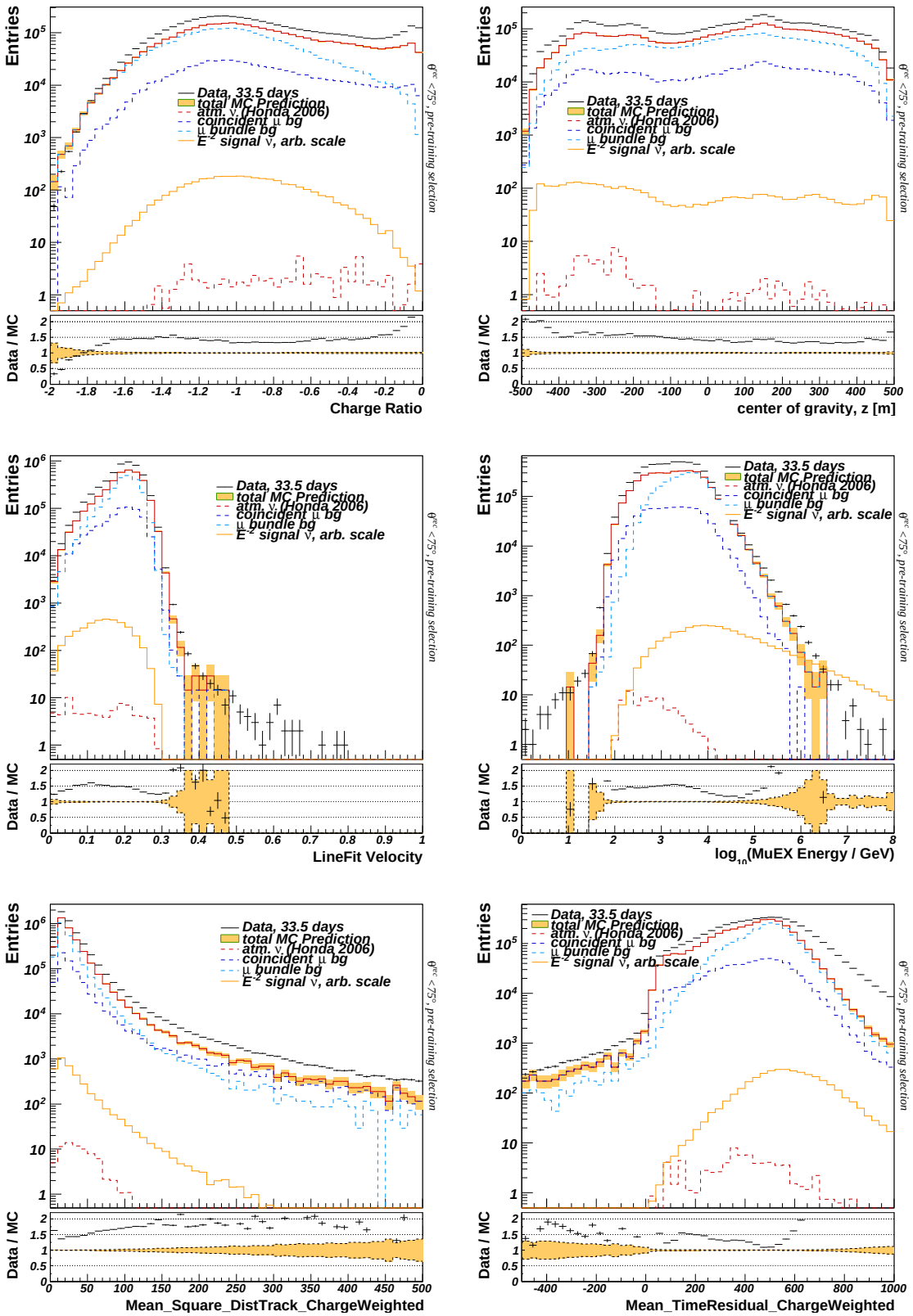

Figure 11.18.: BDT input variables for events in the zenith region $0° \leq \theta^{rec} < 75°$.

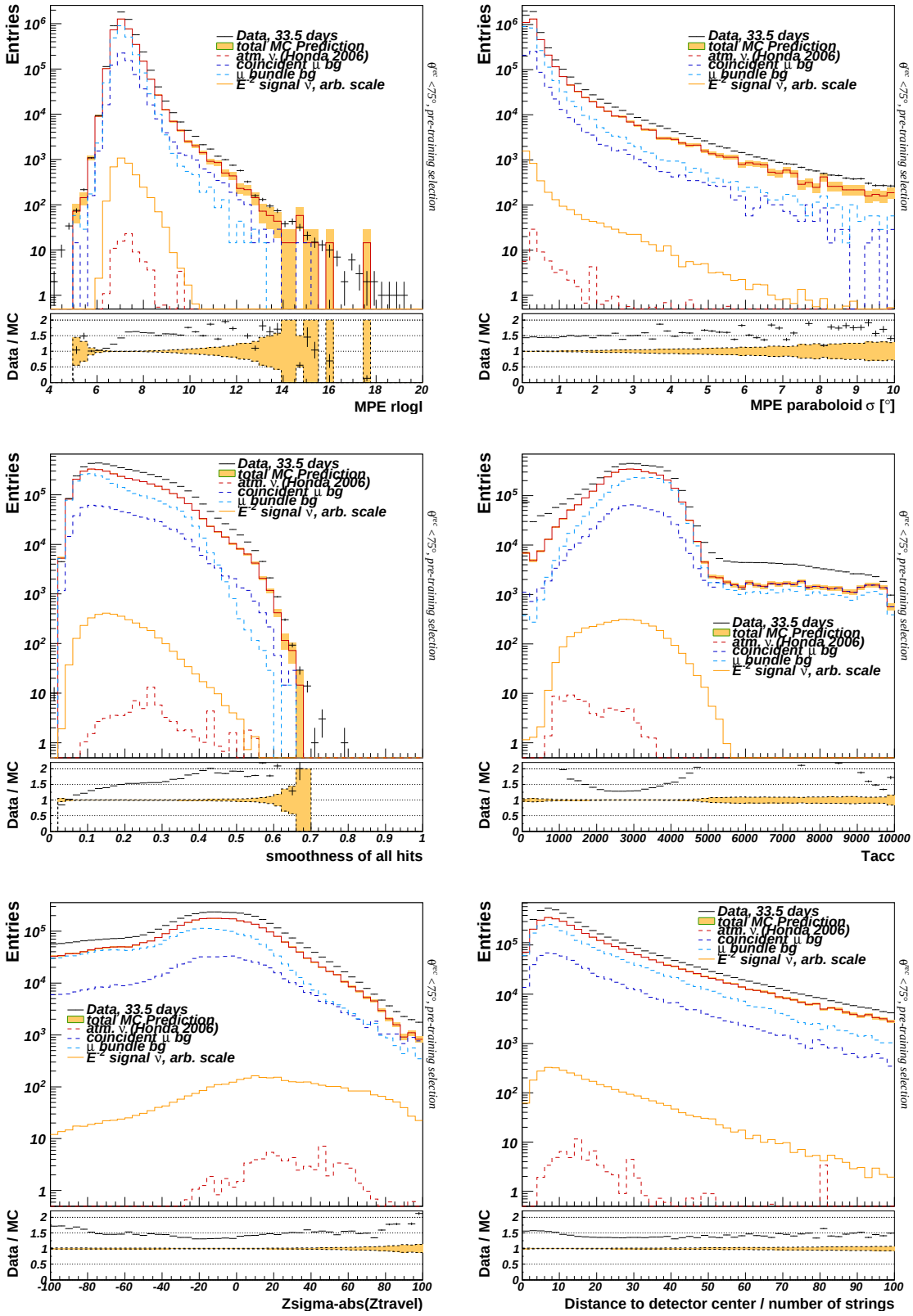

Figure 11.19.: BDT input variables for events in the zenith region $0° \leq \theta^{rec} < 75°$.

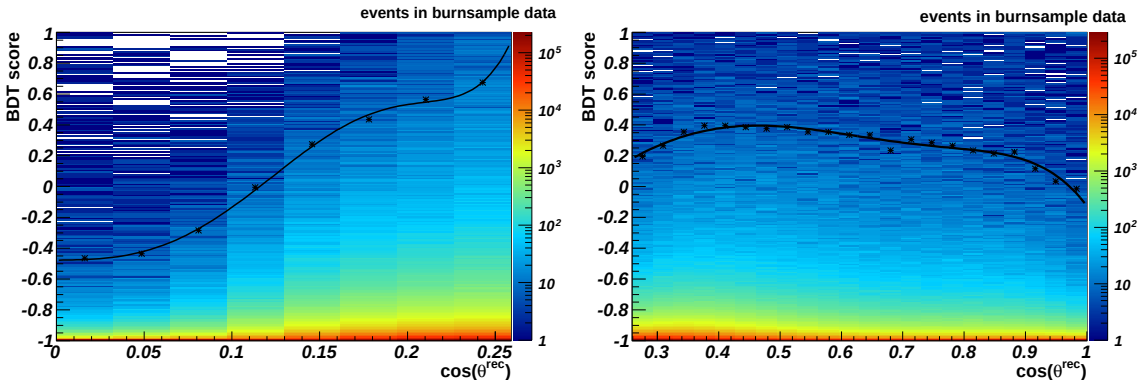

Figure 11.20.: Parametrization of the cut on the BDT scores in the zenith regions $75° \leq \theta^{rec} < 90°$ (left) and $0° \leq \theta^{rec} < 75°$ (right).

Benchmarking the Performance of the IceTop Veto

The IceTop air shower array above the IceCube neutrino telescope can be used to veto down-going muons from cosmic-ray air showers and thus further reduce the background. The method that is considered here has been developed in the context of extremely high-energy neutrino searches in [Auf11]. It is also reported in [ACM11]. The key idea is that an atmospheric muon is accompanied by a shower of particles that can produce hits in IceTop. When the direction of the muon is reconstructed in IceCube, an approximate position of the shower front can be calculated for any time. By counting the number of SLC (soft local coincidence, see Chapter 5) hits in IceTop in a time window around the expected passing time of the shower front, a veto can be defined. The veto is characterized by the chosen time window and the maximum number of IceTop hits that are accepted. As the number of particles in the shower and the lateral extension of the shower depend on the energy of the cosmic-ray primary, the veto capability is energy-dependent. Through the geometry of the detector, it is optimal for vertical down-going events. To illustrate the expected improvement in the selection of very high-energy down-going events for the All-Sky neutrino point source search, a veto time window of (-1000 ns, 500 ns) around the expected

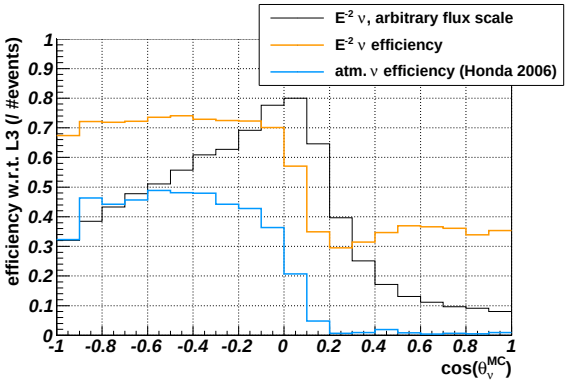

Figure 11.21.: Efficiency of the preliminary event selection with respect to the Level 3 off-line event selection. Two different neutrino spectra are considered: E^{-2} signal neutrinos and the atmospheric neutrino spectrum. For illustration purposes, we show the zenith distribution of E^{-2} signal neutrinos after the Level 3 off-line event selection in the background. The absolute scale of this distribution is arbitrary. The IceTop veto is not considered in this plot.

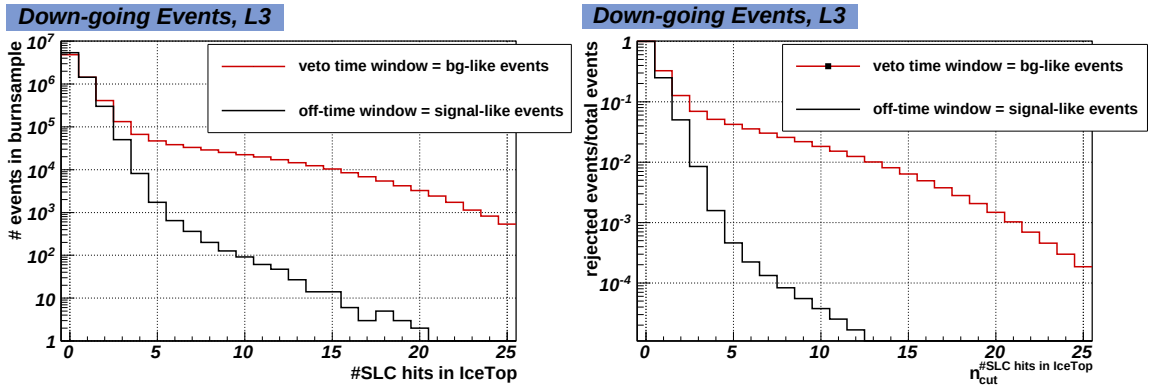

Figure 11.22.: Left: Distribution of the number of SLC hits in IceTop in the veto window and in the off-time window. Right: Background rejection power of the IceTop veto at each cut strength $n_{cut}^{\text{\#SLC hits in IceTop}}$. Events with more than or equal to $n_{cut}^{\text{\#SLC hits in IceTop}}$ hits in IceTop are rejected as air shower events. The signal loss of the same cut is quantified by the use of an off-time window and is shown here in black. All distributions shown here are obtained from experimental data. All down-going events with muon filter from the Level 3 off-line event selection are considered.

passing time of the shower front is considered. To benchmark the veto capability, we also have to characterize the probability for random coincidences between a down-going signal neutrino and SLC hits in IceTop. The best way to do this is to use a data-driven estimation. The probability for random coincidences is studied by the definition of an off-time window of the same length as the veto window where no correlated hits in IceTop and IceCube are expected. Here, an off-time window of (+3500 ns, +5000 ns) with respect to the expected passing time of the shower front is used. The performance of the IceTop veto is benchmarked in Figure 11.22. If all events with at least 5 SLC IceTop hits within the veto time window are rejected, 4% of the background can be removed while only 0.04% of the signal are lost. The veto power is zenith and energy dependent and is considerable larger for small zenith angles and high energies. The signal loss is independent of the neutrino energy and zenith angle.

11.3. First IC79 All-Sky Point Source Sample

A first All-Sky data sample has been produced to study event selections and to benchmark the expected performance of the IceCube 79-strings point source analysis outlined here. The zenith distribution of this first, preliminary data sample is shown in Figure 11.23. In the plot on the left, we have applied the cuts described above. In the plot on the right, we have applied the IceTop veto to the data and obtained a new parametrization of the cut on the BDT scores in the down-going region to keep an approximately uniform event density in the southern sky. The IceTop veto cannot be applied to the simulation as IceTop is not included there. For the study of the agreement between data and simulation, we therefore have to use the event selection without the consideration of the IceTop veto. The estimation of the signal loss of about 0.04% is however robust and presents a negligible effect.
The agreement between data and atmospheric neutrino simulation in the northern hemisphere is very good apart from a deficit of data with respect to the simulation in the region $0 \geq \cos(\theta^{rec}) \geq 0.35$. Possible reasons for this disagreement are uncertainties in the modeling of the energy spectrum of the atmospheric neutrinos and in the description of the detector or the ice. Another possible reason is that coincidences between neutrinos and atmospheric muons are present in the data but not in the simulation used here. This effect will be studied in the near future. More simulation is needed for a study of the agreement between data and simulation in the southern hemisphere and will become available soon.

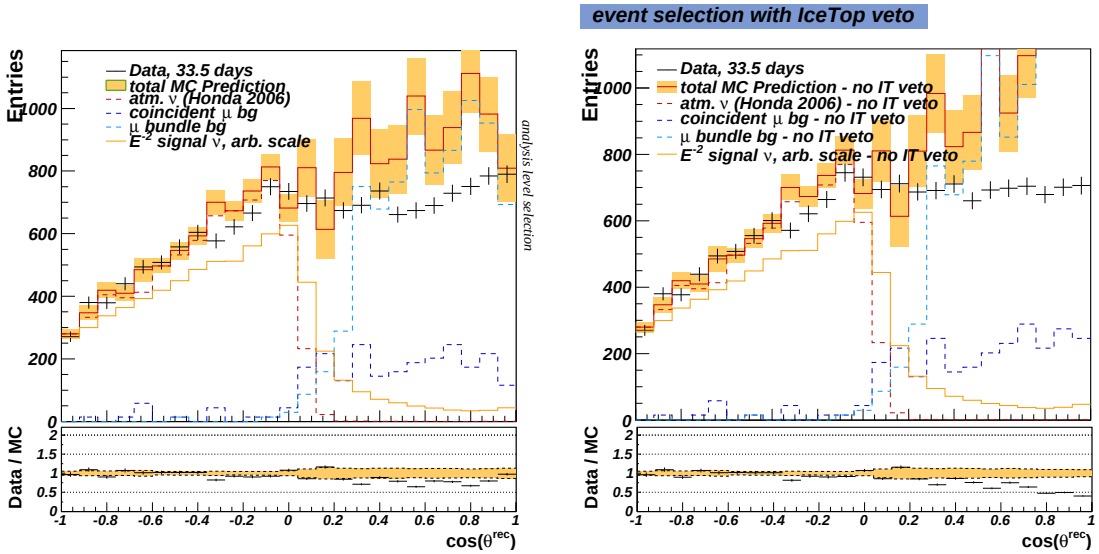

Figure 11.23.: Zenith distribution of the preliminary analysis level event selection for IceCube 79-strings without IceTop veto (left) and with IceTop veto (right).

The event distribution of E^{-2} signal neutrinos and the efficiency for these without the application of the IceTop veto is shown in Figure 11.24 as a function of the zenith angle and the neutrino energy. The IceTop veto leads to a small improvement in the selection of vertical down-going events. An E^{-2} neutrino spectrum is shown here as a compromise since it is relevant for both hemispheres with the current event selection. In the northern hemisphere, a good performance for softer spectra is obtained already now as can be seen by the high number of atmospheric neutrinos that are selected. The final event selection will be developed on the base of the work presented here and will also contain a selection of starting tracks in DeepCore that is not yet included. The analysis will therefore push IceCube's potential to search for soft spectra neutrino sources in the southern sky.

Finally, the effective area of the analysis with the current event selection has been calculated for six different ranges in the declination δ, see Figure 11.25. The event selection without the IceTop veto has been used here. The inclusion of the IceTop veto would increase the effective area in the declination bands $(-90°, -60°)$ and $(-60°, -30°)$ a bit towards lower energies while a small overall decrease in effective area would be expected across all energies in these declination bands due to random coincidences. To first order however, the presented effective area provides a good first estimation of the performance of both event selections.

The comparison of the presented effective area to previous point source analyses with IceCube is difficult as several changes have been made to the simulation since then. These changes include an update of the calculation of the interaction volume for neutrinos and a different description of the ice as well as several minor bug fixes. With the new simulation, the expected number of neutrino events for a given neutrino flux is decreased with respect to the previous simulation at almost all energies. Even the update of the calculation of the interaction volume for neutrinos alone can lead to a 30% decrease in the number of expected events at TeV energies. A complete comparison to previous analyses can therefore not be performed until these are updated with new simulation. For the northern hemisphere we can estimate the improvement in the event selection with respect to the IceCube 59-string analysis by considering the efficiency with respect to the on-line filter. The performance of the on-line filter is expected to be about the same for both detector configurations. For an E^{-2} signal neutrino flux, 62% of all up-going events in the on-line Muon filter are kept in the preliminary event selection presented here. The previous year's analysis [Agu11] kept 44% of the corresponding signal at analysis level at the same level of background contamination. An improvement of a factor 1.4 in the event selection is thus expected here.

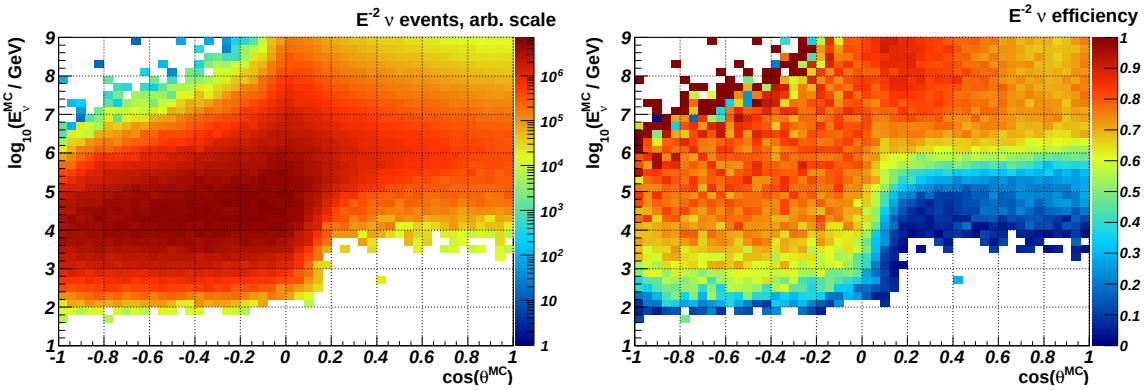

Figure 11.24.: Energy distribution and efficiency of the preliminary analysis level event selection. The event selection without IceTop veto is presented here. The neutrino signal spectrum considered here is an E^{-2} spectrum.

For atmospheric neutrinos, we observe a total improvement of a factor of 1.7 in the efficiency from the on-line filter to the preliminary high-level event selection. However, since only a worse simulation has been available in the work of [Agu11], the effective areas calculated here for the northern hemisphere are of about the same magnitude as the ones in presented there for the IceCube 59-strings configuration. The analysis in [Agu11] did not provide effective areas for the southern hemisphere. For comparison, we will therefore consider the analysis of the IceCube 40-strings data presented in [AAA+11i]. Accounting for the differences in the size of the detector, about a factor of 1.8 improvement in the effective area is expected if the same cut strategy is applied. This expectation is lowered significantly through the updates of the simulation that have happened in the meanwhile. In fact, a factor of at least 1.6 improvement in effective area is achieved across the whole southern hemisphere and all considered energies. The largest improvements are obtained for energies of about 10 TeV for intermediate and vertical down-going neutrino events; the IceCube 40-strings point source analysis and also the IceCube 59-strings point source analysis had no sensitivity at all to these events. At 100 TeV, an improvement of up to a factor of 400 in effective area is observed with respect to the IceCube 40-strings analysis. This is caused by the improved background rejection applied here.

The data sample presented here is still being optimized and improved. It is aimed to provide the base for the most sensitive search for neutrino point sources in the Galaxy and beyond as well as for the search of extended regions of neutrino emission. The event selection presented here makes use of the experience obtained in previous point source analyses, including the work on the combined IceCube 40-strings and AMANDA data sample presented in this thesis, and makes use of various innovations that have been developed inside IceCube. The event selection in the high-energy down-going region has already now been improved significantly. In addition, this analysis will be the first to explore the possibility of a search for southern sky cosmic-ray accelerators with DeepCore. While the size of DeepCore may not be sufficient to reach sensitivity to any expected signal flux by itself, it might improve the sensitivity for soft spectra sources once combined with the other two event streams. Besides, the selection of DeepCore events will then provide further possibilities to study the properties of the atmospheric neutrinos.

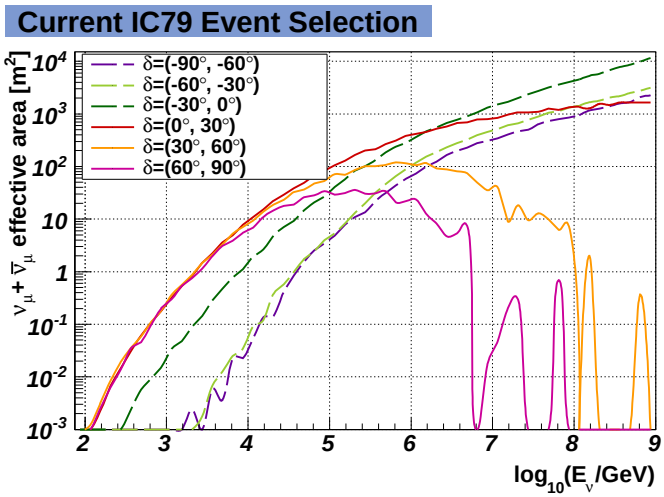

Figure 11.25.: Effective Area of the Preliminary Event Selection for IC79

A. Abbreviations

AGN	Active Galactic Nucleus
BDT	Boosted Decision Tree
CC	Charged Current
DOM	Digital Optical Module, see section 5.2
GRB	Gamma-Ray Burst
GZK cutoff	Greisen-Zatsepin-Kuzmin cutoff, see section 1.1
HLC	Hard Local Coincidence, see section 5.4
IACT	Imaging Air Cherenkov Telescope
IC40	IceCube 40-strings, all IceCube configurations are abbreviated as ICNN with NN being the number of operational strings
ICL	IceCube Laboratory
JAMS	Just Another Muon Search - first guess reconstruction for combined events, see section 7.2
MC	Monte Carlo
MPE	Multi Photo Electron
NCh	number of channels, i.e. number of active DOMs
NC	Neutral Current
PDF	Probability Density Function
SLC	Soft Local Coincidence, see section 5.4
SMT8	Simple Multiplicity Trigger, requiring at least 8 hits with local coincidence within 5 μs, see section 5.4
SNR	Supernova Remnant
SPE	Single Photo Electron

List of Figures

List of Tables

Bibliography

[AAA+06a] The AMANDA Collaboration: A. Achterberg, M. Ackermann, J. Adams, J. Ahrens, and et al. Five years of searches for point sources of astrophysical neutrinos with the AMANDA-II neutrino telescope. *Physical Review D*, 75, 2006. 67, 68

[AAA+06b] The IceCube Collaboration: A. Achterberg, M. Ackermann, J. Adams, J. Ahrens, and et al. First year performance of the IceCube neutrino telescope. *Astroparticle Physics*, 26, 2006. 30

[AAA+07a] The MAGIC Collaboration: J. Albert, E. Aliu, H. Anderhub, P. Antoranz, and et al. Discovery of Very High Energy Gamma Radiation from IC 443 with the MAGIC Telescope. *The Astrophysical Journal Letters*, 664, 2007. 9, 16

[AAA+07b] The MAGIC Collaboration: J. Albert, E. Aliu, H. Anderhub, P. Antoranz, and et al. Observation of VHE gamma-rays from Cassiopeia A with the MAGIC telescope. *Astronomy & Astrophysics*, 474, 2007. 9, 16

[AAA+08a] The HiRes Collaboration: R.U. Abbasi, T. Abu-Zayyad, M. Allen, J.F. Amman, and et al. First Observation of the Greisen-Zatsepin-Kuzmin Suppression. *Phys. Rev. Lett.*, 100, 2008. 6

[AAA+08b] The Pierre Auger Collaboration: J. Abraham, P. Abreu, M. Aglietta, C. Aguirre, and et al. Correlation of the highest-energy cosmic rays with the positions of nearby active galactic nuclei. *Astropar. Phys.*, 29, 2008. 6

[AAA+08c] The Pierre Auger Collaboration: J. Abraham, P. Abreu, M. Aglietta, C. Aguirre, and et al. Observation of the Suppression of the Flux of Cosmic Rays above $4 * 10^{19}$âeV. *Phys. Rev. Lett.*, 101, 2008. 6

[AAA+09a] The IceCube Collaboration: R. Abbasi, Y. Abdou, T. Abu-Zayyad, J. Adams, and et al. Extending the neutrino point sources with IceCube above the horizon. *Physical Review Letters*, 103(22), 2009. 20, 110, 119, 124

[AAA+09b] The IceCube Collaboration: R. Abbasi, M. Ackermann, J. Adams, M. Ahlers, and et al. The IceCube data acquisition system: Signal capture, digitization, and time-stamping. *Nuclear Instruments and Methods in Physics Research A*, 601, 2009. 31, 33

[AAA+09c] The Fermi Collaboration: A.A. Abdo, M. Ackermann, M. Ajello, W.B. Atwood, and et al. Fermi Lat Observations of LS I +61 303: First detection of an orbital modulation in GeV gamma rays. *The Astrophysical Journal*, 701, 2009. 16

[AAA+09d] The Fermi Collaboration: A.A. Abdo, M. Ackermann, M. Ajello, L. Baldini, and et al. Fermi LAT Discovery of extended gamma-ray emission in the direction of the supernova remnant W51C. *The Astrophysical Journal*, 706, 2009. 16

[AAA+09e] The VERITAS Collaboration: V.A. Acciari, E. Aliu, T. Arlen, T. Aune, and et al. Observation of extended very high energy emission from the

supernova remnant IC 443 with VERITAS. *The Astrophysical Journal Letters*, 698, 2009. 16

[AAA+09f] The H.E.S.S. Collaboration: F. Aharonian, A.G. Akhperjanian, G. Anton, U. Barres de Almeida, and et al. Spectrum and variability of the Galactic center VHE gamma-ray source HESS J1745-290. *Astronomy & Astrophysics*, 503, 2009. 9

[AAA+09g] The MAGIC Collaboration: J. Albert, E. Aliu, H. Anderhub, L.A. Antonelli, and et al. Periodic very high energy gamma-ray emission from LS I +61 303 observed with the MAGIC telescope. *The Astrophysical Journal*, 693, 2009. 9, 16

[AAA+10a] The Fermi Collaboration: A.A. Abdo, M. Ackermann, M. Ajello, L. Baldini, and et al. Gamma-Ray Emission from the Shell of Supernova Remnant W44 Revealed by the Fermi LAT. *Science*, 327, 2010. 15

[AAA+10b] The Fermi Collaboration: A.A. Abdo, M. Ackermann, M. Ajello, L. Baldini, and et al. Observation of the supernova remnant IC 443 with the Fermi Large Area Telescope. *The Astrophysical Journal*, 712, 2010. 16

[AAA+10c] The Pierre Auger Collaboration: P. Abreu, M. Aglietta, E.J. Ahn, D. Allard, and et al. Update on the correlation of the highest energy cosmic rays with nearby extragalactic matter. *Astropart. Phys.*, 314, 2010. 6, 7

[AAA+10d] The VERITAS Collaboration: V.A. Acciari, E. Aliu, T. Arlen, T. Aune, and et al. Observations of the shell-type supernova remnant Cassiopeia A at TeV energies with VERITAS. *The Astrophysical Journal*, 714, 2010. 16

[AAA+11a] The IceCube Collaboration: R. Abbasi, Y. Abdou, T. Abu-Zayyad, J. Adams, and et al. Neutrino Analysis of the September 2010 Crab Nebula Flare and time-independent constraints on neutrino emission from the Crab using IceCube, to be published in: The Astrophysical Journal, 2011. 26, 115, 117, 118

[AAA+11b] The IceCube Collaboration: R. Abbasi, Y. Abdou, T. Abu-Zayyad, J. Adams, and et al. Linefit. IceCube SVN, unpublished, 2011. 51

[AAA+11c] The IceCube Collaboration: R. Abbasi, Y. Abdou, T. Abu-Zayyad, J. Adams, and et al. Measurement of acoustic attenuation in South Pole ice. *Astroparticle Physics*, 34, 2011. 10

[AAA+11d] The IceCube Collaboration: R. Abbasi, Y. Abdou, T. Abu-Zayyad, J. Adams, and et al. Measurement of the atmospheric neutrino energy spectrum from 100 GeV to 400 TeV with IceCube. *Phys. Rev. D*, 83, 2011. 21

[AAA+11e] The IceCube Collaboration: R. Abbasi, Y. Abdou, T. Abu-Zayyad, J. Adams, and et al. Multi-year search for dark matter annihilations in the Sun with the AMANDA-II and IceCube detectors. to be published, 2011. 38, 40

[AAA+11f] The IceCube Collaboration: R. Abbasi, Y. Abdou, T. Abu-Zayyad, J. Adams, and et al. Observation of Anisotropy in the Arrival Directions of Galactic Cosmic Rays at Multiple Angular Scales with IceCube. *The Astrophysical Journal*, 740, 2011. 6, 7

[AAA+11g] The IceCube Collaboration: R. Abbasi, Y. Abdou, T. Abu-Zayyad, J. Adams, and et al. Study of South Pole ice transparency with IceCube flashers. to be published, 2011. 34, 64, 65

[AAA+11h] The IceCube Collaboration: R. Abbasi, Y. Abdou, T. Abu-Zayyad, J. Adams, and et al. The Design and

Performance of IceCube DeepCore. to be published, 2011. 31, 40

[AAA+11i] The IceCube Collaboration: R. Abbasi, Y. Abdou, T. Abu-Zayyad, J. Adams, and et al. Time-integrated Searches for Point-like Sources of Neutrinos with the 40-string IceCube Detector. *The Astrophysical Journal*, 732, 2011. 24, 59, 83, 85, 86, 94, 100, 107, 110, 119, 124, 130

[AAA+11j] The Antares Collaboration: M. Ageron, J.A. Aguilar, I. Al Samarai, A. Albert, and et al. ANTARES: the first undersea neutrino telescope. *Science*, (December 2010), 2011. 11

[AAB+00] The AMANDA Collaboration: E. Andres, P. Askebjer, S.W. Barwick, R. Bay, and et al. The AMANDA neutrino telescope: principle of operation and first results. *Astropart. Phys.*, 13, 2000. 37

[AAB+01a] The HEGRA Collaboration: F. Aharonian, A. Akhperjanian, J. Barrio, K. Bernlöhr, and et al. Evidence for TeV gamma ray emission from Cassiopeia A. *Astronomy & Astrophysics*, 370, 2001. 16

[AAB+01b] The IceCube Collaboration: J. Ahrens, J.R. Alonso, J.N. Bahcall, X. Bai, and et al. IceCube Preliminary Design Document. 2001. 32

[AAB+01c] The AMANDA Collaboration: E. Andres, P. Askebjer, X. Bai, G. Barouch, and et al. Observation of high-energy neutrinos using Cerenkov detectors embedded deep in the Antarctic ice. *Nature*, 410, 2001. 29, 37

[AAB+05a] The AMANDA Collaboration: M. Ackermann, J. Ahrens, X. Bai, M. Bartelt, and et al. Optical properties of deep glacial ice at the South Pole. *Journal of Geophysical Research*, 111, 2005. 33, 34, 38, 54, 64, 65

[AAB+05b] The H.E.S.S. Collaboration: F. Aharonian, A.G. Akhperjanian, A.R. Bazer-Bachi, M. Beilicke, and et al. A New Population of Very High Energy Gamma-Ray Sources in the Milky Way. *Science*, 307, 2005. 14

[AAB+06a] The AMANDA Collaboration: M. Ackermann, J. Ahrens, X. Bai, M. Bartelt, and et al. The IceCube prototype string in AMANDA. *Nuclear Instruments and Methods in Physics Research A*, 556, 2006. 37, 38, 39

[AAB+06b] The H.E.S.S. Collaboration: F. Aharonian, A.G. Akhperjanian, A.R. Bazer-Bachi, M. Beilicke, and et al. First detection of a VHE gamma-ray spectral maximum from a cosmic source: HESS discovery of the Vela X nebula. *Astronomy & Astrophysics*, 448, 2006. 9

[AAB+06c] The H.E.S.S. Collaboration: F. Aharonian, A.G. Akhperjanian, A.R. Bazer-Bachi, M. Beilicke, and et al. Observation of the Crab Nebula with H.E.S.S. *Astronomy & Astrophysics*, 2006. 9, 16, 94, 97

[AAB+06d] The H.E.S.S. Collaboration: F. Aharonian, A.G. Akhperjanian, A.R. Bazer-Bachi, M. Beilicke, and et al. The H.E.S.S. Survey of the Inner Galaxy in Very High Energy Gamma Rays. *The Astrophysical Journal*, 636, 2006. 14

[AAB+07] The H.E.S.S. Collaboration: F. Aharonian, A.G. Akhperjanian, A.R. Bazer-Bachi, M. Beilicke, and et al. Primary particle acceleration above 100 TeV in the shell-type supernova remnant RX J1713.7-3946 with deep HESS observations. *Astronomy & Astrophysics*, 464, 2007. 9

[AABB04] The HEGRA Collaboration: F. Aharonian, A. Akhperjanian, M. Beilicke, and K. Bernlöhr. The Crab Nebula and Pulsar between 500 GeV

and 80 TeV: Observations with the HEGRA Stereoscopic Air Cerenkov Telescopes. *The Astrophysical Journal*, 614, 2004. 16, 98

[AABB07] The MILAGRO Collaboration: A.A. Abdo, B. Allen, D. Berley, and E. Blaufuss. Discovery of TeV Gamma-Ray Emission from the Cygnus Region of the Galaxy. *The Astrophysical Journal*, 658, 2007. 17, 98, 99

[ABB+04] The AMANDA Collaboration: J. Ahrens, X. Bai, M. Bartelt, S.W. Barwick, and et al. Muon Track Reconstruction and Data Selection Techniques in AMANDA. *Nuclear Instruments and Methods A*, 524, 2004. 49, 51, 52, 53, 54

[ABB+08] The VERITAS Collaboration: V.A. Acciari, M. Beilicke, G. Blaylock, S.M. Bradbury, and et al. VERITAS Observations of the Gamma-Ray Binary LS I +61 303. *The Astrophysical Journal*, 679, 2008. 16

[ACM11] J. Auffenberg, S. Cohen, and K. Mase. New background rejection methods for the cosmogenic neutrino search with IceCube. In *Proceedings of the 32th International Cosmic Ray Conference*, 2011. 31, 101, 120, 123, 127

[AGLS96] V. Agrawal, T.K. Gaisser, P. Lipari, and T. Stanev. Atmospheric neutrino flux above 1 GeV. *Phys. Rev. D*, 53, 1996. 20

[Agu11] J.A. Aguilar. Time-independent searches for astrophysical neutrino sources with the combined data of 59 and 40 strings of IceCube. In *Proceedings of the 32th International Cosmic Ray Conference*, 2011. 109, 110, 111, 116, 117, 118, 119, 124, 129, 130

[And33] C.D. Anderson. The Positive Electron. *Phys. Rev.*, 43, 1933. 3

[And11] K. Andeen. *First Measurements of Cosmic Ray Composition from 1-50 PeV using New Techniques on Coincident Data from the IceCube Neutrino Observatory*. PhD thesis, University of Wisconsin - Madison, 2011. 31

[Auf11] J. Auffenberg. Who to do a blind analysis with IceTop Veto. IceCube Autumn Collaboration Meeting 2011, unpublished, 2011. 31, 101, 120, 127

[Bak09] M. Baker. Proposal for IceCube 79-Strings Muon Filter. unpublished, 2009. 103, 107

[Baz10] J. L. Bazo Alba. *Search for steady and flaring astrophysical neutrino point sources with the IceCube detector*. PhD thesis, Humboldt Universität zu Berlin, 2010. 27

[BCH+11] The KM3Net Collaboration: P. Bagley, J. Craig, A. Holford, A. Jamieson, T. Niedzielski, and et al. KM3NeT Technical Design Report for a Deep-Sea Research Infrastructure in the Mediterranean Sea Incorporating a Very Large Volume Neutrino Telescope, 2011. 11

[BDD+08] J. Braun, J. Dumm, F. De Palma, C. Finley, A. Karle, and Teresa M. Methods for point source analysis in high energy neutrino telescopes. Jan 2008. 27, 28, 93, 101

[BE87] R. Blandford and D. Eichler. Particle acceleration at astrophysical shocks: A theory of cosmic ray origin. *Phys. Rev.*, 154, 1987. 5

[BEH09] J. Bluemer, R. Engel, and J.R. Hörandel. Cosmic Rays from the Knee to the Highest Energies, 2009. Invited review, submitted to Progress in Particle and Nuclear Physics. 4, 5, 6

[Ber96] E.G. Berezhko. Maximum energy of cosmic rays accelerated by supernova shocks. *Astroparticle Physics*, 5, 1996. 5, 15

[Ber11] P. Berghaus. High energy muons in ic59. IceCube Autumn Collaboration Meeting, unpublished, 2011. 120

[BG00] P. Bhattacharjee and Sigl G. Origin and propagation of extremely high-energy cosmic rays. *Physics Reports*, 327, 2000. 6

[BGK09] D. Boersma, L. Gladstone, and A. Karle. Moon Shadow Observation by IceCube. In *Proceedings of the 31th International Cosmic Ray Conference*, 2009. 57

[BGL+04] G.D. Barr, T.K. Gaisser, P. Lipari, S. Robbins, and T. Stanev. Three-dimensional calculation of atmospheric neutrinos. *Phys. Rev. D*, 70, 2004. 21, 64, 76, 81, 82, 83, 84

[Bla08] E. Blaufuss. TFT 2008 Season Planning. IceCube wiki, unpublished, 2008. 46

[BPV03] E.G. Berezhko, G. Puehlhofer, and H.J. Voelk. Gamma-ray emission from Cassiopeia A produced by accelerated cosmic rays. *Astronomy & Astrophysics*, 400, 2003. 15

[BSW10] M. Baker, A. Schukraft, and M. Walraff. IC59 Muon L3 Processing. IceCube Wiki, unpublished, 2010. 104, 107, 112

[Bur08] T. Burgess. *A Search for Solar Neutralino Dark Matter with the AMANDA-II Neutrino Telescope*. PhD thesis, Universitet Stockholms, 2008. 52

[Bus00] R. Buser. The formation and early evolution of the milky way galaxy. *Science*, 287, 2000. 13

[BV00] E. G. Berezhko and H. J. Völk. Kinetic theory of cosmic ray and gamma-ray production in supernova remnants expanding into wind bubbles. *Astronomy & Astrophysics*, 357, 2000. 5

[BWA+05] W.R. Binns, M.E. Wiedenbeck, M. Arnould, A.C. Cummings, and et al. Cosmic-ray neon, wolf-rayet stars, and the superbubble origin of galactic cosmic rays. *The Astrophysical Journal*, 634, 2005. 5

[BZ34] W. Baade and F. Zwicky. Cosmic Rays from Super-Novae. *Proceedings of the National Academy of Science*, 20, 1934. 15

[Cab11] K.S. Caballero Mora. Low NChannel Discrepancy IC79. IceCube wiki, unpublished, 2011. 114

[CBHP03] J. Conrad, O. Botner, A. Hallgren, and C. Pérez de los Heros. Including systematic uncertainties in confidence interval construction for Poisson statistics. *Phys. Rev. D*, 67:012002, Jan 2003. 96

[CD11] A. Castellina and F. Donato. Astrophysics of Galactic charged cosmic rays. Technical Report arXiv:1110.2981, 2011. Invited review, to appear in Vol.5 of "Planets, Stars and Stellar Systems", 1st Edition., 2012, 4760 p., Springer, ISBN 978-90-481-8817-8 Due: February 15, 2012. 4, 5

[Chi08] D. Chirkin. Neutrino search with icecube. Internal Report, unpublished, 2008. 60, 71, 103, 109, 123

[Chi11] D. Chirkin. Topological trigger algorithm. IceCube SVN, unpublished, 2011. 112

[Cho07] S. Choubey. Signature of sterile species in atmospheric neutrino data at neutrino telescopes. *Journal of High Energy Physics*, 2007, 2007. 84

[CSS08] A. Cooper-Sarkar and S. Sarkar. Predictions for high energy neutrino cross-sections from the ZEUS global PDF fits. *Journal of High Energy Physics*, 2008, 2008. 66

[DA08] L.O'C. Drury and F.A. Aharonian. The puzzling MILAGRO hot spots. *Astroparticle Physics*, 29(6), 2008. 7

[DGWL02] C. Distefano, D. Guetta, E. Waxman, and A. Levinson. Neutrino Flux Predictions for Known Galactic Microquasars. *The Astrophysical Journal*, 575, 2002. 17

[Dru83] L. O'C. Drury. An introduction to the theory of diffusive shock acceleration of energetic particles in tenuous plasmas. *Reports on Progress in Physics*, 46, 1983. 5

[DS11] M. Danninger and E. Strahler. Ic79 solarwimp analysis. IceCube wiki, unpublished, 2011. 113

[Dum09] J. Dumm. Gulliver's "NoiseProbability" Term in (Coincident) Muon Reconstruction. Presentation to the IceCube Muon Working Group, unpublished, 2009. 117

[Eul08] S. Euler. On the Detection of Low Energy Neutrino Events with Full-Sky Acceptance with the IceCube DeepCore Detector. Diplomarbeit, RWTH Aachen, 2008. 103, 104, 114

[FC98] G.J. Feldman and R.D. Cousins. Unified approach to the classical statistical analysis of small signals. *Phys. Rev. D*, 57:3873–3889, Apr 1998. 96

[Fer49] E. Fermi. On the origin of the cosmic radiation. *Phys. Rev.*, 75, 1949. 4

[FMCT09] A. Fiasson, V. Marandony, R.C.G. Chaves, and O. Tibolla. Discovery of a VHE gamma-ray source in the W51 region. In *Proceedings of the International Cosmic Ray Conference*, 2009. 16

[Fra07] R. Franke. A new Approach to the Search for Point-like Sources of Cosmic Neutrinos at PeV Energies with AMANDA-II. Diplomarbeit, Humboldt-Universität zu Berlin, 2007. 52

[Fri00] J.H. Friedman. Greedy Function Approximation: A Gradient Boosting Machine. *Annals of Statistics*, 29:1189–1232, 2000. 25, 26, 124

[FS96] Y. Freund and R. E. Schapire. Experiments with a New Boosting Algorithm. In *International Conference on Machine Learning*, 1996. 25, 118, 124

[Gab09] S. Gabici. Gamma Ray Astronomy and the Origin of Galactic Cosmic Rays, 2009. http://arxiv.org/abs/0811.0836. 6, 15

[Gai06] T.K. Gaisser. Atmospheric Neutrinos. In *Neutrino 2006*, 2006. 21

[GBB+07] The ANITA Collaboration: P.W. Gorham, S.W. Barwick, J.J. Beatty, D.Z. Besson, and et al. Observations of the askaryan effect in ice. *Phys. Rev. Lett.*, 99, 2007. 10

[GBH08] S Grullon, D. Boersma, and G.C. Hill. Photonics-based Log-Likelihood Reconstruction in IceCube. Internal Report, unpublished, 2008. 103

[GK05] A. Gazizov and M. P. Kowalski. ANIS: High energy neutrino generator for neutrino telescopes. *Comput. Phys. Commun.*, 172, 2005. 64, 66

[GQRS98] R. Gandhi, C. Quigg, M.H. Reno, and I. Sarcevic. Neutrino interactions at ultrahigh energies. *Phys. Rev. D*, 58, 1998. 10

[Gra09] D. Grant. Proposal for IceCube 79-Strings DeepCore Filter. unpublished, 2009. 104

[Gre66] K. Greisen. End to the Cosmic-Ray Spectrum? *Phys. Rev. Lett.*, 16, 1966. 6

[Gro07a] A. Gross. Proposal for the JAMS Muon Filter. unpublished, 2007. 43

[Gro07b] A. Gross. TWRFlareChecker. IceCube SVN, unpublished, 2007. 44

[Gro08] C. Amsler (Particle Data Group). Pl b667, 1 and 2009 partial update for the 2010 edition. 2008. 10, 50, 51

[Gro11] A. Gross. Muon L3 Coincident events. IceCube wiki, unpublished, 2011. 106, 111, 113

[GRTT07] A. Gross, E. Resconi, A. Tepe, and M. Tluczykont. The Combined AMANDA and IceCube Neutrino Telescope. In *Proceedings of the 30th International Cosmic Ray Conference*, 2007. 41

[GS11] A. Gross and E. Strahler. IC79 offline processing. IceCube wiki, unpublished, 2011. 103

[Ha11] C.H. Ha. Observation of Atmospheric Neutrino-induced Cascades in IceCube-DeepCore. In *Proceedings of the 32th International Cosmic Ray Conference*, 2011. 26, 101, 115

[Hes12] V.F. Hess. Über Beobachtungen der durchdringenden Strahlung bei sieben Freiballonfahrten. *Phys. Zeitschr.*, 13, 1912. 3

[Hil84] A.M. Hillas. The Origin of Ultra-High-Energy Cosmic Rays. *Annual review of astronomy and astrophysics*, 22, 1984. 5

[Hil03] G.C. Hill. Comment on "Including systematic uncertainties in confidence interval construction for Poisson statistics". *Phys. Rev. D*, 67:118101, Jun 2003. 96

[HK08] F. Halzen and S. Klein. Astronomy and astrophysics with neutrinos. *Physics Today*, 61, 2008. 29

[HKC+98] D. Heck, J. Knapp, J.N. Capdevielle, G Schatz, and D. Thouw. CORSIKA: A Monte Carlo Code to Simulate Extensive Air Showers. Technical report, 1998. 20, 21, 64

[HKKS07] M. Honda, T Kajita, S. Kasahara, K.and Midorikawa, and T. Sanuki. Calculation of atmospheric neutrino flux using the interaction model calibrated with atmospheric muon data. *Phys. Rev. D*, 75, 2007. 21, 64, 84

[HL06] J.C. Higdon and R.E. Lingenfelter. The superbubble origin for galactic cosmic rays. *Advances in Space Research*, 37, 2006. 5

[Hoe03] J. R. Hoerandel. On the knee in the energy spectrum of cosmic rays. *Astropart. Phys.*, 19, 2003. 64

[HSS+07] A. Hoecker, P. Speckmayer, J. Stelzer, J. Therhaag, and et al. TMVA - Toolkit for Multivariate Data Analysis. *POSACAT*, 040, 2007. 24, 25, 26, 116

[HTF09] T. Hastie, R. Tibshirani, and J. Friedman. *The elements of statistical learning: data mining, inference and prediction*. Springer, 2 edition, 2009. 23, 25, 26, 115

[KA08] S.R. Kelner and F.A. Aharonian. Energy spectra of gamma rays, electrons, and neutrinos produced at interactions of relativistic protons with low energy radiation. *Phys. Rev. D*, 78, 2008. 9

[KAB06] S.R. Kelner, F A. Aharonian, and V.V. Bugayov. Energy spectra of gamma rays, electrons, and neutrinos produced at proton-proton interactions in the very high energy regime. *Phys. Rev. D*, 74, 2006. 8, 9, 94, 99

[KCR11] J. Krause, E. Carmona, and I. Reichardt. Probing proton acceleration in W51C with MAGIC. In *Proceedings of the 2011 Fermi Symposium*, 2011. 9, 16

[KKKW09] F. Kislat, S. Klepser, H. Kolanoski, and T. Waldenmaier. A First All-Particle Cosmic Ray Energy Spectrum From IceTop. In *Proceedings of the 31th International Cosmic Ray Conference*, 2009. 31

[Kur11] N. Kurahashi. Muon L3 Issues. Slides circulated to the IceCube muon and point source working groups, unpublished, 2011. 111, 113

[LH07] R. Lauer and W. Huelsnitz. Proposal for the IceCube 40-Strings Muon Filter, unpublished, 2007. 42, 43

[LHK+00] H.L Lai, J. Huston, S. Kuhlmann, J. Morfin, F. Olness, J.F. Owens, J. Pumplin, and W.K. Tung. Global QCD analysis of parton structure of the nucleon: CTEQ5 parton distributions. *European Physical Review Journal C*, 12, 2000. 66

[LM00] J. G. Learned and K. Mannheim. High-Energy Neutrino Astrophysics. *Annual Review of Nuclear and Particle Science*, 50, 2000. 10

[LMW+07] J. Lundberg, P. Miocinovic, K. Woschnagg, T. Burgess, J. Adams, S. Hundertmark, P. Desiati, and P. Niessen. Light tracking through ice and water-Scattering and absorption in heterogeneous media with Photonics. *Nuclear Instruments and Methods in Physics Research Section A*, 2007. 64

[LPRS81] J. G. Learned, V. Z. Peterson, A. Roberts, and V. J. Stenger. DUMAND - An Undersea Neutrino Telescope. In *Bulletin of the American Astronomical Society*, volume 13 of *Bulletin of the American Astronomical Society*, 1981. 11

[LSS11] A. Letessier-Selvon and T. Stanev. Ultrahigh Energy Cosmic Rays, 2011. arXiv:1103.0031v1. 4

[Lub03] B.K. Lubsandorzhiev. The lake Baikal neutrino experiment: present status and future prospects. *Nuclear Instruments and Methods in Physics Research Section A: Accelerators, Spectrometers, Detectors and Associated Equipment*, 502, 2003. 11

[Lue08] J. Luenemann. Lower bounds on muon track reconstruction resolution. IceCube Spring Collaboration Meeting 2008, unpublished, 2008. 103, 104

[MFM02] S. Migliari, R. Fender, and M. Mendez. Iron Emission Lines from Extended X-ray Jets in SS 433: Reheating of Atomic Nuclei. *Science*, 297, 2002. 17

[Mia11] S. Miarecki. I3TruncatedEnergy: Measuring muon energy using the truncated mean of dE/dx. IceCube Collaboration Meeting, Autumn 2011, unpublished, 2011. 101, 118

[Neu06] T. Neunhöffer. Estimating the angular resolution of tracks in neutrino telescopes based on a likelihood analysis. *Astropart.Phys.*, 25, 2006. 58

[NJCS08] NASA, JPL-Caltech, and R. Hurt (SSC/Caltec). A Roadmap to the Milky Way (Annotated), 2008. 14

[NP33] J. Neyman and E.S. Pearson. On the Problem of the Most Efficient Tests of Statistical Hypotheses. *Philosophical Transactions of the Royal Society of London. Series A, Containing Papers of a Mathematical or Physical Character*, 231:289–337, 1933. 24

[PZ03] V.S. Ptuskin and V.N. Zirakashvili. Limits on diffusive shock acceleration in supernova remnants in the presence of cosmic-ray streaming instability and wave dissipation. *Astronomy & Astrophysics*, 403, 2003. 5, 15

[RC01] W. Rhode and D. Chirkin. Muon Monte Carlo: A new high-precision tool for muon propagation through matter. 2001. 50, 64

[Res09] E. Resconi. Status and prospects of the IceCube neutrino telescope. *Nucl. Instrum. Meth. A*, 602, 2009. 38, 40

[RLL+09] B.F. Rauch, J.T. Link, K. Lodders, M.H. Israel, and et al. Cosmic-ray origin in OB associations and preferential acceleration of refractory elements: Evidence from abundances of elements 26Fe through 34Se. *Astrophysical Journal*, 697, 2009. 5

[Sch10] O. Schulz. *The design study of IceCube DeepCore: Characterization and veto studies*. PhD thesis, Universität Heidelberg, 2010. 19, 20, 30, 100, 101, 103

[Sch11a] A. Schukraft. Search for a diffuse flux of astrophysical muon neutrinos with the IceCube Detector. In *Proceedings of the 32th International Cosmic Ray Conference*, 2011. 113

[Sch11b] O. Schulz. Muon L3 Status. IceCube Autumn Collaboration Meeting 2011, unpublished, 2011. 106

[Sec11] D. Seckel. Dom noise rates and deadtime. IceCube Spring Collaboration Meeting 2011, unpublished, 2011. 114

[Ses10] Y. Sestayo. *Search for high energy neutrinos from our Galaxy with IceCube*. PhD thesis, Universität Heidelberg, 2010. 17, 28, 44, 62, 73, 77, 93, 94, 95, 97, 100, 101

[SG10] L.S. Sparke and J.S. Gallagher. *Galaxies in the Universe*. Cambridge University Press, 2nd edition, 2010. 13

[Spi07] C. Spiering. Astroteilchenphysik - Erfolge und Perspektiven, 2007. 10

[SS37] J.C. Street and E.C. Stevenson. New Evidence for the Existence of a Particle of Mass Intermediate Between the Proton and Electron. *Phys. Rev.*, 52, 1937. 3

[Tep09] A. Tepe. *Hardware Integration of the AMANDA into the IceCube Neutrino Telescope and Search for Supersymmetric Particles with the IceCube Neutrino Telescope*. PhD thesis, Bergische Universität Wuppertal, 2009. 39, 40

[TGC+10] The AGILE Collaboration: M. Tavani, A. Giuliani, A.W. Chen, A. Argan, and et al. Direct evdence for hadronic cosmic-ray acceleration on the supernova remnant IC 443. *The Astrophysical Journal*, 710, 2010. 16

[Vog10] M. Voge. Time-Dependent Search for Astrophysical Neutrinos from Microquasar Cygnus X-3 using IceCube and AMANDA. Diplomarbeit, Universität Hamburg, 2010. 26, 100

[WH11] S. Wakely and D. Horan. TeVCat, 2011. http://tevcat.uchicago.edu/. 15

[Whi11] N. Whitehorn. Results from high-energy neutrino searches from gamma-ray bursts with IceCube, 2011. Talk at TAUP 2011, München. 6

[Wol11] M. Wolf. Investigation of IceCube Energy Estimators. IceCube Collaboration Meeting, Autumn 2011, unpublished, 2011. 101, 118, 123

[WRL+04] M.W. Werner, T.L. Roellig, F.J. Low, G.H. Rieke, and et al. The Spitzer Space Telescope Mission. *The Astrophysical Journal Supplement Series*, 154, 2004. 13

[ZC08] J. Zornoza and D. Chirkin. Muon energy reconstruction and atmospheric neutrino spectrum unfolding with the IceCube detector. In *Proceedings of the 30th International Cosmic Ray Conference*, 2008. 60

[ZK66] G. T. Zatsepin and V. A. Kuz'min. Upper Limit of the Spectrum of Cosmic Rays. *Journal of Experimental and Theoretical Physics Letters*, 4, 1966. 6

Acknowledgements

First of all, I want to thank my supervisor, Elisa Resconi, who has always encouraged me, has always been a friend as well as a group leader and who has, in particular towards the end of my PhD, given me an enormous, but really enormous, amount of freedom.
I would also like to thank Prof. Werner Hofmann and Prof. Marek Kowalski who kindly agreed to referee this thesis.
I acknowledge funding through the Klaus Tschira Stiftung for the work presented in this thesis and I would also like to thank the HGSFP (Heidelberg Graduate School of Fundamental Physics) for arranging this fellowship and for financial support of an expensive summer school at SLAC.
I have worked in a small, ever-moving and in the last year spatially distributed group of extraordinary people and would like to thank all of them: Elisa Resconi; Andreas Gross for his unfaltering readiness to look at and understand every plot I produce; Cécile Roucelle; Claudine Colnard; Olaf Schulz, for considering even ”loud and aggressive please” in the office music playlist and for listening patiently to all my non-expert opinions about football; Yolanda Sestayo, for her belief in neutrino sources; Markus Voge and Martin Wolf.
It has been and will be a pleasure to be part of the IceCube collaboration and this work would not have been possible without the everyone’s work on the software and the understanding of the detector. I would like to thank especially the muon and point source working groups where most of my work has been discussed. In particular, I would like to mention Chad Finley, Patrick Berghaus, Jon Dumm, Robert Lauer, Robert Franke, José Luis Bazo Alba and Mike Baker for useful comments, help and refereeing of my work. I would also like to thank Tom Feusels for drawing my attention to the muon bundles.
One of the best experiences during this time has certainly been to travel to the South Pole to work on this amazing detector. I want to thank Mark Krasberg a million times for trusting me enough to let me do commissioning and again Elisa who dedicated a significant amount of the group’s travel budget to this. I would also like to thank the colleagues and friends who made an unbelievable experience even more pleasant: Reina Maruyama, Tom Feusels, Tilo Waldenmaier, Paul McGuire, Lisa Gerhardt, Jason Koskinen and Boobah.
I would like to thank all past and present high-energy astrophysicists from our corridor as well as the cooking ladies Olga Zacharopoulou, Kathrin Koch, Kelly Foyle and Dave Jones for having made many lunches and dinners more sociable.
Meinen Eltern, Gela und Piet, danke ich für ihre Liebe und Unterstützung, und für ihren Glauben, dass ich “trotz Physik noch normal” sei.
Even if I have seen some of them only very rarely during this time in Heidelberg, I would like to thank also my friends Jessica, Susanne, Olaf, particularly Alexandra for all her assistance, and for the best memories I have of this time also all the great guys and girls who studied with me (Christian, Birthe, Lisa, Theo, Christoph, Christoph and Thorsten).
Finally but most importantly, I want to thank Thorsten for making me laugh (about my own clumsiness) every day.